

**THE COMPOSITION OF THE LUNAR CRUST:
RADIATIVE TRANSFER MODELING AND ANALYSIS OF LUNAR VISIBLE AND
NEAR-INFRARED SPECTRA**

A DISSERTATION SUBMITTED TO THE GRADUATE DIVISION OF THE
UNIVERSITY OF HAWAI'I IN PARTIAL FULFILLMENT OF THE
REQUIREMENTS FOR THE DEGREE OF

DOCTOR OF PHILOSOPHY

IN

GEOLOGY AND GEOPHYSICS

DECEMBER 2009

By
Joshua T.S. Cahill

Dissertation Committee:

Paul G. Lucey, Chairperson
G. Jeffrey Taylor
Patricia Fryer
Jeffrey J. Gillis-Davis
Trevor Sorensen

Student: Joshua T.S. Cahill
Student ID#: 1565-1460
Field: Geology and Geophysics
Graduation date: December 2009

Title: The Composition of the Lunar Crust: Radiative Transfer Modeling and Analysis of Lunar Visible and Near-Infrared Spectra

We certify that we have read this dissertation and that, in our opinion, it is satisfactory in scope and quality as a dissertation for the degree of Doctor of Philosophy in Geology and Geophysics.

Dissertation Committee:

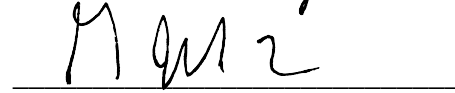
Names

Signatures

Paul G. Lucey, Chairperson



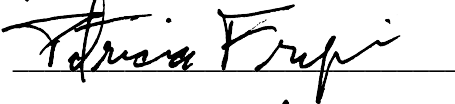
G. Jeffrey Taylor



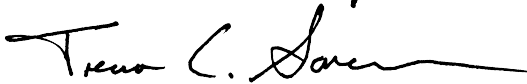
Jeffrey J. Gillis-Davis



Patricia Fryer



Trevor Sorensen



ACKNOWLEDGEMENTS

I must first express my love and appreciation to my family. Thank you to my wife Karen for providing love, support, and perspective. And to our little girl Maggie who only recently became part of our family and has already provided priceless memories in the form of beautiful smiles, belly laughs, and little bear hugs. The two of you provided me with the most meaningful reasons to push towards the "finish line". I would also like to thank my immediate and extended family. Many of them do not fully understand much about what I do, but support the endeavor acknowledging that if it is something I'm willing to put this much effort into, it must be worthwhile.

I am forever thankful to my research advisor, Dr. Paul Lucey. It is difficult to calculate how grateful I am that he granted me the opportunity to be a part of his scientific world of lunar geology and spectroscopy. It has been a privilege to learn from a man with a unique blend of scientific ambition and creativity tempered with a large dose of humor, extraordinary patience, and solid family values. I do not remember a time when he was more critical of me than he was of himself. Although naïve, I can only hope I may one day measure up to at least his example if not his status as a scientist.

Thank you to my remaining committee members Dr. Jeff Taylor, Dr. Jeff Gillis-Davis, Dr. Patty Fryer, Dr. Eric Hochberg, and Dr. Trevor Sorensen. I simply couldn't have requested a better, more fun, or sensible group of scientific evaluators. I would also like to thank Dr. Will Koeppen, Dr. Brett Denevi, Dr. Samuel Lawrence, Dr. Meryl McDowell, Dr. Miriam Riner, Christopher Hamilton, and Donovan Steutel for their council and friendship during varying stages of this degree. I hope these friendships both personally and professionally continue indefinitely into the future.

ABSTRACT

This dissertation has two focuses: (1) the evaluation and validation of algorithms used for analysis of lunar visible and near-infrared data sets, and (2) the determination of lunar surface and sub-surface crustal composition by virtue of these algorithms. To that end, the results and interpretation reported herein further enhance knowledge of lunar ferroan anorthosite (FAN) and magnesium-suite (Mg-suite) mineralogy, chemistry, and distribution on and in our Moon's crust.

TABLE OF CONTENTS

ACKNOWLEDGEMENTS	IV
ABSTRACT	V
TABLE OF CONTENTS.....	VI
LIST OF TABLES	IX
LIST OF FIGURES	X
LIST OF ABBREVIATIONS AND VARIABLES	XIII
CHAPTER 1. INTRODUCTION	1
OVERVIEW	2
BASIC LUNAR PETROLOGY, A BRIEF SUMMARY	3
OUTLINE OF STUDIES	6
<i>Modeling of lunar highlands spectral classes.....</i>	<i>6</i>
<i>The composition of impact crater central peaks.....</i>	<i>6</i>
<i>Modeling of lunar mare and highland soils:</i>	<i>8</i>
<i>Modeling of lunar nearside, near-infrared telescopic spectra.....</i>	<i>9</i>
CHAPTER 2. RADIATIVE TRANSFER MODELING OF LUNAR HIGHLANDS SPECTRAL CLASSES AND RELATIONSHIP TO LUNAR SAMPLES	11
ABSTRACT	12
INTRODUCTION.....	13
APPROACH	15
RESULTS.....	27
<i>Mineralogy of Lunar Spectral Classes.....</i>	<i>29</i>
<i>Analysis of Bullialdus Crater.....</i>	<i>36</i>
DISCUSSION	47
CONCLUSIONS	50
FUTURE WORK	51
ACKNOWLEDGEMENTS.....	52
CHAPTER 3. THE COMPOSITIONAL VARIATIONS OF THE LUNAR CRUST: RESULTS FROM RADIATIVE TRANSFER MODELING OF CENTRAL PEAK SPECTRA.....	53
ABSTRACT	54
INTRODUCTION.....	55
APPROACH	57
<i>Modeling Crustal Thickness.....</i>	<i>57</i>
<i>Modeling Peak Depth of Origin.....</i>	<i>59</i>
<i>Determination of Central Peak Origin in the Crust.....</i>	<i>60</i>
<i>Spectral Analysis Approach</i>	<i>62</i>
RESULTS.....	66
<i>Analysis of Finsen central peak</i>	<i>66</i>

<i>Central Peak Composition Relative to Lunar samples</i>	66
<i>Composition relative to crustal thickness</i>	75
<i>Composition relative to peak origin</i>	75
<i>Composition of peaks laterally</i>	77
DISCUSSION	81
CONCLUSIONS	85
FUTURE WORK	86
ACKNOWLEDGEMENTS.....	87
CHAPTER 4. RADIATIVE TRANSFER MODELING OF NEAR-INFRARED REFLECTANCE OF LUNAR HIGHLAND AND MARE SOILS	88
ABSTRACT	89
INTRODUCTION	90
THE ALGORITHM	90
<i>Spectral Mixing Model</i>	93
<i>Physical and Chemical Assumptions</i>	96
<i>Fit Criteria</i>	97
<i>Iron Abundance</i>	97
<i>Spectral Slope</i>	99
<i>Spectral Correlation and Contrast</i>	99
<i>Gradient Descent Methodology</i>	100
MODEL VALIDATION.....	100
<i>Validation Data</i>	100
<i>Preparing for Model and Measurement Comparison</i>	101
<i>Optical Constant Selection</i>	104
PERFORMANCE AGAINST LSCC SOILS	107
<i>Lunar Soil Spectral Modeling</i>	107
<i>Model Mineralogy of Lunar Soils</i>	107
<i>Chemical Modeling of Lunar Soils</i>	113
DISCUSSION	116
CONCLUSIONS	119
FUTURE WORK	120
ACKNOWLEDGEMENTS.....	121
CHAPTER 5. RADIATIVE TRANSFER MODELING OF NEAR-INFRARED TELESCOPIC SPECTRA OF SELECTED LOCATIONS ON THE LUNAR NEARSIDE	122
ABSTRACT	123
INTRODUCTION	124
COMPOSITION EXTRACTION ALGORITHM	125
<i>Spectral Computation and Mixing Model</i>	128
<i>Physical and Chemical Assumptions</i>	131
<i>Fit Criteria</i>	132
<i>Gradient Descent Methodology</i>	133
TELESCOPIC SPECTRA	134
MODEL FITS OF TELESCOPIC SPECTRA.....	134
MODEL MINERALOGY RELATIVE TO LUNAR SAMPLES.....	137

<i>Lunar Highlands and Mare Samples</i>	137
RESULTS.....	141
<i>Model Composition</i>	141
MODELING AT A FIXED MG'	146
DISCUSSION.....	146
<i>Model Performance</i>	146
<i>Modeling Implications</i>	152
CONCLUSIONS.....	155
ACKNOWLEDGEMENTS.....	156
APPENDIX A	157
APPENDIX B	194
REFERENCES	200

LIST OF TABLES

TABLE 2.1: ESTABLISHED SPECTRAL CLASS THRESHOLDS	25
TABLE 2.2: COMPILATION OF FERROAN ANORTHOSITE MINERALOGIES AND CHEMISTRIES	30
TABLE 2.3: COMPILATION OF MG-SUITE MINERALOGIES AND CHEMISTRIES	31
TABLE 2.4: MODEL RESULTS OF SPECTRAL CLASS AN SPECTRA IDENTIFIED ON BULLIALDUS	41
TABLE 2.5: MODEL RESULTS OF SPECTRAL CLASS AGN SPECTRA IDENTIFIED ON BULLIALDUS	42
TABLE 2.6: MODEL RESULTS OF SPECTRAL CLASS N SPECTRA IDENTIFIED ON BULLIALDUS	43
TABLE 3.1: SUMMARY OF NEAR-INFRARED CORRECTION FACTORS	65
TABLE 3.2: IMPACT CRATER PHYSICAL AND MODEL CHARACTERISTICS.....	68
TABLE 3.3: MODEL COMPOSITION OF LUNAR CENTRAL PEAKS	71
TABLE 4.1: LUNAR SOIL MODAL MINERALOGIES.....	102
TABLE 4.2: LUNAR SOIL FUSED BEAD BULK CHEMISTRY	103
TABLE 4.3: OPTICAL CONSTANT EVALUATION RESULTS	106
TABLE 4.4: MEAN MODEL MINERALOGY OF LUNAR SOILS	111
TABLE 4.5: OVERALL MODELING STATISTICS OF LUNAR SOILS	112
TABLE 4.6: MODEL RELATIVE TO MEASURED MG' STATISTICS FOR LUNAR SOILS	117
TABLE 5.1: FITTING STATISTICS FOR EACH TELESCOPIC SPECTRUM	138
TABLE 5.2: MODELED MINERALOGY DETERMINED FROM LUNAR TELESCOPIC SPECTRA	143
TABLE 5.3: MODELED MINERALOGY (FIXED MG') DETERMINED FROM LUNAR TELESCOPIC SPECTRA	149
TABLE B5.1: MARE BASALT MINERALOGIES (DOMINANT SILICATES) AND MG'.....	195

LIST OF FIGURES

FIGURE 1.1: LUNAR ROCK Mg' RELATIVE TO AN	4
FIGURE 1.2: LUNAR ROCK CLASSIFICATION SYSTEM	7
FIGURE 2.1: LUNAR SPECTRAL CLASSES	16
FIGURE 2.2: SPECTRAL CLASS N RELATIVE TO “NOISY” SPECTRAL CLASSES.....	19
FIGURE 2.3: SPECTRAL CLASS THRESHOLD DETERMINATION.....	21
FIGURE 2.4: EXAMPLE OF EXCURSION PARAMETER APPLICATION.....	26
FIGURE 2.5: MODEL MATCH VARIATION IN ABSOLUTE REFLECTANCE AND MINERALOGY	28
FIGURE 2.6: BULLIALDUS CRATER	37
FIGURE 2.7: SPECTRAL CLASSES IDENTIFIED ON BULLIALDUS CENTRAL PEAK	38
FIGURE 2.8: SPECTRAL CLASS MATCHES TO BULLIALDUS CENTRAL PEAK SPECTRA	40
FIGURE 2.9: PLAUSIBLE MODELS OF MINERALOGY PROJECTED ON STÖFFLER DIAGRAMS	44
FIGURE 3.1: GRAPHICAL SYNTHESIS OF LUNAR CRUST MODEL PARAMETERS	61
FIGURE 3.2: GLOBAL DISTRIBUTION OF CENTRAL PEAKS EXAMINED	63
FIGURE 3.3: FINSSEN CRATER AND CENTRAL PEAK	67
FIGURE 3.4: EXAMPLE MODEL SPECTRAL FIT TO CLEMENTINE SPECTRUM	69
FIGURE 3.5: MINERAL MAPS OF FINSSEN CENTRAL PEAK.....	70
FIGURE 3.6: CENTRAL PEAK AND LUNAR SAMPLE MINERALOGY PROJECTED ON STÖFFLER DIAGRAMS ...	73
FIGURE 3.7: CENTRAL PEAK AND LUNAR SAMPLE Mg' RELATIVE TO PLAGIOCLASE ABUNDANCE	74
FIGURE 3.8: CENTRAL PEAK COMPOSITION RELATIVE TO CRUSTAL THICKNESS.....	76
FIGURE 3.9: CENTRAL PEAK PLAGIOCLASE ABUNDANCE RELATIVE TO CRUSTAL RATIO.....	78
FIGURE 3.10: CENTRAL PEAK COMPOSITION RELATIVE TO CRUST/MANTLE BOUNDARY.....	79
FIGURE 3.11: CENTRAL PEAK MINERALOGIES VIEWED GLOBALLY.....	80
FIGURE 4.1: ITERATIVE MODELING STARTING FROM FOUR DIFFERENT ENDMEMBERS	92
FIGURE 4.2: SELECTING A MATCH VIA SPECTRAL SHAPE RELATIVE TO Mg'	94
FIGURE 4.3: MODEL MATCH COMPLICATIONS.....	95
FIGURE 4.4: LUNAR SAMPLE MAFIC MINERAL Mg' RELATIONSHIPS	98
FIGURE 4.5: LUNAR SOIL BULK CHEMISTRY RELATIVE TO MINERAL CHEMISTRY	105

FIGURE 4.6: MODEL RELATIVE TO MEASURED CONTINUUM REMOVED REFLECTANCE COMPARISONS ...	108
FIGURE 4.7: MODEL RELATIVE TO MEASURED SCALED REFLECTANCE COMPARISONS.....	109
FIGURE 4.8: MODELED RELATIVE TO MEASURED MINERALOGY OF LUNAR SOILS	110
FIGURE 4.9: STÖFFLER DIAGRAMS OF LUNAR SOIL MODELED AND MEASURED MINERALOGY	114
FIGURE 4.10: MODEL RELATIVE TO MEASURED Mg' OF LUNAR SOILS	115
FIGURE 5.1: LOCATIONS OF TELESCOPIC SPECTRA ANALYZED	126
FIGURE 5.2: ARISTARCHUS PLATEAU AND HADLEY-APENNINE MOUNTAINS	127
FIGURE 5.3: PLOT OF SHAPE RELATIVE TO Mg'	129
FIGURE 5.4: STARTING AND FINISHING MODEL COMPOSITIONS.....	130
FIGURE 5.5: MODEL AND MEASURED SPECTRAL FITS (CONTINUUM-REMOVED REFLECTANCE)	135
FIGURE 5.6: MODEL AND MEASURED SPECTRAL FITS (SCALED REFLECTANCE).....	136
FIGURE 5.7: MODEL MINERALOGY RELATIVE TO LUNAR SAMPLES	140
FIGURE 5.8: PLAGIOCLASE RELATIVE TO Mg'	142
FIGURE 5.9: MODEL AND MEASURED FeO RELATIVE TO PLAGIOCLASE.....	145
FIGURE 5.10: MODEL AND MEASURED FeO RELATIVE TO PLAGIOCLASE (FIXED Mg')	147
FIGURE 5.11: MODEL MINERALOGY (FIXED Mg') RELATIVE TO LUNAR SAMPLES	148
FIGURE 5.12: Mg' OF LUNAR SOILS, BULK CHEMISTRY RELATIVE TO MINERAL CHEMISTRY	153
FIGURE A2.1: MODEL MINERALOGY OF SPECTRAL CLASS A.....	158
FIGURE A2.2: MODEL MINERALOGY OF SPECTRAL CLASS AG	161
FIGURE A2.3: MODEL MINERALOGY OF SPECTRAL CLASS AGN.....	164
FIGURE A2.4: MODEL MINERALOGY OF SPECTRAL CLASS AN	167
FIGURE A2.5: MODEL MINERALOGY OF SPECTRAL CLASS AT	170
FIGURE A2.6: MODEL MINERALOGY OF SPECTRAL CLASS G.....	173
FIGURE A2.7: MODEL MINERALOGY OF SPECTRAL CLASS GN	176
FIGURE A2.8: MODEL MINERALOGY OF SPECTRAL CLASS GNTA1.....	179
FIGURE A2.9: MODEL MINERALOGY OF SPECTRAL CLASS GNTA2	182
FIGURE A2.10: MODEL MINERALOGY OF SPECTRAL CLASS N	184
FIGURE A2.11: MODEL MINERALOGY OF SPECTRAL CLASS T	187

FIGURE A3.1: CENTRAL PEAK MINERALOGY RELATIVE TO CRUSTAL THICKNESS (T_2)..... 190

FIGURE A3.2: CENTRAL PEAK MINERALOGY RELATIVE TO CRUST-MANTLE BOUNDARY (E.G., T_2 - D_1) 191

FIGURE A3.3: CENTRAL PEAK MINERALOGY RELATIVE TO CRUST-MANTLE BOUNDARY (E.G., T_1 - D_2)192

FIGURE A3.4: CENTRAL PEAK MINERALOGY RELATIVE TO CRUST-MANTLE BOUNDARY (E.G., T_2 - D_2).....193

LIST OF ABBREVIATIONS AND VARIABLES

<u>Abbreviation/Variable</u>	<u>Explanation</u>
An	molar Ca/(Ca + Na)
anorth	anorthosite
<i>b</i>	scale coefficient (correlation in spectral contrast comparison between two spectra)
<i>b'</i>	spectral comparison intermediate product
<i>b''</i>	correlation coefficient (correlation in spectral shape comparison between two spectra)
Cpx	clinopyroxene
CVF	circular-variable-filter
<i>D</i>	impact crater depth of origin
<i>d</i>	impact crater diameter
<i>e</i>	excursion parameter
FAN	ferroan anorthosite
FHT	Feldspathic Highlands Terrane
<i>g</i>	goodness of fit
gl	glass
GRAIL	Gravity Recovery and Interior Laboratory
h	highlands
ilm	ilmenite
<i>k</i>	imaginary index of refraction
KREEP	potassium (K), rare earth elements (REE), phosphorous (P)
λ	wavelength
LKFM	low-potassium Fra Mauro basalts
LSCC	Lunar Soil Characterization Consortium
<i>m</i>	spectral slope
m	mare
M ³	Moon Mineralogy Mapper
Mg'	molar Mg/(Mg + Fe)
MGM	Modified Gaussian Modeling
Mg-suite	magnesium(an) suite
m-HTi	mare high titanium
m-LTi	mare low titanium
μm	micron
<i>n</i>	real index of refraction
NIR	near-infrared
nor	norite
Ol	olivine
OMAT	optical maturity index
Opx	orthopyroxene

<u>Abbreviation/Variable</u>	<u>Explanation</u>
<i>P</i>	central peak origin in crustal column relative to the crust-mantle interface
PCA	principle component analysis
PKT	Procellarum KREEP Terrane
Pl	plagioclase
PLS	partial least squares
pr	pristine
px	pyroxene
<i>R</i>	central peak origin in crustal column relative to local crustal thickness (Ratio) or Reflectance
RELAB	Brown University Reflectance Laboratory
RMSE	real mean squared error
SMFe	sub-microscopic iron
<i>S_o</i>	model spectrum
sp	spinel
SPA	South-Pole Aitken
<i>S_u</i>	unknown spectrum
<i>T</i>	crustal thickness
troc	troctolite
UVVIS	ultraviolet/visible
VIS	visible
vol%	volume percent
<i>w</i>	weighting parameter or single scattering albedo
wt%	weight percent

CHAPTER 1. INTRODUCTION

Overview

This thesis is focused on the extraction of accurate quantitative mineralogic and chemical information from visible (VIS) and near-infrared (NIR) reflectance spectra to make fundamental insights in lunar geology. I do this through the application of radiative transfer theory which *Bruce Hapke* pioneered. This is a theoretical approach that is gaining significant favor as its methods are continually scrutinized, validated, and readjusted. In the last several years, the Hawaii group led by Dr. Paul Lucey has been at the forefront of this area of study as it relates primarily to the Moon, but other airless bodies as well.

In this methodology, a first-principles approach is taken where reflectance spectra are modeled as the result of light interaction with mineral grains (i.e., volumetrically) in naturally occurring intimate mixtures of the major lunar minerals (e.g., olivine, pyroxene, and plagioclase). *Hapke* [1981; 1993; 2001]'s methods enable an incorporation of mafic mineral chemistry effects, grain size, and the explicit treatment of space weathering effects. In the last four-to-five years the Lucey research group's effort using these techniques has shown significant progress and made fundamental insights for interpretation of lunar geology (e.g., [*Gillis-Davis et al.*, 2006; *Lawrence and Lucey*, 2007; *Lucey*, 2004; *Lucey et al.*, 2004; *Lucey*, 2006; *Lucey and Noble*, 2008; *Wilcox et al.*, 2006]).

This thesis holds the contributions (all data analysis, scientific interpretation, and writing) I have made towards this goal as a member of Dr. Lucey's group and guidance from my committee and other coauthors. However, from this point on I will refer to myself as "our" or "we" for consistency. These contributions include an analysis of previously identified lunar highland spectral classes [*Cahill and Lucey*, 2007], an analysis of lunar impact crater central peaks [*Cahill et al.*, 2009], evaluation and validation of the model using lunar hyperspectral reflectance spectra of lunar mare and highland soils [*Cahill et al.*, 2010a], and evaluation and compositional analysis of Earth-based hyperspectral telescopic spectra of the nearside of the Moon [*Cahill et al.*, 2010b]. All of these studies are put into the geochemical and petrologic context of known lunar sample compositions.

Recently pivotal lunar remote sensing missions (e.g., Chang-E, Chandrayaan-1, KAGUYA/SELENE, Lunar Reconnaissance Orbiter, and LCROSS) carrying high quality spectral remote sensing instruments are returning vast new data sets with higher spatial and spectral resolution (≤ 10 m/pixel and ~ 260 channels) than Clementine (~ 100 - 200 m/pixel and 11 channels) and will soon become available to the general scientific community. The higher signal-to-noise ratios of these new data sets will provide abundant opportunities for scientific discovery, potentially enabling major breakthroughs in lunar science. Both the analytical techniques and the geologic insights detailed in this volume should prove to be valuable scientific stepping stones for these missions.

Basic Lunar Petrology, A Brief Summary

The lunar highlands suites are particularly important for understanding the evolution of the lunar crust via the magma ocean hypothesis. A relatively small number of the Apollo samples have compositions thought to have been spared mixing by meteorite impact and have the original compositions of the lunar crust. These so-called *pristine* rocks have very low siderophile abundances and sometimes feature cumulate textures, among other characteristics [Warren, 1985]. On a plot of Mg' (i.e., molar $(\text{Mg}/(\text{Mg}+\text{Fe})) \times 100$) of mafic minerals vs. An (i.e., molar $(\text{Ca}/(\text{Ca}+\text{Na})) \times 100$) of coexisting plagioclase, pristine lunar rocks are separable into major fields ([Longhi, 2003; Warren, 1985]; **Fig. 1.1**). The ferroan anorthosites (FAN), characterized by very high feldspar contents, plot in a field exhibiting no correlation between the parameters and feature relatively low Mg' (~ 40 - 75) and high An (94-98) content. A second group of diverse rocks that has much lower modal plagioclase contents plot in a correlated trend that does not intersect the anorthosite field, and lies above the anorthosite trend in terms of Mg'. These more mafic and relatively more magnesian rocks are called the Mg-suite rocks.

The characteristics of the Mg-suite rocks suggest an origin in moderate sized magma bodies intruded into the highlands crust [James and Flohr, 1983], but their volumetric importance and Moon-wide occurrence is very poorly known. Jolliff *et al.* [2000] suggests that Mg-suite materials are a peculiarity of the Procellarum KREEP Terrane (PKT), an area on the nearside of the Moon characterized by high iron and thorium concentrations suggested to be a product of the

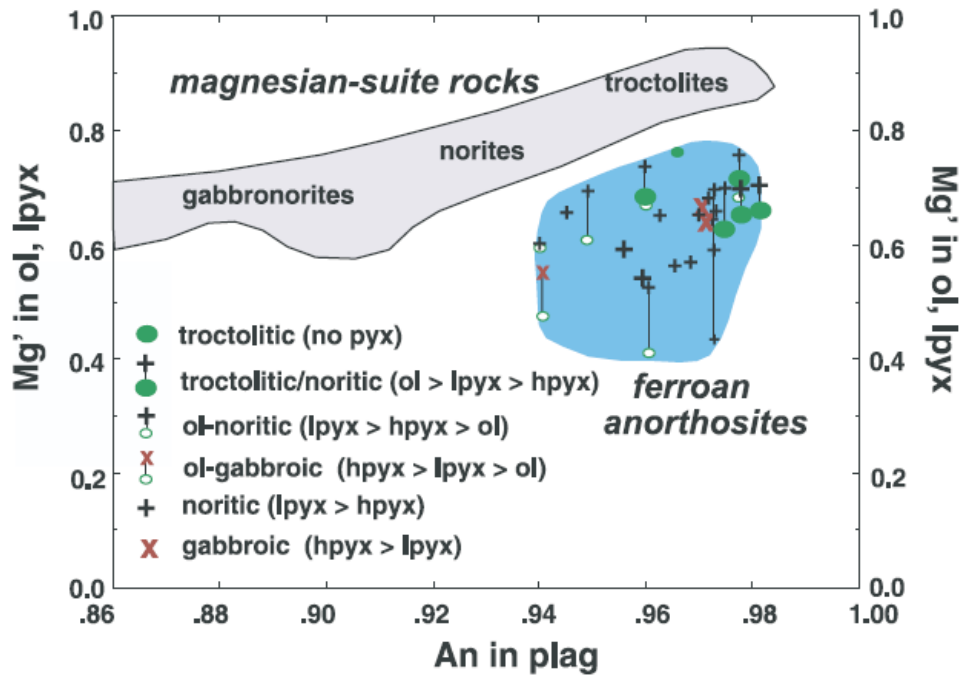


Figure 1.1: Mafic mineral Mg' relative to coexisting plagioclase An of lunar rocks reported by Longhi [2003].

unique thermal environment that influenced the evolution of that terrain. However, in recent studies of KREEP-poor feldspathic meteorites, *Warren* [2005] and *Warren et al.* [2005] attempt to extend the presence of Mg-suite globally by suggested that the magnesian component in these meteorites is derived from a KREEP-poor or KREEP-free variety of Mg-suite (a characteristic that is not observed in the Apollo and Luna samples). But, in a study of many of the same rocks, *Korotev* [2005b] notes that mafic magnesian lithologies are absent from these meteorites and the magnesian component within these meteorites is derived from a source other than the Mg-suite, or that the feldspathic meteorites are derived from magnesian (rather than ferroan) anorthosites. Regardless, both *Warren* [2005] and *Hess* [1994] (the former in the context of magnesian feldspathic meteorites and the latter magnesian troctolites), point out that source magmas for magnesian feldspathic material would have to be extremely magnesian themselves, with Mg's approaching that of the terrestrial mantle (~90's).

Although it is unclear whether the characteristics that *Warren* [2005] and *Hess* [1994] propose for the magnesian feldspathic material fit the characteristics of Mg-suite or not, it is clear that knowing the distribution of mafic and/or magnesian rocks in general and the Mg-suite in particular is important to solving this discussion. In their ground-breaking study, *Tompkins and Pieters* [1999] reported mafic lithologies in a number of central peaks using Clementine spectral reflectance data, and attributed these to the presence of Mg-suite rocks, but that association was principally based on the lack of other candidates in the pristine rock collection. Furthermore, *Shearer et al.* [2006], pointed out that these analyses lacked information on Mg', and it was possible that these occurrences are due to more mafic varieties of FAN rocks.

Among the questions and issues related to mafic rock types are: What is the nature of the magnesian component in feldspathic meteorites and some feldspathic granulitic breccias? Is the Mg-suite a special product of the PKT, or is it a Moon-wide phenomenon? Do magnesian anorthosites exist or are they mixtures of Mg-suite and very-low-mafic anorthosite? If so, what is their distribution and why are they not found in the pristine rock collection? What is the mineralogy and chemistry of the mafic-rock types identified by *Tompkins and Pieters* [1999] and what is their relationship to the Mg-suite? The research herein is aimed at addressing these questions.

Outline of Studies

Here we intend to use radiative transfer modeling methods to aid in my analysis of various lunar data sets to both evaluate the model and determine further insights into lunar geology. In summary, the first two studies focus on the analysis of lunar impact crater central peaks and previously interpreted spectral classes using Clementine multi-spectral data sets. The final two studies focus the examination of hyperspectral reflectance spectra in preparation for more recent data sets. Study three evaluates the model using lunar soils characterized spectrally and compositionally by the Lunar Soil Characterization Consortium (LSCC), and study four examines telescopic data sets collected in the 1970's and 1980's to determine composition of lunar nearside materials.

Modeling of lunar highlands spectral classes: Tompkins and Pieters [1999] studied the spectral properties of 109 central peaks of large craters to gain insight on the vertical and horizontal composition of the lunar crust. In the process they identified eleven spectral classes abundant on the lunar surface and used them to compositionally characterize the peaks they studied. *Tompkins and Pieters* [1999] interpreted their spectral classes in terms of the classification scheme of *Stöffler et al.* [1980] and here we retain that convention (**Fig. 1.2**). Our enhancement to previous work is the ability to more quantitatively associate spectral classes with compositions. To estimate the composition of *Tompkins and Pieters* [1999] spectral classes, we directly compare and identify model spectra with the highest similarity to each spectral class within the noise of Clementine data. We then compare the resulting model mineralogy to the lunar samples suite to provide additional context. Comparisons of the model spectra and the *Tompkins and Pieters* [1999] class spectra are made using a slightly modified version of *Clark et al.* [2003] shape and contrast matching algorithm. This calculation is based upon the similarity between two spectra which entails a calculation of the correlation coefficient (i.e., similarity in spectral shape), and spectral scale (i.e., the similarity in spectral contrast).

The composition of impact crater central peaks: Pieters [1986] presented a particularly useful remote sensing approach by inspecting the telescopic spectra of central peaks of large impact craters to determine crustal mineralogy. Impact craters >35 km have central peaks that

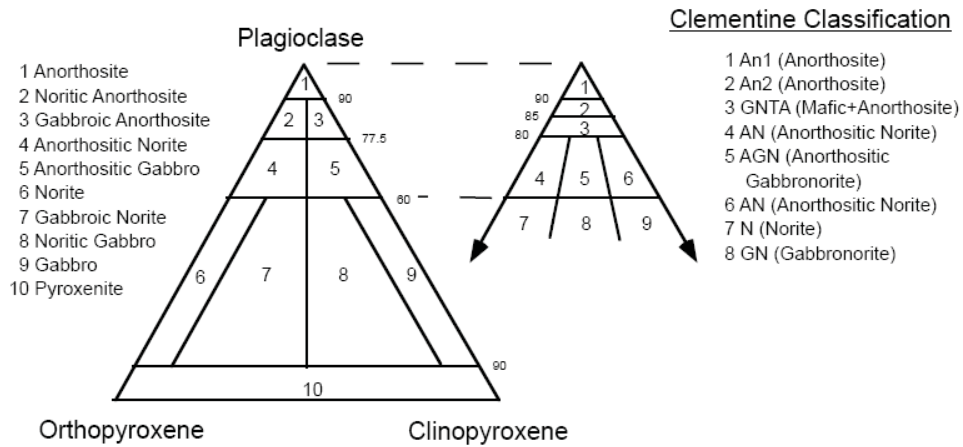
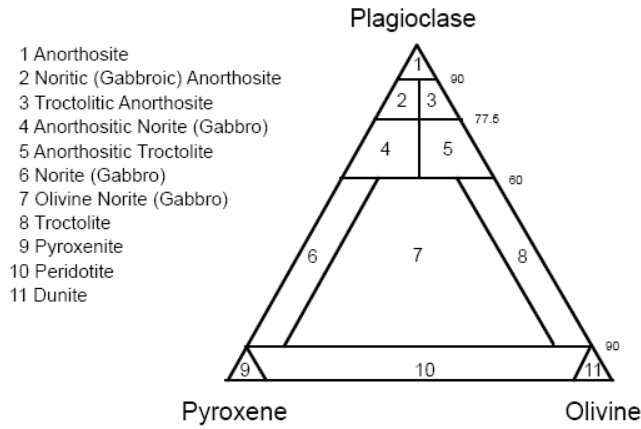


Figure 1.2: Lunar rock classification scheme developed by *Stoffler et al.* [1980], and *Tompkins and Pieters* [1999] modified classification scheme for interpretation of Clementine spectra of lunar impact crater central peaks. Figure borrowed from *Wieczorek et al.* [2006].

terrestrial field studies and impact theory suggest are uplift structures and represent material exhumed from depth (0.1 to 0.2 times the crater diameter) [*Dence, 1968; Melosh, 1989; Roddy, 1977*]. Hence, inspection of central peaks allows us to probe the crust several kilometers below the surface. As mentioned earlier, this strategy of central peak analyses was again implemented by *Tompkins and Pieters [1999]* using global multispectral data collected by Clementine that allowed extension of this approach to the lunar farside. Their study documented the spectral properties of 109 craters distributed globally that range in diameter from 40-180 km and are believed to have exhumed material from depths of 5-30 km.

A null result of *Tompkins and Pieters [1999]* study was the lack of distinct relationships between depth, spectral class and inferred composition. Their result suggests a highly heterogeneous crust lacking systematic compositional structure. Factors that may have obscured relationships present include a too-approximate estimate of depth of origin for central peaks and imprecise compositional estimates. *Wieczorek and Zuber [2001]* extended the concept of *Tompkins and Pieters [1999]* by conducting a compositional assessment in conjunction with a geophysically derived dual-layered crustal thickness model. This model takes into explicit account variations in crustal thickness caused by basins. Following this approach *Wieczorek and Zuber [2001]* found that only 18 craters were predicted to have sampled the lower crust of the Moon, in contrast to the 44 craters *Tompkins and Pieters [1999]* inferred to have tapped the lower crust.

Here we build upon these works with improved estimates of material depth of origin and spectral analysis tools. In this task, we use a variation of *Wieczorek et al. [2006]*'s one-layer crustal thickness model to derive the local thickness of the crust and assume a fixed depth of origin of a central peak proportional to crater size. We then redefine central peak material depth of origin to be distance above the crust/mantle boundary (i.e., Moho). If we assume that the Moho and the above stratigraphy is less modified by impact relative to the lunar surface this methodology and reference point allows an improved measure of the original emplacement depth of the rocks and/or stratigraphy sampled by a peak.

Modeling of lunar mare and highland soils: Here we examine lunar soils with the objective to test and validate a new algorithm, based on radiative transfer theory developed by *Hapke*

[1981; 1993; 2001], to extract mineralogy and chemistry from hyperspectral data sets. This study's purpose is to prepare for analysis of vast new hyperspectral near-infrared data sets returned by KAGUYA/SELENE and the Moon Mineralogy Mapper (M³) [Matsunaga *et al.*, 2008; Noble *et al.*, 2001; Pieters *et al.*, 2009a]. Lunar soils used here as our validation data set, were previously characterized for mineral modal abundances (in volume percent), chemistry (in weight percent), and spectra (in reflectance) by the Lunar Soil Characterization Consortium (LSCC) [Chambers *et al.*, 1995; Higgins *et al.*, 1996; Noble *et al.*, 2001; Pieters *et al.*, 2000; Taylor *et al.*, 1996; Taylor *et al.*, 2001b]. Modal proportions and chemistry of minerals are reported in different units (i.e., weight percent versus volume percent) that are nearly, but not, numerically equal. However, chemistry is conventionally documented and analyzed in weight percent and we maintain this convention for ease of comparison. However, modal abundances of minerals are documented and analyzed in volume percent. We use this unit of measure for mineral proportions because light interacts with a mineral grain as a volume and radiative transfer theory generally uses this convention. Although, these are not equal knowledge of mineral density and its volumetric proportions can allow a conversion to similar units if necessary.

Our focus in this section is determining the relative abundances of the major lunar silicates (i.e., plagioclase, orthopyroxene, clinopyroxene, and olivine) and their chemistry (i.e., Mg' and FeO). Denevi *et al.* [2008] previously performed an analysis of lunar mare soils using radiative transfer modeling techniques. Here we build upon Denevi *et al.* [2008]'s work by: 1) modeling both mare and highlands soils, 2) approaching lunar soils spectra as unknowns, and 3) examine lunar soil spectra with a new gradient descent fitting algorithm.

Modeling of lunar nearside, near-infrared telescopic spectra: Although new hyperspectral data sets returning from the SELENE/KAGUYA Spectral Profiler and Chandrayaan-1's Moon Mineralogy Mapper (M³) promise significant advances in our understanding of lunar compositional relationships [Matsunaga *et al.*, 2008; Pieters *et al.*, 2009a], "older" Earth-based telescopic hyperspectral data sets are scientifically no less significant and have provided valuable compositional information and a reference for calibration of more recent data sets for decades (e.g., [Cahill *et al.*, 2009; Le Mouélic *et al.*, 1999; Matsunaga *et al.*, 2008; McCord *et al.*, 1981;

Pieters, 1986; Pieters and Pratt, 2000]). These data are also yet to be evaluated with more recent analysis techniques.

Here we select approximately 60 of these spectra for more quantitative compositional analysis. Approximately half of the ~60 spectra modeled are of deposits in and around Imbrium basin (e.g., Aristarchus Plateau and the Hadley-Apennine ridge). This region of the Moon garners considerable attention due to its inferred compositional complexity and proximity to scientifically significant deposits both in and outside the basin [*Cahill et al., 2009; Lucey et al., 1986; Lucey and Hawke, 1989; Spudis et al., 1988*]. Other spectra examined are of eastern Nectaris near Apollo 16, mare Frigoris, and several impact crater central peaks. Previous interpretations of these spectra inferred areas of highly anorthositic materials similar to FAN rocks (e.g., [*Hawke et al., 2003; Spudis et al., 1984; Spudis et al., 1989*]), and areas with significant mafic mineral content similar to Mg-suite rocks (e.g., [*Lucey et al., 1986; Lucey and Hawke, 1989; Pieters, 1986; Spudis et al., 1988*]). We build upon these interpretations by examining these spectra with our new radiative transfer compositional inversion algorithm and place them directly in the context of lunar highlands and mare rocks of the lunar sample collection.

**CHAPTER 2. RADIATIVE TRANSFER MODELING OF LUNAR HIGHLANDS
SPECTRAL CLASSES AND RELATIONSHIP TO LUNAR SAMPLES¹**

¹ Cahill, J. T., and P. G. Lucey (2007), Radiative transfer modeling of lunar highlands spectral classes and relationship to lunar samples, *J. Geophys. Res.-Planets*, 112, 10.1029/2006JE002868.

Abstract

A previous study identified eleven spectral classes present on the surface of the Moon [Tompkins and Pieters, 1999]. Here we model these spectral classes to determine the compositions that define them. We do this by mathematically matching spectral classes to radiative transfer computed spectra using spectral shape, contrast, and excursion parameters as defining characteristics. Model spectra are based upon known mineralogies, mafic-mineral Mg's (molar $(\text{Mg}/(\text{Mg}+\text{Fe}))\cdot 100$), and maturities. We compare these compositional results to a compilation of ~100 Apollo samples to determine plausible representative samples for these spectra. Results indicate that unique mineralogic solutions for several spectral classes can be determined unambiguously, however classes previously interpreted to be pyroxene-rich are compositionally ambiguous. Results suggest these ambiguous mineral assemblages are not random, but correlate with variations in absolute reflectance. These data further suggest absolute reflectance is a compositionally diagnostic spectral parameter that should be used in conjunction with relative reflectance analysis to constrain mineralogy. Although absolute reflectance for the eleven spectral classes is not available to constrain their composition, we detail mineral, chemical (i.e. Mg'), and absolute reflectance variations of matching model relative reflectance spectra to narrow the possibilities. This information is used in a pilot study of Bullialdus crater, for which Clementine absolute reflectance is known. Results indicate Bullialdus' central peak consists of Tompkins and Pieters spectral classes AN, AGN, and N. Bullialdus' spectra that match class N are roughly consistent with previous compositional interpretations, however, matches to classes AN and AGN indicate more mafic assemblages typical of Mg-suite norite/gabbro-norite rocks.

Introduction

To the human eye the Moon appears simple, consisting of only two units; the bright highlands and the dark maria. However, geophysical and petrologic studies of lunar samples indicate that the Moon was formed by complex geologic processes [*Longhi, 1980; Shearer and Newsom, 2000; Solomon and Longhi, 1977*]. In this regard, remote spectroscopy has proven its utility by placing the compositional diversity of the lunar crust into continually improving regional and global contexts for geologic interpretation [*Gaddis et al., 1985; McCord et al., 1981; Pieters, 1978; Pieters, 1982; 1986; Pieters, 1993; Spudis et al., 1984; Whitaker, 1972*]. Now, increasing integration of sample studies with remote determination of global surficial mineralogy and geochemistry is a central focus for lunar science in order to understand the crust and its evolution [*Jolliff et al., 2000; Pieters et al., 2006; Wieczorek and Phillips, 2000*].

Pieters [1986] presented a particularly useful remote approach by inspecting the telescopic spectra of central peaks of large impact craters to determine crustal mineralogy. Impact craters >35 km in diameter have central peaks that terrestrial field studies and impact theory suggest are uplift structures and represent material exhumed from depth (0.1 to 0.2 times the crater diameter) [*Dence, 1968; Melosh, 1989; Roddy, 1977*]. Hence, inspection of central peaks allows probing the crust several kilometers below the surface.

The strategy of central peak analyses was implemented by *Tompkins and Pieters [1999]* using global multispectral data collected by Clementine that allowed extension of this approach to the lunar farside. Their study documented the spectral properties of 109 craters distributed globally that range in diameter from 40-180 km and are believed to have exhumed material from depths of 5-30 km. They defined eleven spectral classes from this database of spectra from which they interpreted mineralogy and placed in the context of the Stöffler rock-type classification diagram for lunar materials [*Stöffler et al., 1980*]. In the process, they demonstrated that mineralogy could be determined even from the sparse sampling of the Clementine multispectral imaging data. They also aided their interpretation using radiative transfer theory based on the work of Bruce Hapke [*1981; 1993*] showing that radiative transfer modeling was a productive approach to understanding the complexities of lunar spectroscopy. The significant scientific results of this

study revealed for the first time the global mineralogic diversity of the lunar surface. Subsequent work has exploited these results to make new inferences about the composition and evolution of the Moon's crust [*Wieczorek and Zuber, 2001*].

Here we build upon this foundation by using tools unavailable to *Tompkins and Pieters* [1999] at the time of their study. The radiative transfer mixing models used by *Tompkins and Pieters* did not include the optical effects of space weathering that substantially alter the appearance of lunar surface materials [*Fischer and Pieters, 1994; 1996*]. The recent theoretical contribution of *Hapke* [2001] to quantitatively describe space weathering in ultraviolet, visible, and near-infrared spectra supplements his previous work [*Hapke, 1981; 1993*] and now allows a direct comparison of lunar spectra to model spectra and modeled mineralogy to lunar sample data. We use the model here to generate spectra of mixtures of the major lunar minerals (plagioclase, clinopyroxene, orthopyroxene, and olivine) while accounting for the effects of space weathering. Using this computed spectral library as a guide, we quantitatively determine the range of compositions represented by *Tompkins and Pieters* spectral classes.

Our model results are consistent with the mineralogic interpretation of many of the spectral classes of *Tompkins and Pieters* [1999]. However, we find wide ranges of mineral compositions have model spectra that are consistent within the noise of Clementine data to some of the *Tompkins and Pieters* spectral classes, introducing considerable imprecision in compositional interpretation. We find that the spectrally consistent model compositions within these ranges are not continuous, but are clustered. On inspection, we find that within each cluster, model spectra show a narrow range of absolute reflectance. This indicates that including reflectance as a parameter can narrow the range of permissible compositions for certain classes. While deriving reflectances for all of the study areas of *Tompkins and Pieters* is beyond the scope of this paper, we illustrate how reflectance can be used to aid interpretation of composition in a pilot study of the crater Bullialdus.

Bullialdus crater is of interest here because it has relatively favorable lighting conditions for this study and is a scientifically significant locality. Due to its location at a middle latitude (Lat.

21S/Lon. 338) its image collection at low phase angles (~23-24 degrees) keeps topographic shading relatively low for optimum spectral interpretation. Mineralogically, Bullialdus also stands out as the only crater on the nearside of the Moon documented with norite mineralogy [Tompkins and Pieters, 1999]. This type of mineralogy may be widespread on the surface of the Moon, but the only other craters documented with this composition are within South Pole Aitken basin (e.g., Birkeland, Bhabha, Finsen, Lyman, and White). Geophysical modeling of the lunar crust by *Wieczorek and Zuber* [2001] also makes the case that these craters consist of “lower crustal” material (i.e., from the lower half of the crust). Thus, study of Bullialdus’ central peak may prove useful for inferring the composition of the lower crust of the Moon. For a description of the regional geology surrounding Bullialdus see *Tompkins et al.* [1994].

Approach

To quantify the composition of *Tompkins and Pieters* [1999] spectral classes, our approach is to directly and quantitatively compare model spectra with known mineralogy and chemistry to each spectral class and determine the model spectra that are similar to each class spectrum within the noise of the Clementine data. Spectral classes used in this study were digitized from Figure 7 of *Tompkins and Pieters* [1999] (**Fig. 2.1**). Model spectra are computed using radiative transfer theory developed by *Hapke* [1981; 1993; 2001] and use optical constant data of *Lucey* [1998]. This model is similar to that implemented by *Clark et al.* [2001] and explained in detail by *Lawrence and Lucey* [2007]. In general, the model uses the optical constants (real, n , and complex indices, k , of refraction) of minerals to calculate single scattering albedo (the probability a photon will survive an encounter with a material) for each component at a specified particle size, maturity, and mineral chemistry. Single scattering albedo of each mineral component is added linearly, weighted by abundance, and are converted to reflectance. Mineral modes used for this study span a plagioclase-olivine-orthopyroxene-clinopyroxene system at 5 vol% intervals (1771 modal combinations). Mafic mineral chemistry is varied in the form of Mg’ (i.e., the molar $(\text{Mg}/(\text{Mg}+\text{Fe}))\cdot 100$) ranging from 50-95 in increments of 5.

Space weathering (the alteration of lunar surface by exposure to space, e.g., micrometeorite impacts and solar wind sputtering) on the lunar surface causes lunar soils to exhibit an overall

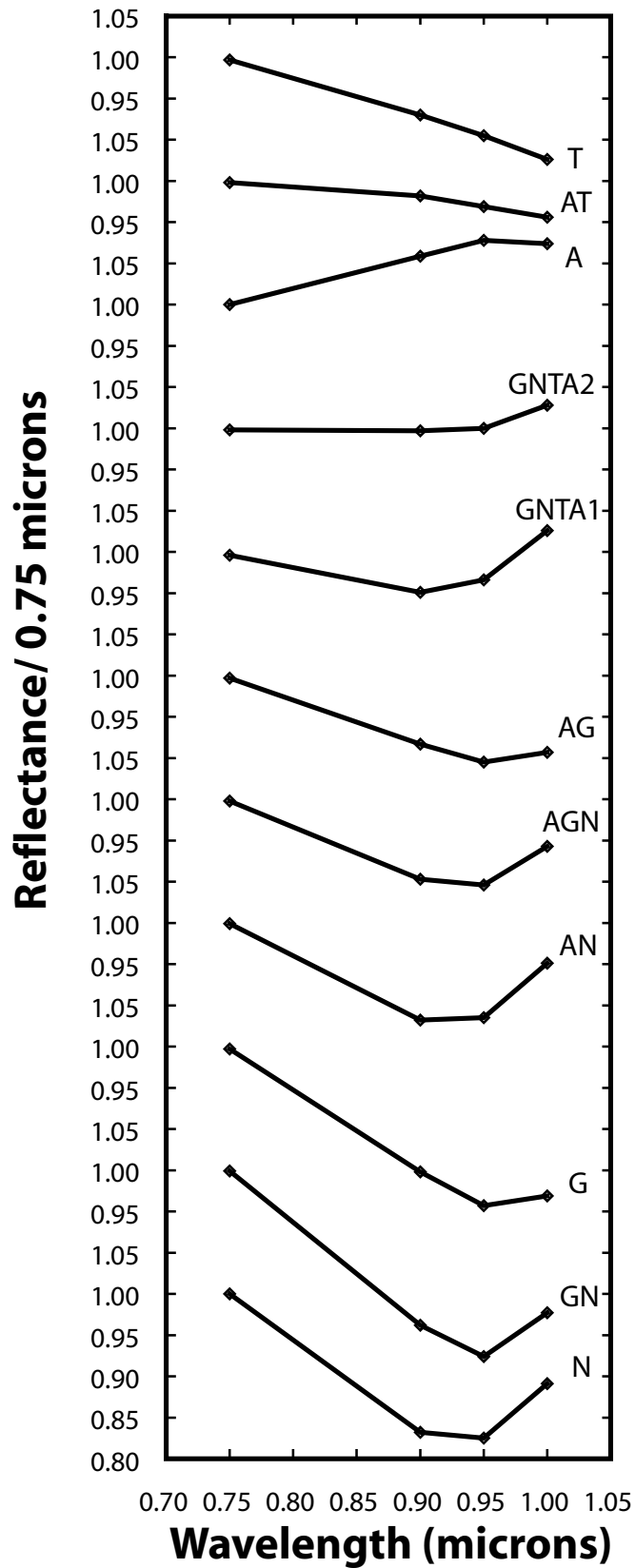


Figure 2.1: The eleven spectral classes identified on the lunar surface and documented by *Tompkins and Pieters* [1999] and now used in this study.

reduction in reflectance, attenuation of absorption bands, and reddening of the spectral continuum [*Fischer and Pieters*, 1994; 1996]. These optical effects appear to be primarily due to the presence of coatings on grains that contain abundant nanophase iron particles [*Pieters et al.*, 2000] resulting from sputtering or vapor deposition from micrometeorite impact. To ensure that we account for space weathering on the Moon, we quantify it using the optical maturity method of *Lucey et al.* [2000] and compute our models based upon the full range of immature compositions. *Lucey et al.'s* [2000] optical maturity parameter (OMAT) quantifies optical maturity combining the reflectance and spectral contrast of each spectrum in a manner that is largely insensitive to composition. At 1 km spatial resolution the Moon ranges from .2 (highly mature) to .5 (immature) in this parameter. Here we force our models to cover 10 levels of maturity from 0.275 to 0.5 OMAT in increments of 0.025, which covers the full range of immature compositions on the surface of the Moon.

Model assumptions include equilibrated mineral assemblage chemistries (i.e., the Mg' number of the mafic minerals are all made equal and there is no mixing or non-equilibrated assemblages) and grain size. Mineral assemblages are considered chemically equilibrated because estimates of composition from a spectrum are considered a bulk-rock analysis (i.e., the chemical contribution of a single mineral species in a mixture is not constrained). Grain size, also a critical parameter because of its significant influence on spectral properties, is held to a constant value of 17 μm . This is because *Pieters et al.* [1993] show that lunar soils are optically dominated by a narrow range (10-20 μm) of grain size and reason that this is due to this fraction's dominant surface area. The work of *Hapke* [1981] supports this hypothesis by showing that the relative contribution of a soil fraction to a spectrum is characterized by the cross-sectional area of that fraction as determined by its abundance and size. *Lucey* [2006] also performs an independent test of this hypothesis and shows it to be acceptable for most mineral mixtures, save olivine-plagioclase mixtures. These studies show that only a narrow grain size range needs to be considered for modeling to function constructively. Here we hold the grain size constant at 17 μm , which is consistent with the range (10-20 μm) of optically dominant grain sizes contributing to lunar surface spectra.

Comparisons of the model spectra and the *Tompkins and Pieters* [1999] class spectra are made in relative reflectance (i.e., spectra normalized to the 0.75 μm band) using a slightly modified version of *Clark et al.*'s [2003] shape and contrast matching algorithm. This calculation is based upon the similarity between two spectra which entails a calculation of the correlation coefficient (i.e., similarity in spectral shape), and spectral scale (i.e., the similarity in spectral contrast). The algorithm is defined by these equations:

$$b = \frac{\sum S_u * S_o - (\sum S_u * \sum S_o) / n}{\sum S_o^2 - (\sum S_o)^2 / n} \quad (1)$$

$$b' = \frac{\sum S_u * S_o - (\sum S_u * \sum S_o) / n}{\sum S_u^2 - (\sum S_u)^2 / n} \quad (2)$$

$$b'' = b * b' \quad (3)$$

Here n is the number of spectral channels in the fit, S_o is a spectral class spectrum, S_u is an “unknown” spectrum (i.e., model or Clementine spectrum here), b is the spectral contrast and b' is an intermediate product used by *Clark et al.* [2003]. Spectral contrast, b , refers to the absorption depth of a spectrum in relative reflectance. Equation 1 determines b by making a quantitative least-squares comparison of the contrast (i.e., absorption depth) over all the wavelength channels available between a spectral class, S_o , and an unknown spectrum, S_u . In equation 3, the term b'' is the correlation coefficient which quantifies the amount of correlations between the shapes of two spectra over all the wavelength channels available, regardless of differences in spectral contrast.

Here we test the effectiveness of this algorithm to distinguish *Tompkins and Pieters* [1999] spectral classes in the presence of a realistic amount of noise. We do this by creating a “noisy” spectral library for comparison by replicating each class spectrum 10,000 times and adding noise comparable to that of Clementine UVVIS data (0.5%) [*Cahill et al.*, 2004] (**Fig. 2.2a-b**). We then use the spectral correlation metric (b'') to compare an original spectral class to the database

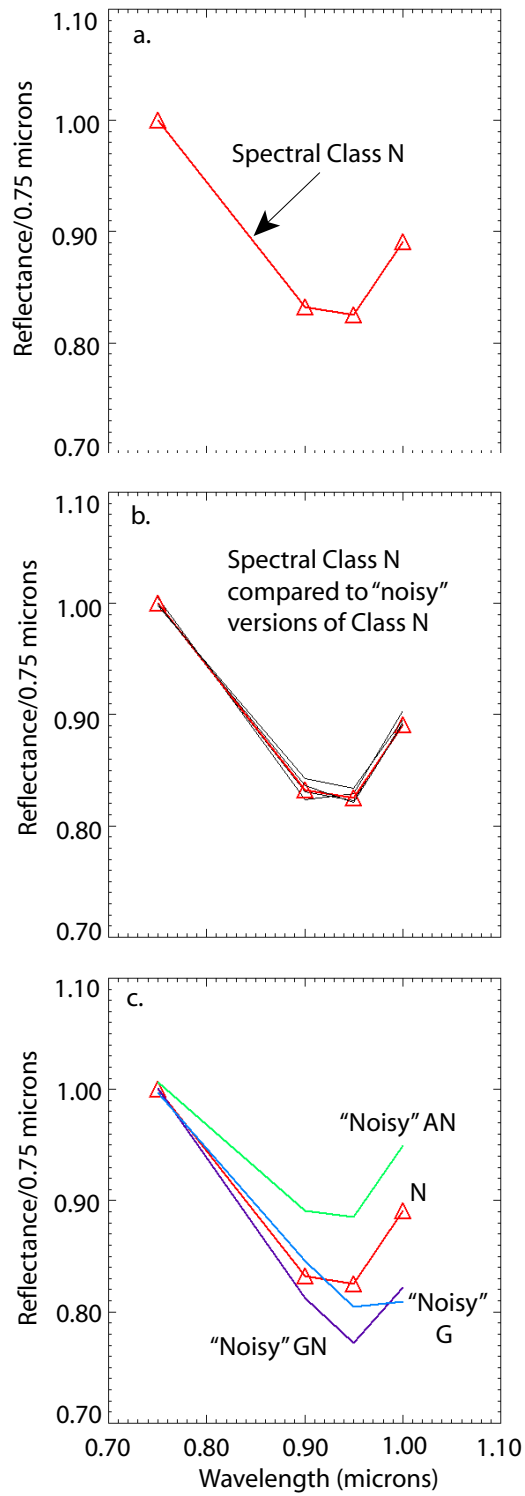


Figure 2.2: (a) Spectral class N. (b) Class N (red) compared to "noisy" versions of itself (black). (c) Class N (red) compared to "noisy" versions of other classes: AN (green), G (lt blue), and GN (purple).

of noisy spectral classes (**Fig. 2.2c**). The results of this test indicate that spectral shape alone (i.e., shape with spectral contrast removed) is not a sufficient discriminator because a significant number of matches are false alarms (**Fig. 2.3**). This ambiguity is present because several classes have similar spectral shapes and only differ in spectral contrast. Adding spectral contrast as an additional search criterion allows thresholds to be put in place that reduce false positives to a minimum. In several cases, classes can easily be differentiated using spectral contrast thresholds despite significant ambiguities in spectral shape. Because of this, we loosened initially tight spectral shape thresholds to maximize true positives that were originally overlooked due to the previously overly-rigorous criterion. The parameter threshold ranges we use to identify model spectra that match *Tompkins and Pieters* [1999] spectral classes are reported in **Table 2.1**.

When we apply the algorithm to make a comparison between the *Tompkins and Pieters* [1999] spectral classes and model spectra, some classes show compositions that span most of Stöffler diagrams. On inspection, we find that some of these compositions have spectra that match 3 of 4 bands very well, but differ significantly in the fourth band, enabling distinct compositions to constitute a match. However, these spectra still have statistical correlations within the thresholds (**Fig. 2.4a-b**); that is their average similarity is within the noise, but one band differs well outside the Clementine noise limit. Tightening the thresholds is one option, however this results in too few detections. Our solution is to add a third metric, “excursion”, which restricts the deviation of any individual band within the noise in the Clementine data. We define this parameter as:

$$e(x) = |S_u(x) - S_o(x)| \quad (4)$$

This calculation is computed between two spectra, an unknown (S_u) and the original spectral class (S_o), for each band, x , where we take the maximum e as the value for spectral excursion. The addition of this parameter allows the identification of spectral matches with fewer false positives (**Fig. 2.4c**). For the evaluation of most spectral classes in this study the e was held to 0.005. However, for spectral classes where no model matches were found initially within the thresholds

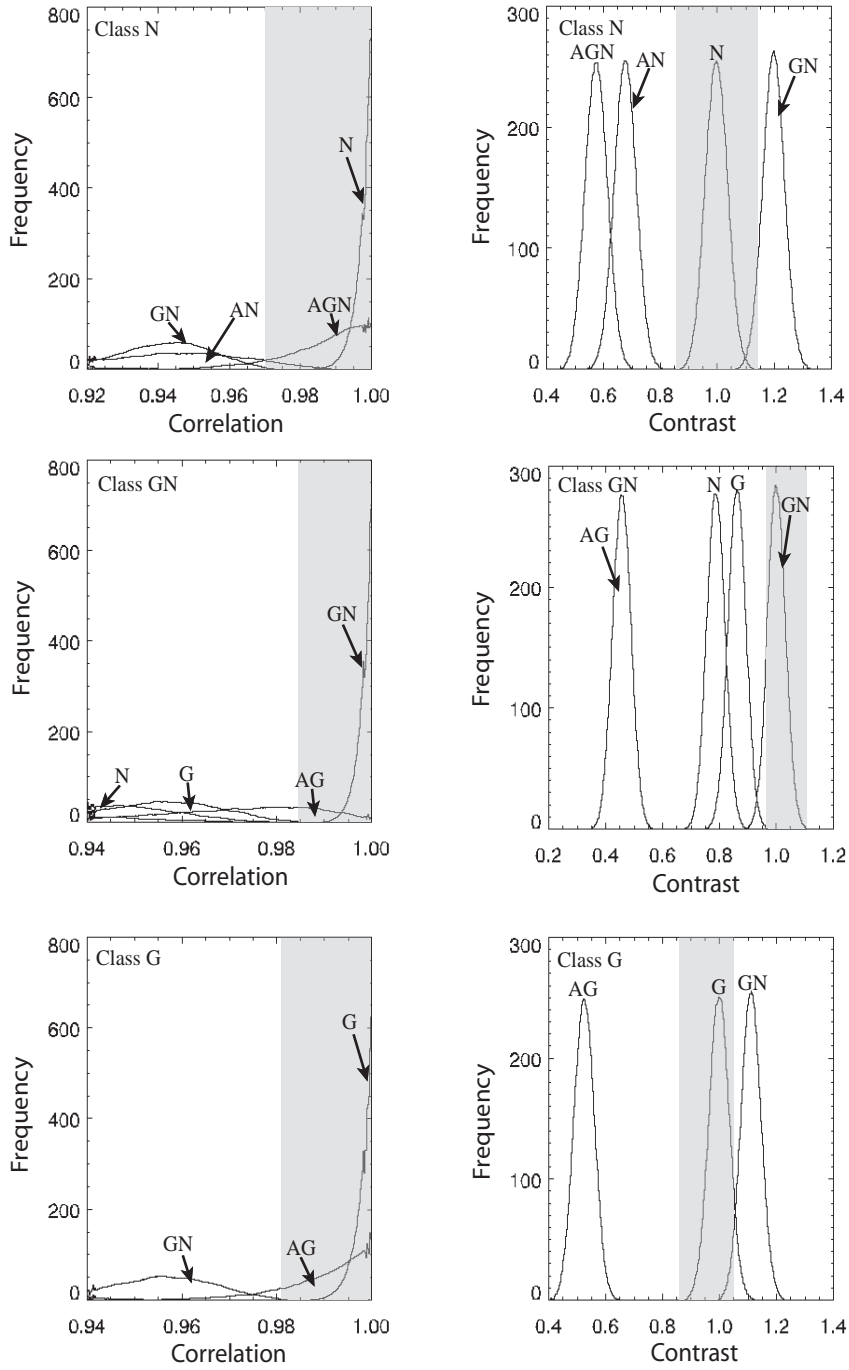


Figure 2.3: Noisy versions of the spectral classes were quantitatively compared to the original spectral classes to determine how easily they could be recognized. Shown is the quantitative measure of fit for noisy spectra to the original eleven spectral classes. Figures on the left indicate data for spectral shape (i.e., correlation) and figures on the right show data for absorption feature scale (i.e., spectral contrast). Grey shading indicates the maximum and minimum accepted thresholds for spectral shape and band depth for differentiation of these classes and identification of matches in radiative transfer model and Clementine data.

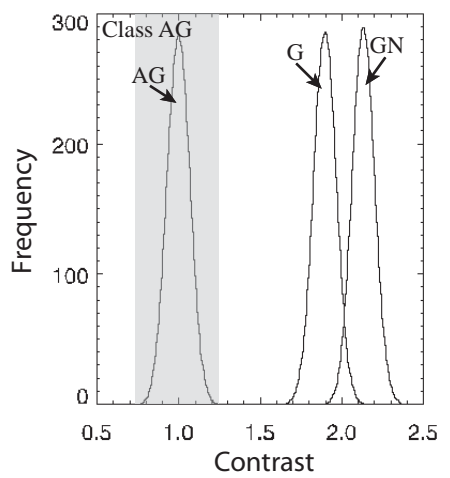
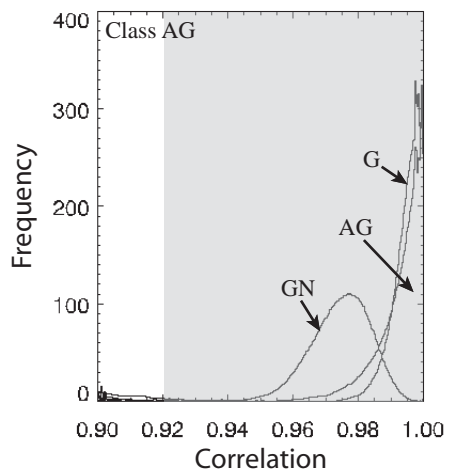
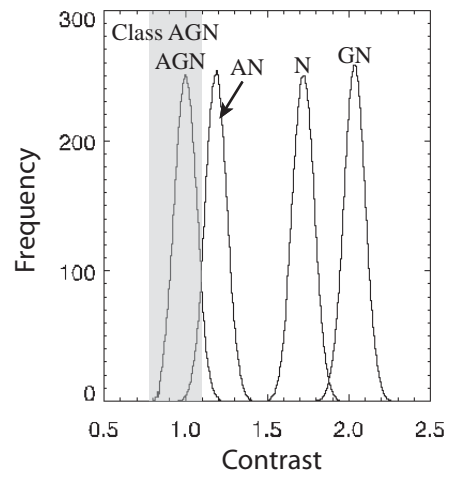
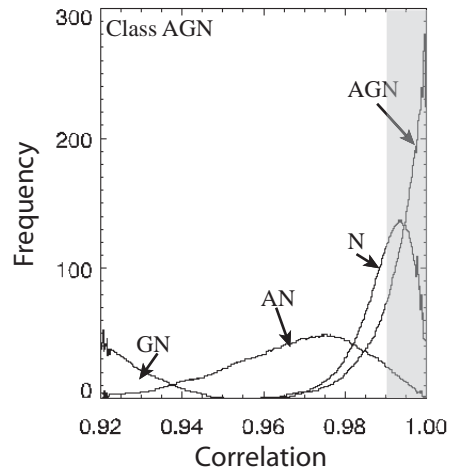
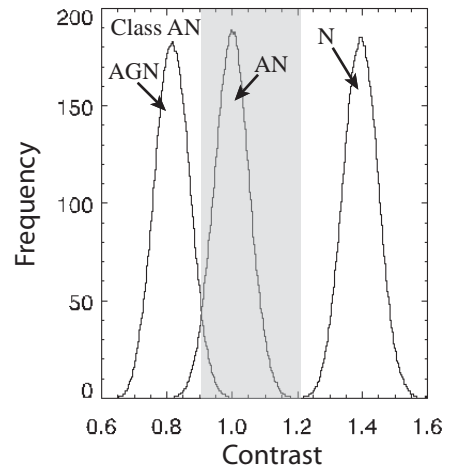
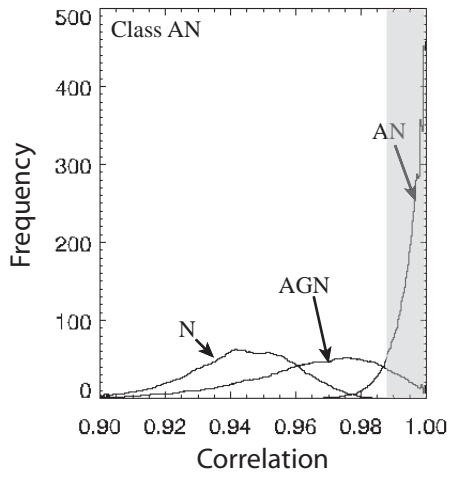


Figure 2.3 cont.:

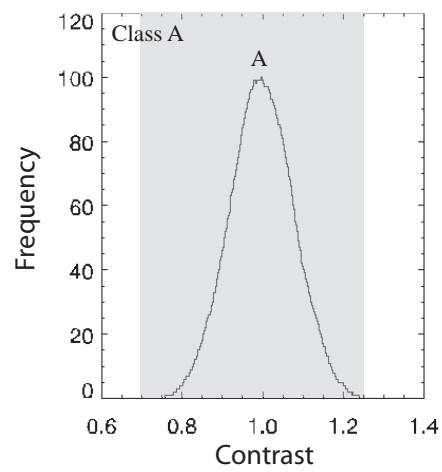
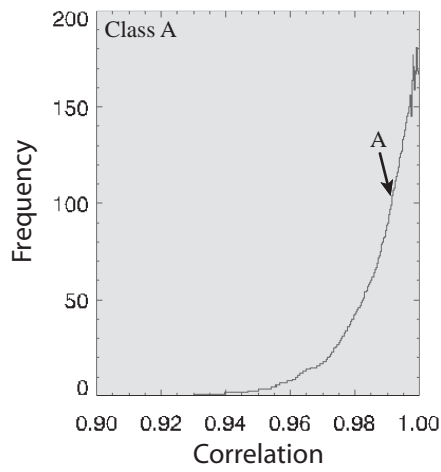
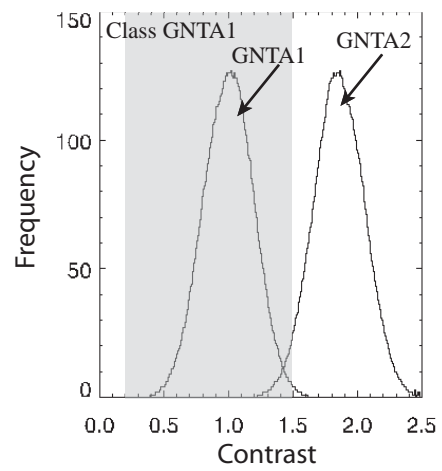
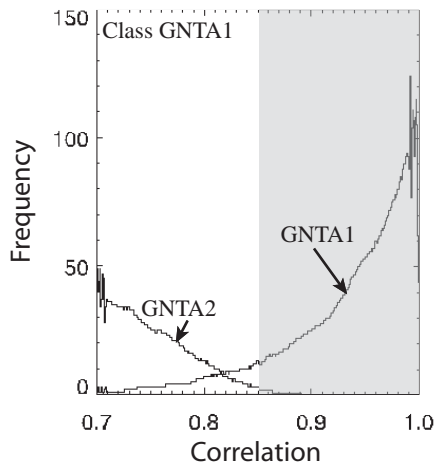
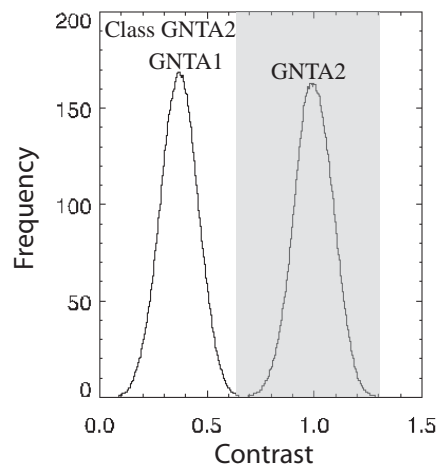
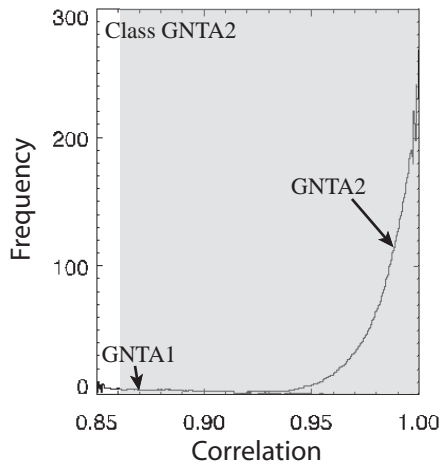


Figure 2.3 cont.:

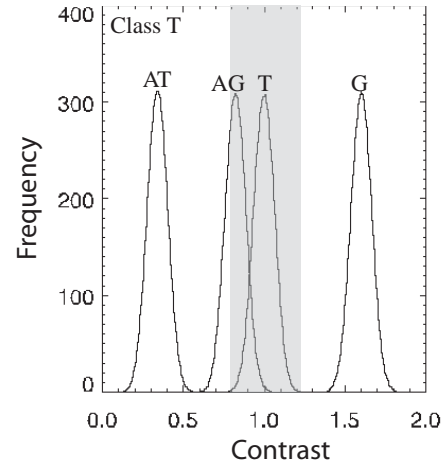
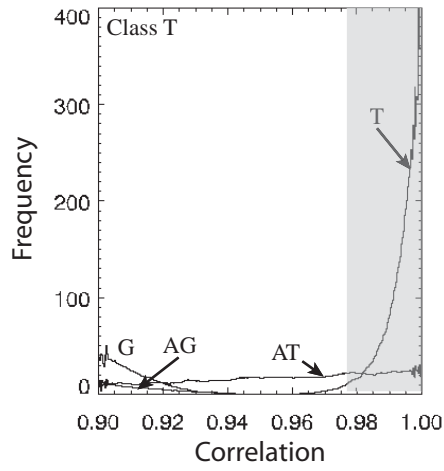
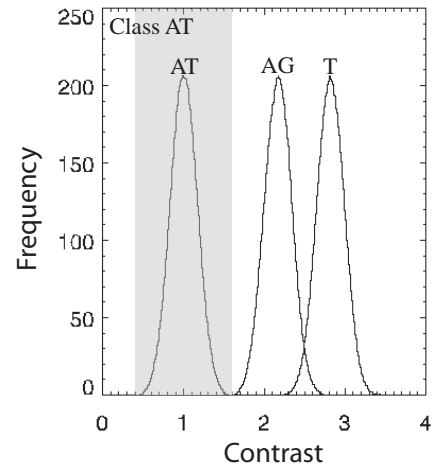
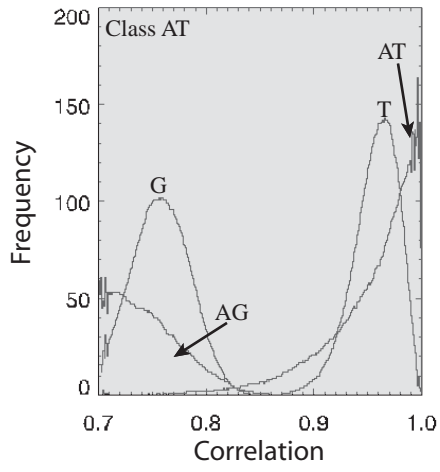


Figure 2.3 cont.:

Table 2.1: Threshold criteria for identifying matches to spectral classes.

Spectral Class	*Spectral Shape Range		**Spectral Contrast Range	
	<u>Min</u>	<u>Max</u>	<u>Min</u>	<u>Max</u>
N	0.970	1.000	0.860	1.140
GN	0.984	1.000	0.970	1.110
G	0.981	1.000	0.860	1.050
AN	0.988	1.000	0.900	1.220
AGN	0.990	1.000	0.760	1.100
AG	0.920	1.000	0.770	1.250
GNTA2	0.860	1.000	0.620	1.310
GNTA1	0.850	1.000	0.200	1.500
A	0.900	1.000	0.700	1.300
AT	0.580	1.000	0.390	1.600
T	0.940	1.000	0.790	1.220

Here are the minimum parameter thresholds (e.g., spectral shape and contrast). Model spectra calculated to have shape and contrast characteristics within these ranges and within the accepted excursion parameter bounds are considered matches. *Also referred to as the correlation coefficient (b'). **Also referred to as spectral scale (b).

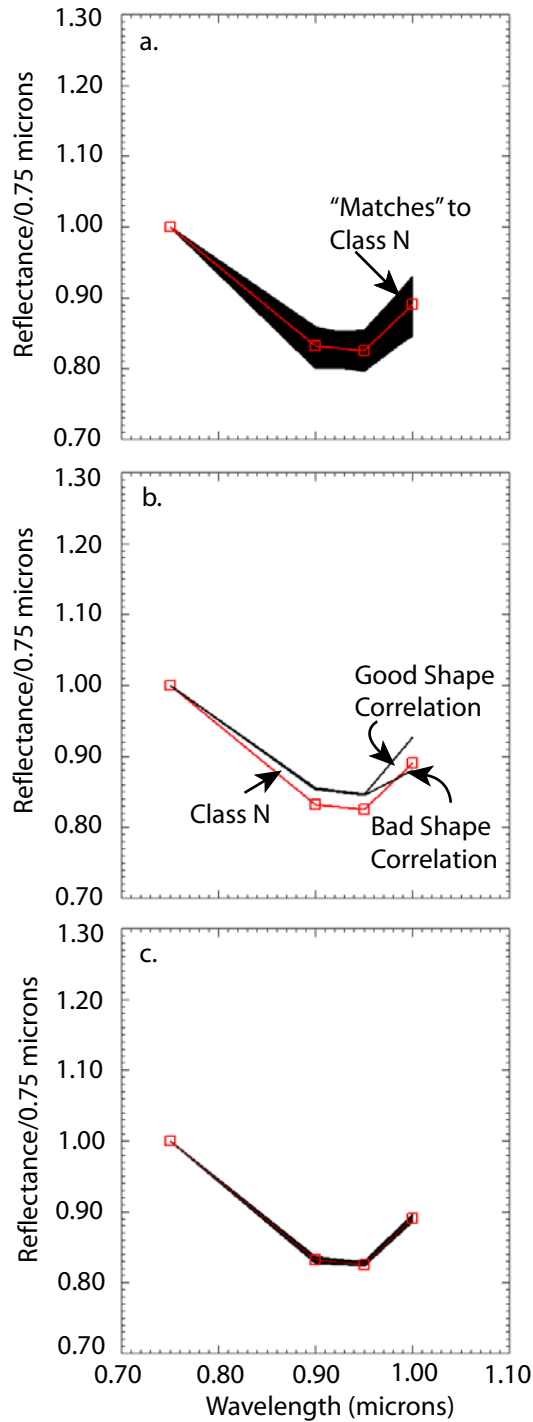


Figure 2.4: In (a) spectral class N is shown in red compared to model matches (black) using only spectral correlation ($>.97$ threshold) as a shape fitting criterion. In (b) spectral class N (in red) is compared to two spectra that fit the spectral shape and scale threshold criteria. However, one is a true positive that has similar shape and one is a false positive that has a high percentage match in bands 1-3 that has allowed the 4th band to differ significantly that the model interprets to be a distinctly different composition. In (c) the matches (in black) to spectral class N (in red) are shown after implementation of a spectral excursion parameter that tightens the match to limit false positives.

established for correlation and scale, we loosened e to 0.01 and 0.02 until matches were found. In **Figure 2.4c** model matches for spectral class N (Table 1) are shown using an e of 0.005.

Results

We find spectral matches to our model spectra with high ($e=0.005$) to good ($e=0.02$) precision fits for all classes. Modeled mineral assemblages for some classes are compositionally unambiguous. On the other hand, classes that show strong evidence for abundant pyroxene (e.g., N, GN, G, etc.) are mineralogically imprecise. Models that match these classes within our criteria cover a wide range of compositions, especially in relative abundances of plagioclase and other mafic minerals. However, the compositional variability of these model spectra is not random. Model matches tend to “clump” or fall into groups that correspond to smaller ranges of mineral mixtures and maturity that vary from group to group (**Fig. 2.5b**). Closer inspection of these clusters shows that the spectra also cluster in their reflectance (**Fig. 2.5**) suggesting that adding reflectance as a search criterion can help narrow the compositional uncertainty. The quantized nature of the clusters in terms of reflectance also suggests that the precision of the reflectance need not be very high, on the order of 5% in absolute units.

Tompkins and Pieters [1999] did not report absolute reflectance values for these spectral classes because of the difficulties inherent in extracting reliable reflectance spectra on these topographically rugged surfaces. Because of this, we cannot assign definitive compositions for many of the spectral classes as *Tompkins and Pieters* [1999] describe them. However, when we analyze the spectra from the lunar surface we get around this obstacle in two steps with Clementine data. First, we create a database of the theoretical compositional possibilities for each spectral class with varying absolute reflectance. Clementine spectra with relative reflectance characteristics falling within the range of spectral shape, contrast, and excursion of spectral classes are identified. At this point, the absolute reflectance data of these spectra can be used to further constrain composition. Ideally, Clementine data photometrically corrected for topography should be used to narrow compositional uncertainty at this point. However, data like this is not available for most crater central peaks. Instead, we compute the mean absolute

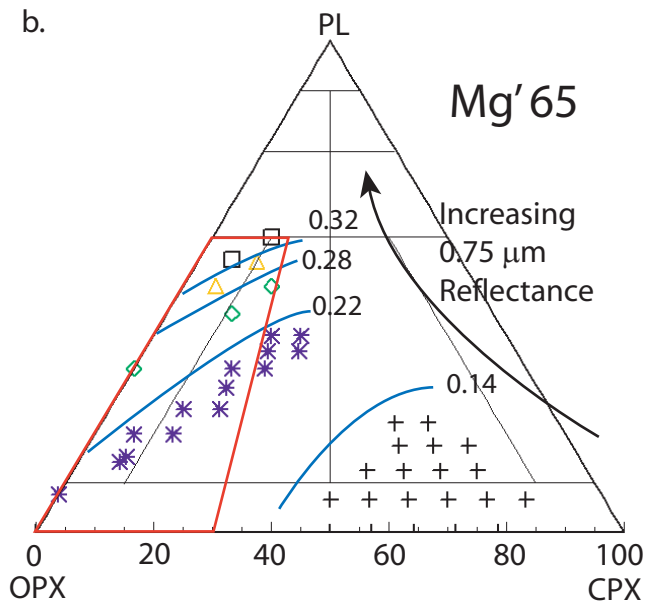
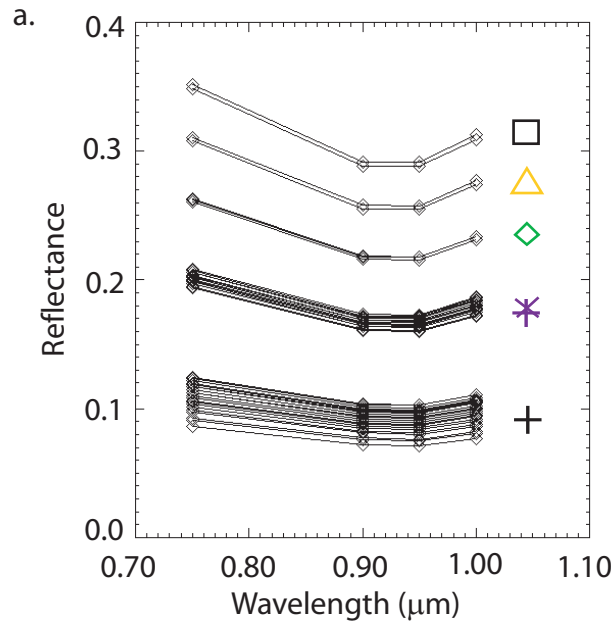


Figure 2.5 a-b: In (a) the spectra of model matches to class N for Mg' 65 are shown and separated into groups with corresponding symbols based upon absolute reflectance. In (b) the mineralogy of these spectral groups are shown with the same symbols and the value of the 0.75 μm band of absolute reflectance is contoured in blue.

reflectance for spectra that match each class. By doing this, our assumption is that class matches with absolute reflectance values greater and less than the mean are attributed to variations in surface slopes. Now, absolute reflectance can be used as a search parameter to lessen the compositional ambiguity while searching for classes on lunar localities with Clementine coverage.

Below we report the modeled results for all eleven spectral classes paying particular attention to changes in mineralogy with reflectance. Supporting figures are posted online at the Journal of Geophysical Research website supplement repository (<ftp://agu.org/apend/je/>) and in the appendix enclosed. For classes that show little compositional ambiguity with varying reflectance, we place our results in lunar sample context. Using the Apollo collection as a reference for what we know is already on the lunar surface, we compiled modal mineralogies and Mg's for 94 lunar samples (**Table 2.2-2.3**). Since spectral reflectance only detects the overall Mg' for all the minerals combined, we weighted Apollo sample Mg' based upon modal mineralogy. Some of the samples for which we compile compositional characteristics are Mg-suite spinel-troctolites. Although spinel is not a mineral modeled here, all samples listed in this study have a modal mineralogy containing less than 10% of this mineral [Cloutis *et al.*, 2004].

Mineralogy of Lunar Spectral Classes

Class A: Spectral matching ($e=0.01$) of this class yields two models with plagioclase-rich (95-100%) mineralogies. Both models are consistent with *Tompkins and Pieters* [1999] mineralogical interpretation of class A, but they have substantially different Mg' values compared to each other. One model has an Mg' of 75 and is compositionally consistent with four ferroan anorthosites (FAN; pristinity range 6-8). These samples include 67635;8, 76224;5, 15007;296, and 73217c35 [Floss *et al.*, 1998; Warren *et al.*, 1983a; Warren *et al.*, 1991]. However, lunar samples consistent with the second model, a highly magnesian (Mg' 95) anorthosite, are not present in the Apollo collection. However, given the small proportion of mafic minerals in this model, it is difficult to say much regarding Mg'.

Class GNTA1: Although the precision of this spectral match is the lowest of all classes ($e=0.02$) it has a relatively unambiguous modeled mineralogy and narrow range of reflectance

Table 2.2 Compiled mineralogy and geochemistry of some ferroan anorthosites.

Sample	Interpreted Rock-Type (Previous Studies)	Rock-Type (This Study)	Pristinity Class	Mass (g)	Modal %Pl	Modal %Ol	Modal %Cpx	Modal An	Pl An	Ol Mg'	Cpx Mg'	Weighted Mean Mg'	Ternary Mg'	Reference
67455C30	anorthosite	anorthosite	7	1.7	95	3	1	1	97	50	61	58	55	Minkin et al., 1977; Ryder and Norman 1978
60515	anorthosite	anorthosite	8	17	98	0	2	0	96	0	54	0	54	Warren et al. 1983b
67915C12-1	troct anorth	troct anorth	7	50	85	15	0	0	96	55	0	0	55	Roedder and Weiblen 1974; Taylor and Mosie 1979
67915C26	troct anorth	troct anorth	7	1	85	15	0	0	97	55	0	0	55	Marth et al. 1983
15295C41	anorthosite	anorthosite	9	5.3	99	0	0.25	0.75	96	0	44	59	55	Warren et al. 1990
15362	anorthosite	anorthosite	5	4.2	98	0	1	1	97	0	58	55	57	Ryder 1985
62255	anorthosite	anorthosite	8	800	97	0	2	1	96	0	53	65	57	Ryder and Norman 1979; McGee 1993; Floss et al. 1998
67075C17	anorthosite	anorthosite	7	50	96	1	2	2	97	50	54	65	60	Ryder and Norman 1978; Dixon and Paplike 1975; Haskin et al. 1973
61015	anorthosite	anorthosite	6	300	96	0	3	1	96	0	55.5	67	58	James et al. 1984
74114:5	anorthosite	anorthosite	7	2.078	96	1	1	2	94	47	57	67	60	Warren et al. 1991
62237	troct anorth	troct anorth	8	62	83	16	1	0	97	60	68	0	60	James et al. 1991; Ebihara et al. 1992;
62275	anorthosite	anorthosite	8	443	93	6	1	0	98	60	69	0	61	Warren et al. 1983b; Prinz et al. 1973
67535	anorthosite	anorthosite	6	0.99	93	0	3.6	3.6	97	0	55	68.5	62	Stöffler et al. 1985; McGee 1993
60025:691	anorthosite	anorth troc	8	1836	70	20	10	0.1	97	64	59	71	62	Warren and Wasson 1978; James et al. 1991; McGee 1993
64435:268	anorthosite	anorthosite	pr.	n.r.	98	0	1	1	98	0	57	69	63	James et al. 1989; Floss et al. 1998
62236	nor anorth	troct anorth	8	57	80	19	1	0	98	63	70	0	63	James et al. 1991; Nord and Wandless 1983
65325	anorthosite	anorthosite	7	65	99	0	1	0	97	0	64	0	64	Warren and Wasson 1978
65315:82	anorthosite	anorthosite	8	n.r.	99	0	1	0	98	0	64	0	64	McGee 1993; Floss et al. 1998
15415	anorthosite	anorthosite	9	269	99	0	0.5	0.5	97	0	60	71	66	Ryder 1985; McGee 1993
60056	anorthosite	anorthosite	5	16	95	2.5	0	2.5	97	0	67	0	66	Warren et al. 1983b
60135	norite	nor anorth	7	120	87	0	13	0	97	0	66	0	66	Warren et al. 1983b; Ryder and Norman 1980
65327	anorthosite	anorthosite	7	7	99	0	1	0	97	0	66	0	66	Warren and Wasson 1978
60025:702	anorthosite	anorthosite	8	n.r.	99	0	0.5	0.5	97	0	60	72	66	James et al. 1991; Floss et al. 1998
67215	anorth nor	anorth nor	3	n.r.	71	3	13	12	96	50	70	70	68	Warren et al. 1983a; Norman et al. 2000; Norman et al. 2003
10056	anorthosite	anorthosite	7	n.r.	99	0.7	0	0	96	68	0	0	68	Warren et al. 1983a
15437	troct anorth	troct anorth	7	1.1	81	15	2	2	96	67	74	78	69	James et al. 1991; Ryder 1985
60015	anorthosite	anorthosite	7	4600	99	0	0.5	0.5	94	0	64	74	69	Ryder and Norman (1978, 1980); Dixon and Paplike (1975)
60055	anorthosite	anorthosite	8	36	98	0	1	1	97	0	64	74	69	Ryder and Norman 1978; Ryder and Norman 1980; McGee 1993; Floss et al. 1991
60215C30	anorthosite	anorthosite	8	300	97	1	1	1	97	67	65	76	69	Rose et al. 1975; McGee 1993; Meyer and McCallister, 1973
15007:299	anorthosite	anorthosite	6	n.r.	93	0	6	1	97	0	69	74	70	Warren et al. 1983b
65315	anorthosite	anorthosite	8	285	98	0	1	1	97	0	68	72	70	Dixon and Paplike 1975; Ebihara et al. 1992;
60639C19	anorthosite	anorthosite	8	10	99	0	0.5	0.5	98	0	66	75	71	Warren and Wasson 1978
14312C55	anorthosite	anorthosite	7	n.r.	99	0.5	0	0	95	69	73	0	71	Warren et al. 1983a
77539C15	anorthosite	anorthosite	6	6.2	99	0	1	0	96	0	71	0	71	Warren et al. 1991
64435:270	troct anorth	troct anorth	pr.	100	84	12	3	1	97	72	75	83	73	James et al. 1989; Floss et al. 1998
64435C239	troct anorth	troct anorth	6	6	84	12	3	1	97	72	76	83	73	James et al. 1989; McGee 1993
67635:8	anorthosite	anorthosite	8	n.r.	98	0	1	1	95	0	69	78	74	Warren and Wasson 1980; James et al. 1989; Floss et al. 1998
76224:5	anorthosite	anorthosite	7	0.15	97	3	0	0	97	76	0	0	76	Warren et al. 1991
15007:296	anorthosite	anorthosite	8	n.r.	97	0	1.5	1.5	96	0	72	81	77	Warren et al. 1983b
73217C35	anorthosite	anorthosite	6	1.7	99	0	1	0	94	0	77	0	77	Warren et al. 1983a

Reported here are lunar ferroan anorthosite samples and their compositional characteristics. Lunar samples studies have petrologic and modal mineralogy interpretations that sometimes contradict each other. Here we report both interpretations. The Mg value is recorded for each mineral and a weighted mean is determined based upon the modal mineral proportions documented for that sample. Ternary Mg - refers to the ternary diagram this sample is displayed on in Figure 9. Abbreviations represent: nor-norite; troc-troctolite; anorth-anorthosite; pr-pristine; n.r.-not recorded.

Table 2.3: Compiled mineralogy and geochemistry data for some Mg-suite rocks.

Sample	Interpreted Rock-Type (Previous Studies)	Rock-Type (This Study)	Pristinity Class	Mass (g)	Modal % Pl	Modal % Ol	Modal % Cpx	PI An	Ol Mg'	Opx Mg'	Cpx Mg'	Weighted Mean Mg'	Ternary Mg'	Reference
76255c72("Unit 5A")	gabbro	gabbro	7	0.1	39	0	4	57	86	0	67	55	56	Warner et al. 1976; Ryder and Norman 1979
14161:7044	gabbro	gabbro	6	<0.1	49	0	32	10	88	0	64	43	59	Jolliff et al. 1993
61224:6	gabbro	gabbro	8	0.3	34	0	40	22	83	0	67	49	61	Marvin and Warren 1980
12007:174	mare?	norite	7	0.062	30	0	70	0	92	0	67	0	67	Warren et al. 1990
70375:77215	noritic	norite	8	840	54	0	41	0	91	0	71	0	71	Ryder and Norman 1979
73255c27:45	gabbro	norite	6	0.9	53	0	40	5	89	0	74	53	72	James and McGee 1979
14318c149	noritic	norite	7	1.5	55	12	35	0	87	71	73	0	70	Warren et al. 1983a
72435	sp-troctolite	sp-troctolite	n.r.	n.r.	80	10	1	0	96	73	73	0	73	Dymek et al. 1976
14305:396	norite	nor-anorth	pr	n.r.	80	0	20	0	91	0	73	0	73	Shervais et al. 1984
76255c82("U4")	gabbro	gabbro	6	300	39	0	4	57	87	0	68	75	75	Warner et al. 1976; Warren et al. 1986
67667	gabbro	gabbro	7	7.9	20	50	15	15	91	71	80	83	75	Ryder and Norman 1979
72255c42	noritic	norite	8	10	40	0	60	0	93	0	75	0	75	Ryder 1979
67667	gabbro	gabbro	7	7.9	30	20	25	25	91	71	78	78	76	Steele and Smith 1973; Warren and Wasson 1978
14318c150	noritic	anorth-nor	6	0.5	65	10	25	0	83	74	78	0	77	Warren et al. 1986
15360:11	noritic	anorth-nor	9	0.7	65	0	35	0	93	0	78	0	78	Warren et al. 1990
77035c130	noritic	norite	7	100	60	0	40	0	93	0	79	0	79	Warren and Wasson 1979
78527	noritic	norite	4	5.2	52	2	46	0	93	77	80	0	80	Nehru et al. 1978; Warren et al. 1983a
14321c1024	troctolite	troctolite	7	0.7	85	15	0	0	95	80	0	0	80	Warren et al. 1982
78235:78255	noritic	troctolite	8	395	47	0	53	0	93	0	81	0	81	Warren and Wasson 1979
15445c17("B")	noritic	anorth-nor	8	10	63	0	37	0	95	0	82	0	82	Ryder and Bower 1977; Shih 1990
14305:394("W1")	troctolite	troctolite	5	<0.1	0	100	0	0	93	0	83	0	83	Ryder 1985
14321c1140	troctolite	troctolite	9	200	70	0	30	0	93	0	83	0	83	Warren and Wasson 1979
73255c136	troctolite	anorth-troc	pr	0.7	66	34	0	0	96	83	0	0	83	Warren and Wasson 1979
65785c4	sp-troctolite	sp-troctolite	pr	0.3	65	30	1	1	96	83	84	84	83	Dowty et al. 1974
15455c2	troctolite	troctolite	pr	3	58	29	13	0	95	83	85	0	84	Warren and Wasson 1979
15361	noritic	norite	8	0.9	40	0	59	1	94	0	84	81	84	Warren et al. 1990
14161:212:4	dunite	dunite	5	<0.1	0	100	0	0	85	0	0	0	85	Morris et al. 1990
14305:394("W1")	troctolite	troctolite	5	0.34	90	10	0.25	0	95	85	89	0	85	Shervais et al. 1984
14321c1140	troctolite	troctolite	6	n.r.	40	60	0	0	95	86	0	92	86	Lindstrom et al. 1984
14321c3	anorth-troc	anorth-troc	pr	0.1	71	28	0	0	95	86	0	0	86	Warren et al. 1983a
73146	troctolite	troctolite	7	3	85	15	0.25	0	95	86	88	0	86	Warren and Wasson 1979
14161:212:1	peridotite	peridotite	7	<0.1	1	35	65	0	85	87	0	0	86	Morris et al. 1990
76335	troctolite	troctolite	8	465	88	12	0	0	96	87	0	0	87	Warren and Wasson 1978
14172c11	troctolite	troctolite	7	0.7	65	30	0	0	94	87	0	0	87	Warren and Wasson 1980
14179c	troctolite	troctolite	pr	0.7	70	30	0	0	94	87	0	0	87	Warren et al. 1981
14304c95("a")	troctolite	troctolite	7	0.9	55	45	0	0	94	87	0	0	87	Goodrich et al. 1986
14305c268	troctolite	troctolite	pr	0.2	70	30	0	0	70	87	0	0	87	Warren and Wasson 1980
14321c1142	troctolite	troctolite	5	n.r.	45	55	0	0	95	87	0	0	87	Lindstrom et al. 1984
14321c1154	troctolite	troctolite	pr	n.r.	60	40	0	0	95	87	0	0	87	Lindstrom et al. 1984
14321c1237	troctolite	troctolite	pr	n.r.	45	55	0	0	96	87	0	0	87	Knapp et al. 1984
72415/8	dunite	dunite	9	55.2	4	93	3	0	94	87	0	0	87	Ryder and Norman 1979
76504:19	anorth-troc	anorth-troc	pr	0.1	85	15	0	0	97	87	0	0	87	Warren et al. 1986
76535	troctolite	troctolite	9	155	58	37	4	0	96	88	86	0	88	Ryder and Norman 1979
14303c199	troctolite	anorth-troc	pr	2	70	30	0	0	95	88	0	0	88	Warren and Wasson 1980
14321:1211	troctolite	anorthosite	6	n.r.	98	1	0	1	94	84	0	93	90	Lindstrom et al. 1984
14321c1141	dunite	dunite	6	0.1	2	98	0	0	89	0	0	0	89	Lindstrom et al. 1984
12033:503	harzburgite	harzburgite	6	0.1	0	55	45	0	89	91	0	0	90	Warren et al. 1990
14305:361/2	troctolite	anorthosite	8	n.r.	99	1	0	0	97	90	0	0	90	Lindstrom et al. 1984
73263particles	sp-troctolite	sp-troctolite	n.r.	n.r.	70	20	5	0	96	90	90	0	90	Bence et al. 1974
76255c57("U5B")	troctolite	anorth-troc	8	2	77	23	0.25	0	96	90	0	0	90	Ryder and Norman 1979
14305c389	pyroxenite	pyroxenite	7	<0.1	0	2	98	0	90	91	0	0	91	Shervais et al. 1984
15295c	sp-troctolite	sp-troctolite	n.r.	n.r.	75	11	0	0	93	91	0	0	91	Marvin et al. 1989
15455H	sp-troctolite	sp-troctolite	n.r.	2?	25	65	0.25	0	96	92	91	0	92	Baker and Herzberg 1980; Ryder 1985
15445c71-A	sp-troctolite	sp-troctolite	5	1.5	35	50	0	0	98	92	0	0	92	Ridley et al. 1973; Ryder 1985
67485:14/77	sp-troctolite	sp-troctolite	8	0.083	20	69	0	0	97	92	0	0	92	Prinz et al. 1973; Ma et al. 1981

Reported here are lunar magnesium suite samples and their compositional characteristics. Abbreviations represent: sp-spinel; nor-norite; troc-troctolite; anorth-anorthosite; pr-pristine; n.r.-not recorded.

(0.4-0.5). Matches with low to intermediate Mg' (65-75) models are plagioclase-rich (90-95%) while higher Mg' (80-90) models are increasingly mafic (10-20%) but roughly consistent with *Tompkins and Pieters* [1999] interpretation of this spectral class. However, models with an Mg' of 95 have a higher and more variable mafic mineral abundance (10-45%). Numerous lunar FANs have similar plagioclase-rich mineral assemblages to the models identified as matches here.

Class GNTA2: Results show this class represents a more magnesian (Mg' >80) and dominantly plagioclase-rich (~70-80%) lithology. Models indicate more variation in reflectance (0.35-0.5) than class GNTA1, but an unambiguous mineral assemblage is modeled and is consistent with *Tompkins and Pieters* [1999] interpretation. Compositional characteristics suggest 15455 (c228) is the most representative lunar sample for this class. Although *Ryder* [1985] interpreted the petrology of this sample to be a pristine (class 9) Mg-suite norite, it has an anorthositic norite mineral assemblage and Mg' of 83.

Class AT: Because of a noticeable absorption feature indicating a spectral minimum at or beyond 1 μm *Tompkins and Pieters* [1999] interpreted this class to represent a mixture of feldspar and olivine and be classified as an anorthositic troctolite. Although our search identifies spectral matches at every Mg' modeled, every match has a mineral assemblage roughly consistent with *Tompkins and Pieters* interpretation. A few models have troctolitic anorthosite or troctolite mineralogies, however the majority of models center on an anorthositic troctolite mineralogy. These model spectra are characterized with lower albedo reflectances between 0.25-0.3. Matches generally have mineral assemblages that correlate with reflectance. Models with higher reflectance (0.3-0.4) have anorthositic mineralogy while lower reflectance (0.25-0.3) models have mafic assemblages. However, higher Mg' (90-95) matching models do not follow this trend as closely. This is because relative spectral matches differ in absolute reflectance due to differences in maturity, but have similar mineral assemblages. Although the mineral assemblage for this class is established well, similar lithologies in the lunar sample collection are many and have variable Mg'. Similar troctolitic anorthosite FAN samples 15437 and 64435 (clasts 239 and 270) are consistent with these spectral models in mineralogy and Mg' range (70-75) [*Floss et al.*, 1998; *James et al.*, 1989; *McGee*, 1993; *Warren and Wasson*, 1980]. However, Mg-suite samples

with anorthositic troctolite assemblages from Apollo 17 (73235c136 and 76255c57) and Apollo 14 (14321c3, 14172c11, 14179c, 14305c268, and 14321c1154) are also consistent with spectral models that have an Mg' range of 85-90 [*Lindstrom et al.*, 1984; *Warren and Wasson*, 1980; *Warren et al.*, 1981; *Warren et al.*, 1983a; *Warren et al.*, 1983b].

Class T: Modeling shows that this class is a troctolite to dunite similar to *Tompkins and Pieters* [1999] interpretation. However, the mineral assemblage possibilities for this class spectrum vary greatly within the troctolite to dunite classification. Models have anywhere between 40-100% olivine. Lower to intermediate Mg' (55-65) models have mineralogy that varies systematically with reflectance. Reflectance values between 0.35-0.4, 0.3-0.35, 0.25-0.3, and 0.2-0.25 have 40-50%, 50-60%, 60-80%, and 80-100% olivine respectively. At higher Mg' (70-85) this trend is not as easily distinguished because matching spectra have similar mineral assemblages with differing reflectance values. Again this is due to spectra with differing maturity values. Lunar troctolite sample 14321(c1140) shows similar mineralogy to models with reflectance values of ~0.35 and an Mg' 85. Dunite samples 14161(c212,4) and 72415/8 also show compositional similarities to models with 0.25-0.3 reflectance and Mg' of 85 [*Lindstrom et al.*, 1984; *Morris et al.*, 1990; *Ryder and Norman*, 1979].

Class AN: Only at the Mg' range 75 to 85 and absolute reflectance ranges of 0.3 to 0.5 does spectral class AN begin to approach anorthositic norite assemblages consistent with both *Tompkins and Pieters* [1999] and *Stöffler et al.* [1985] lithology classification systems. Other model matches to this spectral class are predominantly mafic and vary in absolute reflectance from 0.1 to 0.5. Like most cases, the model reflectances do not vary continuously across this range, but occur in distinct clusters. Spectral matches with Mg' between 60-65 have mineral assemblages that range from orthopyroxenite with 0 to 35% olivine to plagioclase-rich (40%) norite and have absolute reflectance values ranging between 0.10-0.25, respectively. Intermediate to high Mg' (70-95) assemblages have dominantly gabbro-norite mineralogy, with 0 to 40% olivine. However, some spectral matches indicate norite and anorthositic norite mineral assemblages with a little less olivine (0-20%) are possible interpretations as well. In general,

model matches with gabbro-norite assemblages usually have low (0.1-0.2) absolute reflectance values, while models with norite assemblages have slightly higher (0.2-0.3) reflectance values.

Class AGN: This spectral class found throughout the lunar highlands was interpreted by *Tompkins and Pieters* [1999] to be the intermediate mineral assemblage, anorthositic-gabbro-norite. Lower Mg' (55-60) model matches show only norite and gabbro-norite mineral assemblages with low absolute reflectance values (0.1-0.25). Model matches with intermediate Mg' (70-75) have gabbro-norite to olivine-bearing (10-30%) gabbro-norite mineral assemblages and low reflectance values (0.1-0.2). Only at high Mg' (80-90) do a few model matches exist with anorthositic-gabbro and anorthositic-norite mineral assemblages that agree with *Tompkins and Pieters* [1999] interpretation. These model matches have high absolute reflectance values (0.3-0.4) and a wide range of olivine contents (0-50%). Models with gabbro-norite to olivine-bearing (10-45%) gabbro-norite assemblages at high Mg' (80-95) are also a possible interpretation. These models have a reflectance range of 0.15-0.25.

Class AG: Spectral class AG was interpreted by *Tompkins and Pieters* [1999] to be an anorthositic gabbro. Model spectra that match this class exist for all Mg' variations considered and are characterized with a wide range of reflectance (0.1-0.45) and mineralogy. Olivine abundance is variable (0-60%), but decreases with increasing reflectance. Models with 0.1-0.2 reflectance have olivine-gabbro to olivine-gabbro-noritic mineral assemblages. Model matches with 0.2-0.3 reflectance show olivine-bearing anorthositic gabbro assemblages with the exception of a few Mg' 60 models that have anorthositic norite assemblages. Higher reflectance (0.3-0.45) models have more gabbroic anorthosite mineral assemblages.

Class N: This spectral class was interpreted by *Tompkins and Pieters* [1999] to represent a lunar norite characterized with less than 60% plagioclase and a large portion of the mafic mineral orthopyroxene. *Tompkins and Pieters* loosened the original *Stöffler et al.* [1985] classification to allow more clinopyroxene within this lithologic classification since they felt they could not distinguish these differing mineral assemblages well enough spectrally to satisfy the original *Stöffler et al.* classification. Low Mg' (55) model spectra that match this class have

clinopyroxene-rich gabbro and pyroxenite mineral assemblages. Intermediate Mg' (60-75) model mineral assemblages have significant variation in pyroxene mineralogy varying from norite to gabbroic-pyroxenite. At high Mg' (80-90) mineral assemblages become more gabbroic to gabbroic. Lower absolute reflectance values (<0.14) match mineral assemblages with higher percentages of clinopyroxene. Intermediate absolute reflectance (0.14-0.22) models have norite to gabbroic mineral assemblages. Higher absolute reflectance (>0.22) models have norite assemblages at lower Mg' (60 to 65) and gabbroic assemblages at intermediate to high Mg' (70 to 90). Throughout this progression, plagioclase also is shown to increase in proportion with increasing absolute reflectance.

Class GN: This spectral class is interpreted to be the intermediate mineral assemblage, gabbroic. Low Mg' (55-60) models that match this class have olivine-gabbro (0-40%) to gabbro and gabbroic mineral assemblages. Intermediate Mg' (65-75) model matches show mineral assemblages that range from olivine-bearing gabbro to gabbroic. And at high Mg' (80-90) model matches show mineral assemblages that are olivine-bearing gabbro to gabbro in composition. In general, models grade from plagioclase-poor (0-40%) gabbroic to gabbroic assemblages with low reflectance (0.1-0.2), to plagioclase-rich (40-60%) gabbroic with high reflectance values (0.25-0.3).

Class G: This spectral class was interpreted by *Tompkins and Pieters* [1999] to be a gabbro to gabbroic-pyroxenite assemblage. An initial search for matching models yielded no results, so we loosened the excursion parameter to 0.01. Our results show considerable variability at low to intermediate Mg' (55-65) with model mineralogy ranging from olivine-bearing (25%) gabbroic to olivine-rich (75%) peridotite. Model spectra have reflectance values ranging from 0.15-0.35. Higher albedo spectra show greater plagioclase and orthopyroxene proportions, while lower albedo spectra show greater olivine and clinopyroxene proportions. Models that have intermediate to high Mg' (70-90) become more olivine-rich and have a higher clinopyroxene to orthopyroxene ratio. Counterbalancing this description is the fact that this spectral class is very common in the mare, and is sensibly interpreted to represent a low Mg' clinopyroxene-rich assemblage. However, our modeling shows that this is not required, and in the highlands where

prejudging the permissible compositions is risky, this spectral class may represent material quite different than mare basalt.

Analysis of Bullialdus Crater

Recognizing the potential utility of reflectance for mineralogic interpretation of surface spectra we perform a pilot study of Bullialdus' central peak (**Fig. 2.6**). Using the algorithms and thresholds explained earlier we search Clementine VIS data of Bullialdus for occurrences of the eleven *Tompkins and Pieters* [1999] spectral classes.

Tompkins and Pieters initial study of this crater found the classes GNTA1, GNTA2, N, and AN to be present. Using our search criterion, we indeed identify these classes and others on Bullialdus. We find that matches to several spectral classes are present on much of the peak and surrounding floor (**Fig. 2.7a**). Classes these spectra match include N, AN, AGN, AG, GNTA1, and GNTA2. Classes GNTA1 and GNTA2 are particularly ubiquitous and they usually appear on the crater floor, peak slopes, or in shadowed areas of the central uplift. This is in contrast to the spectral classes N, AN, AGN, and AG that are generally detected on or near the crests of Bullialdus' central peak.

Using the optical maturity parameter OMAT of *Lucey et al.* [2000], the floor of Bullialdus is completely mature (**Fig. 2.7b**), and all of the above analysis (including that of *Tompkins and Pieters* [1999]) presumes immature or submature surfaces. Our modeling does not include spectra that are optically mature so we exclude optically mature surfaces from our analysis. The wide occurrence of GNTA1 and GNTA2 on the crater floor underlines the caution expressed by *Tompkins and Pieters* that these spectral classes may in some cases represent mature versions of other classes.

Spectral classes identified within the immature regions that are confined to the peak include N, AN, AGN, and AG (**Fig. 2.7c**). However, when we tighten the excursion parameter to 0.01 for tighter spectral matches only classes N, AN, and AGN are identified (**Fig. 2.7d**). This leaves much of the immature peak regions unclassified, and may indicate *Tompkins and Pieters* [1999] eleven spectral classes may need new additions. However, it is possible that the tightness of our

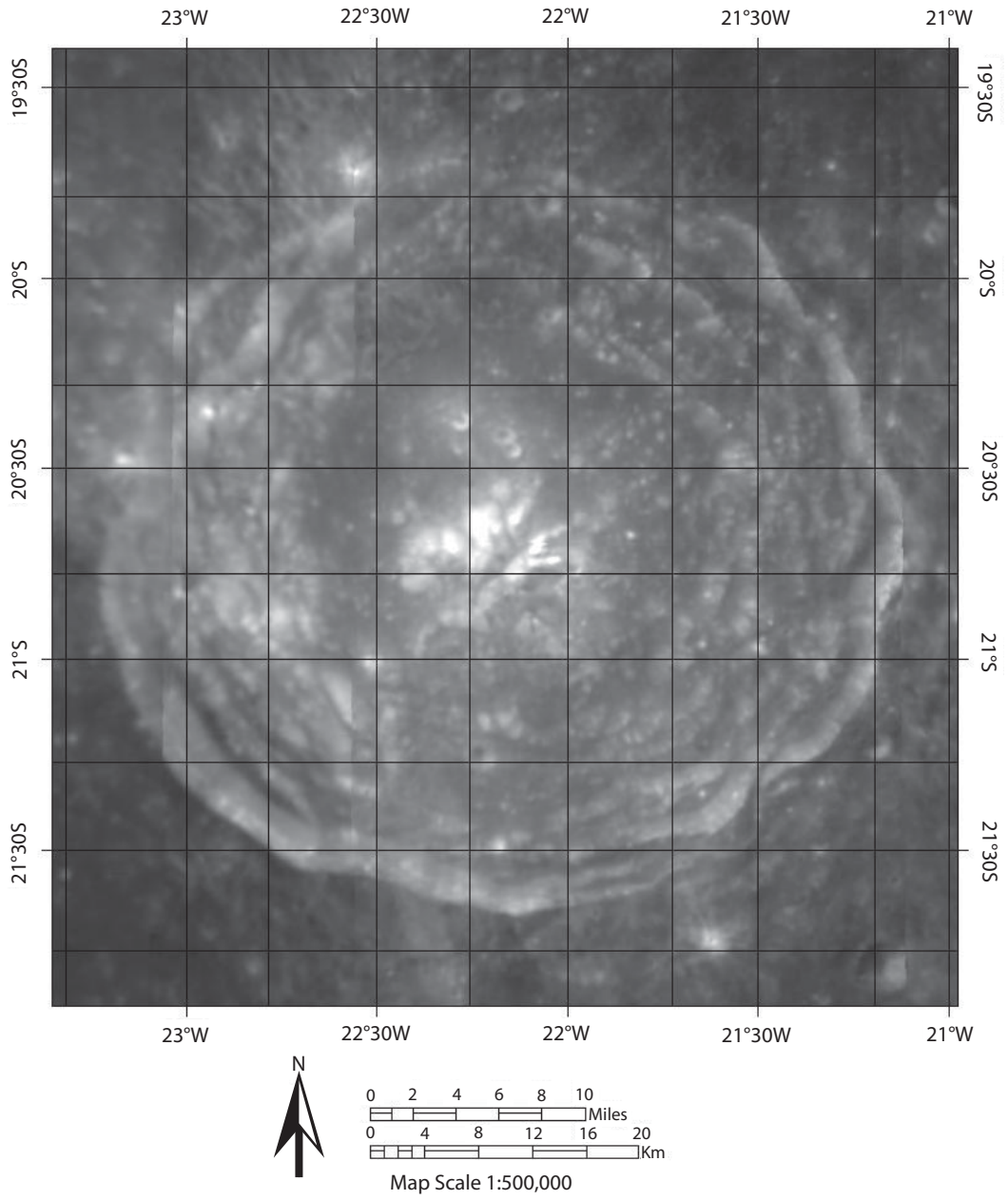


Figure 2.6: A Clementine grayscale 0.75 μm mosaic of Bullialdus crater.

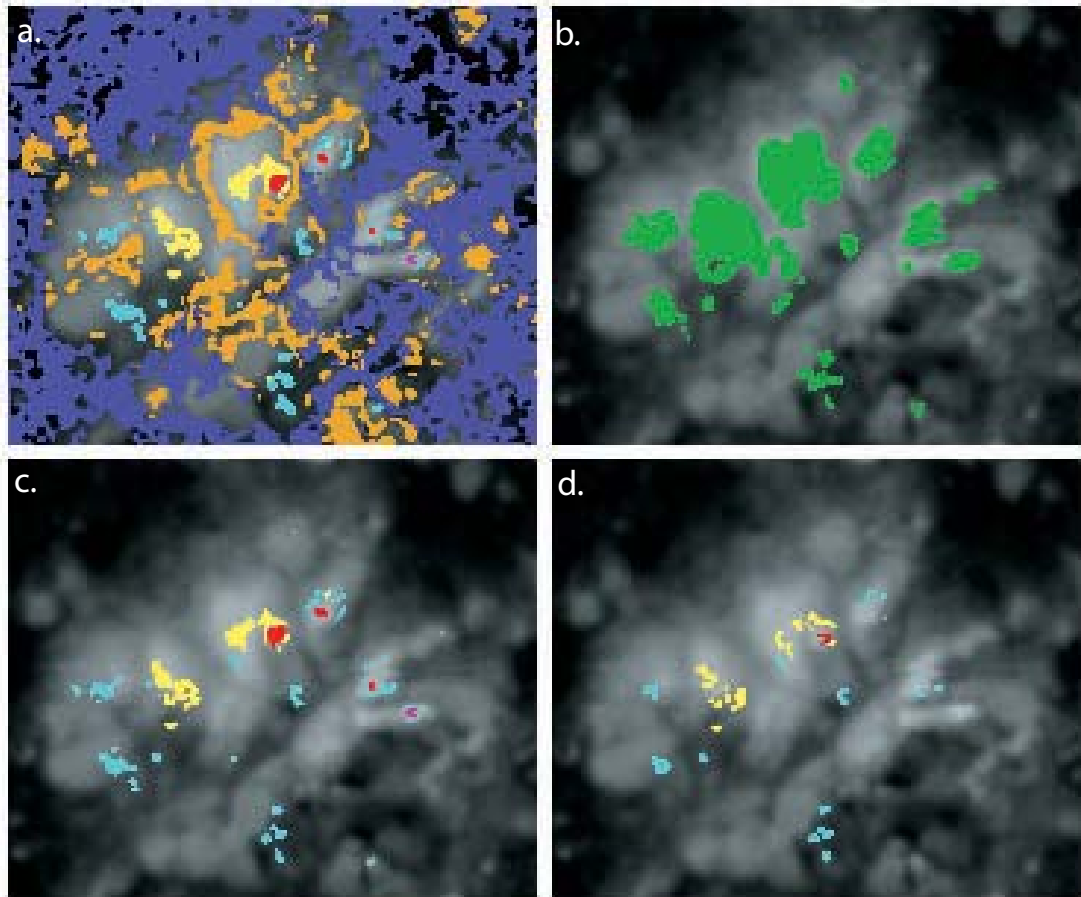


Figure 2.7a-d: Image (a) shows the spectral classes identified on Bullialdus' central peak fitting the spectral shape and band depth requirements. In (b) the immature material on Bullialdus is shown in green (not all of this material was matched to a spectral class). In (c) the spectral classes identified on the peak that fit the spectral shape and band depth requirements and also have ≥ 0.3 OMAT value. In (d) the areas where spectral classes are identified that fit the spectral shape, band depth, OMAT, and excursion parameter ($e=0.01$) requirements are highlighted. Spectral classes correspond with the colors: GNTA1-purple; GNTA2-orange; AN-yellow; AGN-light blue; N-red; and AG-maroon.

thresholds may exclude mixtures of the classes already recognized. Because Bullialdus' central peak exhibits steep slopes, mass wasting continuously uncovers material that is relatively unaltered by exposure to space. However, mineral mixing is likely to occur and pure end member spectra, such as *Tompkins and Pieters* spectral classes, and the search criterion in place here, may not be able to account for this.

The Clementine spectra that are found to correspond to a class are extracted and averaged to further minimize topographic shading effects (**Fig. 2.8**). The mean reflectance of the 0.75 μm band for model matches to N, AN, and AGN are 0.25, 0.22, and 0.27, respectively. Models that match these spectra are then identified using the same algorithms, thresholds, and excursions used to identify spectral classes on Bullialdus' central peak (**Table 2.4-2.6**). Models within ± 0.05 of the unknown Clementine 0.75 μm band have mineral assemblages within the dotted envelopes in **Figure 2.9**. These models are further discriminated by selecting the spectra with 0.75 μm reflectance band values within ± 0.02 of the unknown Clementine spectrum. Mineralogy for these models is shown in **Figure 2.9** in symbol form.

Our models suggest that all three of these mean Bullialdus spectra have a norite to gabbro-norite mineral assemblage. Spectra representative of class AGN have a norite model mineral assemblage and Mg' of 60. The only Apollo sample with a similar composition to this model result is Mg-suite gabbro-norite 14161 (clast 7044; pl: 49%, ol: 0%, opx: 32%, cpx: 10%) [Jolliff *et al.*, 1993]. Although 14161 is characterized with 10% more clinopyroxene than the best models, it falls within the envelope of model compositions with matching relative reflectance spectra and absolute reflectance within ± 0.05 .

Bullialdus spectra that are representative of class AN show a similar mineral assemblage to several lunar samples between Mg' 70-80. However, only the samples 14318 (clast 149), 77075/77215, and 73255 from Apollo 14 & 17 have nearly identical compositions to this model. These samples are characterized as Mg-suite norites containing 53-55% plagioclase, 0-12% olivine, 35-41% orthopyroxene, 0-5% clinopyroxene and an $\text{Mg}' \sim 70$ [James and McGee, 1979; Ryder and Norman, 1979; Warren *et al.*, 1983a; Warren *et al.*, 1983b].

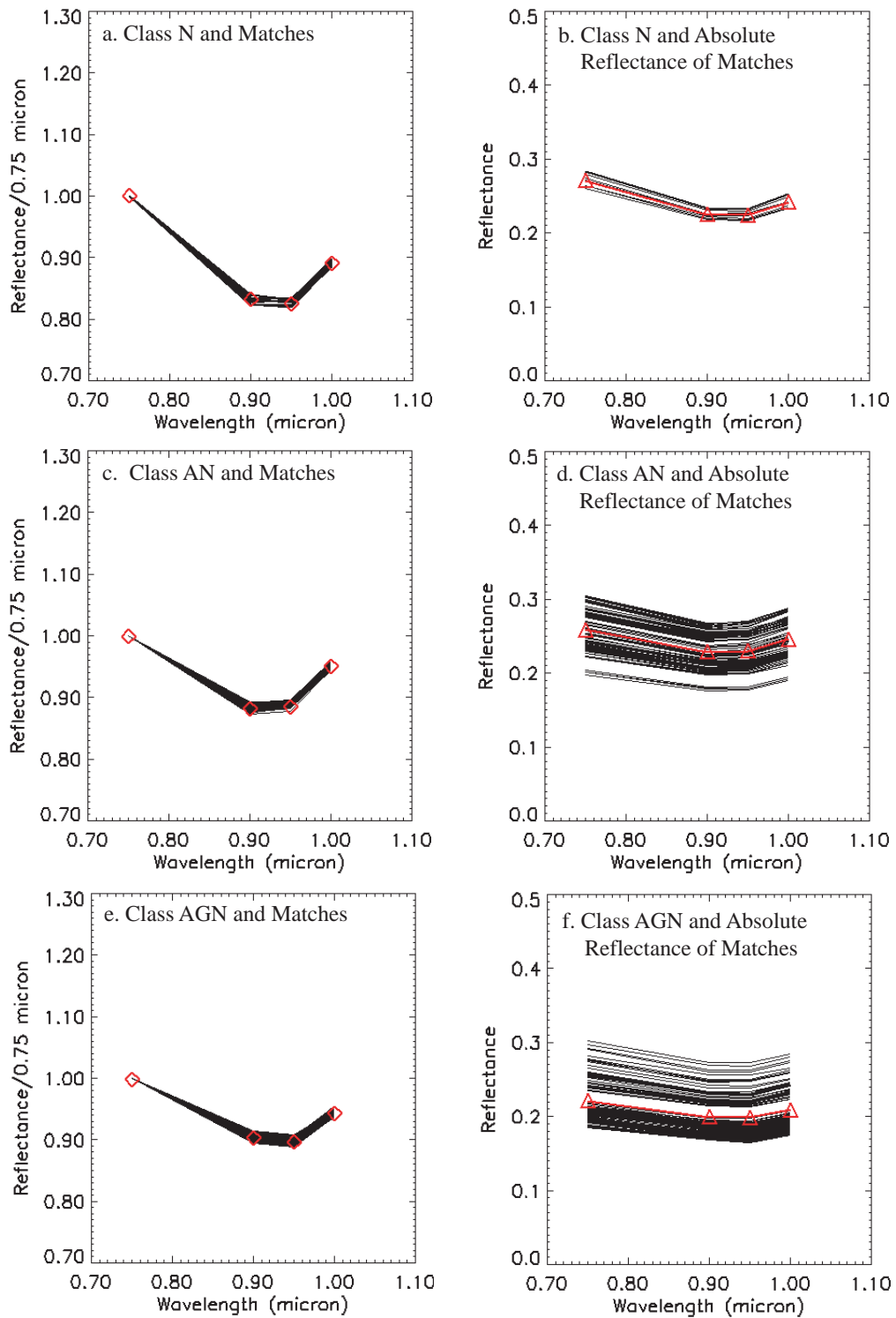


Figure 2.8a-f: In a, c, and e normalized spectral (in black) within Bullialdus fitting spectral shape, band depth, excursion, and OMAT criteria are matched to the spectral classes N, AN, and AGN, respectively (in red). In b, d, and f the absolute reflectance of these matches is shown in black with the mean of these spectra shown in red.

Table 2.4: Models within 0.02 absolute reflectance of Bullialdus spectra that match spectral class AN.

Mg'	Modeled Mineralogy				Model Reflectance Spectra (Wavelength-μm)					Model Spectrum Characteristics			
	Ol	Opx	Cpx	Pl	0.75	0.9	0.95	1.0	Correlation	Scale	Excursion	OMAT	
70	0	45	0	55	0.265	0.233	0.236	0.253	0.997	0.990	0.004	0.353	
	5	45	0	50	0.260	0.228	0.231	0.247	0.998	0.978	0.005	0.353	
75	0	40	5	55	0.263	0.230	0.233	0.250	0.997	0.972	0.005	0.353	
80	0	35	10	55	0.261	0.229	0.231	0.247	0.998	0.977	0.005	0.353	
	10	40	5	45	0.264	0.232	0.235	0.252	0.996	0.978	0.005	0.353	
85	10	35	10	45	0.265	0.233	0.236	0.251	0.997	1.013	0.004	0.353	
	55	45	0	0	0.265	0.233	0.236	0.251	0.995	0.995	0.004	0.353	
90	15	45	10	30	0.264	0.232	0.235	0.252	0.996	0.983	0.004	0.353	
95	0	55	15	30	0.264	0.232	0.234	0.250	0.998	1.002	0.003	0.353	
	5	55	15	25	0.262	0.231	0.233	0.248	0.997	0.996	0.004	0.353	

Table 2.5: Models within 0.02 absolute reflectance of Bullialdus spectra that match spectral class AGN.

<u>Mg'</u>	<u>Modeled Mineralogy</u>			<u>Model Reflectance Spectra (Wavelength--μm)</u>						<u>Model Spectrum Characteristics</u>			
	Ol	Opx	Cpx	Pl	0.75	0.9	0.95	1.0	Correlation	Scale	Excursion	OMAT	
60	0	45	0	55	0.234	0.210	0.210	0.220	0.996	0.976	0.004	0.329	
65	0	30	10	60	0.233	0.209	0.209	0.219	0.996	0.973	0.004	0.329	
85	5	35	5	55	0.235	0.212	0.212	0.222	0.995	0.983	0.004	0.329	
	0	20	20	60	0.233	0.210	0.209	0.219	0.995	0.977	0.004	0.329	
	15	25	15	45	0.235	0.212	0.212	0.222	0.994	0.982	0.004	0.329	
90	0	25	20	55	0.234	0.210	0.210	0.220	0.996	0.975	0.004	0.329	
	25	30	15	30	0.236	0.212	0.212	0.222	0.994	0.980	0.004	0.329	
95	0	35	20	45	0.237	0.214	0.214	0.223	0.995	0.997	0.005	0.329	
	5	35	20	40	0.236	0.212	0.212	0.222	0.995	0.989	0.004	0.329	
	10	35	20	35	0.234	0.211	0.210	0.220	0.994	0.981	0.004	0.329	

Table 2.6: Models within 0.02 absolute reflectance of Bullialdus spectra that match spectral class N.

<u>Mg'</u>	<u>Modeled Mineralogy</u>					<u>Model Reflectance Spectra (Wavelength—μm)</u>					<u>Model Spectrum Characteristics</u>				
	Ol	Opx	Cpx	Pl	PI	0.75	0.9	0.95	1.0	Correlation	Scale	Excursion	OMAT		
60	0	60	0	40	40	0.260	0.215	0.215	0.233	0.998	0.993	0.004	0.405		
65	10	55	0	35	35	0.261	0.217	0.216	0.231	0.998	1.006	0.005	0.405		
	0	35	15	50	50	0.263	0.219	0.218	0.234	0.999	1.012	0.004	0.405		
70	10	40	10	40	40	0.261	0.216	0.216	0.231	0.999	1.003	0.004	0.405		
	25	50	0	25	25	0.263	0.218	0.218	0.233	0.998	1.004	0.004	0.404		
75	0	30	20	50	50	0.257	0.213	0.213	0.229	0.999	0.993	0.004	0.405		
	5	35	15	45	45	0.262	0.217	0.218	0.235	0.998	1.000	0.004	0.405		
80	0	25	25	50	50	0.259	0.214	0.214	0.231	0.999	0.993	0.004	0.405		
	10	30	20	40	40	0.263	0.217	0.218	0.235	0.998	0.998	0.004	0.404		
85	5	25	25	45	45	0.264	0.219	0.219	0.235	0.999	1.012	0.005	0.405		
	10	25	25	40	40	0.260	0.216	0.215	0.231	0.999	1.002	0.004	0.405		
90	25	30	20	25	25	0.264	0.219	0.219	0.235	0.999	1.008	0.005	0.405		
	30	30	20	20	20	0.261	0.216	0.216	0.231	0.998	0.999	0.004	0.405		
95	50	35	15	0	0	0.262	0.217	0.217	0.233	0.998	0.999	0.004	0.404		
	15	30	25	30	30	0.263	0.218	0.218	0.234	0.999	1.006	0.004	0.405		
95	20	30	25	25	25	0.260	0.216	0.215	0.231	0.999	1.000	0.004	0.405		
	45	35	20	0	0	0.264	0.219	0.219	0.235	0.999	1.006	0.005	0.405		
	30	45	25	0	0	0.263	0.218	0.218	0.235	0.998	1.003	0.004	0.404		

Bullialdus Central Peak Mineralogy

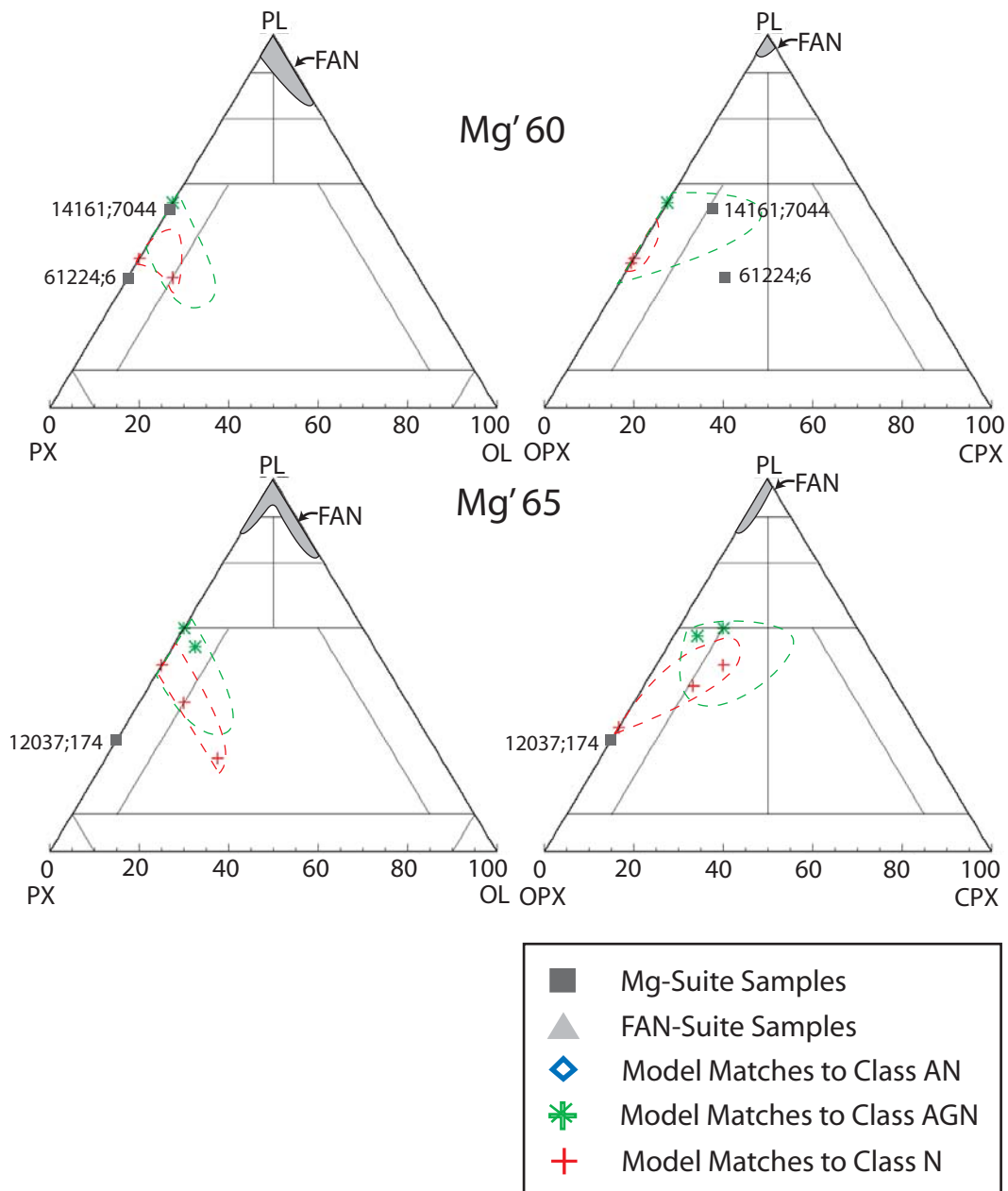


Figure 2.9: Shown on pl-ol-px and pl-opx-cpx Stöffler diagrams is the model mineralogy of mean Bullialdus reflectance spectra that match classes AGN, AN, and N (in green asterisks, blue diamonds, and red crosses, respectively) per Mg' [Stöffler, *et al.*, 1980]. Envelopes surrounding these analyses represent the variation in model mineralogy of relative reflectance matches within ± 0.05 of Bullialdus 0.75 micron band spectral values. They are also compared to FAN (light grey envelopes-sample clusters; light grey triangles-single samples) and Mg-suite (dark grey envelopes-sample clusters; dark grey squares-single samples) sample data. Single Apollo samples are labeled and sample clusters can be referenced by Mg' in **Table 2.2 and 2.3**.

Bullialdus Central Peak Mineralogy

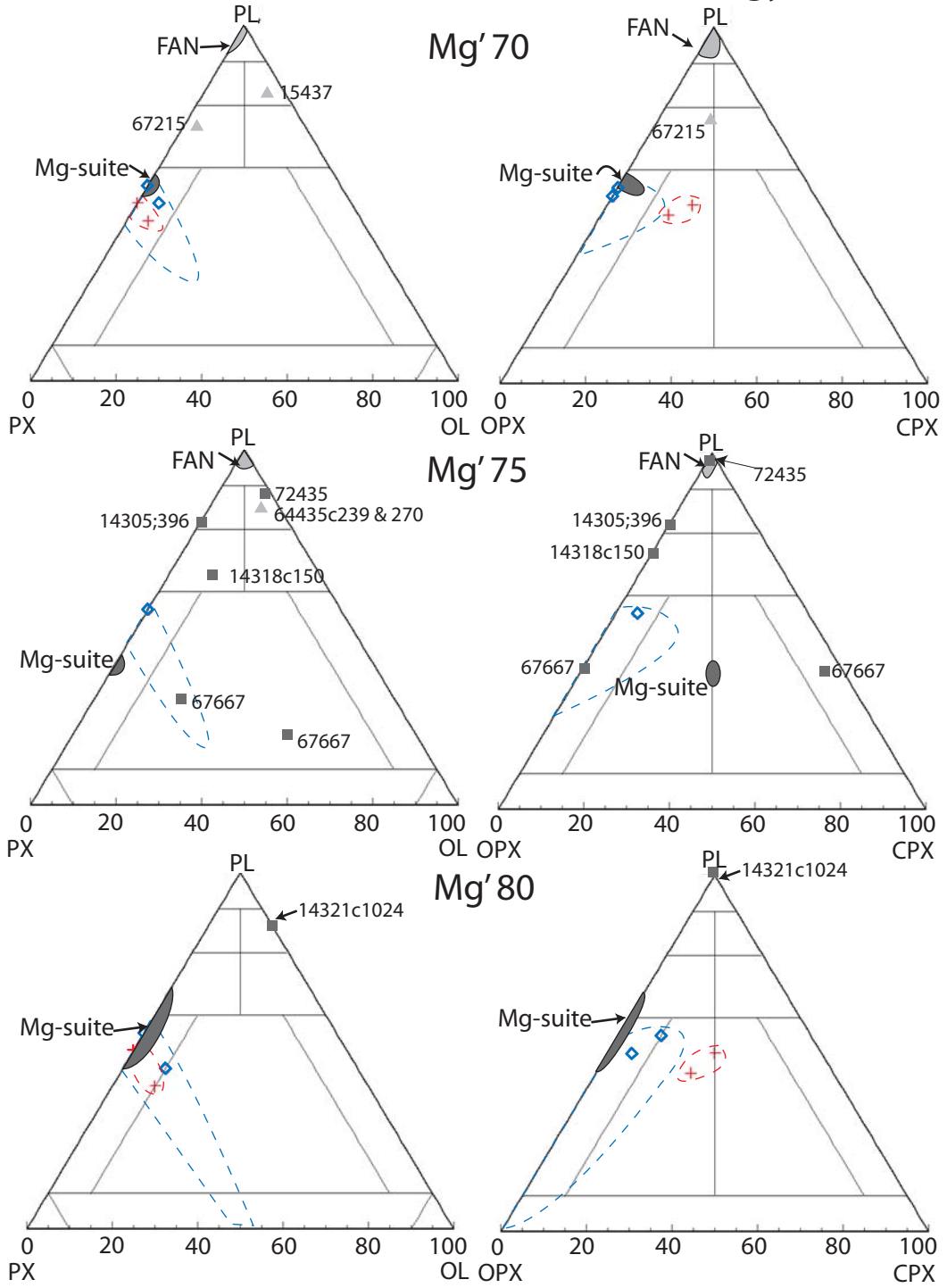


Figure 2.9 cont.:

Bullialdus Central Peak Mineralogy

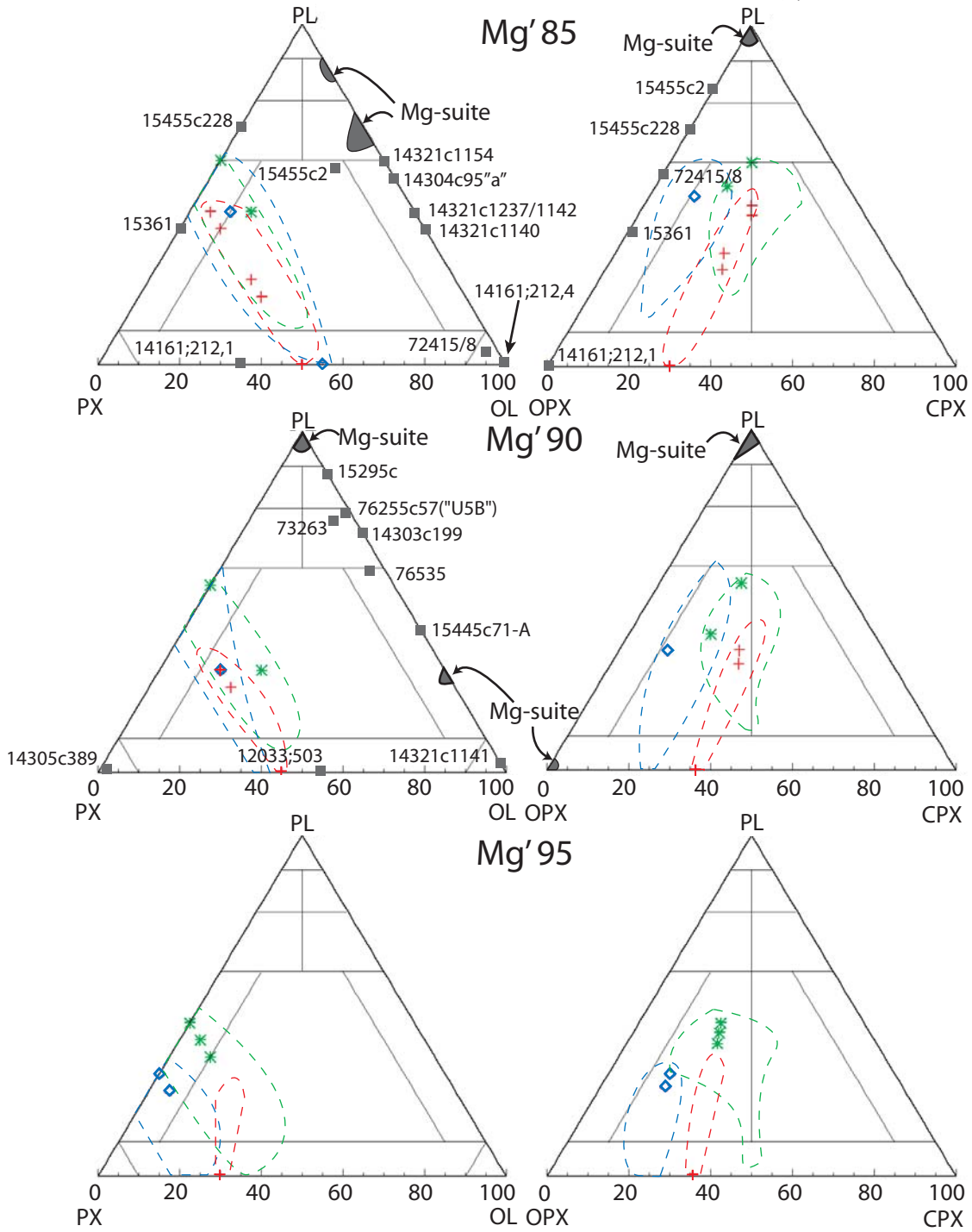


Figure 2.9 cont.:

Spectra identified as matches to class N have some modeled compositional characteristics similar to ten Mg-suite lunar samples. However, none of these samples have mineral assemblages close enough to modeling results to be considered representative of class N spectra on Bullialdus' central peak. Although, Mg-suite sample 12037 (clast 174) is probably the most compositionally similar to our models with a similar orthopyroxene to clinopyroxene proportions, it also has too much pyroxene and too little olivine in comparison [Warren *et al.*, 1990]. Despite not being able to identify a representative Apollo sample, modeling suggests spectra on Bullialdus representative of class N are indicative of an intermediate Mg' (~60) norite or a high Mg'(80-90) olivine-bearing gabbro-norite.

Discussion

Modeling shows that several spectral classes have mineral assemblages that can be interpreted unambiguously and are in agreement with *Tompkins and Pieters* [1999] interpretations. Knowledge of lunar sample modal mineralogy and chemistry helps supplement these model results substantively. This is done by comparing the compositional characteristics of Apollo samples to models in order to determine plausible representative lithologies for class spectra. Here we find that class A is compositionally similar to FAN samples 67635;8, 76224;5, 15007;296, and 73217c35 (Mg' 75), while class GNTA1 models suggest numerous FANs with similar characteristics [Floss *et al.*, 1998; Warren *et al.*, 1983a; Warren *et al.*, 1991]. Other classes, such as GNTA2 and T, have model mineral assemblages that suggest Mg-suite representative similarities. Class GNTA2 models are representative of 15455 (c228; Mg' 80) and class T models are consistent with troctolite sample 14321(c1140) and dunite samples 14161 and 72415/8 (Mg' 85 for each sample) [Lindstrom *et al.*, 1984; Morris *et al.*, 1990; Ryder and Norman, 1979; Ryder, 1985].

Modeling results also suggest that caution be exercised when analyzing relative (normalized) reflectance spectra. We find that spectra that are normalized can often be consistent with a very wide range of compositions, so that other criteria, such as reflectance, are needed to narrow the possible compositions. Our results suggest that analysis of relative reflectance should be used in conjunction with the additional diagnostic tool of absolute reflectance for more accurate

compositional determination. *Tompkins and Pieters* [1999] did not supplement their reported spectral class relative reflectance characteristics with absolute reflectance measurements because of inherent problems with the accuracy of Clementine reflectance in topographically rugged terrains. However, our modeling results suggest that reflectance is a useful discriminator for compositional determination that should be considered for analysis in future data sets. This is apparent from modeling of other spectral classes that result in ambiguous and dramatically different mineral assemblages that have nearly identical relative reflectance spectra.

Our pilot study of Bullialdus' central peak demonstrates how shape and contrast matching of Clementine and model relative reflectance spectra in conjunction with absolute reflectance knowledge further constrains the mineral assemblage possibilities. *Tompkins and Pieters* [1999] suggested the presence of classes GNTA1, GNTA2, AN, and N on Bullialdus' central peak. However, here we show a more mafic picture of Bullialdus' central peak by considering the optical maturity, relative reflectance, and absolute reflectance characteristics of its spectra. Anorthositic materials, GNTA1 and GNTA2, are identified on the crater floor and peaks slopes in abundance but are mature material. These spectral matches probably represent material that have been modified by space weathering processes that mimic the spectra of classes GNTA1 and GNTA2 but may or may not have the same mineralogy as immature exposures. Spectral analysis of Bullialdus with modeling also suggests other classes identified (AGN, AN, and N) are much more mafic than *Tompkins and Pieters* interpreted and have more Mg-suite characteristics.

Results of all three confirmed classes identified on Bullialdus have norite to gabbronorite mineral assemblages and only show compositional similarities to Mg-suite lithologies from the Apollo collection. Bullialdus spectra matching class AGN have a norite model mineral assemblage that is most similar to Mg-suite gabbronorite 14161 (clast 7044; Mg' of 60) [*Jolliff et al.*, 1993]. Models of class AN spectra on Bullialdus suggest nearly identical mineral assemblages to Mg-suite norites from Apollo 14 and 17 samples 14318 (clast 149), 77075/77215, and 73255 (Mg' 70-80) [*James and McGee*, 1979; *Ryder*, 1979; *Warren et al.*, 1983a; *Warren et al.*, 1983b; *Warren et al.*, 1983c]. And although class N spectra identified on Bullialdus are roughly consistent with *Tompkins and Pieters* [1999] interpretation, they are the only spectra here that

are ambiguous regarding compositional similarity to FAN or Mg-suite rocks. To our knowledge, no lunar samples have similar compositional characteristics to our models of these spectra. However, modeling does suggest that Bullialdus class N spectra are indicative of an intermediate Mg' (~60) norite or a high Mg' (80-90) gabbro-norite based upon the models that match its relative and absolute reflectance spectra.

We also find that not all immature spectra on Bullialdus are matched to one of *Tompkins and Pieters* [1999] spectral classes. Because of how our search criterion is set up we feel these immature and unmatched spectra differ enough from the eleven spectral classes that they may have a different mineralogy and chemistry. *Tompkins and Pieters* eleven spectral classes may be insufficient to account for all the spectral variation on Bullialdus crater central peak. However, it is also possible that mixtures of these eleven classes may account for the spectral diversity apparent on Bullialdus. Therefore, the eleven spectral classes may need adjustment or further additions.

In the future, compositional knowledge of Bullialdus classes and spectral classes in general can be further enhanced by better constraining Mg'. For example, although we determine a relatively unambiguous mineral assemblage for class AT by using a shape, scale, and excursion analysis of its relative reflectance spectrum, a representative lunar sample or petrologic suite cannot be definitively determined. Instead, class AT models suggest similarities to compositionally different FAN troctolitic anorthosites 15437 and 64435 (Mg' 70-75) and Mg-suite anorthositic troctolites (Mg' 85-90) from Apollo 17 (73235 and 76255) and Apollo 14 (14321c3, 14172c11, 14179c, 14305c268, and 14321c1154) [*Floss et al.*, 1998; *James et al.*, 1989; *Lindstrom et al.*, 1984; *McGee*, 1993; *Warren and Wasson*, 1980; *Warren et al.*, 1981; *Warren et al.*, 1983a; *Warren et al.*, 1983b]. Although, both interpretations are relatively magnesian, constraining Mg' would allow a more quantitatively diagnostic determination of petrologic suite and representative lithology for this class. Here we do not constrain Mg' when modeling spectral class or Bullialdus spectra because (1) *Tompkins and Pieters* did not report the necessary spectral class absolute reflectance values and (2) a topographically independent calculation of FeO for the visible spectral range is not available.

The addition of near-IR spectral information for spectral classes identified on the lunar surface will help resolve these issues. One advantage the near-IR provides is extra information in the form of additional diagnostic mineral absorption features for more accurate mineral proportion determination. This information will be useful to help resolve modeled olivine abundance in “gabbroic” classes AG, AGN, GN, and G reported here. These classes are characterized spectrally with varying 0.95 μm absorption features typically interpreted to be exclusively clinopyroxene-rich lithologies. However, here these “gabbroic” classes match models with significant olivine abundances (0-60%) in many cases. This may be due, in part, to a model artifact. However, the internal error of this model is $\pm 15\%$ [Lucey, 2004; Lucey, 2006], which does not account for all the variability in olivine abundance suggested in our results. Another plausible explanation may be that clinopyroxene is being mistaken for olivine. Modeling shows that high Mg’ clinopyroxene is nearly indistinguishable spectrally from olivine. But, this explanation does not explain high olivine abundances at low or intermediate Mg’ models. We are left to interpret these results in one of two ways. Either the model mineralogy of these classes is correct within a 15% internal error, or visible spectra do not give enough information to make a reliable interpretation regarding olivine content for these particular classes. We suggest caution when interpreting these “gabbroic” classes on the lunar surface until this issue is resolved.

Near-IR data can be further exploited using the FeO calculation developed by *Le Mouélic et al.* [2002] that nullifies topographic shading effects in visible and near-IR spectra in specific regional localities. *Lucey* [2006] has demonstrated that this algorithm is the most proficient and accurate FeO calculation algorithm to date. Constraining Mg’ with a topographically independent measure of FeO will be an important next step in radiative transfer models of lunar surface spectra.

Conclusions

In this work we further constrain the composition of lunar spectral classes initially documented by *Tompkins and Pieters* [1999] and their distribution on Bullialdus’ central peak and surroundings. We do this by implementing the recent theoretical contribution of *Hapke* [2001] to quantitatively describe space weathering in our radiative transfer models of VIS spectra.

This methodology allows us to make a direct comparison of lunar spectra to model spectra and modeled mineralogy to lunar sample data.

Modeling suggests that classes A, GNTA1, GNTA2, AT, and T are mineralogically unambiguous and roughly consistent with the interpretations of *Tompkins and Pieters* [1999]. In contrast, modeling suggests that the remaining mafic classes AN, AGN, AG, N, GN, and G are mineralogically ambiguous and often inconsistent with *Tompkins and Pieters* interpretations. We show this ambiguity is inherent in using spectra that are normalized. Absolute reflectance can also play an important role in identifying mineral assemblages for surface spectra with less compositional ambiguity. *Tompkins and Pieters* did not report absolute reflectance for the spectral classes they documented because of inherent topographic shading issues that lessened the accuracy of Clementine absolute reflectance spectra. Because of this, mineralogy cannot be determined unambiguously for these mafic classes. However, we do show that this knowledge can be applied to lunar imagery data to help constrain mineralogy.

A search of Bullialdus crater for spectral classes shows that locations on the crater floor and portions of the central peak match spectral classes GNTA1 and GNTA2. However, these areas are also shown to be optically mature and spectrally dark. It is unlikely that they are related to GNTA1 or GNTA2 which are immature and have high reflectance values. Spectral matches to immature spectra confined to Bullialdus' central peak include classes AN, AGN, and N. Modeling suggests these classes each have at least 40% mafics modally. Best match models have compositions that encompass several known variations of Apollo Mg-suite norite and gabbro-norite rocks with Mg' between 60-80.

Future Work

Work towards increasing the compositional precision of this study is a high priority. The best available method to do this is to capitalize on near-IR data collected by Clementine. *Le Mouélic et al.* [1999] have implemented a successful pixel-by-pixel calibration of the near-IR over several crater localities (e.g., Aristarchus, Tycho, Kepler). Using *Le Mouélic et al.'s* [2002] FeO calculation to calculate FeO free of topographic shading effects, we will be able to constrain the

Mg' for unknown spectra. Mafic mineral determination ambiguity will also benefit from additional spectral information in the near-IR and more precise optical constants. Future missions, such as Chandrayaan-1 and SELENE will provide higher spectral and spatial resolution data that will help this area of study immensely.

Acknowledgements

We would like to thank Dr. Sarah Noble, Dr. Lin Li, and Dr. Robert Carlson for thoughtful and thorough reviews, which improved this manuscript. We also want to recognize and thank Dr. B. Wilcox Denevi for reviewing an early draft of this manuscript. This work was funded by NASA Planetary Geology and Geophysics grant NNG05GJ51G to P.G.L. This is HIGP publication 1499 and SOEST publication 7169.

**CHAPTER 3. THE COMPOSITIONAL VARIATIONS OF THE LUNAR CRUST:
RESULTS FROM RADIATIVE TRANSFER MODELING OF CENTRAL PEAK
SPECTRA²**

² Cahill, J. T. S., P. G. Lucey, and M. A. Wieczorek (2009), Compositional variations of the lunar crust: Results from radiative transfer modeling of central peak spectra, *J. Geophys. Res.-Planets*, 10.1029/2008JE003282.

Abstract

We present model mineralogy of impact crater central peaks combined with crustal thickness and crater central peak depth of origin models to report multiple perspectives of lunar crustal composition with depth. Here we report the analyses of 55 impact crater central peaks and how their compositions directly relate to the lunar highlands sample suite. A radiative transfer model is used to analyze Clementine visible + near-infrared spectra to place compositional constraints on these central peak materials. Central peaks analyzed are dominantly magnesian and plagioclase poor; strong compositional similarities to lunar Mg-suite materials are evident. Relative to crustal thickness estimates, central peak mineralogy becomes more plagioclase-rich as the crust thickens. Relative to the crust-mantle boundary, the origin of peaks with dominantly mafic mineralogy are confined to the lower crust and primarily within the South-Pole Aitken (SPA) and Procellarum KREEP Terranes (PKT); additionally, central peaks with anorthositic mineralogy (> 60 vol. % plagioclase) are transported to the surface from all depths in the crustal column and confined to the Feldspathic Highlands Terrane (FHT). The discovery of mafic and magnesian materials, consistent with Mg-suite rocks of the sample collection, in all lunar terranes suggests that the process and sources that give rise to these types of rocks is not unique to the PKT and not necessarily dependent on incompatible elements for formation. The identification of ferroan and magnesian anorthositic material near the crust-mantle boundary of the FHT is also inconsistent with an increasing mafic/feldspar ratio and Mg' with depth in the crust.

Introduction

Many lines of evidence suggest that the lunar crust varies in composition with depth. The first evidence to support this was the discovery of tiny flecks of feldspar within the first lunar soil sample collected (10084) [*Smith et al.*, 1970; *Wood et al.*, 1970]; these grains of feldspar were inferred to originate from the nearby highlands and suggested the lunar crust consisted predominantly of plagioclase-rich rocks. This discovery led *Wood et al.* [1970] to hypothesize that the Moon formed from a global magma ocean and the first compositional constituents to float to the surface and build a crust consisted of anorthite. Further examination of lunar rocks also revealed mafic, magnesian samples that added compositional complexity to our view of crustal composition and formation subsequent to anorthositic crust emplacement [*Warner et al.*, 1976b; *Warren and Wasson*, 1977].

In order to better understand these complexities scientists looked to additional samples and data sets to analyze ever deeper lunar material. *Ryder and Wood* [1977] hypothesized that the “black-and-white” impact melt rocks of 15445 and 15455, associated with the Serenitatis and Imbrium impact basins, suggested that lunar crust consisted of three layers of systematically increasing mafic mineralogy with depth. Other sample studies, including those of Luna 24 regolith, suggested the crust showed lateral compositional heterogeneity [*Warner et al.*, 1978]. *Warren* [1979] and *James* [1980] synthesized these complexities and hypothesized that they could be explained via intrusions of separate ultramafic partial melts from the mantle (i.e., Mg-suite rocks) into a ferroan anorthosite (FAN) lunar crust formed via plagioclase flotation.

Other scientists focused their research efforts on the deeply excavating exposures of impact craters and basins, using Earth-based telescopic and orbital remote sensing data sets. *Spudis et al.* [1984] and *Spudis and Davis* [1986] observed a systematic trend in composition with basin diameter which they interpreted to indicate vertical chemical structure within the crust. *Spudis and Davis*' [1986] analysis of several impact basins led to their hypothesis that the crust consisted of an upper crustal mixture of anorthositic gabbro overlying mafic noritic (e.g., norite, LKFM basalts, and KREEP-bearing) basement rocks intruded sporadically by Mg-suite lithologies.

Pieters [1986] focused on examination of telescopic spectra of large impact crater central peaks on the lunar nearside. *Pieters'*[1986] study detected significant compositional complexity in the crust, laterally and vertically. *Tompkins and Pieters* [1999] expanded upon *Pieters'*[1986] study, for the first time examining a global distribution of impact central peaks with ultraviolet and visible multispectral Clementine images. *Tompkins and Pieters* [1999] spectral analysis of 109 crater peaks showed an unprecedented amount of compositional heterogeneity in the crust, but yielded no clear vertical or lateral patterns in lithology. Building upon these findings, *Wieczorek and Zuber* [2001] combined quantitative geophysical model estimates of lunar crustal thickness with the compositional results of *Tompkins and Pieters* [1999] to detect distinct compositional differences between the upper and lower portion of the crust; the upper crust averaged ~85 vol. % plagioclase compared to a more mafic 65 vol. % plagioclase for the lower crust.

Here we aim to build upon these studies combining quantitative spectral reflectance and crustal thickness algorithms to examine the stratigraphic composition of the lunar crust. *Wieczorek and Zuber's*[2001] model predicted that 17 craters of the *Tompkins and Pieters* [1999] data set sampled the lower crust of the Moon. In this study we specifically target craters that plausibly transport material from the deepest crust (and perhaps mantle) by using the lunar crust-mantle boundary as a point of reference when examining each crater peak. Our approach to modeling the crust is similar to that of *Wieczorek and Zuber* [2001] where we consider impact crater central peak origin relative to a single layered crustal thickness model. With this information we prioritize our selection of craters to survey for central peaks that plausibly excavated lower crust and/or mantle material. Out of the 55 impact crater central peaks reported here, approximately half are calculated to plausibly excavate material from within 5 km or below the crust-mantle interface. *Tompkins and Pieters* [1999] spectral interpretation approach of designating spectral classes for different rock-types is then refined by analyzing combined Clementine visible (UVVIS) and near-infrared (NIR) reflectance spectra with a quantitative radiative transfer model based upon the work of *Hapke* [1981; 1993; 2001]. Similar versions of this model have been implemented and validated in the lunar and asteroid literature [*Cahill and*

Lucey, 2007; Denevi et al., 2008; Lawrence and Lucey, 2007; Lucey, 2004; Lucey and Noble, 2008]. We demonstrate this method on the impact crater central peak Finsen which is a typical example of the crater sample examined here. Compositionally, *Tompkins and Pieters* [1999] observed an exceptional amount of spectral variability in Finsen including some of the only central peak spectra interpreted to be orthopyroxene-rich (other craters include Bullialdus, Birkeland, Bhabha, Lyman and White). It has been hypothesized by some that these orthopyroxene-rich peaks may indicate a compositional transition to lower crustal material [*Wieczorek and Zuber, 2001*].

Our crater sample shows compositional complexity similar to that reported by *Tompkins and Pieters* [1999], however our combined estimates of crustal thickness, crater depth of origin, and composition for these peaks have allowed us to identify trends in composition vertically and horizontally. Our results suggest a more mafic crust than reported by *Tompkins and Pieters* [1999]. The most mafic of these lithologies are largely confined to within 40 km of the crust-mantle boundary and in the South-Pole Aitken (SPA) and Procellarum KREEP Terranes (PKT). Anorthositic peaks are largely confined to the Feldspathic Highlands Terrane (FHT), but are found at all levels of the crustal column. Despite these findings peaks with an average composition indicative of anorthosite are rarely detected. Previous studies show that anorthosite is abundant in peak rings, but these are not examined here [*Hawke et al., 1991; Hawke et al., 1993; Hawke et al., 2003; Spudis et al., 1984*]. The majority of peaks in this study show remarkable compositional similarity to Mg-suite lithologies in the lunar sample collection. The likely reason for this is our sampling of craters which is dominated by models that suggest their peaks originated within lower crust or mantle.

Approach

Modeling Crustal Thickness: In order to select craters to analyze and examine any correlations in composition they may have with depth we first need to define the thickness of the crust globally. The models presented here are based upon the models of *Wieczorek and Phillips* [1998] and *Wieczorek et al.* [2006]. First, the gravity field that results from surface topography is computed (i.e., the Bouguer correction). This contribution is subtracted from the observed free-

air gravity field of the body, resulting in the Bouguer anomaly which is interpreted as relief along a subsurface density interface. These models assume that the crust is uniform in density (excluding a thin veneer of mare basalts in some areas) but do not assume that the Moon is isostatically compensated. A crustal thickness of 45 km at the Apollo 12 and 14 sites serves as our modeling anchor points [Wieczorek *et al.*, 2006]. This thickness is consistent with recent seismic inversions which suggest that the crustal thickness at these two sites is probably considerably thinner than the 65 km suggested by Toksöz *et al.* [1972]. Current thickness estimates of these sites include 45 ± 5 km [Khan *et al.*, 2000], 38 ± 8 km [Khan and Mosegaard, 2002], and 30 ± 2.5 km [Lognonne *et al.*, 2003].

Our first model, Model 1, is a canonical model in which the lunar gravity field is assumed to be solely the result of surface topography, a thin veneer of dense mare basalts, and relief along the crust-mantle interface. For this model the gravitational attraction of the mare basalts within the nearside mascon basins was taken into account using the mare thickness model of Solomon and Head [1980] modified by the maximum thickness constraints of Williams and Zuber [1998]. A density of 2900 and 3300 kg m⁻³ was assumed for the crust and mare basalts, respectively. For this model, a density of 3320 kg m⁻³ was assumed for the upper mantle.

Model 2 has one substantial difference from Model 1. In Model 2 we allow for the possibility that the degree-1 shape of the Moon might not be the result of crustal thickness variations (i.e., the 1.9 km center-of-mass/center-of-figure offset) but might instead be a result of lateral variations in density of the crust and/or mantle. In particular, the spherical harmonic degree-1 Bouguer anomaly terms were set to zero before inverting for the crustal thickness.

The resulting average crustal thicknesses for Models 1 and 2 are 53 and 43 km. The uncertainty of our crustal thickness maps is difficult to quantify as this depends upon our choice of the crustal and mantle densities, which are, a priori, not well known, as well as the uncertainty in the gravity model, which is poorly constrained over the farside hemisphere. Given that our models are also anchored by the Apollo seismic data, and the most recent inversion results differ

by about 10 km, it is probably prudent to use an uncertainty of at least ± 5 km for the absolute crustal thickness at any locale on the Moon.

Both Model 1 and 2 are used to determine a sample of potential mantle candidate peaks to examine here. Both models are valid scientific estimates of crustal thickness. However, in this study we simplify and focus on Model 1 but recognize that aspects of each model are plausibly occurring in the lunar crust. Figures detailing aspects of Model 2 are located in the appendix.

Modeling Peak Depth of Origin: Peak depth of origin is difficult to estimate due to the number of variables that influence the calculation. Each impact crater was created with a unique set of variables that characterize the initial impactor, its path, as well as the target material that ultimately influence the depth a peak will originate. However, studies of both impact theory and terrestrial craters have provided some benchmarks to make estimates of peak origin. Previous estimates of crater depth of excavation, which is referring to the depth of origin of crater ejecta, are estimated to be 0.1 to 0.2 times the diameter, d , of complex craters [Croft, 1980; Dence, 1968; Melosh, 1989; O'Keefe and Ahrens, 1993; Roddy, 1977]. However, another estimate to consider is the depth of melting. Cintala and Grieve [1998] suggest that the minimum depth of origin for a central peak coincides with the maximum depth of melting, and this origin is a function of crater diameter. The resulting depth of melting incurred by the crust follows an estimate of $0.109d^{0.08}$, where d is the final rim diameter of the crater in kilometers. This approximation method falls somewhere in between $0.1d$ to $0.2d$ depending on the diameter of the crater being examined.

Here, we consider both approximations of peak depth of origin; one estimating a depth of origin at $0.1D$ and the other at $0.109d^{0.08}$. The concept for estimating peak depth of origin is that the peak must originate from below the melt, so that the Cintala and Grieve [1998] estimates for depth of melting provide an lower limit or the maximum possible depth of origin, that can differ substantially from $0.1d$ for large craters. We use both estimates to determine our sampling of craters to examine, but neither is shown to have a higher correlation with composition. For this reason here we simplify and focus on the method of Cintala and Grieve [1998]. Impact crater diameter and location are determined from the online database of McDowell [2004] (available at

<http://host.planet4589.org/astro/lunar/>). With this information craters were evaluated for discernable peaks before they were examined spectrally.

Determination of Central Peak Origin in the Crust: Once we have constructed our crustal thickness models and estimated peak depth of origin we combine them to select craters of interest and determine vertical and lateral correlations with composition. Two methods of relating crater peak position and origin with composition are used. First, composition relative to the crustal thickness in the vicinity of each peak is examined to determine if composition is correlated with the overall thickness of the lunar crust. Second, we also examine where peak material originated within the crust relative to the crust-mantle boundary. This is examined in two ways. One estimate is calculated by determining the difference between the crustal thickness and peak excavation depth (**Fig. 3.1**). This is expressed by the equation,

$$P = T - D \quad (1)$$

where P is proximity to the crust-mantle boundary, T is crustal thickness estimates for Model 1 or Model 2 respectively, and D is the depth of origin using estimates for the maximum depth of melting (D_1) or maximum depth of excavation (D_2) respectively. For peaks where P is negative, crater peaks plausibly expose mantle material and for craters where P is positive peaks are modeled as having no chance of exhuming lunar mantle material.

For our second estimate, we examine where peak material originates relative to the current state of the crustal column. To do this, we scale P to the crustal thickness under that crater giving us knowledge of peak origin vertically relative to crustal thickness. This is expressed by the equations,

$$R = (T - D) / T \quad (2)$$

where R is a dimensionless quantity less than 1 that estimates the original position of central peaks in the context of the crustal column. For peaks where R is positive, material originated within the crust (e.g., 0 to 1); and for peaks where R is negative (e.g., <0), material originated from the lunar mantle.

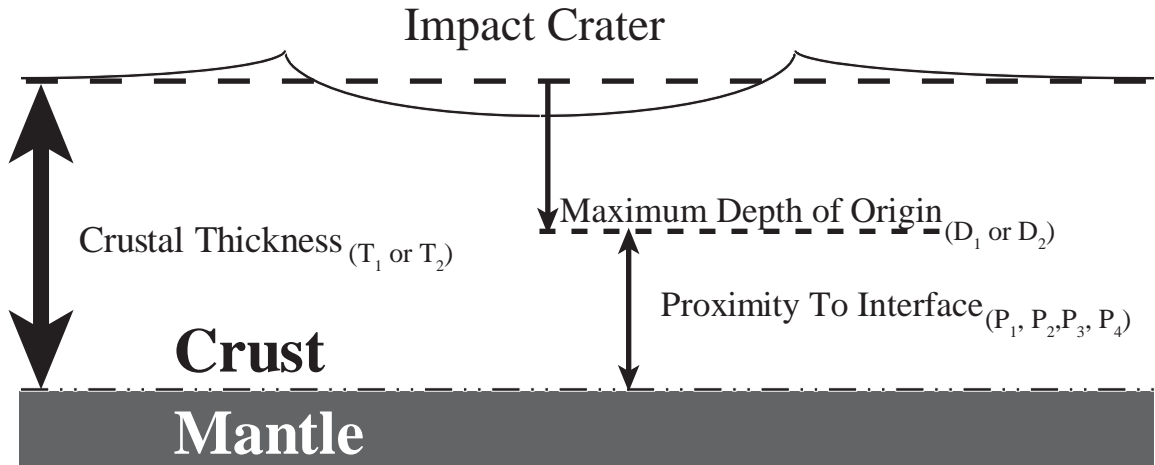


Figure 3.1: For each crater the proximity to the lunar crust-mantle boundary was calculated by subtracting the depth of origin (D) from the crustal thickness (T). Here proximity to the crust (P) mantle boundary via the maximum depth of origin is illustrated.

Crater peaks are prioritized for analysis using the parameter P . Crater central peaks modeled as plausibly originating in the lunar mantle, or at least lower crust, are given first priority for analysis. From this list we evaluate impact craters with high resolution Clementine data (100m/pixel) to determine if a peak is present and that immature material (>0.3 OMAT value) is available for analysis via the optical maturity parameter of *Lucey et al.* [2000]. This yields 28 central peaks we examine with material estimated to plausibly originate in or near the mantle. An additional 27 central peaks selected at random are examined for which no models predict the excavation of mantle rocks. This yields a total of 55 peaks and their compositions reported here out of the ~ 100 craters evaluated for a central peak and immature material based upon the optical maturity parameter of *Lucey et al.* [2000] (**Fig. 3.2**).

Spectral Analysis Approach: Crater central peaks are analyzed by comparing Clementine reflectance spectra to radiative transfer modeled spectra. The radiative transfer theory of *Hapke* [1981; 1993; 2001], mineral optical constant data of *Lucey* [1998] and iron optical constant data of *Paquin* [1995] are used in this model. Similar implementations of the model used here are reported by *Clark et al.* [2001], *Cahill and Lucey* [2007], and explained in detail by *Lawrence and Lucey* [2007]. In general, the model uses the optical constants (real, n , and complex indices, k , of refraction) of minerals to calculate single scattering albedo (the probability a photon will survive an encounter with a material) for each component at a specified particle size, maturity, and mineral chemistry. Single scattering albedo of each mineral component is added linearly, weighted by abundance, and converted to reflectance. Mineral modes used for this study span a plagioclase-olivine-orthopyroxene-clinopyroxene system at 5 vol. % intervals (17,710 modal combinations). Model spectra are computed and compared to Clementine spectra as a function of Mg-number ($Mg' = \text{molar Mg} / (\text{Mg} + \text{Fe}) * 100$) ranging from 50-95 in increments of 5.

We account for space weathering by using the optical maturity method of *Lucey et al.* [2000] and compute our models based upon the full range of immature compositions. *Lucey et al.'s*

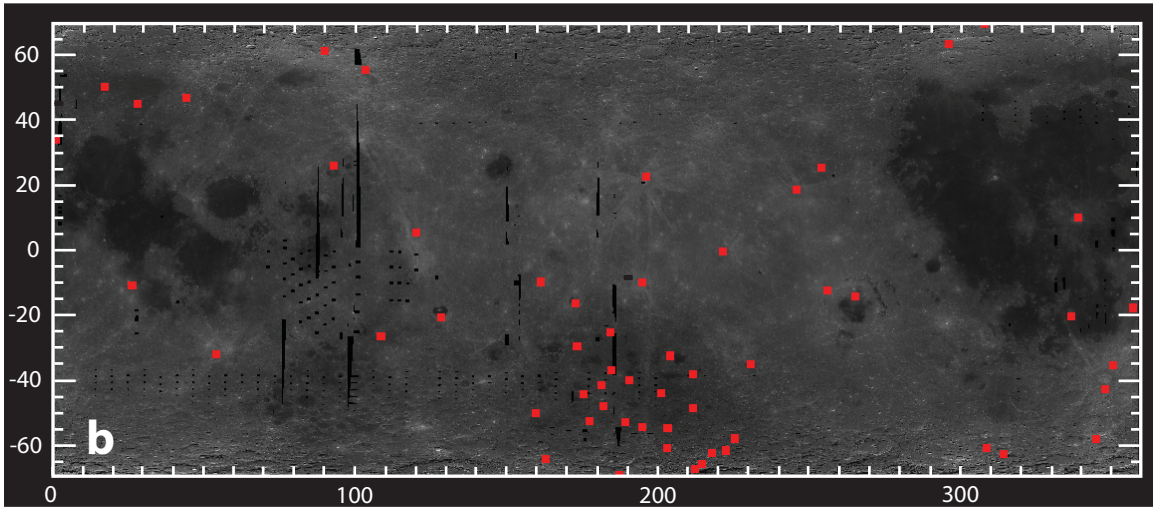
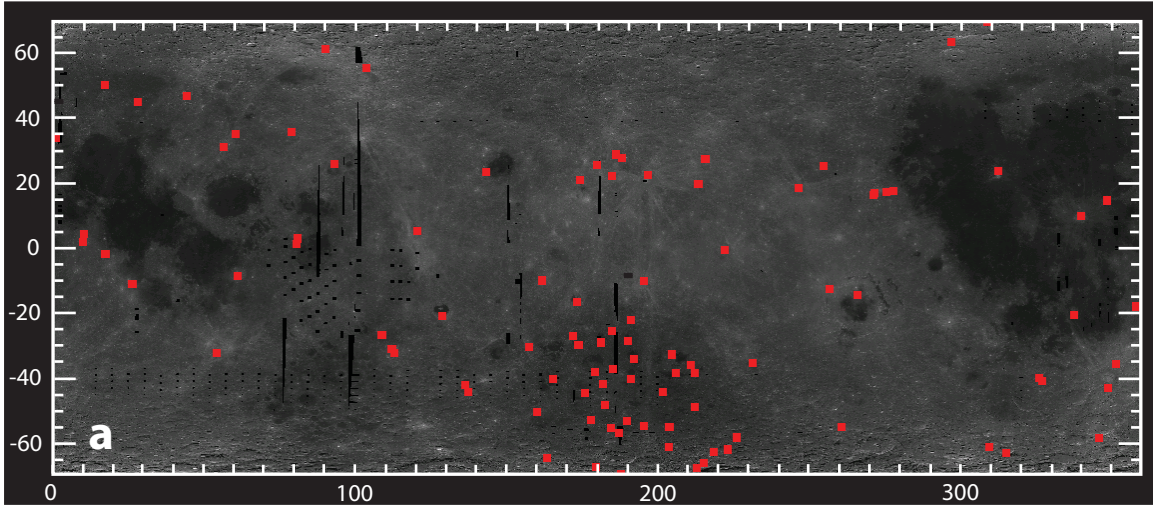


Figure 3.2: Location map of the impact crater central peaks examined in this study plotted on a Clementine 750 nm simple cylindrical image of the global lunar surface (1 km/pixel). (a) Red boxes denote the impact crater central peaks that were considered for compositional modeling. (b) Red boxes denote the impact crater central peaks that have immature material and were analyzed in this study.

[2000] optical maturity parameter (OMAT) quantifies optical maturity combining the reflectance and spectral contrast of each spectrum in a manner that is largely insensitive to composition. At 1 km spatial resolution the Moon ranges from .2 (highly mature) to .5 (immature) in this parameter. Here we compute models to cover 46 levels of maturity from 0.275 to 0.5 OMAT in increments of 0.005, which covers the full range of immature compositions on the surface of the Moon.

Cahill and Lucey [2007] demonstrate that several models can have the same relative reflectance shape but very different absolute reflectance values. So, here the model with the most similar relative reflectance spectral fit and estimated FeO (which is a function of absolute reflectance) to that of each Clementine spectrum is chosen as a match. Clementine estimated FeO is determined via the method of *Lawrence et al.* [2002] and model FeO is determined stoichiometrically for each model mineralogy. Using FeO as a constraint exposes the method to errors due to the influence of the local slope relative to the Sun on the derivation of FeO, so our uncertainties in estimating plagioclase content in particular are increased relative to a data set without this artifact. The relative error for individual minerals, Mg', and FeO is conservatively $\pm 10\text{-}15\%$, ± 8 units, and 1-2 wt% respectively [*Denevi et al.*, 2008; *Lucey*, 2004].

The data analyzed here differs from *Lucey* [2004] and *Cahill and Lucey* [2007] by including both Clementine UVVIS and NIR data (e.g., eight wavelengths including 0.75, 0.9, 0.95, 1.0, 1.1, 1.25, 1.5, and 2.0 μm) to enable better mineralogical interpretations. Both data sets are examined at a spatial resolution of 100 meters. Clementine near-infrared spectra are calibrated to Earth-based telescopic spectra collected of various locations on the lunar nearside. Documentation for these correction procedures and their results are posted on the USGS website (<http://astrogeology.usgs.gov/Projects/ClementineNIR/>) courtesy of *Denevi and Lucey* (personal communication). Spectra gain and offset corrections per near-infrared spectral band are reported in **Table 3.1**.

Table 3.1: Summary of near-infrared correction factors.

Spectra Band (nm)	Gain	Offset
1100	0.87	0.0246
1250	0.854	0.0316
1500	0.792	0.0514
2000	0.742	0.068

Results

Our results are reported in several sections, each section gradually adds additional perspectives to our overall view of the lunar crust. We first illustrate our method of spectral analysis by reporting compositional and crustal thickness estimates on an example central peak. We then place all the peaks analyzed into the perspective of the lunar sample suite for compositional and petrologic context. Finally, we add “depth” to this petrologic context by placing our compositional results into several perspectives of estimated lunar crustal thickness and central peak point of origin in the crust.

Analysis of Finsen central peak: Here we illustrate our analytical method applied to the impact crater Finsen as an example (**Fig. 3.3**). Finsen is located within SPA at 42° S and 177.4° W and has a diameter of 72 km. We estimate the local lunar crust in this area is between 5-16 km (T_1 and T_2 respectively) in thickness and Finsen likely transported material from 7 to 11 km of depth. Finsen peak is also modeled to originate from 5 km above or 5 km below the lunar crust-mantle boundary (P_1 and P_2 respectively; **Table 3.2**). The inferred proximity to the crust-mantle boundary makes Finsen a typical example of the deepest originating peaks we analyze here.

Our derived compositions of Finsen central peak spectra are more mafic than previously reported *Tompkins and Pieters* [1999] (**Fig. 3.4 and 3.5**). Mineral maps of Finsen show that olivine and plagioclase abundances on average are low, 9.4% and 25.4% respectively, while the average abundances of orthopyroxene and clinopyroxene are higher, 32.7% and 32.5% respectively (**Fig. 3.5**). On the lunar rock type classification scheme of Stöffler (1980) Finsen’s average lithology is a gabbroic norite; however, other lithologies present include norite, noritic gabbro, pyroxenite, and olivine-bearing gabbro-norite. The average Mg’ for Finsen central peak is 63.7, but the range of Mg’ is 40-75 indicating the presence of both ferroan and magnesian lithologies. Mean FeO determined from Clementine spectra is 14 wt% and ranges from 10-22 wt%.

Central Peak Composition Relative to Lunar samples: All other central peaks are analyzed in the same way as described for Finsen (**Tables 3.2-3.3**). Here we establish the modeled

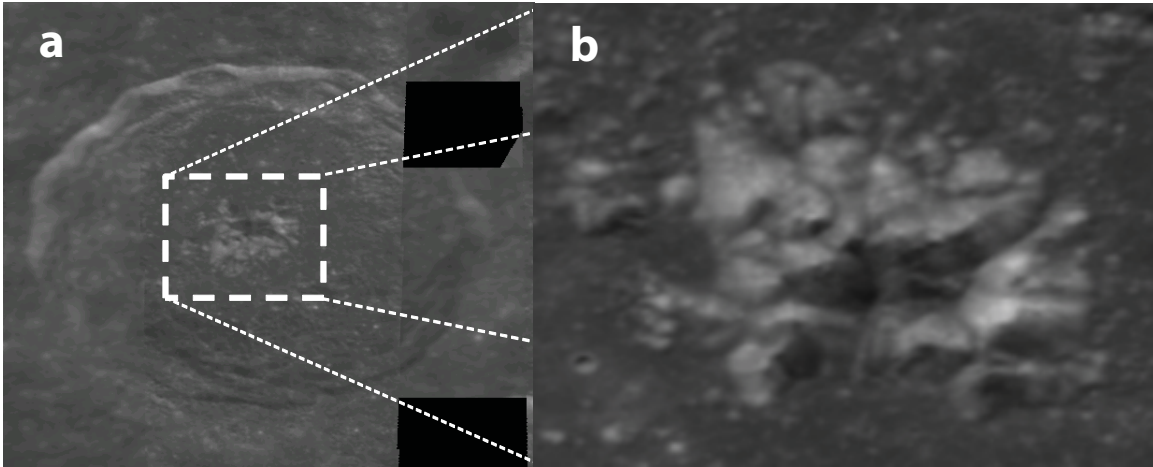


Figure 3.3: (a) Finsen crater is 72 km in diameter and we estimate that it overlays crust that is 5-16 km in thickness. Black areas are void of Clementine data. (b) Finsen central peak is estimated to have exhumed material from between 7-11 km of depth.

Table 3.2: Impact crater characteristics, estimated depth of origin, and crustal thickness values.

Crater Name	Diameter	Lat	Long	T ₁	T ₂	D ₁	D ₂	P ₁ ¹	P ₂ ²	P ₃ ³	P ₄ ⁴	R ₁ ⁵	R ₂ ⁶	R ₃ ⁷	R ₄ ⁸
Aitken	135	-16.8	173.4	41.0	26.4	22.2	13.5	18.8	4.2	27.5	12.9	0.5	0.2	0.7	0.5
Alder	77	-48.6	-177.4	17.1	6.7	12.1	7.7	5.0	-5.3	9.4	-1.0	0.3	-0.8	0.5	-0.1
Antoniadi	143	-69.7	-172.0	16.2	9.3	23.6	14.3	-7.4	-14.4	1.9	-5.0	-0.5	-1.5	0.1	-0.5
Aristillus	55	33.9	1.2	30.8	31.8	8.4	5.5	22.4	23.4	25.3	26.3	0.7	0.7	0.8	0.8
Aristoteles	87	50.2	17.4	29.6	28.9	13.8	8.7	15.8	15.2	20.9	20.2	0.5	0.5	0.7	0.7
Arzachel	96	-18.2	-1.9	38.8	41.7	15.3	9.6	23.5	26.4	29.2	32.1	0.6	0.6	0.8	0.8
Atlas	87	46.7	44.4	33.7	32.9	13.8	8.7	20.0	19.1	25.0	24.2	0.6	0.6	0.7	0.7
Bel'kovich	214	61.1	90.2	36.0	30.0	36.6	21.4	-0.6	-6.6	14.6	8.6	0.0	-0.2	0.4	0.3
Berkner	86	25.2	-105.2	50.6	36.5	13.6	8.6	36.9	22.9	42.0	27.9	0.7	0.6	0.8	0.8
Bettinus	71	-63.4	-44.8	40.2	36.8	11.1	7.1	29.1	25.7	33.1	29.7	0.7	0.7	0.8	0.8
Bhabha	64	-55.1	-164.5	15.5	5.9	9.9	6.4	5.6	-4.0	9.1	-0.5	0.4	-0.7	0.6	-0.1
Birkeland	82	-30.2	173.9	22.9	10.9	12.9	8.2	10.0	-2.0	14.7	2.7	0.4	-0.2	0.6	0.2
Borman	50	-38.8	-147.7	16.0	5.2	7.6	5.0	8.4	-2.4	11.0	0.2	0.5	-0.5	0.7	0.0
Bose	91	-53.5	-170.0	16.2	6.4	14.5	9.1	1.8	-8.0	7.1	-2.7	0.1	-1.3	0.4	-0.4
Boyle	57	-53.1	178.1	13.9	4.9	8.7	5.7	5.2	-3.8	8.2	-0.8	0.4	-0.8	0.6	-0.2
Bullialdus	60	-20.7	-22.2	25.0	26.6	9.2	6.0	15.8	17.4	19.0	20.6	0.6	0.7	0.8	0.8
Burg	39	45.0	28.2	32.7	32.6	5.8	3.9	26.9	26.9	28.8	28.7	0.8	0.8	0.9	0.9
Carpenter	59	69.4	-50.9	38.5	31.3	9.0	5.9	29.4	22.2	32.6	25.4	0.8	0.7	0.8	0.8
Clavius	245	-58.8	-14.1	39.3	38.3	42.4	24.5	-3.0	-4.1	14.8	13.8	-0.1	-0.1	0.4	0.4
Compton	162	55.3	103.8	33.0	26.6	27.1	16.2	5.9	-0.5	16.8	10.4	0.2	0.0	0.5	0.4
Copernicus	93	9.7	-20.1	33.3	34.2	14.8	9.3	18.5	19.3	24.0	24.9	0.6	0.6	0.7	0.7
Crommelin	94	-68.1	-146.9	18.5	10.9	15.0	9.4	3.5	-4.1	9.1	1.5	0.2	-0.4	0.5	0.1
Crommelin C	44	-66.4	-144.8	16.1	8.6	6.6	4.4	9.6	2.0	11.7	4.2	0.6	0.2	0.7	0.5
Crookes	49	-10.3	-164.5	78.1	56.9	7.4	4.9	70.7	49.5	73.2	52.0	0.9	0.9	0.9	0.9
Davisson	87	-37.5	-174.6	15.9	4.7	13.8	8.7	2.1	-9.1	7.2	-4.0	0.1	-1.9	0.5	-0.9
Dryden	51	-33.0	-155.2	21.6	9.0	7.7	5.1	13.9	1.3	16.5	3.9	0.6	0.1	0.8	0.4
Eijkman	54	-63.1	-141.5	15.9	7.9	8.2	5.4	7.7	-0.3	10.5	2.5	0.5	0.0	0.7	0.3
Eijkman D	25	-62.3	-136.9	16.3	8.3	3.6	2.5	12.8	4.8	13.8	5.8	0.8	0.6	0.8	0.7
Finsen	72	-42.0	-177.9	16.3	5.4	11.2	7.2	5.1	-5.8	9.1	-1.8	0.3	-1.1	0.6	-0.3
Fizeau	111	-58.6	-133.9	19.0	10.4	18.0	11.1	1.0	-7.5	7.9	-0.7	0.1	-0.7	0.4	-0.1
Grisson M	38	-49.1	-147.7	18.1	7.5	5.6	3.8	12.4	1.9	14.3	3.7	0.7	0.3	0.8	0.5
Hopmann	88	-50.8	160.3	18.8	10.3	14.0	8.8	4.9	-3.7	10.0	1.5	0.3	-0.4	0.5	0.1
Jackson	71	22.4	-163.1	72.0	52.1	11.1	7.1	61.0	41.1	64.9	45.0	0.8	0.8	0.9	0.9
Joliot	164	25.8	93.1	38.5	34.4	27.4	16.4	11.0	7.0	22.1	18.0	0.3	0.2	0.6	0.5
Keeler	160	-10.2	161.9	47.2	32.8	26.7	16.0	20.5	6.1	31.2	16.8	0.4	0.2	0.7	0.5
King	76	5.0	120.5	50.0	41.3	11.9	7.6	38.1	29.4	42.4	33.7	0.8	0.7	0.8	0.8
Langmuir	91	-35.7	-128.4	56.0	41.5	14.5	9.1	41.5	27.1	46.9	32.4	0.7	0.7	0.8	0.8
Lemaître S	34	-61.6	-156.3	16.2	7.5	5.0	3.4	11.3	2.5	12.8	4.1	0.7	0.3	0.8	0.5
Lowell	66	-12.9	-103.1	63.7	48.5	10.2	6.6	53.5	38.2	57.1	41.9	0.8	0.8	0.9	0.9
Lyman	84	-64.8	163.6	18.0	10.9	13.3	8.4	4.7	-2.4	9.6	2.5	0.3	-0.2	0.5	0.2
Maksutov	83	-40.5	-168.7	17.3	5.9	13.1	8.3	4.2	-7.2	9.0	-2.4	0.2	-1.2	0.5	-0.4
Maunder	55	-14.6	-93.8	30.6	21.7	8.4	5.5	22.2	13.4	25.1	16.2	0.7	0.6	0.8	0.7
Ohm	64	18.4	-113.5	58.7	42.7	9.9	6.4	48.8	32.8	52.3	36.3	0.8	0.8	0.9	0.9
Orlov	81	-25.7	-175.0	27.2	13.8	12.8	8.1	14.4	1.0	19.1	5.7	0.5	0.1	0.7	0.4
Pythagoras	142	63.5	-63.0	37.4	29.7	23.5	14.2	13.9	6.2	23.2	15.5	0.4	0.2	0.6	0.5
Scaliger	84	-27.1	108.9	41.8	36.6	13.3	8.4	28.5	23.3	33.4	28.2	0.7	0.6	0.8	0.8
Stevinus	74	-32.5	54.2	42.9	44.5	11.6	7.4	31.3	33.0	35.5	37.1	0.7	0.7	0.8	0.8
Stoney	45	-55.3	-156.1	13.6	4.4	6.7	4.5	6.8	-2.4	9.1	-0.1	0.5	-0.5	0.7	0.0
Theophilus	110	-11.4	26.4	29.2	33.6	17.8	11.0	11.4	15.8	18.2	22.6	0.4	0.5	0.6	0.7
Tsiolkovsky	185	-21.2	128.9	49.2	40.1	31.2	18.5	18.0	8.8	30.7	21.6	0.4	0.2	0.6	0.5
Tycho	102	-43.4	-11.1	40.9	41.5	16.4	10.2	24.5	25.1	30.7	31.3	0.6	0.6	0.8	0.8
Vavilov	98	-0.8	-137.9	76.5	56.6	15.7	9.8	60.8	40.9	66.7	46.8	0.8	0.7	0.9	0.8
Von Karman	180	-44.8	175.9	17.1	6.9	30.3	18.0	-13.3	-23.5	-0.9	-11.1	-0.8	-3.4	-0.1	-1.6
White	39	-44.6	-158.3	20.1	8.5	5.8	3.9	14.3	2.7	16.2	4.6	0.7	0.3	0.8	0.5
Zucchi	64	-61.4	-50.3	40.0	36.3	9.9	6.4	30.1	26.4	33.6	29.9	0.8	0.7	0.8	0.8

¹P₁ = T₁ - D₁

²P₂ = T₂ - D₁

³P₃ = T₁ - D₂

⁴P₄ = T₂ - D₂

⁵R₁ = (T₁ - D₁)/T₁

⁶R₂ = (T₂ - D₁)/T₂

⁷R₃ = (T₁ - D₂)/T₁

⁸R₄ = (T₂ - D₂)/T₂

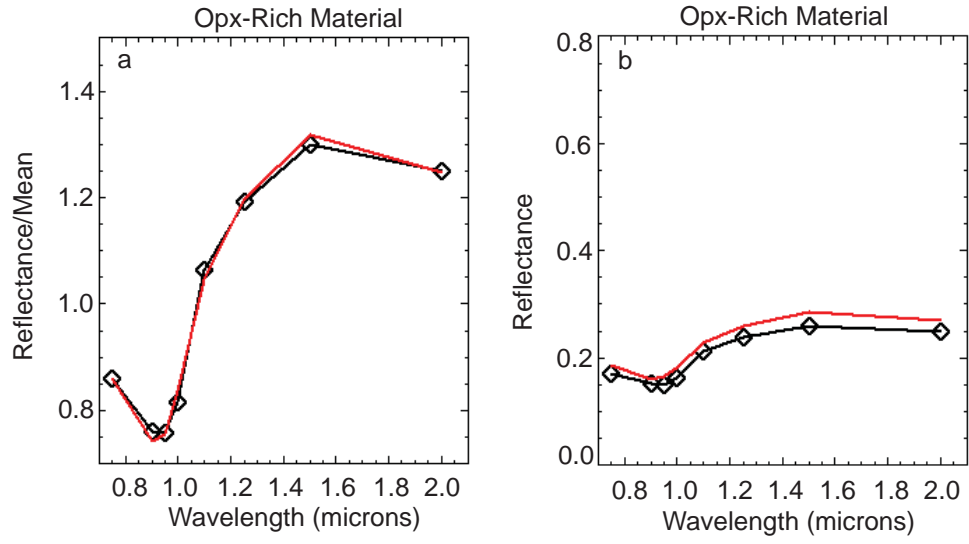


Figure 3.4: Representative Clementine and model VIS-NIR spectra in (a) relative and (b) absolute reflectance formats.

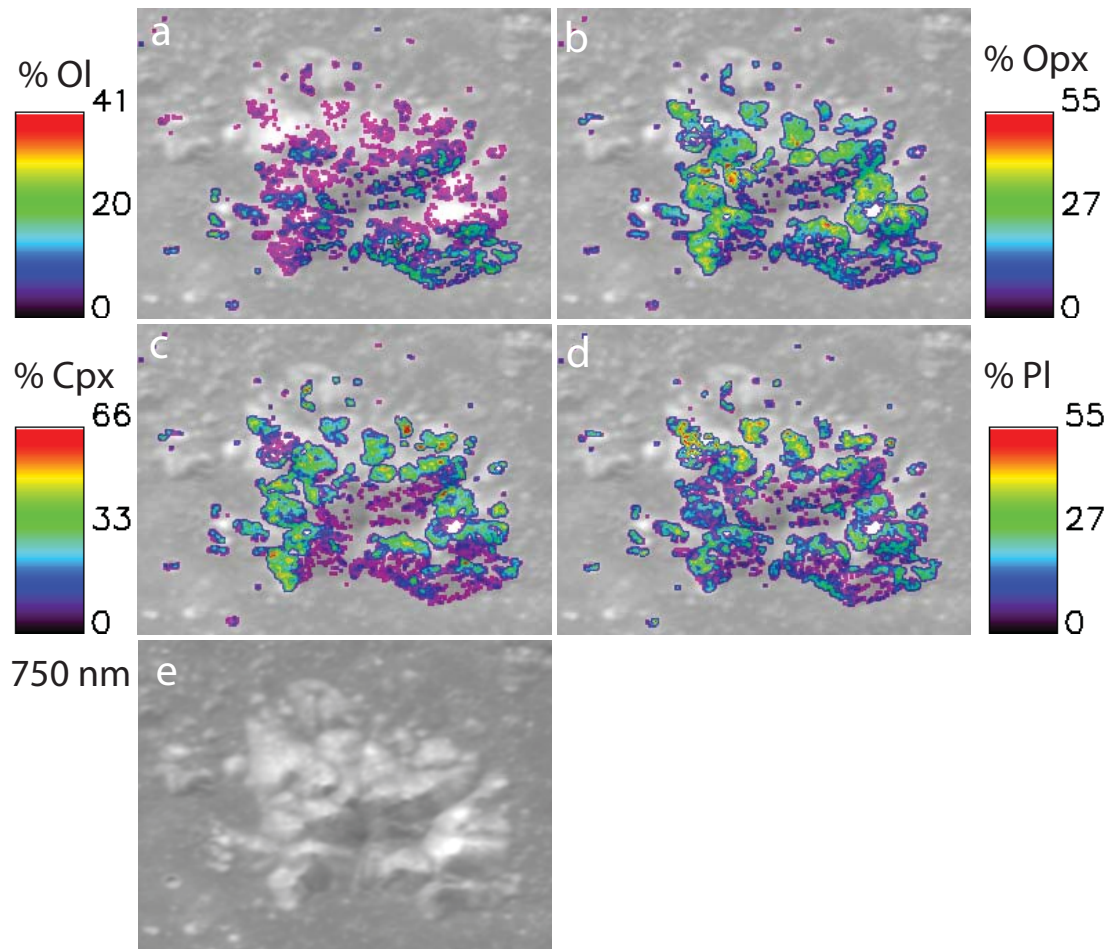


Figure 3.5: Model mineral maps of Finsen central peak inverted from Clementine VISNIR reflectance spectra and overlaid on a Clementine 750 nm reflectance image. Mineral abundance data for (a) olivine, (b) orthopyroxene, (c) clinopyroxene, and (d) plagioclase are displayed. Color scales are determined for the maximum abundance of each mineral. A Clementine 750 nm band image of Finsen central peak (e) is shown for context.

Table 3.3: Model mineralogy for lunar impact crater central peaks.

Crater Name	Lithology	Ol vol. %	Opx vol. %	Cpx vol. %	Pl vol. %	Mafics/Pl	Opx/Cpx	Mg'
Aitken	troctolite	33	5	4	59	0.7	1.3	76
Alder	ol-noritic gabbro	15	18	28	39	1.6	0.7	67
Antoniadi	ol-norite	17	35	8	41	1.5	4.5	75
Aristillus	ol-gabbroic norite	15	36	30	20	4.1	1.2	70
Aristoteles	ol-noritic gabbro	13	23	29	35	1.8	0.8	68
Arzachel	anorth troctolite	26	8	4	62	0.6	2.0	73
Atlas	anorth gabbro	9	12	17	62	0.6	0.7	72
Bel'kovich	gabbroic anorthosite	4	5	8	84	0.2	0.6	85
Berkner	anorth norite	7	9	9	75	0.3	1.0	70
Bettinus	noritic anorthosite	3	14	4	79	0.3	3.4	79
Bhabha	ol-noritic gabbro	22	27	30	22	3.7	0.9	71
Birkeland	ol-noritic gabbro	16	23	40	20	4.0	0.6	64
Borman	ol-norite	38	10	0	53	0.9		77
Bose	ol-gabbroic norite	15	27	26	32	2.1	1.0	65
Boyle	ol-gabbroic norite	28	25	9	38	1.6	2.7	77
Bullialdus	gabbroic norite	10	34	14	43	1.3	2.4	70
Burg	noritic gabbro	8	15	41	36	1.8	0.4	66
Carpenter	noritic anorthosite	3	10	5	82	0.2	2.0	80
Clavius	anorth gabbro	7	7	11	75	0.3	0.7	83
Compton	anorth gabbro	17	8	11	64	0.6	0.7	80
Copernicus	troctolite	72	1	5	22	3.6	0.3	92
Crommelin	ol-noritic gabbro	13	19	20	48	1.1	0.9	76
Crommelin C	ol-noritic gabbro	22	17	12	49	1.0	1.5	77
Crookes	anorth gabbro	13	4	22	61	0.6	0.2	71
Davisson	peridotite (pyroxenite)	35	17	41	6	14.8	0.4	64
Dryden	ol-gabbroic norite	7	29	27	38	1.7	1.1	66
Eijkman	ol-gabbroic norite	11	29	12	48	1.1	2.4	66
Eijkman D	ol-noritic gabbro	13	14	40	33	2.0	0.3	60
Finsen	gabbroic norite	9	33	32	25	2.9	1.0	64
Fizeau	gabbroic norite	6	33	23	39	1.6	1.4	67
Grissom M	ol-gabbroic norite	24	18	12	46	1.2	1.5	69
Hopmann	ol-noritic gabbro	21	19	20	40	1.5	0.9	66
Jackson	anorth gabbro	11	6	18	65	0.5	0.3	80
Joliot	troc anorthosite	11	1	5	82	0.2	0.3	69
Keeler	troc anorthosite	13	0	1	86	0.2	0.3	70
King	ol-gabbro	20	8	39	34	2.0	0.2	78
Langmuir	ol-noritic gabbro	18	10	20	53	0.9	0.5	72
Lemaitre S	ol-norite	31	21	6	43	1.3	3.6	74
Lowell	anorth troctolite	20	10	9	62	0.6	1.1	71
Lyman	gabbroic norite	6	41	10	42	1.4	4.0	75
Maksutov	ol-gabbroic norite	12	41	32	15	5.5	1.3	67
Maunder	noritic gabbro	9	15	50	25	3.0	0.3	63
Ohm	gabbro	9	7	45	38	1.6	0.2	68
Orlov	ol-noritic gabbro	13	15	31	41	1.5	0.5	64
Pythagoras	anorth gabbro	9	5	12	74	0.3	0.4	82
Scaliger	ol-noritic gabbro	29	8	23	40	1.5	0.4	74
Stevinus	ol-gabbroic norite	19	14	10	57	0.7	1.4	71
Stoney	ol-noritic gabbro	39	21	28	12	7.0	0.7	73
Theophilus	anorth troctolite	25	4	10	60	0.7	0.4	78
Tsiolkovsky	ol-gabbro	19	7	26	48	1.1	0.3	78
Tycho	ol-noritic gabbro	16	9	23	52	0.9	0.4	72
Vavilov	anorth gabbro	8	5	16	70	0.4	0.3	75
Von Karman	ol-noritic gabbro	23	12	19	46	1.2	0.6	67
White	ol-gabbroic norite	46	26	17	11	8.5	1.5	71
Zucchius	noritic gabbro	10	13	18	59	0.7	0.7	72

composition of each peak relative to the known compositions of lunar highlands samples. Models of central peak spectra show a large diversity of average lithologies but most of them are dominantly mafic (**Fig. 3.6**). Peaks with mafic model mineralogy also show many similarities to olivine-bearing gabbroic Mg-suite rocks of the lunar sample collection. However, peak pyroxene abundances show more diversity with orthopyroxene-rich gabbroic norite and clinopyroxene-rich noritic gabbro lithologies both being present. Several peaks modeled also have anorthositic mineralogies and show similarities to both lunar FANs and anorthositic Mg-suite rocks.

The typical method to discern lunar petrologic suites is to compare mafic mineral Mg' with one of the numerous "plagiophile loving" elements or ratios (e.g., Ca/Ca+Na, Al, Ti/Sm, Al/Eu, etc.) [Warren and Kallemeyn, 1984]. The mafic Mg' versus plagioclase An method is the most often used because it can be accomplished easily and nondestructively with electron microprobe analysis of coexisting mafic and plagioclase minerals. However, in the context of spectral reflectance analysis these chemical distinctions for plagioclase cannot be achieved (at present). What we can determine with confidence is mafic Mg' and plagioclase abundance. Cahill and Lucey [2007] reported a compilation of modal mineralogy and Mg' for ~100 lunar FAN and Mg-suite rocks. In **figure 3.7a**, examination of these data show that taking the mean Mg' of the mafic minerals weighted by their relative proportions and the mean plagioclase abundance effectively separate the lunar FAN and Mg'- petrologic suites. To a large degree this method also separates the rock types within the Mg-suite. With this knowledge we have a method to make direct comparisons between remotely determined impact crater central peak composition and the lunar sample collection. Here, model results show that the selection of lunar central peaks analyzed are dominantly similar to Mg-suite rocks (**Figure 3.7b**). These Mg-suite-like peaks are plagioclase-poor (<60 vol. %) and vary from ferroan to magnesian varieties (Mg' 55-94), or may be plagioclase-rich (>60 vol. %) with an Mg' of 78-85. A few central peaks also show some similarity to FAN rocks with greater than 70 vol. % plagioclase and Mg's of ~ 70-75. Although the central peak modeled rock types do not necessarily perfectly overlap the fields defined by the samples, the basic distinction between ferroan and magnesian rocks is present, as is the general

VISNIR Modeling

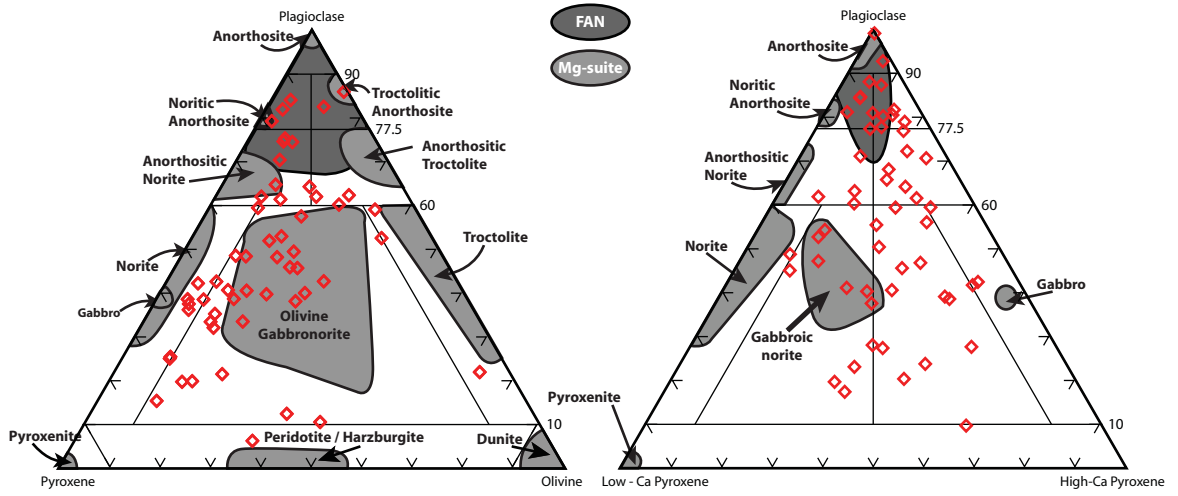


Figure 3.6: Mean mineral assemblages for each impact crater central peak analyzed compared to known assemblages of the lunar sample suites (dark grey—FAN; grey—Mg-suite) on plutonic rock classification diagrams [Stöfler, *et al.* 1980].

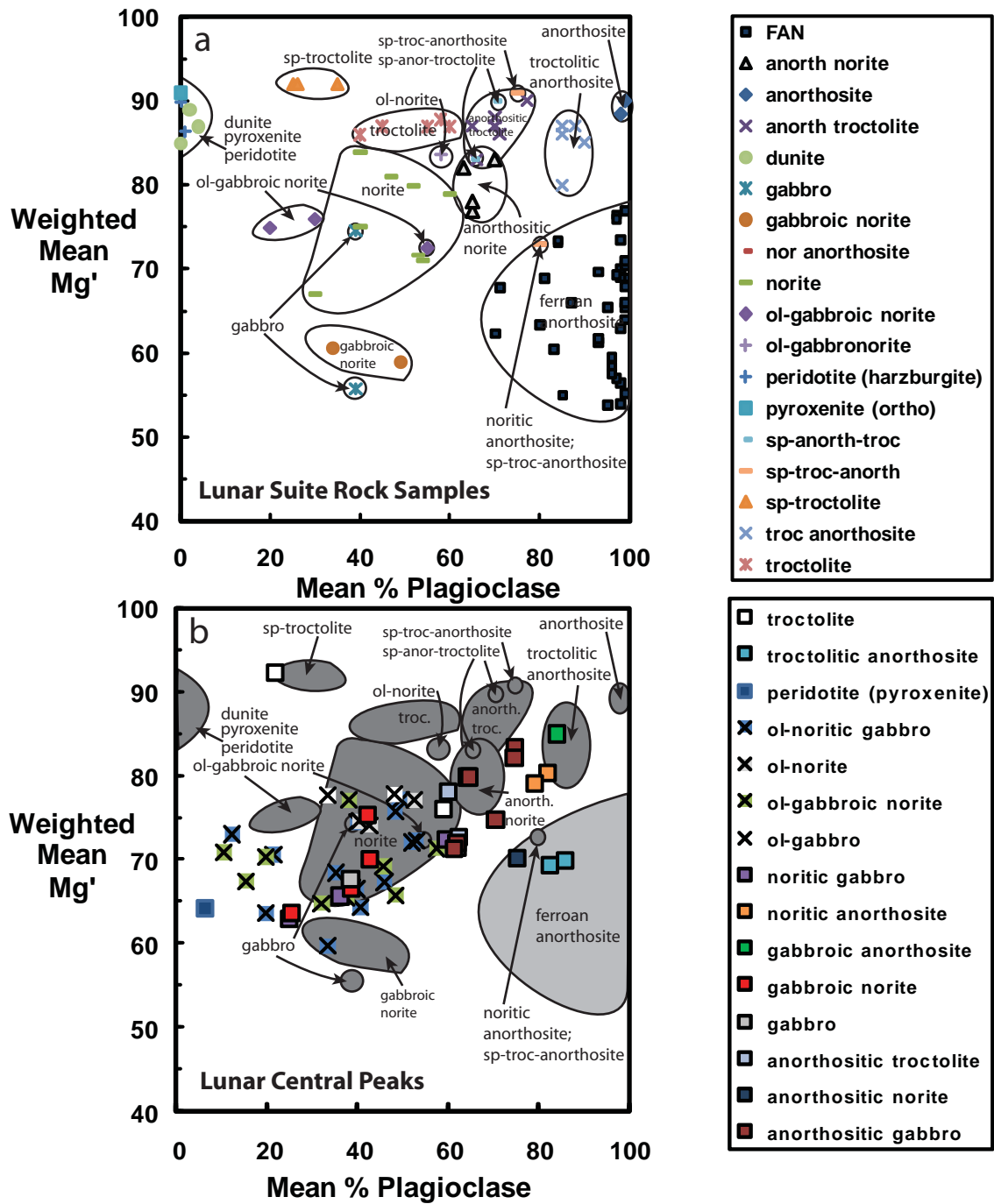


Figure 3.7: Lunar FAN and Mg-suite sample comparison using mafic weighted mean Mg' versus plagioclase abundance. In (a) sample data points are displayed and Mg-suite samples are denoted by lithology; in (b) peak average assemblages are displayed.

correlation of plagioclase with Mg' in the mafic peaks. We should also note that this diagram cannot distinguish alkali from ferroan anorthosites. Here we will assume ferroan, plagioclase-rich compositions are FAN.

Composition relative to crustal thickness: Although the correlation is weak, it is apparent that plagioclase gradually increases as the crust thickens with peaks often having anorthositic (>60 vol. % plagioclase) mineral assemblages above crustal thicknesses of 60 km (**Fig. 3.8**). For crust thinner than 60 km, peaks tend to be mafic (> ~50 vol. % mafics). Olivine and orthopyroxene abundances range from near 0 to ~45 vol. % and do vary as crustal thickness changes. Again, this variation is not highly correlated but is apparent. In thicker crust (i.e., >50 km), both olivine and orthopyroxene abundances are low (< 15 to 20 vol. %) in all peaks analyzed. However, as the crust thins the maximum observed abundance of these two minerals for many peaks increases until they each reach their highest overall abundances (~45 vol. %) in crust less than ~30 km thick. But, although olivine- and orthopyroxene-rich lithologies are observed exclusively in thin crust, other varieties of lithologies with less abundant proportions of these two minerals are observed in thin crust as well. This increase in orthopyroxene as the crust thins is also reflected in the overall pyroxene abundance, as the orthopyroxene/clinopyroxene ratio increases from less than 0.5 in thick crust to greater than 4 in thin crust. In crust greater than 60 km thick average clinopyroxene abundance is less than 25 volume percent; but in crust less than 60 km thick clinopyroxene maximum abundance increases to ~45 vol. % but has an overall range of 0-45 vol. %. Model Mg' shows a relatively magnesian Mg' range of 70-85 in both thick and thin crust; however, as the crust thins to less than 35 km, more ferroan (Mg' 58-70) peaks are also present. Although FeO increases in thin crust relative to thick, several peaks show more ferroan compositions as FeO increases from thick (~7 wt. %) to thin (>18 wt. %) crust.

Composition relative to peak origin: Here we relate the composition of the central peaks analyzed to their origin in the crustal column. An estimate of exhumation depth scaled to the thickness of the crust, R , (e.g., Ratio = [thickness – depth]/thickness]) shows that most peaks

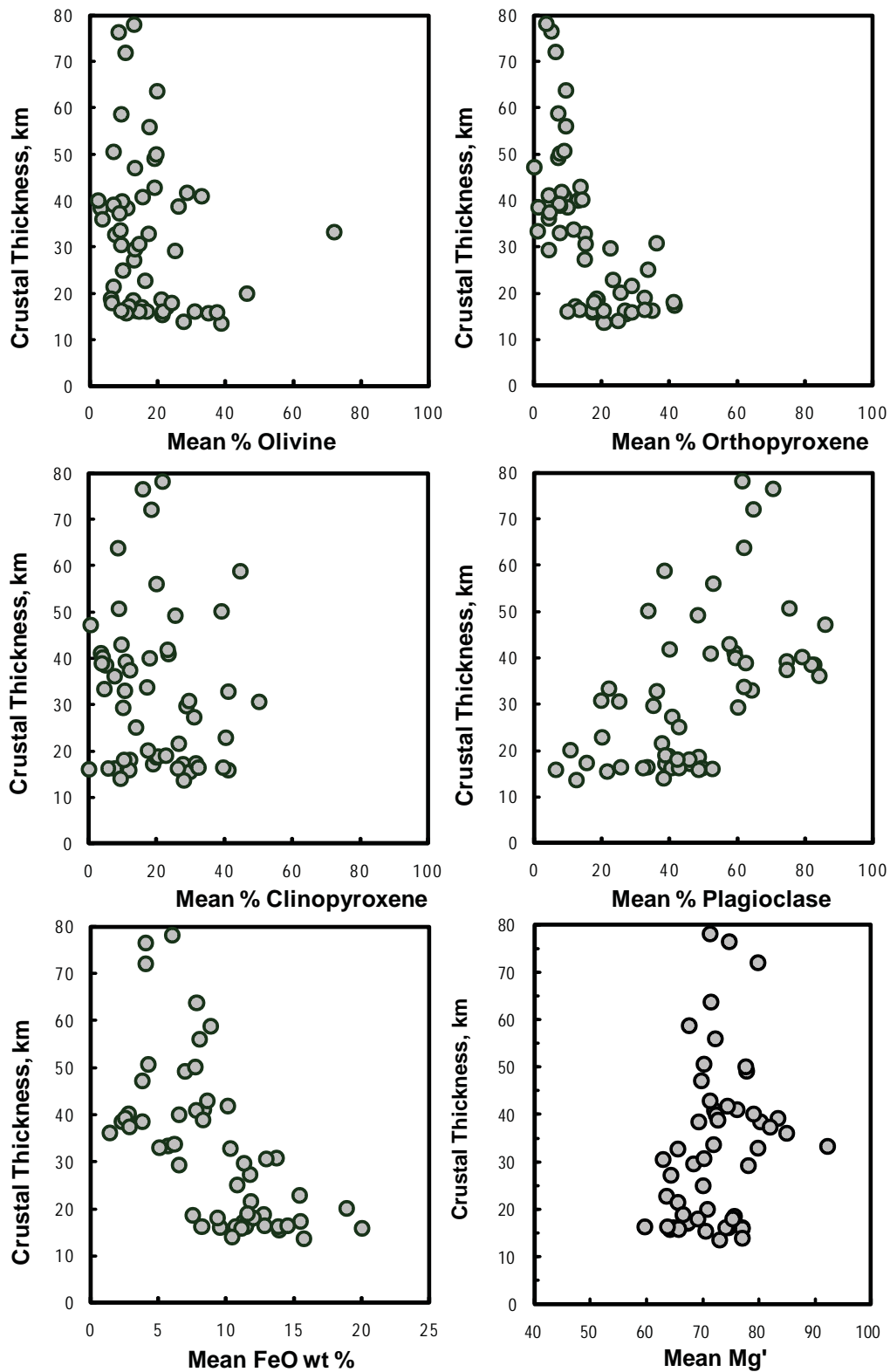


Figure 3.8: Mean lunar impact crater central peak mineralogy and chemistry versus crustal thickness (T_c).

analyzed originated from nearly all depths possible in the crustal column, but no compositional trends are discerned (**Fig. 3.9**). This may suggest that there are no compositional trends within the crust and that composition is only a function of crustal thickness, but this assumes crustal structure is independent of thickness, and has been preserved since it was established. When we use the crust-mantle boundary as our reference point by determining P (e.g., Proximity = thickness – depth) compositional trends, although weakly correlated, are shown to be present (**Fig. 3.10**). The crust-mantle boundary acts as a good reference point because it was established at the same time as crustal formation and is not affected by material stripped away by impact bombardment. Even in the case of SPA and its plausible isostatic rebound after basin formation, stratigraphic compositional relationships should be more intact near the crust-mantle boundary unless impact melting occurred deeply enough to destroy these relationships by creating an impact melt sheet that extends deep below SPA [Morrison, 1998].

Model mineralogy between 40 and 80 km from the crust-mantle interface show low abundances of olivine and orthopyroxene (<15 to 20 vol. %); only clinopyroxene maintains greater than 20 vol. % within this proximity to the mantle boundary. Model peak plagioclase abundance is on average largely anorthositic (>60 vol. % plagioclase) 50 km above the interface. Mineralogy within 40 km of the crust-mantle boundary and below is diverse, with both highly mafic and plagioclase-rich lithologies present. Mafic lithologies (>40 vol. % mafics) are largely confined to the crust within 40 km of the crust-mantle boundary, whereas plagioclase-rich (>60 vol. %) lithologies are seen throughout the crustal column.

Peak chemistry 40-80 km away from the crust-mantle boundary is magnesian (Mg' 70-80) despite low FeO (<7 wt. %) and anorthositic (>60 vol. %) lithologies. More compositional diversity is observed from peaks that originate closer to (i.e., within 0 to 40 km) the crust-mantle boundary; these peaks range in Mg' from ferroan (~60) to more magnesian (~93) lithologies.

Composition of peaks laterally. The compositional diversity of peaks in the lateral perspective is largely consistent with lunar terrane [Jolliff *et al.*, 2000; Wieczorek and Phillips, 2000]. In **figure 3.11**, peaks with anorthositic (≥ 60 vol. %) modeled mineralogy are nearly

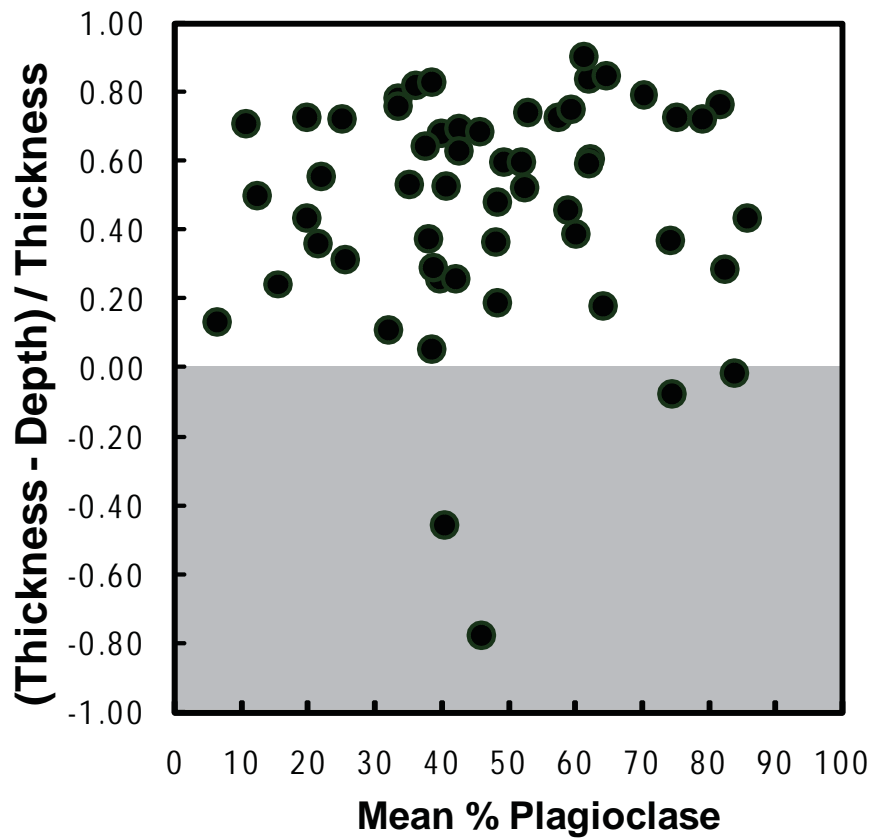


Figure 3.9: Plagioclase abundances versus the origin of impact crater central peak materials. The origin of the central peak materials are represented by ratios calculated based on the proximity to mantle relative to the local crustal thickness. Peaks with ratios greater than zero originated in the crust; peaks with ratios less than zero (in grey) originated in the mantle (e.g., $(T_1 - D_1) / T_1$).

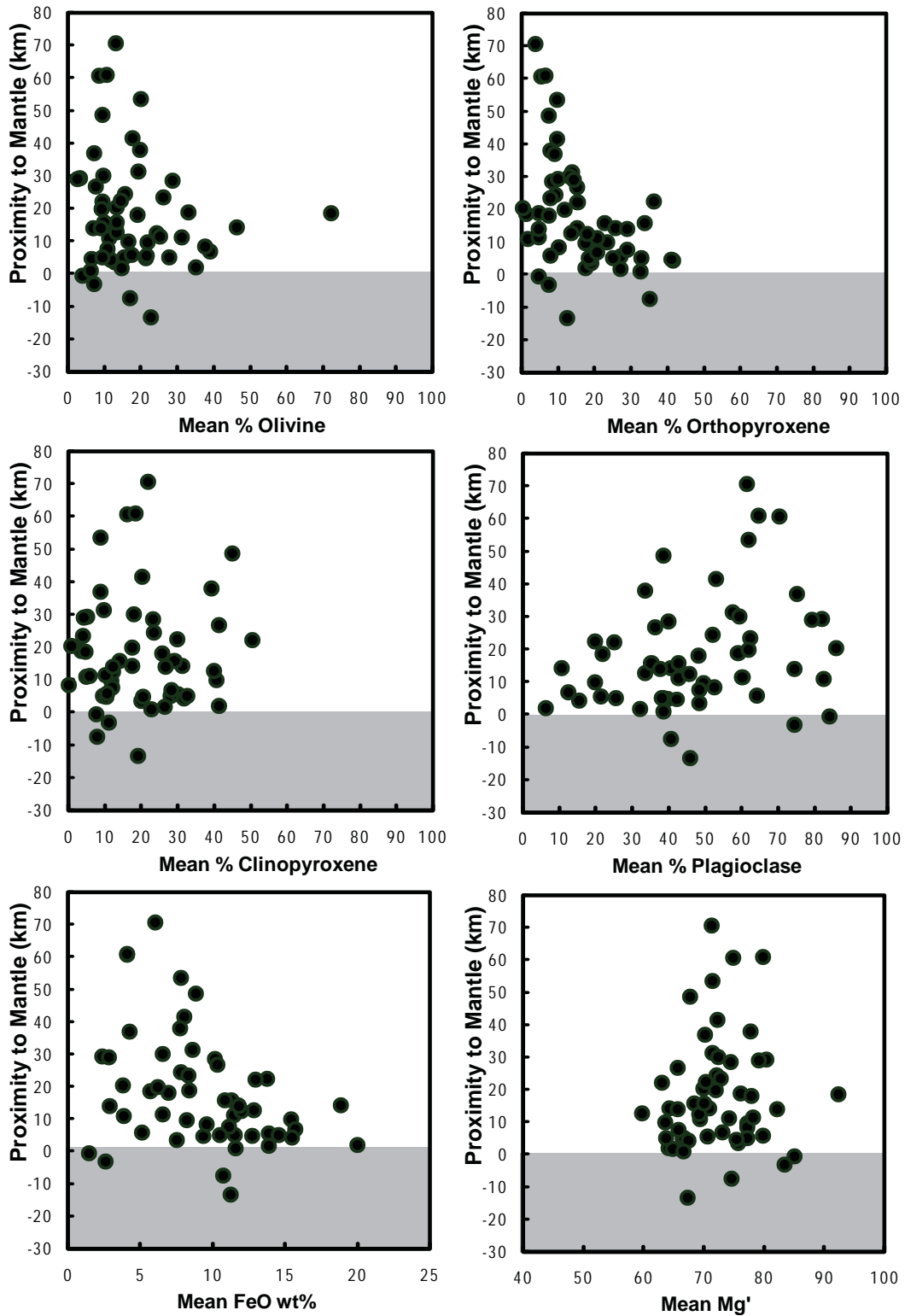


Figure 3.10: Mean lunar impact crater central peak mineralogy and chemistry versus peak origin relative to the crust mantle boundary (e.g., T₁-D₁). Proximity to mantle less than zero denotes materials plausibly derived from the lunar mantle (in grey).

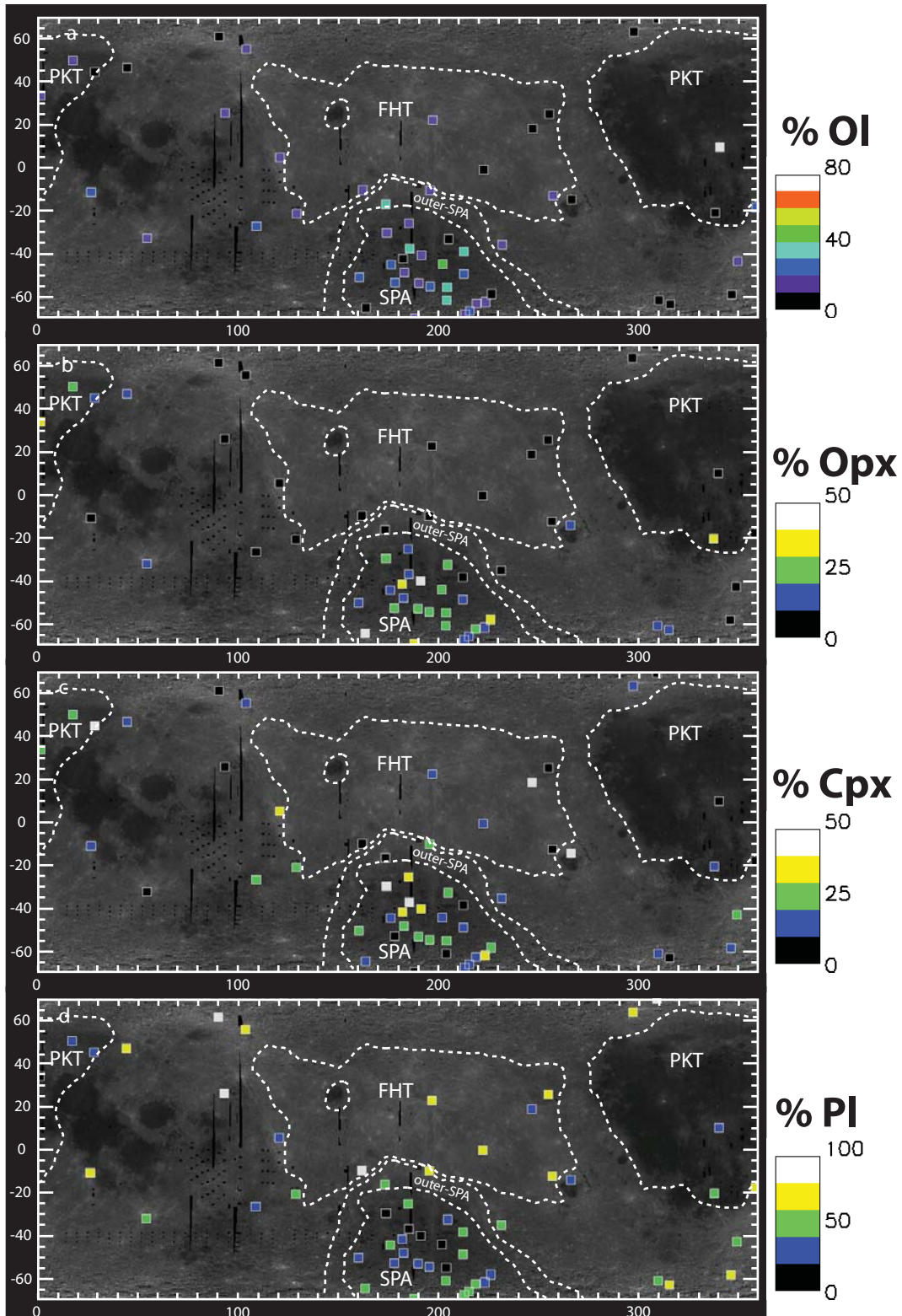


Figure 3.11: The location of crater peaks examined and their mean (a) olivine, (b) clinopyroxene, (c) orthopyroxene, and (d) plagioclase abundances plotted on Clementine 750 nm simple cylindrical images of the lunar surface. Dashed lines denote approximate lunar terrane boundaries interpreted from thorium maps [Jolliff *et al.* 2000; Lawrence, *et al.* 2002].

exclusively confined to the FHT terrane. Crater peaks in this terrane with some of the highest modeled plagioclase abundances (>80 vol. %), including Bel'kovich, Carpenter, Joliot, and Keeler are also shown to originate in the lower crust or mantle. Only Mauser on the northern end of Orientale and Ohm crater have less than 60 vol. % plagioclase. The outer FHT shows a little more diversity with a few peaks averaging less than 60 vol. % plagioclase, but the majority of peaks still have anorthositic average mineralogies. Model peak mineralogy within the PKT and SPA is all mafic (<60 vol. % plagioclase); SPA peaks also show less plagioclase (<50 vol. %) abundances than the PKT and vary from basin edges (20-50 vol. %) to the basin center (<20 vol. % plagioclase).

Mafic minerals also associate with terrane, with olivine primarily concentrated within SPA (6-46 vol. %, outer to inner basin respectively). Only Copernicus peak within the PKT is modeled to have greater olivine abundance (72 vol. %) than peaks within SPA. Orthopyroxene is also concentrated within SPA with range of 12 to 41 vol. %, but is also prevalent on the PKT crater peaks Aristoteles (22 vol. %), Bullialdus (33 vol. %), and Aristillus (36 vol. %). Clinopyroxene is the only mineral with abundances that appear to be independent of terrane. This result may be real, or may indicate a systematic error in the modeling results.

Discussion

Previous studies have reported compelling evidence to suspect that the crust changes composition with depth. These observations include (1) the identification of large impact basin ejecta that are more mafic than the surrounding highlands (e.g., [Reid *et al.*, 1977; Ryder and Wood, 1977; Spudis and Davis, 1986], (2) central peaks of some complex craters that are inferred to contain mafic lithologies (e.g., [Tompkins and Pieters, 1999]), and (3) the inferred noritic composition of the SPA basin floor which is suggested to represent lower crustal materials (e.g., [Lucey *et al.*, 1995; Pieters *et al.*, 1997; Pieters *et al.*, 2001; Wieczorek and Zuber, 2001]).

All peaks examined here have strong mineral and major element abundances consistent with rocks of the lunar sample collection. The majority of the peaks examined consist of material with mafic and magnesian composition similar to Mg-suite rocks that are spread among all of the lunar

terraces. We suggest that our direct comparison of lunar samples and peaks provide evidence that the majority of these peaks consist of Mg-suite rocks. The few peaks where FAN compositions are identified are confined within the FHT (craters Berkner, Joliot, and Keeler). This prevalence of mafic and magnesian peaks and the paucity of peaks with anorthosite and FAN composition may be explained by our method of crater peak sampling. The peaks examined are all estimated to originate at least 10 km or more below the lunar surface. The observed compositional bias might be expected especially if the crust becomes more mafic with depth. Additional anorthositic peaks may be apparent if peaks originating in the top 10 km of the lunar crust are examined in future work.

Despite the commonalities between these peak analyses and Mg-suite rocks, it is a possible interpretation that some of these peaks may consist of mafic ferroan rocks (e.g., “mafic FANs”) [Wieczorek and Zuber, 2001]. Although this is a reasonable hypothesis, little evidence is available for this in the sample collection and several samples that are suggested to be representative mafic ferroan rocks are far less mafic than the peaks reported here and still plot within the FAN field in **figure 3.7** [Jolliff and Haskin, 1995; Wieczorek et al., 2006]. However, the presence of mafic ferroan rocks on the Moon merits further investigation in the future.

The mineral and major element results presented here suggest these peaks are consistent with Mg-suite rocks, but many of these peaks lack thorium anomalies that would suggest KREEP signatures. Previous studies of Mg-suite rocks show significant enrichments (at least 1-2 orders of magnitude) in KREEP and other incompatible elements relative to FAN rocks (e.g., *Papike et al.* [1994; 1996]; *Shervais and McGee* [1998a; 1998b]; *Wieczorek et al.*, [2006]). The current hypothesis for lunar Mg-suite formation suggests high concentrations of incompatible elements are at least assimilated [Warren, 1986]; whether high incompatibles are necessary for Mg-suite formation remains unknown. However, since the rocks of this suite were collected from every Apollo landing site within the PKT and this region has a pronounced thorium anomaly, it has been suggested that Mg-suite rocks may be spatially confined to this region and incompatible elements are a genetic signature of this suite [Jolliff et al., 2000; Korotev, 2000; Korotev and Gillis, 2001; Wieczorek and Phillips, 2000].

However, it should be pointed out that although “magnesian” and “Mg-suite” might be equivalent, magnesian rocks that do not contain KREEP might also exist, and may or may not be genetically related to the Mg-suite rocks. An increasing body of evidence suggests that, at the very least, magnesian compositions on the Moon are not limited to the PKT. Recent studies of KREEP-poor, feldspathic and magnesian lunar meteorites inferred to originate in the farside FHT suggest the presence of a magnesian component that influenced their formation [Korotev *et al.*, 2003; Warren *et al.*, 2005]; however, the characterization of this magnesian component is under question. Korotev [2005a] suggests that the magnesian component of these meteorites is not from a Mg-suite source. Since these meteorites do not contain mafic magnesian and KREEP bearing lithologies typical of Mg-suite rocks, Korotev [2005a] suggests these feldspathic meteorites are derived from magnesian, rather than ferroan, anorthosites. Warren [2005] and Warren *et al.* [2005] support an attempt to extend the presence of the Mg-suite globally by suggesting that the magnesian component in these meteorites is derived from a KREEP-poor or free variety of Mg-suite (a characteristic that is not observed in the Apollo and Luna samples). The difficulty with either argument is the genesis of magnesian anorthositic rocks. Both Warren [2005] and Hess [1994] (the former addressing magnesian feldspathic meteorites and the latter addressing magnesian troctolites), point out that source magmas for magnesian feldspathic material would have to be extremely magnesian themselves, with Mg’ approaching that of the terrestrial mantle (Mg’ ~93).

The central peaks analyzed here not only suggest a magnesian component in both KREEP-rich and KREEP-poor areas but may have sampled the source component suggested to be influencing the chemistry of lunar meteorites. Stoichiometrically estimating oxide abundance from mineralogy, these peaks have a similar Al₂O₃ range (2-31 wt. %) to the meteorite collection, but are also more magnesian. Greater compositional similarities are actually found between peaks and Mg-suite rocks of the lunar sample collection; however a large sample of peaks are not located in areas of significant or even mild KREEP influence. In this context, positive identification of mafic and magnesian rocks here supports the hypothesis that high incompatible element abundances may not be a necessary genetic characteristic of Mg-suite rocks and this suite

may not be confined to the PKT. Whether incompatible elements help or speed Mg-suite rock formation is still a subject for debate, but the probable identification of Mg-suite rocks within the FHT and SPA suggests high incompatible element abundances are not absolutely necessary for their production.

Central peak compositions also roughly follow terrane boundaries. Peaks modeled with magnesian and ferroan anorthositic compositions are primarily confined to the FHT; while peaks with mafic model mineralogies are generally confined to the PKT and SPA with a few exceptions. This translates vertically within each terrane as a function of crustal thickness. As the crust thickens it becomes more anorthositic and magnesian, and as it thins it becomes more mafic and ferroan. The thinnest lunar crust (<30 km), central SPA, shows the most mafic mineralogy (>50 vol. % outer SPA, >80 vol. % inner SPA); while thicker crust (>30 km; not necessarily the thickest), in the FHT, is more plagioclase-rich (>60 vol. % plagioclase). This compositional relationship is also found relative to the crust-mantle boundary. Mafic lithologies, both magnesian and more ferroan, are confined to within 50 km of the crust mantle boundary in SPA and the PKT. Anorthositic lithologies are largely confined within the FHT, however, they exist at all levels of the crustal column and with a significant magnesian sampling.

These results suggest the FHT, SPA, and the PKT may not only be distinct from each other on the surface but subsurface as well. Model compositional results for SPA and PKT central peaks are consistent with a crust gradually increasing in mafic mineralogy with depth. This is consistent with previous interpretations of PKT impact melts and basins noted early in this discussion. Not consistent with this hypothesis are peaks that show mafic mineralogies and more ferroan chemistries at significant depth in the crust. However, this is consistent with a scenario suggested by *Warren et al.* [2005] for the petrogenesis of lunar meteorites. In this scenario mafic and magnesian minerals crystallize first and begin to settle, but during the process of settling some of these mafic and magnesian crystals are entrained with subsequently crystallizing and more buoyant plagioclase minerals. These assemblages are transported upward in the magma ocean to become part of the crust in a higher stratigraphic location. Crystallization proceeds until less buoyant ferroan and more mafic lithologies crystallize and settle low in the crustal column with

some of the initial early crystallizing and more magnesian mafic minerals. This scenario may be applicable for PKT and SPA crustal formation, but may not be sufficient for the FHT.

Peaks within the FHT suggest that at least portions of this terrane (near the craters Bel'kovich, Carpenter, Joliot, Keeler, and others) can either (1) consist entirely of anorthositic rocks throughout the crustal column, or (2) have a plagioclase-rich lower crustal layer with stalled plutons within 40 km of the crust-mantle boundary. The identification of anorthosite transported to the surface via impact basin inner rings and peaks of Orientale, Grimaldi, Humorum, Nectaris, and Apollo corroborate this interpretation [Hawke *et al.*, 2003; Spudis *et al.*, 1984]. However, the result here suggests both scenarios must have ferroan and magnesian anorthositic rocks at significant depth. This is inconsistent with previous hypotheses that the FHT has a generally increasing mafic composition with depth; but it is consistent with separate magnesian and ferroan magmas somewhat simultaneously constructing an anorthositic FHT, at least in the areas sampled. This is also consistent with FAN and Mg-suite radiometric ages which suggest that these suites crystallized simultaneously through a significant portion of lunar geologic history [Borg *et al.*, 1999; Wieczorek *et al.*, 2006], although caution is suggested for ages of plagioclase-rich samples due to impact metamorphism modification [Norman *et al.*, 2003].

Conclusions

Here we provide several new insights into the relationship between lunar crustal composition and structure in both vertical and lateral perspectives.

- We show that lunar composition varies with crustal thickness. As the crust thickens it becomes more plagioclase-rich, and as the crust thins it becomes more mafic.
- Our method of using the crust-mantle boundary as a reference point has allowed us to pinpoint crater peaks that have sampled the lower crust and plausibly the mantle. Approximately half the peaks analyzed here plausibly represent mantle material.
- No systematic compositional variability with respect to the depth of origin normalized to local crustal thickness is found; however, significant compositional relationships are shown relative to the crust-mantle boundary. This suggests that the majority of

compositional variations in the crust were in place before major surface modifications took place.

- Mafic lithologies (≥ 40 vol. % mafics) are confined to thin crust that is within 50 km of the lunar crust-mantle boundary and within the SPA and PKT terranes with a few exceptions; the most mafic lithologies (> 80 vol. % mafics) are confined within 30 km of the crust-mantle boundary within SPA. These results are consistent with a gradually increasing mafic/plagioclase ratio traveling down into the crust.
- Anorthositic (≥ 60 vol. % plagioclase) rocks are found throughout the crustal column, but are dominantly confined within the FHT and outer FHT; however, some peaks with greater than 70 vol. % plagioclase do exist in crust that is 30-50 km thick and relatively near the crust-mantle boundary. These results are inconsistent with a generally increasing mafic composition with depth, and instead support a dominantly anorthositic crustal column with a distinct layer or intrusions of more plagioclase-rich magnesian and ferroan anorthositic rocks at significant depth in the crust.
- The majority of peaks analyzed have compositions similar to Mg-suite rocks of the lunar sample collection and they are found to be independent of lunar terrane. This suggests that Mg-suite rocks may not be confined to the PKT and may not be dependent on incompatible element concentrations for formation. These results also suggest Mg-suite rocks may be a global phenomenon and may have wide ranging incompatible element and mineral abundances; but the main factors that determine Mg-suite rock formation are major element chemistry and geophysical dynamics. Incompatible element enrichment may be an added attribute of Mg-suite rocks within PKT and perhaps to a lesser extent SPA.

Future Work

Future work will entail a continuation of analysis of lunar impact crater central peaks especially within the FHT and PKT. Integration of new data from Chang'e, Chandrayaan-1, Kaguya, Lunar Reconnaissance Orbiter, and Gravity Recovery And Interior Laboratory (GRAIL) will be essential. These data will be beneficial for more rigorously calibrated reflectance data

relative to surface slopes and determining subsurface crustal structure to correlate with compositional interpretations. Further research and development of quantitative analysis models, mineral optical constants, and supporting validation data sets are essential.

The results shown here appear to confirm that SPA is a window into the lunar lower crust. However, it is possible that the floor of SPA basin may represent an impact melt sheet that may have partially differentiated and represent something very different from a cross-section of the original crust [*Morrison, 1998*]. Further analysis of impact crater walls in addition to central peaks will help resolve this issue. Additional cataloging and assessments of lunar samples for mafic ferroan rocks is also necessary.

Acknowledgements

The authors give their gratitude to B. Denevi and K.R. Stockstill-Cahill for constructive discussions on spectral modeling, as well as W. Koeppen, E. Pilger, and R. Snider for helpful discussions and advice on IDL programming and Condor parallel processing techniques. Use of the Hawaii Institute of Geophysics and Planetology (HIGP) computer cluster and parallel processing facilities was instrumental for this study. This work was funded by NASA grant #NNX07AU96G (e.g., Mineral Mapping of the Moon) to P.G. Lucey. This is SOEST, HIGP, and IPGP contributions #7746, #1786, and #2501 respectively.

**CHAPTER 4. RADIATIVE TRANSFER MODELING OF NEAR-INFRARED
REFLECTANCE OF LUNAR HIGHLAND AND MARE SOILS³**

³ Cahill, J. T. S., P. G. Lucey, K. R. Stockstill-Cahill, and B. R. Hawke (2010), Radiative transfer modeling of near-infrared reflectance of lunar highland and mare soils *J. Geophys. Res. - Planets*, *accepted pending revision*.

Abstract

With near-infrared hyperspectral data sets returning from KAGUYA and Chandrayaan-1's Moon Mineralogic Mapper (M³), accurate evaluation and interpretation of lunar data sets with higher spectral resolution has never been more critical. Here we test a new radiative transfer spectral modeling algorithm to determine composition from hyperspectral reflectance spectra of lunar soils. Data for nineteen lunar mare and highland soil samples previously characterized by the Lunar Soil Characterization Consortium (LSCC) are used for validation. Spectral fits are made using a goodness of fit metric considering spectral shape, spectral contrast, spectral slope, and iron abundance. High precision fits are achieved for nearly every soil with this algorithm. Using a plot of spectral shape relative to the ratio Mg' determines the winning model and composition. Mg' is determined with a average difference of ~11-15 and ~3-8 units before and after a correction is applied, respectively. Mineralogy is determined with a average difference of ~5-15 vol % depending upon the mineral constituent.

Introduction

When light interacts with the lunar surface it is reflected in a way unique to each of the most common silicate minerals (e.g., plagioclase, pyroxene, and olivine) [Burns, 1993]. To exploit this interaction between light and matter near-infrared data sets, new (e.g., KAGUYA and the Moon Mineralogical Mapper (M³)) and old (e.g., telescopic and laboratory), are being analyzed for compositional interpretation of the lunar surface [Matsunaga *et al.*, 2008; McCord *et al.*, 1981; Noble *et al.*, 2001; Pieters and Pratt, 2000; Pieters *et al.*, 2009a]. Several methods for determination of composition from near-infrared reflectance spectra are in active use and under continuing development for the analysis of these data sets. These methods include the Modified-Gaussian modeling (MGM) method (e.g., [Noble *et al.*, 2006; Sunshine and Pieters, 1993]), the statistical partial least squares (PLS) and principal component approach (e.g., [Li, 2006]), and radiative transfer theory (e.g., [Hapke, 1981]). The objective of this work is to test the ability of a new algorithm using Hapke's radiative transfer theory to extract mineralogy and chemistry from near-infrared reflectance spectra. We use lunar mare and highland soils characterized by the Lunar Soil Characterization Consortium (LSCC) as our validation data set [Chambers *et al.*, 1995; Higgins *et al.*, 1996; Noble *et al.*, 2001; Pieters *et al.*, 2000; Taylor *et al.*, 1996; Taylor *et al.*, 2001b]. Our focus is determining the abundances of the major lunar silicates plagioclase, orthopyroxene, clinopyroxene, and olivine.

Here modal mineralogy is determined with a mean absolute difference of ~5-15 volume percent depending upon the mineral constituent. Model Mg' (i.e., molar (Mg/(Mg+Fe)) x 100) is reproduced with a mean absolute difference of ~3-8 units after a correction is applied. Additionally, we detail the strengths, limitations and the challenges that must be solved to improve this model.

The Algorithm

The compositional extraction algorithm has multiple parts (e.g., theory, sub-algorithms, and assumptions) that require description. The algorithm uses a non-linear mixing model based upon

the work of Bruce Hapke and summarized by *Lawrence and Lucey* [2007]. Combined with inputs of plausible mineralogy and basic chemistry it allows the computation of near infrared spectral candidates that include the effects of space weathering [*Denevi et al.*, 2007]. In principle one can use such a mixing model with a very large library of endmembers to produce a fit to an unknown spectrum, and report the abundance inputs for the best fit as the model modal mineralogy. *Lucey* [2004] chose a slightly different approach; by systematically selecting fixed Mg' values he produced intermediate candidate fits for portions of the plausible mineral and chemical parameter space. *Lucey* [2004] based the final selection from the remaining candidates on an independent parameter, estimated iron content. This step-wise process was adopted to deal with compositional ambiguity inherent to the Clementine data set due to its small number of spectral channels and signal to noise ratio that limit discrimination among the full range of plausible lunar compositions. The inherent limitation of those data enabled equally good fits for many compositions in some cases. *Cahill and Lucey* [2007] discuss these compositional and spectral ambiguities in detail.

Unlike that of *Lucey* [2004], our algorithm is aimed at true hyperspectral data, data that contains many contiguous bands that cover the information-rich near-infrared spectral range, mitigating the ambiguity issue. However, we retain the stepwise process, and enhance it, to prevent the possibility that our fitting process will be trapped in a local compositional minima.

Specifically, the process is as follows:

For each unknown spectrum four individual fits are conducted. The fitting processes is a gradient descent operating from four starting compositions covering the system olivine, plagioclase, orthopyroxene and clinopyroxene at 1% compositional intervals, and Mg' ranging from 20 to 95 in 5 unit compositional steps. The space weathering components nanophase iron and agglutinates are allowed to vary in the fitting process (described below). The wide range of starting mineral abundances allow us to determine that the final fits are independent of starting composition, avoiding local minima (**Fig. 4.1**).

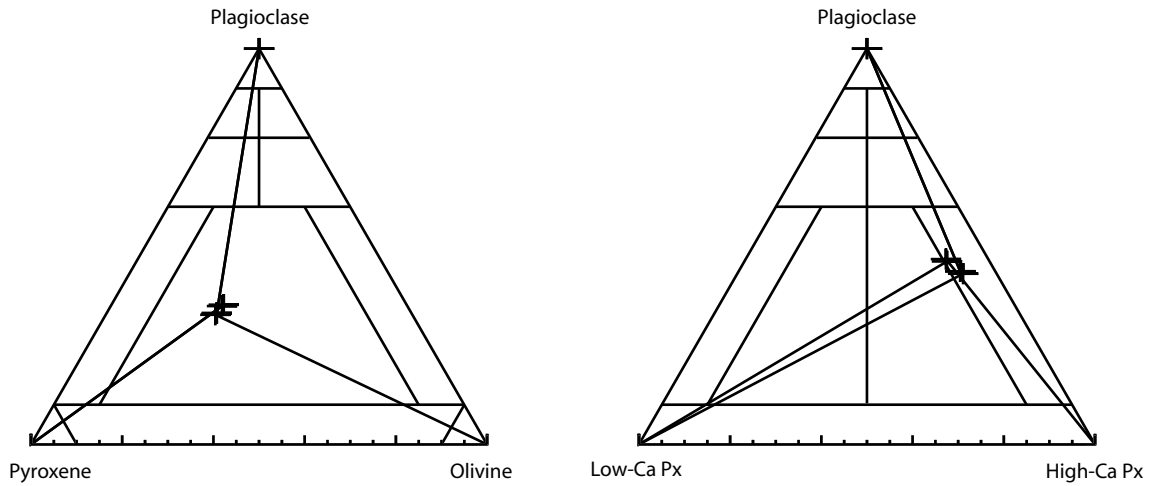


Figure 4.1: A visual representation of how our starting mineralogies of 100% olivine, 100% low-Ca pyroxene, 100% high-Ca pyroxene, and 100% plagioclase are iteratively adjusted until a spectral match is attained. The standard deviation of these four solutions gives us a measure of how well our model finds a compositionally-unique answer for each lunar soil.

From these four fits at each fixed Mg' we arrive at a final composition by optimizing a goodness of fit criterion used in a gradient descent algorithm (defined and described below). The set of model winners is selected by determining the one with the highest quality fit on a plot of spectral shape versus Mg' (**Fig. 4.2**). The majority (14 of 19) of soil spectra modeled result in a gaussian-like distribution on this plot, with an obvious peak and winning set of four models. The modal abundances of all four winning fits at that fixed Mg' are averaged to produce the final reported composition. However, model fits of some (4) lunar soil spectra are more difficult to discriminate an obvious winner using this plot. These may involve relatively "flat" distributions where differences in shape (i.e., correlation) relative to Mg' are less apparent. These flat distributions usually occur towards lower Mg' values. Or, a quantitative maxima may be determined but the winning set of four models may be less unique (higher standard deviation in shape fit) relative to another set of models at a different fixed Mg' with a similar spectral. The difference between these sets of models is usually 5-20 Mg' . **Figure 4.3** shows an example fit which has aspects of each problem.

Spectral Mixing Model: Model spectra are computed using radiative transfer theory developed by *Hapke* [1981; 1993; 2001]. The spectra of mineral mixtures can be computed from linear mixtures of their component single scattering albedoes (i.e., the probability a photon will survive an encounter with a material) weighted by relative abundance and grain size. The reflectance of the mixture is then related to the mixture single scattering albedo by Hapke's equations that account for multiple anisotropic scattering, lunar-like backscatter behavior and photometric viewing geometry.

The single scattering albedo of the individual components are computed using Hapke's equations that relate the optical constants of the materials, their grain size and internal scattering behavior to the component single scattering albedo, including the effects of coating of nanophase iron. Optical constants for plagioclase were derived from a reflectance spectrum of plagioclase (Anorthite HS201) in the U.S.G.S. spectral library [*Clark et al.*, 2003]. Optical constants for olivine were derived from spectra obtained by Ed Cloutis and also Jessica Sunshine, available

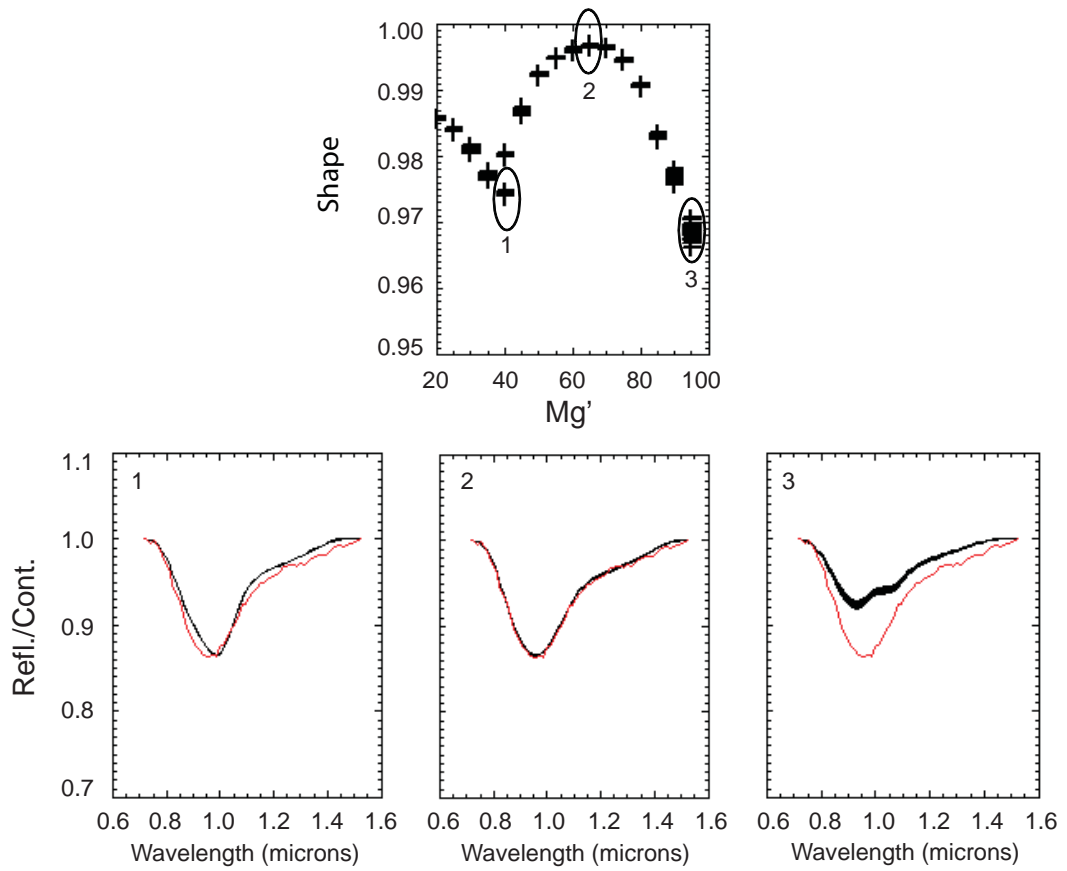


Figure 4.2: An example spectrum is examined with our model. A calculated estimate of model spectral shape relative to the spectral unknown is displayed relative to Mg'. Spectral comparisons are given for three different sets of models. Models for (2) are selected as the “winner” and averaged for a final model compositional estimate. The unknown spectrum is displayed in red and model spectra are displayed in black.

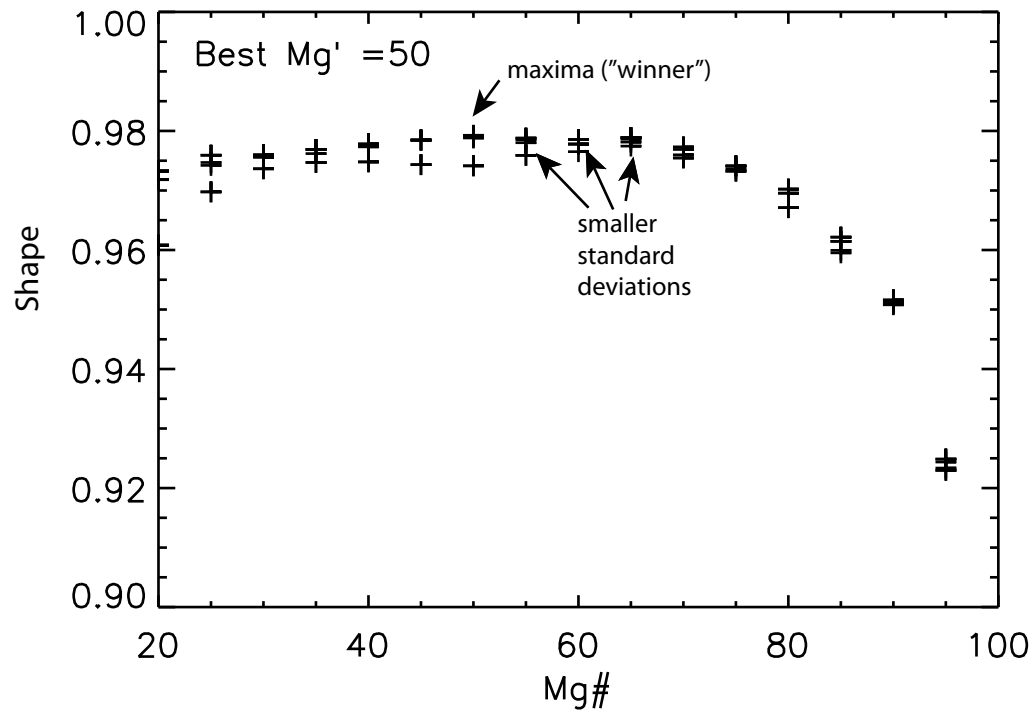


Figure 4.3: Modeling of an unknown results in an ambiguous case where a maxima is chosen as the winner, but surrounding models are highly similar and are more "unique" (i.e., have lower standard deviations) solutions.

from RELAB (<http://www.planetary.brown.edu/pds/LSCCsoil.htm>) using the methods of *Lucey* [1998]. These constants are computed from coefficients that allow computation of olivine optical constants at any Mg'. Two sets of pyroxene optical constants are available in the lunar literature. *Lucey* [1998] derived pyroxene solid solution series optical constants with a similar treatment to that of olivine. *Denevi et al.* [2007] attempted to improve upon this set of optical constants using a MGM approach to estimate absorption coefficients, influenced by FeO and CaO abundance, of the same set of terrestrial pyroxene samples [*Cloutis*, 1985; *Cloutis et al.*, 1986; *Cloutis et al.*, 1990a; *Cloutis et al.*, 1990b]. We explore the use of both the optical constants of *Lucey* [1998] and *Denevi et al.* [2007]. Iron optical constant data of *Paquin* [1995] are used to model sub-microscopic iron (SMFe). Agglutinates are treated as a fundamentally dark and neutral optical component [*Keller et al.*, 1998] with a spectrally flat single scattering albedo of 0.1. Since a particularly strong relationship is observed between agglutinates and SMFe (e.g., [*Hapke*, 2001; *Keller and McKay*, 1997]) we link their relative proportions in the model.

Physical and Chemical Assumptions: To reduce the number of variables to a manageable number, we make simplifying assumptions. These assumptions include grain size, mineralogy, and the coupling of mafic mineral Mg'. Grain size is held to 15 microns, which is in agreement with the most optically dominant size fraction (10-20 μm) on the lunar surface [*Lucey*, 2006; *Pieters et al.*, 1993]. Lunar mineralogy is relatively simple, dominated at the 99% level by plagioclase, pyroxene, olivine, ilmenite and the important non-mineral component glass [*Heiken et al.*, 1991]. However, the impact on the spectra of these materials by typical variations in lunar chemistry and modes of occurrence is very large. Inversion of a spectrum to the typical distribution of chemistries of the mafic minerals alone in a random lunar sample is simply impractical; some simplifying assumptions must be made to limit the number of components. How many pyroxene components are needed is addressed by *Noble et al.* [2006] and *Denevi et al.* [2008] in their respective modeling of spectral and modal data from the LSCC. *Denevi et al.* [2008] explored using four pyroxene end members, similar to the four LSCC pyroxene groups (e.g., orthopyroxene, pigeonite, Mg-clinopyroxene, and Fe-clinopyroxene). However, this method cannot model high Mg' pyroxenes effectively because the LSCC pyroxene classes do not contain

them. *Noble et al.* [2006] showed acceptable results modeling lunar soils using two pyroxene (e.g., low-calcium and high-calcium pyroxene) similar to other (e.g., [*Cahill and Lucey*, 2007; *Cahill et al.*, 2009; *Lucey*, 2004]) applications to Clementine spectra.

Here we also use two pyroxene (low-calcium and high-calcium pyroxene) groups for modeling. Model mafic mineral Mg' is assumed to be in "equilibrium" and is coupled, one-to-one, between pyroxene and olivine minerals. This is roughly consistent with highland ferroan anorthosite (FAN) and magnesium-suite (Mg-suite) plutonic rocks of the lunar sample collection (**Fig. 4.4**). Olivine and orthopyroxene Mg' being highly correlated with slope close to 1 and intercept near zero. Clinopyroxene falls off this trend, but for simplicity, we also set clinopyroxene Mg' equal in these mixtures.

Fit Criteria: We use four metrics to assess the quality of the fit of the model to each spectrum: FeO of the mixture compared to the remotely estimated FeO of the unknown spectrum; the slope of the model spectrum compared to the unknown spectrum; and two parameters that quantify the similarity in shape and contrast between a model and unknown spectra. We include FeO content to partly overcome the insensitivity of near-infrared spectra to feldspar content when mafic mineral content exceeds several percent. We explicitly include the slope of the spectrum to better constrain the degree of space weathering that can affect both the shape and contrast of the spectrum. We include the contrast-normalized shape of the spectrum because it contains the richest information regarding relative abundance of mafic minerals and their Mg'. The spectral contrast is explicitly included because of its strong dependence on degree of space weathering and plagioclase content. In a large number of numerical experiments these metrics were weighted relative to one another to maximize the accuracy of the inversion from spectrum to composition.

Iron Abundance: The model FeO content, is derived stoichiometrically with knowledge of Mg' and mineralogy. For testing against LSCC data FeO contents are available for use as a constraint. For remote data we assume iron will be derived using the various algorithms available.

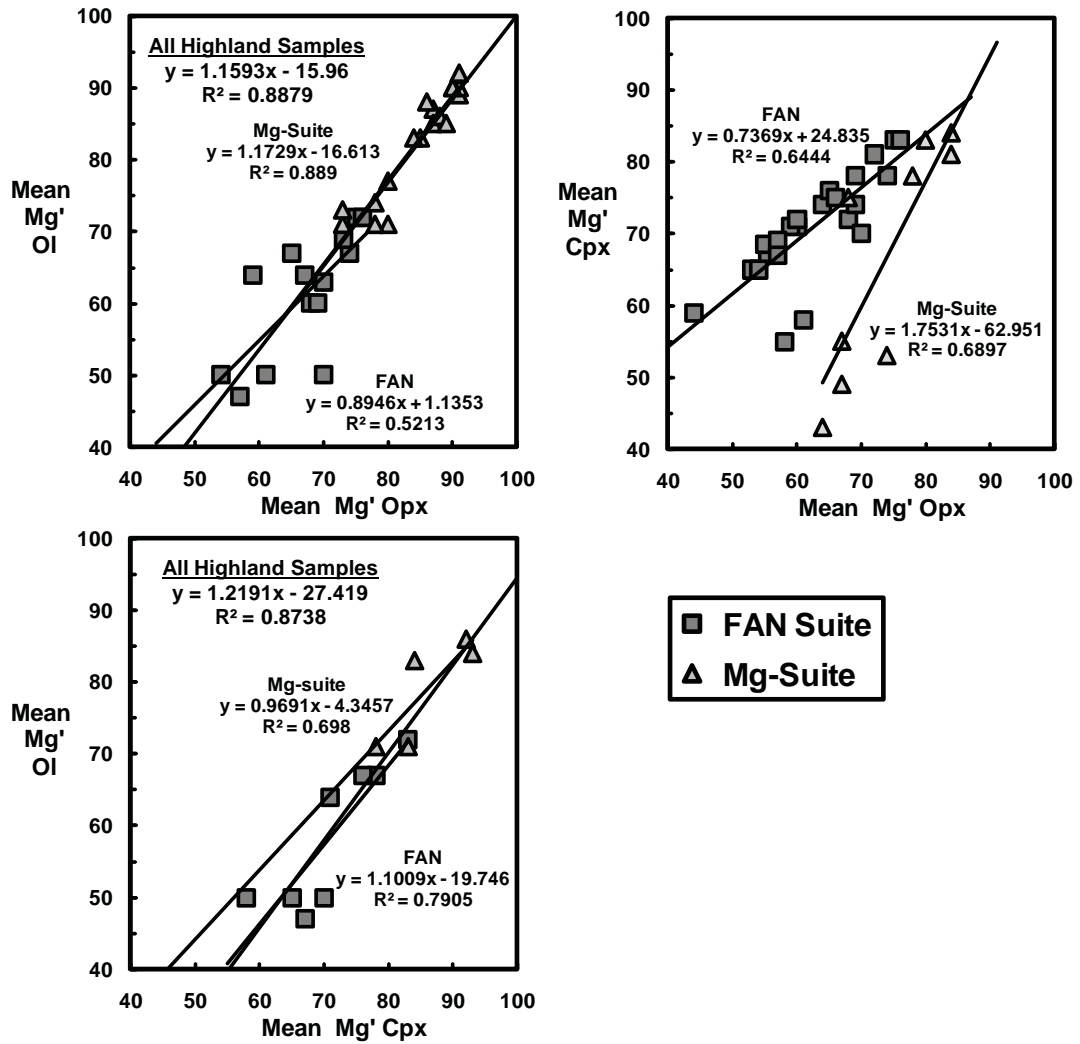


Figure 4.4: Mg' comparisons between the main three mafic minerals (orthopyroxene, clinopyroxene, and olivine) in lunar highland rocks.

Spectral Slope: Slope is determined from a straight line tangent to each spectrum near the 0.7 and 1.5 μm relative maxima. It is defined using the equation:

$$m = \frac{(R_{0.7} - R_{1.5})}{(\lambda_{0.7} - \lambda_{1.5})} \quad (1)$$

Here m is slope, R is reflectance, and λ is wavelength.

Spectral Correlation and Contrast: Quantitative estimates of spectral fit are determined using a slightly modified version of *Clark et al.* [2003]'s spectral shape and contrast matching algorithm. *Clark et al.* [2003]'s spectral comparison calculation is based upon the similarity between two spectra, which entails a calculation of the correlation coefficient (i.e., similarity in spectral shape) and spectral scale (i.e., similarity in spectral contrast). The algorithm is defined by these equations:

$$b = \frac{\sum S_u * S_o - (\sum S_u * \sum S_o) / n}{\sum S_o^2 - (\sum S_o)^2 / n} \quad (2)$$

$$b' = \frac{\sum S_u * S_o - (\sum S_u * \sum S_o) / n}{\sum S_u^2 - (\sum S_u)^2 / n} \quad (3)$$

$$b'' = b * b' \quad (4)$$

Here n is the number of spectral channels in the fit, S_o is a model spectrum, S_u is the lunar soil spectrum (i.e., unknown), b is the spectral contrast and b' is an intermediate product used by *Clark et al.* [2003]. In equation 4, the term b'' is the correlation coefficient which quantifies the amount of correlations between the shapes of two spectra over all the wavelength channels available, regardless of differences in spectral contrast.

Gradient Descent Methodology: Each model has six mineral or other inputs. At the outset of the process, the initial major mineral composition is entered as well as a nominal value for space weathering components. The value of each parameter is both incremented and decremented in turn, and the effect of these small changes on the weighted fit criterion recorded. This criterion is defined by the equation:

$$g = (1 - b'')w_{b''} + |1 - b|w_b + \Delta m w_m + \Delta FeO w_{FeO} \quad (5)$$

Here g is the goodness of fit, $w_{b''}$ is the weight given to spectral shape, w_b is the weight given to contrast, w_m is the weight given to slope, and w_{FeO} is the weight given to FeO abundance. When all inputs are tested, new values for all parameters are updated in the direction that produced an improvement in the aggregate metric, or left unchanged if no improvement was detected. This process is repeated until a candidate meets a preset goal criterion for spectral shape ($1 - b'' < 0.01$), contrast ($|1 - b| < 0.001$), slope ($\Delta m < 0.01$), and FeO ($\Delta FeO < 2$). If this spectral criteria is not achieved after 500 iterations, we consider the algorithm to have achieved the best possible fit given the unknown spectrum and algorithm.

Model Validation

Validation Data: The gold standard, the only standard, against which to test models that derive lunar mineralogy from spectra is the LSCC data set [*Higgins et al., 1996; Noble et al., 2001; Pieters and Hiroi, 2004; Taylor et al., 1996; Taylor et al., 2001a; Taylor et al., 2001b*]. These data include spectra of lunar soils, both bulk and separated into several size fractions, and modal mineralogy derived from automatic X-ray microprobing of grain mounts. We focus on the 10-20 μm size fraction for sample numbers: 10084, 12001, 12030, 14141, 14163, 14259, 14260, 15041, 15071, 61141, 61221, 62231, 64801, 67461, 67481, 70181, 71061, 71501, and 79221. Measurements of lunar soil laboratory reflectance spectra are available at <http://www.planetary.brown.edu/pds/LSCCsoil.html>. Compositional data for these lunar soils are found at <http://web.utk.edu/~pgi/data.html>.

There are two issues that make using LSCC data for validation of our model not completely straightforward. First, our model employs two pyroxenes with continuously variable Mg', while the LSCC pyroxenes are classified into four varieties. This raises the issue of specifically assigning a degree of accuracy to the comparison of our model and the LSCC data set. Second, our model is designed to cover a much wider range of composition and chemistry than contained in the LSCC data, so the testing cannot be comprehensive.

Preparing for Model and Measurement Comparison: Lunar soil mineralogy and chemistry is prepared for comparison to model results in several ways (**Table 4.1-4.2**). The LSCC classifies pyroxene into four categories based upon solid solution composition: orthopyroxene, pigeonite, Mg-rich clinopyroxene, and Fe-rich clinopyroxene [Taylor *et al.*, 2001a; Taylor *et al.*, 2001b]. For the modeling, we have two pyroxene categories, "low-Ca" and "high-Ca pyroxene". Similar to the approach of Noble *et al.* [2006], Mg-rich and Fe-rich clinopyroxene are combined within the high-Ca pyroxene group. Unlike Noble *et al.* [2006], where orthopyroxene and pigeonite are combined into a low-Ca pyroxene group, we try various combinations to determine the best approach for classifying pigeonite. Pigeonite has a relatively low Ca²⁺ composition similar to orthopyroxene, but with the monoclinic crystallographic structure of clinopyroxene. We explore classifying pigeonite four ways. Thus, model mineralogy is compared to the four versions of the LSCC reported pyroxene mineralogy. These versions include, 1) grouping pigeonite with Mg- and Fe-rich clinopyroxene, 2) grouping pigeonite with orthopyroxene, 3) splitting pigeonite between orthopyroxene and Mg- and Fe-rich clinopyroxene abundances, and 4) omitting pigeonite altogether. The reported LSCC mineral abundances are then normalized to the sum of the four major lunar silicate categories plagioclase, low-Ca pyroxene, high-Ca pyroxene, and olivine for comparison to model abundances of these four phases. The Mg' is computed from fused bead analyses as well as various combinations of the other soil constituents for comparison to our model results.

LSCC fused bead oxide abundances of FeO are used in both reported form and renormalized to exclude ilmenite, since this mineral is spectrally flat within near-infrared spectral range being

Table 4.1: Renormalized LSC modal mineral proportions of 10-20 μm lunar soil size fraction.

Sample	Relab ID	Description	Is/FeO*	Pl	Ol	Cpx	Pig	Opx	Grouping I		Grouping II		Grouping III		Grouping IV	
									Low-Ca	High-Ca	Low-Ca	High-Ca	Low-Ca	High-Ca	Low-Ca	High-Ca
10084	LR-CMP-070	m-HTi	78	56	4	28	11	2	2	38	13	28	7	33	3	37
12001	LR-CMP-074	m-LTi	56	39	12	23	20	6	6	44	27	23	16	33	11	39
12030	LR-CMP-066	m-LTi	14	36	9	21	26	7	7	47	33	21	20	34	14	41
14141	LR-CMP-095	h	5.7	69	4	6	11	10	10	17	21	6	16	11	17	10
14163	LR-CMP-091	h	57	53	6	9	14	17	17	24	31	9	24	17	26	15
14259	LR-CMP-087	h	85	60	5	8	12	14	14	21	27	8	21	15	22	13
14260	LR-CMP-082	h	72	54	5	9	14	17	17	23	32	9	25	16	27	14
15041	LR-CMP-063	m-LTi	94	46	7	18	23	7	7	41	29	18	18	30	13	35
15071	LR-CMP-061	m-LTi	52	50	7	18	20	5	5	37	25	18	15	28	10	33
61141	LR-CMP-111	h	56	85	3	3	5	4	4	8	8	3	6	5	6	5
61221	LR-CMP-107	h	9.2	89	3	3	2	3	3	5	5	3	4	4	4	4
62231	LR-CMP-099	h	91	84	4	4	3	4	4	8	8	4	6	6	6	6
64801	LR-CMP-103	h	82	90	3	2	3	3	3	4	6	2	4	3	5	2
67461	LR-CMP-115	h	25	92	2	2	2	2	2	4	4	2	3	3	3	3
67481	LR-CMP-119	h	31	88	4	3	2	4	4	4	5	3	5	4	5	3
70181	LR-CMP-047	m-HTi	47	60	12	15	8	4	4	24	12	15	8	20	6	22
71061	LR-CMP-059	m-HTi	14	47	14	22	13	4	4	35	17	22	10	28	6	33
71501	LR-CMP-055	m-HTi	35	54	9	21	13	4	4	33	16	21	10	27	6	31
79221	LR-CMP-040	m-HTi	81	55	12	17	10	6	6	27	16	17	11	22	8	25

*Morris [1978]

m-HTi = High titanium mare sample

m-LTi = Low titanium mare sample

h = Highlands sample

I - Low-Ca = opx; High-Ca = pig + Mg-cpx + Fe-cpx

II - Low-Ca = opx + pig; High-Ca = Mg-cpx + Fe-cpx

III - pig split between Low-Ca and High-Ca pyroxene

IV - no pig

Table 4.2: LSCC fused bead chemistry of the 10-20 μm lunar soil size fraction.

Sample	SiO₂	Al₂O₃	MgO	CaO	FeO	Mg'
10084	41.2	13.2	7.98	11.8	14.7	49.2
12001	45.0	12.3	10.00	10.2	15.9	52.9
12030	46.3	10.7	9.86	9.6	17.2	50.5
14141	48.4	17.2	9.08	10.7	9.5	63.1
14163	47.4	17.0	9.57	10.8	10.1	62.8
14259	47.5	17.4	9.44	11.0	9.7	63.4
14260	47.5	17.3	9.53	11.0	9.8	63.3
15041	46.2	13.5	10.80	10.2	14.4	57.2
15071	45.7	12.9	11.00	10.2	15.4	56.0
61141	44.6	25.6	6.84	15.2	5.1	70.3
61221	44.5	27.5	5.16	16.0	4.4	67.6
62231	44.7	26.3	6.38	15.5	4.9	70.1
64801	44.5	26.3	6.18	15.6	4.8	69.7
67461	44.1	27.8	4.80	16.5	4.6	64.8
67481	44.4	28.4	4.54	16.4	4.0	66.7
70181	40.4	12.7	9.97	10.4	15.5	53.4
71061	39.5	10.8	10.40	9.8	17.5	51.4
71501	39.0	11.6	9.52	10.1	16.4	50.9
79221	40.9	12.9	10.40	10.4	15.0	55.3

used. To remove FeO associated with ilmenite, oxide abundances are first converted to molecular proportions. All TiO₂ was allocated to ilmenite and FeO is reduced by an equal amount. Using the new FeO molecular proportions, a new ilmenite-free Mg' and oxide abundances are calculated for each soil for comparison to model results.

A comparison of fused bead (e.g., bulk soil) chemistry and model-derived bulk chemistry calculated from the collective mineral chemistry of each soil is performed (**Fig. 4.5**). These comparisons show that there is some disagreement between fused bead and microprobed sample mineral chemistry. Average differences between bulk and mineral chemistry ranges from 0.8 to 1.9 wt% (std. dev. of 0.5 to 1.1 wt%), and maximum differences may be as high as 2.2 to 3.8 wt% depending upon the oxide or 5 units for Mg'. This disagreement may be due to variations in phase abundances between soil splits prepared for determination of modal abundance, bulk chemistry, and spectral reflectance. Although these differences in chemistry between sample splits are minor for most samples these variations are important to keep in mind due to the sensitivity of near-infrared spectroscopy to composition.

Optical Constant Selection: Two methods for estimating optical constants for pyroxene as a function of Mg' are available [*Denevi et al.*, 2007; *Lucey*, 1998]. Modeling of lunar soil spectra is performed four times, each time with a different set of pyroxene optical constants. Four sets of pyroxene optical constants are used: 1) those of *Lucey* [1998], 2) those of *Denevi et al.* [2007], 3) a combination of *Lucey* [1998]'s orthopyroxene and *Denevi et al.* [2007]'s clinopyroxene optical constants, and 4) a combination of *Denevi et al.* [2007]'s orthopyroxene and *Lucey* [1998]'s clinopyroxene optical constants. The combination of *Denevi et al.* [2007]'s orthopyroxene and *Lucey* [1998]'s clinopyroxene optical constants provide the best model spectral fits and compositional accuracy (average goodness of fit of 0.43). Model spectral fits with these optical constants are the best for each parameter except spectral slope (shape of 0.98, contrast 1.0001, Δ slope 0.0037, and Δ FeO 0.335; **Table 4.3**).

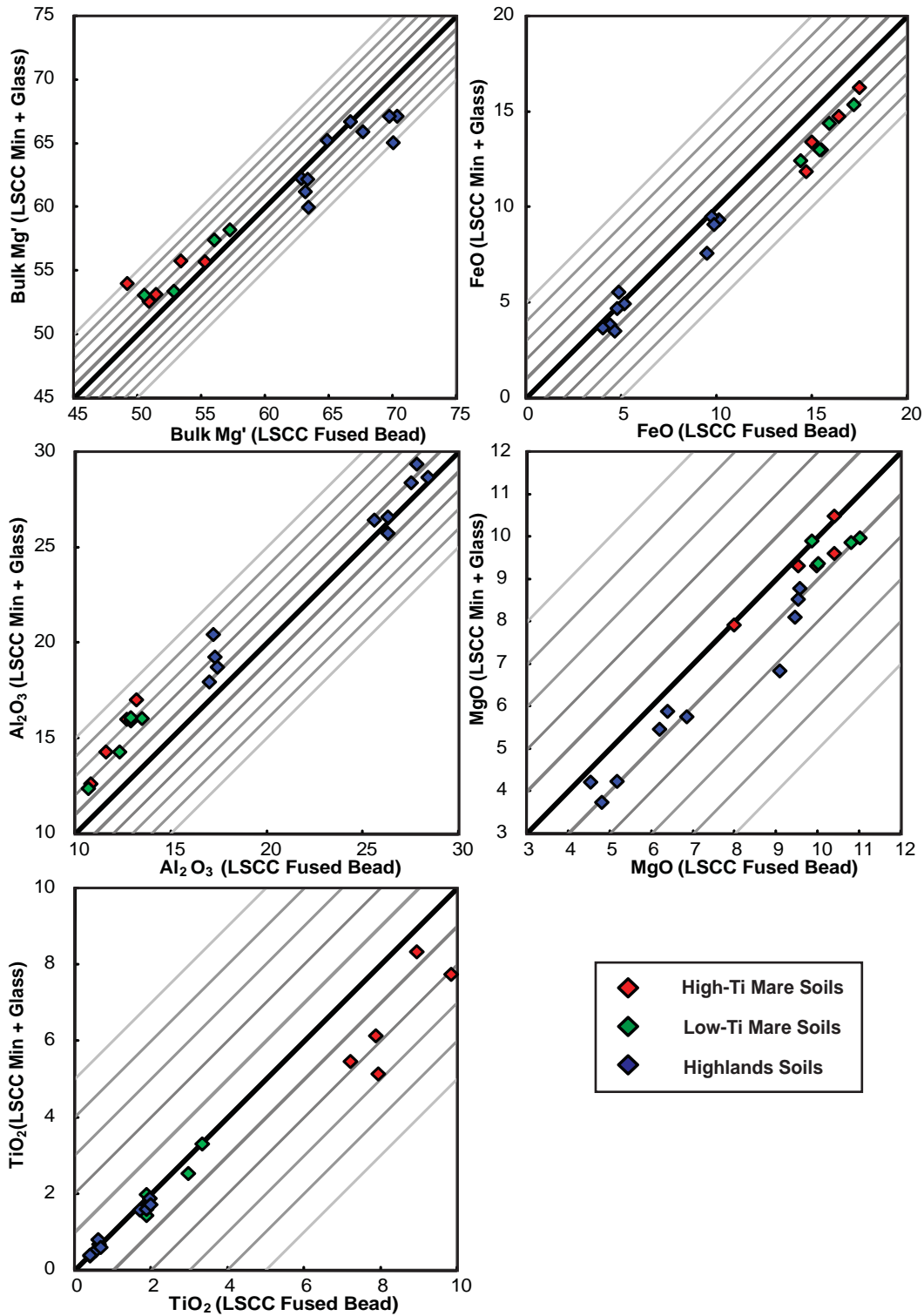


Figure 4.5: LSCC-reported mineral and fused bead bulk chemistry are compared. High-titanium mare soils, low-titanium mare soils, and highland soils are designated by red, green, and blue diamonds, respectively.

Table 4.3: Mean goodness of fit, contrast, Δ slope, and Δ FeO for models of each lunar soil using various optical constants.

Sample	1			2			3			4					
	g	b''	b	Δ slope	Δ FeO	g	b''	b	Δ slope	Δ FeO	g	b''	b	Δ slope	Δ FeO
10084	0.44	0.97	1.000	0.003	0.003	0.41	0.97	1.000	0.002	0.001	0.48	0.97	1.000	0.003	0.003
12001	0.12	0.99	1.000	0.002	0.000	0.96	0.97	1.035	0.019	4.063	0.42	0.97	1.000	0.010	0.000
12030	0.13	0.99	1.000	0.001	0.028	0.53	0.97	1.000	0.000	0.001	0.45	0.97	1.002	0.022	0.009
14141	0.48	0.97	1.000	0.000	0.005	0.47	0.98	1.000	0.033	0.646	0.39	0.98	1.000	0.000	0.003
14163	0.33	0.98	1.001	0.000	0.002	0.26	0.98	1.000	0.000	0.001	0.30	0.98	1.000	0.000	0.001
14259	0.36	0.98	1.000	0.004	0.002	0.41	0.97	1.000	0.000	0.001	0.44	0.98	1.000	0.000	0.667
14260	0.73	0.97	1.002	0.001	2.305	0.85	0.95	1.000	0.001	0.001	0.86	0.95	1.000	0.000	0.002
15041	0.12	0.99	1.000	0.000	0.001	0.45	0.97	1.000	0.000	0.000	0.41	0.97	1.000	0.000	0.002
15071	0.27	0.98	1.000	0.000	0.005	0.28	0.98	1.000	0.001	0.001	0.25	0.98	1.000	0.000	0.001
61141	0.39	0.98	1.000	0.000	0.045	0.28	0.98	1.000	0.000	0.023	0.36	0.98	1.000	0.001	0.074
61221	0.79	0.95	1.000	0.004	0.336	0.36	0.99	1.002	0.040	1.389	0.98	0.98	1.000	0.074	1.989
62231	0.51	0.98	1.000	0.018	1.280	0.31	0.98	1.000	0.002	0.002	0.50	0.97	1.000	0.016	0.235
64801	0.41	0.98	1.000	0.000	0.878	0.53	0.98	1.000	0.018	0.890	0.68	0.97	1.000	0.000	1.682
67461	0.55	0.97	1.000	0.016	0.109	0.21	0.99	1.000	0.000	0.120	1.08	0.98	1.000	0.081	3.228
67481	0.69	0.97	1.000	0.047	0.111	0.26	0.98	1.004	0.006	0.007	0.67	0.98	1.000	0.052	0.931
70181	0.37	0.98	0.999	0.011	0.001	0.69	0.96	1.000	0.006	0.030	0.73	0.96	0.999	0.015	0.009
71061	2.26	0.91	1.003	0.061	5.310	-	-	-	-	-	2.79	0.86	1.001	0.043	4.907
71501	0.57	0.96	1.000	0.004	0.003	1.93	0.93	1.002	0.000	7.836	1.05	0.94	1.000	0.005	0.331
79221	0.23	0.99	1.000	0.005	0.001	0.19	0.99	1.000	0.000	0.004	0.20	0.99	1.000	0.000	0.001
mean	0.51	0.97	1.000	0.009	0.834	0.52	0.97	1.002	0.007	0.834	0.69	0.97	1.000	0.017	0.741
std. dev.	0.47	0.02	0.001	0.017	2.008	0.41	0.02	0.008	0.012	2.008	0.57	0.03	0.001	0.026	1.341

1 - pyroxene optical constants of Lucey (1998)

2 - pyroxene optical constants of Devevi et al. (2007)

3 - orthopyroxene and clinopyroxene optical constants of Lucey (1998) and Denevi et al. (2007), respectively

4 - orthopyroxene and clinopyroxene optical constants of Denevi et al. (2007) and Lucey (1998), respectively

g - goodness of fit (closer to 0 the better the fit)

b'' - spectral shape (closer to 1 the better the fit)

b - spectral contrast (the closer to 1 the better the fit)

Δ slope - difference between model and lunar soil spectral slope

Δ FeO - difference between model and lunar soil FeO

Performance Against LSCC Soils

Lunar Soil Spectral Modeling: **Figure 4.6 and 4.7** show our model spectral results and residual differences when compared to each of the lunar mare and highlands soils in continuum removed and scaled reflectance. The average goodness of fit for lunar soils is 0.43 and ranges from 0.11 to 2.25 (**Table 4.3**). Only lunar soil sample 71061 has a goodness of fit value over 0.7 (2.25) with large mismatches apparent for every fitting parameter relative to other samples. Sample 71061 is particularly difficult to model since it consists of a significant abundance (9.6 vol %) of partially crystalline black pyroclastic beads [*Heiken and McKay, 1974*], which is not included in our modeling.

Residual differences for continuum removed spectra models of soil samples 12030, 14141, 15071, 71061, and 71501 show mismatches in modeling different portions of the 1 micron absorption feature. However, differences between models and spectra do not appear to be consistent in all cases. For instance, models for lunar soil samples 12030 and 14141 do not match the full spectral contrast. Whereas, models of lunar soil spectra for samples 15071, 67481, 70181, 71061, and 71501 replicate contrast sufficiently but not absorption width. And finally, models of soils 12030, 14163, 14260, 15041, and 15071 display model absorption features that are shifted to longer wavelengths indicating these models likely need a different pyroxene than clinopyroxene; however, orthopyroxene would shift the absorption feature too far to shorter wavelengths [*Denevi et al., 2007; Denevi et al., 2008; Noble et al., 2006*].

Model Mineralogy of Lunar Soils: Although spectral fit is the initial indicator of modeling quality our ultimate concern is compositional accuracy. In **Figure 4.8**, the model mineralogy estimates for each soil are compared to lunar soil modal mineral abundances reported by the LSCC; model mineralogy and differences between model of individual lunar soil mineralogy are reported in **Table 4.4**. Although olivine is a relatively minor constituent (i.e., usually <20 vol %) in lunar soils it is modeled effectively with a mean absolute difference of 4.8 vol % (RMSE of 7.1 vol %; **Table 4.5**). Plagioclase, which constitutes a significant portion of the modal mineral proportions (~40-95 vol %) of each soil's silicate budget is estimated with a average difference of

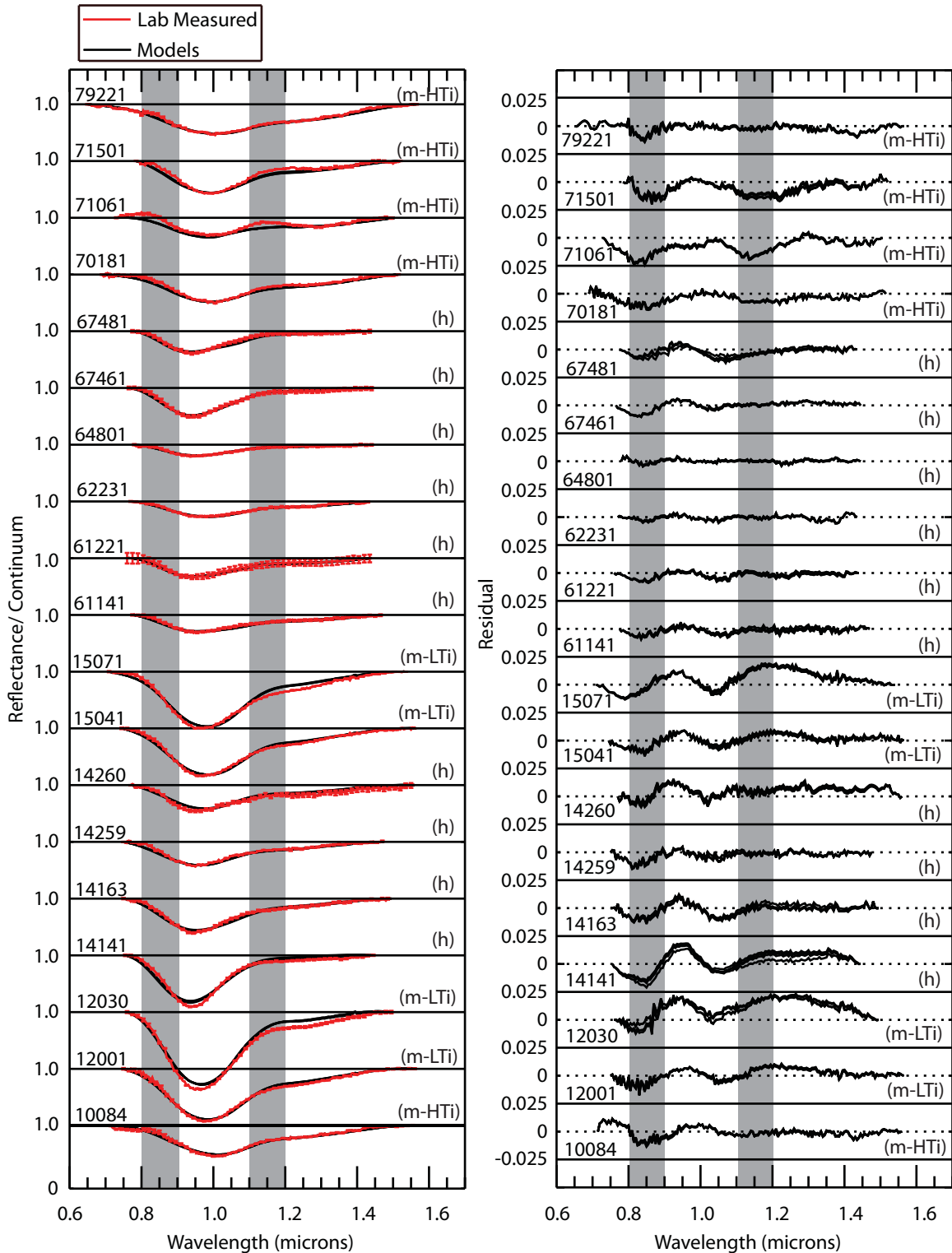


Figure 4.6: Continuum removed spectral comparisons between lunar soils (red) and model (black) spectra. Residual differences between model and lunar soils spectra are displayed in the adjacent figure. Soils are designated by soil number and soil type: highlands (h), mare high-titanium (m-HTi), mare low-titanium (m-LTi). Vertical gray fields provide points of context for the limbs of the 1 micron absorption feature so a comparison between model and modeled spectra and their residual differences can be more easily made.

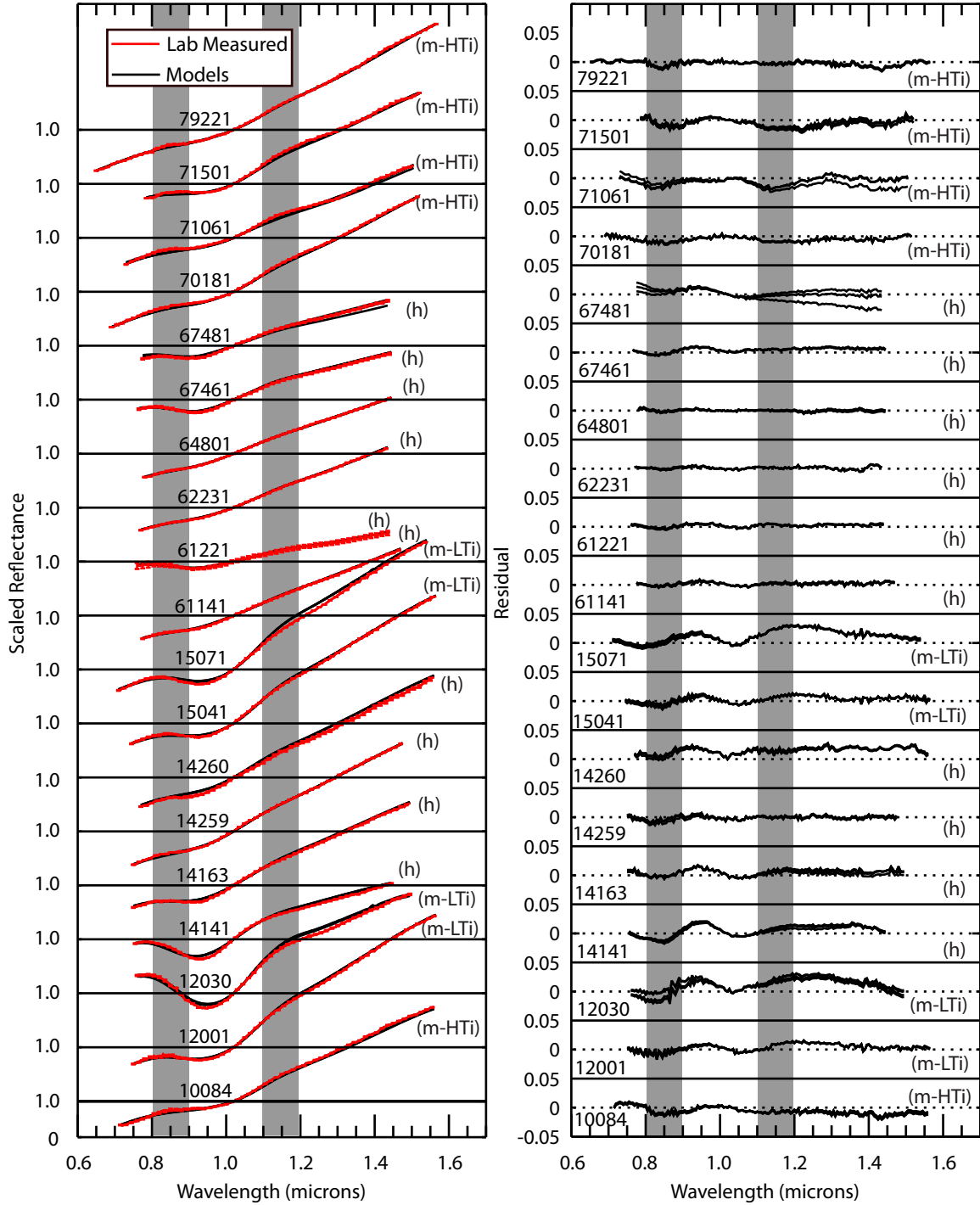


Figure 4.7: Comparisons of lunar soil (red) and model (black) spectra scaled to 1.02 microns are displayed. Residual differences between model and lunar soil spectra are displayed in the adjacent figure. Soils are designated by soil number and soil type: highlands (h), mare high-titanium (m-HTi), mare low-titanium (m-LTi). Vertical gray fields provide points of context for the limbs of the 1 micron absorption feature so a comparison between model and modeled spectra and their residual differences can be more easily made.

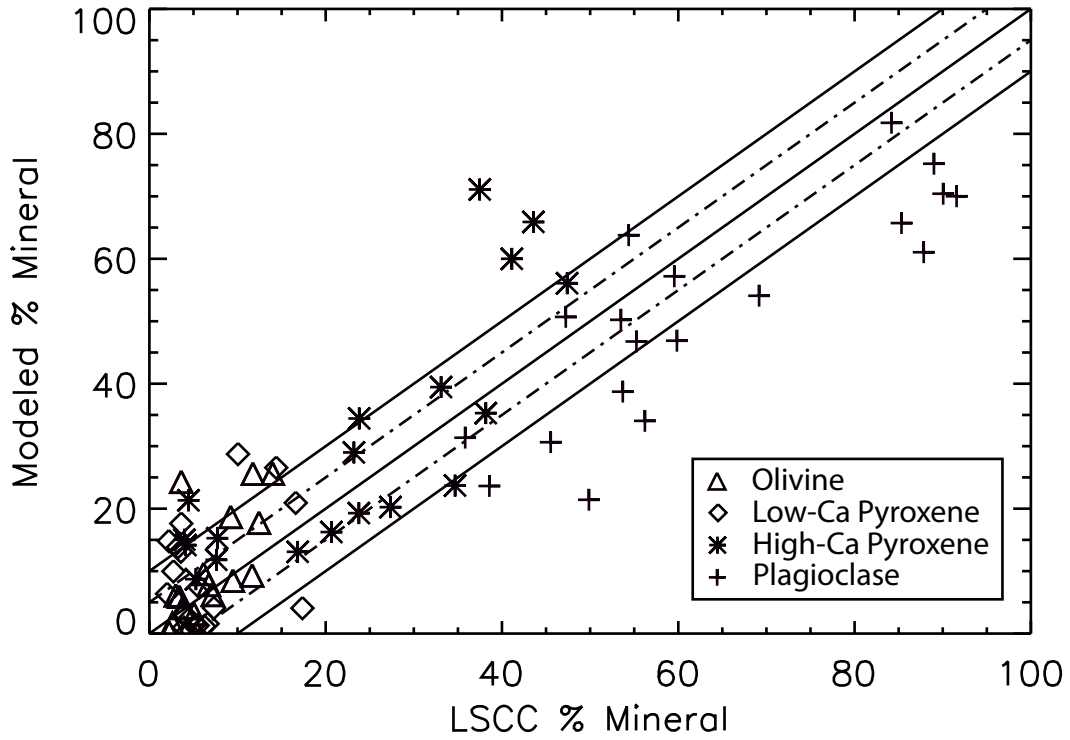


Figure 4.8: Model and LSCC-reported mineralogy for nineteen lunar soil samples. Mineralogy is designated with olivine (triangles), low-Ca pyroxene (diamonds), high-Ca pyroxene (stars), and plagioclase (+).

Table 4.4: Mean model mineralogy determined of nineteen lunar soil spectra.

Sample	Ol	δ	Low-Ca Px	δ	High-Ca Px	δ	Pl	δ
10084	24.3	0.3	6.4	0.8	35.3	2.3	34.1	1.3
12001	9.3	0.3	1.2	1.0	65.9	1.1	23.6	0.4
12030	8.5	0.5	4.1	3.6	56.1	5.6	31.4	2.6
14141	4.1	1.7	28.7	0.8	13.1	3.1	54.1	2.2
14163	9.6	1.0	20.9	0.4	19.3	2.4	50.2	1.6
14259	0.0	0.0	26.6	1.3	16.2	3.9	57.2	2.7
14260	3.2	0.8	4.1	3.7	29.0	7.2	63.8	3.6
15041	7.8	0.4	1.6	1.5	60.0	1.9	30.6	0.8
15071	6.2	0.5	1.3	1.6	71.1	1.9	21.4	0.8
61141	5.9	0.8	13.1	0.6	15.3	1.9	65.7	1.4
61221	6.1	1.4	10.0	1.1	8.7	0.7	75.2	3.1
62231	4.1	0.1	2.3	0.5	11.8	0.6	81.8	0.3
64801	1.6	0.6	13.8	0.4	14.2	1.3	70.4	0.9
67461	0.2	0.3	14.8	0.2	15.0	0.4	70.0	0.3
67481	0.0	0.0	18.2	1.6	23.8	1.9	57.9	3.6
70181	17.7	0.2	1.0	0.9	34.4	2.1	46.9	1.1
71061	25.6	1.0	0.0	0.0	23.7	0.9	50.7	0.9
71501	18.7	0.8	3.1	1.4	39.5	4.8	38.7	2.7
79221	25.6	0.3	7.4	1.0	20.2	2.2	46.8	1.2

Table 4.5: Mean difference, standard deviation, and RMSE between model and lunar soils.

Method	OI	δ	RMSE	Low-Ca Px	δ	RMSE	High-Ca Px	δ	RMSE	PI	δ	RMSE
I	4.8	5.4	7.1	7.2	5.1	8.7	10.3	8.0	12.9	13.8	8.5	16.1
II	4.8	5.4	7.1	13.4	9.0	16.0	17.9	14.8	23.0	13.8	8.5	16.1
III	4.8	5.4	7.1	9.8	5.4	11.1	13.0	11.9	17.4	13.8	8.5	16.1
IV	4.8	5.4	7.1	8.0	5.0	9.4	12.3	9.5	15.4	13.8	8.5	16.1
mean	4.8	5.4	7.1	9.6	6.1	11.3	13.4	11.0	17.2	13.8	8.5	16.1

I - Low-Ca = opx; High-Ca = pig + Mg-cpx + Fe-cpx

II - Low-Ca = opx + pig; High-Ca = Mg-cpx + Fe-cpx

III - pig split between Low-Ca and High-Ca pyroxene

IV - no pig

13.5 vol % (RMSE of 16.1 vol %). All groupings of LSCC pyroxene considered, model estimates of low-Ca and high-Ca pyroxene have an average difference of 9.6 and 13.4 vol %, respectively (RMSE 11.3 and 17.2 vol %, respectively). Low-Ca pyroxene has an average difference of 7.2 vol % (RMSE 8.7 vol %). High-Ca pyroxene estimates are less accurate with a mean difference of 10.3 vol.% (RMSE 12.9 vol %) relative to LSCC reported pyroxene values.

In **Figure 4.9** these results are put into further individual sample and overall data set context on a slightly modified Stöffler rock-type diagram [*Stöffler et al.*, 1980]. Lunar soils have small envelopes of composition relative to lunar highland samples [*Cahill and Lucey*, 2007; *Cahill et al.*, 2009]. Lunar soil sample "silicate mineral assemblages" fall into two general groups; anorthosite to gabbroic anorthosite (~85-95 vol % plagioclase) and anorthositic gabbro to olivine-bearing gabbro. Relative to these lunar soils, estimates of their compositions are relatively accurate with significant overlap in data fields, but improvement is necessary. **Figure 4.9** shows consistent underestimates of 5-20 vol % for plagioclase resulting in misinterpretations in finer scale mineral assemblage distinctions. For example, lunar soils of anorthosite and gabbroic anorthosite are modeled to have gabbroic anorthosite and anorthositic gabbro compositions, respectively. However, underestimates in plagioclase are not reflected in overestimates of any single mafic mineral. Although high-Ca pyroxene may be the most noticeable mafic in terms of relative inaccuracy, overestimates of olivine and low-Ca pyroxene are distinctive for several samples.

Chemical Modeling of Lunar Soils: **Figure 4.10** shows the relationship between derived Mg' and lunar soil sample Mg'. Initial model estimates of Mg' differ from LSCC values by 11-15 units (RMSE 14.7-19.7 units). The model becomes less effective at accurately modeling lunar soil Mg' as the model approaches 50. Although mare materials generally have lower Mg' values there does not appear to be accuracy dependence based upon soil type (i.e., highland versus mare). This suggests that this technique for computing Mg' is not robust. On the other hand, the range of Mg' in the LSCC data is relatively small, ranging from just under 50 to slightly over 70, considerably

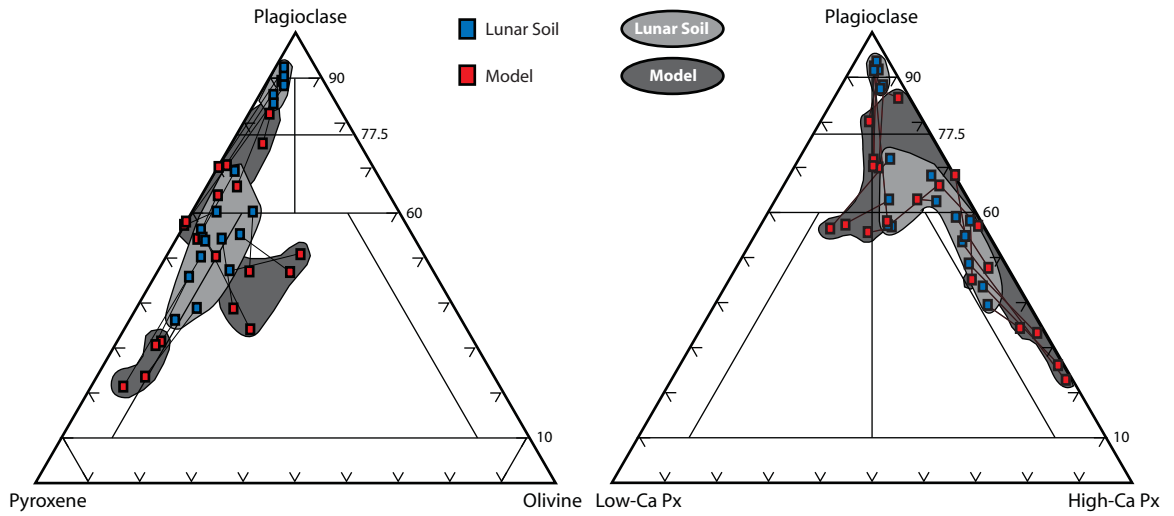


Figure 4.9: Slightly modified Stöffler lunar highland rock diagrams comparing mineral proportions of the four major silicates (plagioclase, olivine, low-Ca pyroxene, and high-Ca pyroxene) of lunar soils (blue squares and light gray fields) to modeling (red squares and dark gray fields) results [Stöffler *et al.*, 1980]. Tie lines between data points indicate actual versus model mineralogy of a particular lunar soil.

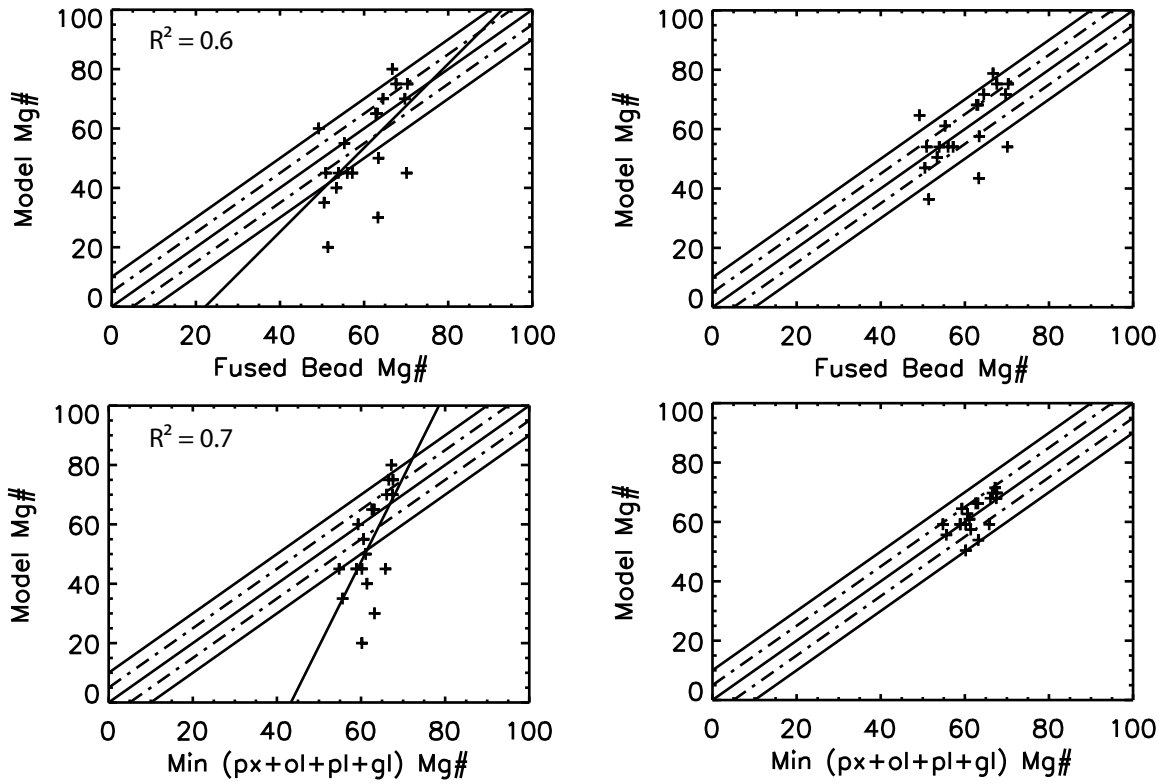


Figure 4.10: Model Mg' relative to different computations of lunar soil Mg' from LSCC-reported bulk and mineral chemistry data sets. The left and right columns provide the uncorrected and corrected comparisons, respectively.

less than observed in lunar rocks (40-95). It is plausible that a correlation may emerge if a validation data set with a larger range of Mg' were available.

Comparing weak trends between model and lunar soil Mg' computed from bulk soil fused bead analyses and mineral chemistry (excluding ilmenite) show how their correlation may be dependent upon the mineralogy (**Table 4.6**). Although model estimates of Mg' for less magnesian lunar soils prove inaccurate, they fall along a trend that becomes more correlated as the Mg' contribution of additional soil constituents are integrated into our mean Mg' value for each soil (**Figure 4.10**). Using these trends to make a correction, Mg' estimates improve to a mean difference of 3.3-8.1 units (RMSE 4.4-10.3 units) relative to lunar soils.

Discussion

Significant effort has been put forth to model near infrared spectra of terrestrial silicate minerals (e.g., [Denevi *et al.*, 2008; Sunshine and Pieters, 1993]). Relative to terrestrial samples, lunar soils contain additional problems created by space weathering [Denevi *et al.*, 2008; Li, 2006; Noble *et al.*, 2006]. While the finer fractions of lunar soil are the most optically dominant, they also have a higher surface to volume ratio relative to larger grain sizes which allows larger portions of vapor-deposited SMFe to adhere to grain surfaces [Noble *et al.*, 2001; Taylor *et al.*, 2001b]. This SMFe coating negatively influences near-infrared reflectance spectra significantly, making the 10-20 μm size fraction the second most difficult size fraction to interpret and model. Despite these challenges, progress is being made on multiple fronts with at least three methods of compositional modeling under development and in active use [Denevi *et al.*, 2008; Li, 2006; Noble *et al.*, 2006].

Unlike the study of Denevi *et al.* [2008] we approach lunar soils spectra as unknowns. Model results suggest that our spectral fitting approach is robust. Model matches of spectral slope and contrast are nearly always attained and measures of goodness of fit are well optimized (g of 0.43; 0.0 being a perfect fit). However, model band center and width comparisons relative to lunar soil spectra remain an area where additional improvement is necessary. Noble *et al.* [2006] and

Table 4.6: Model relative to lunar soil Mg' statistics before and after correction.

Sample	Mg' _{Model}	Mg' _{LSCC Bulk}	Δ Mg'	Δ Mg' ^a	Mg' _{LSCC Bulk - Ilm}	Δ Mg'	Δ Mg' ^b	Mg' _{Px+Ol+Pl+Gl}	Δ Mg'	Δ Mg' ^c
10084	60	49.2	10.8	15.4	65.3	5.3	5.6	59.3	0.7	5.2
12001	45	52.9	7.9	1.2	57.4	12.4	3.3	54.8	9.8	4.4
12030	35	50.5	15.5	3.6	55.3	20.3	1.5	55.6	20.6	0.1
14141	65	63.1	1.9	5.0	67.1	2.1	7.2	62.6	2.4	3.6
14163	65	62.8	2.2	5.3	67.0	2.0	7.3	63.1	1.9	3.1
14259	50	63.4	13.4	5.9	67.9	17.9	3.8	61.1	11.1	0.2
14260	30	63.3	33.3	19.9	67.8	37.8	17.4	63.2	33.2	9.3
15041	45	57.2	12.2	3.2	60.2	15.2	0.5	58.9	13.9	0.3
15071	45	56.0	11.0	2.0	58.9	13.9	1.8	58.9	13.9	0.3
61141	75	70.3	4.7	4.9	72.8	2.2	8.4	67.6	7.4	2.1
61221	75	67.6	7.4	7.6	70.1	4.9	11.1	66.6	8.4	3.1
62231	45	70.1	25.1	16.0	72.5	27.5	11.8	65.8	20.8	6.6
64801	70	69.7	0.3	1.9	72.5	2.5	5.3	67.5	2.5	0.5
67461	70	64.8	5.2	6.8	66.6	3.4	11.2	66.1	3.9	1.9
67481	80	66.7	13.3	12.0	68.7	11.3	15.9	67.2	12.8	4.3
70181	40	53.4	13.4	2.9	67.9	27.9	10.7	61.4	21.4	4.0
71061	20	51.4	31.4	15.1	66.2	46.2	22.6	60.2	40.2	9.8
71501	45	50.9	5.9	3.2	69.2	24.2	8.5	60.2	15.2	1.0
79221	55	55.3	0.3	5.8	68.5	13.5	1.0	60.6	5.6	2.1
Mean			11.3	7.3		15.3	8.1		12.9	3.3
Std. Dev			9.6	5.6		12.8	6.0		10.7	2.9
RMSE			14.7	9.2		19.7	10.3		16.6	4.4

a - Model corrected from comparison with lunar soil bulk chemistry.

b - Model corrected from comparison with lunar soil bulk chemistry minus the contribution of ilmenite.

c - Model corrected from comparison with lunar soil mineral chemistry (excluding ilmenite).

Denevi et al. [2008] both report similar spectral fitting issues. *Denevi et al.* [2008] discusses many of the issues related to spectral mismatches and suggests many of the problems may be attributed to naturally occurring differences in terrestrial high-Ca pyroxene chemistry, formation, as well as other missing pyroxene components relative to lunar samples. These issues include minor element contaminants (e.g., Cr, Ti, Mn, etc.), differing cooling rates, and the lack of an explicit modeling treatment for pigeonite.

Although achieving a high quality spectral fit is our initial goal our main objective is accurate compositional estimates. The best model mineral estimates determined here have a relative accuracy of 5-15 vol % on average depending on the mineral constituent. Given the high quality of spectral fits these results are expected to be better. Several factors, some obvious some perhaps unavoidable, may be contributing to these results. Underestimates of plagioclase may prove unavoidable due to the overall dark character and small grain sizes of lunar soils modeled. Plagioclase absorption features diminish in spectral contrast even with relatively high plagioclase to mafic ratios. Mismatches between LSCC data reports and our model may also be a source of error. For example, the LSCC reports four types of pyroxene but our modeling only estimates the abundances of two types of pyroxene that have fixed CaO abundances. Our only method of comparison is dependent upon accurately lumping of LSCC pyroxenes to conform to this setup. This is a problem, but mainly a function of suitable sample availability and accurate optical constant determination. Our model is also missing mineral constituents that may prove important in these results. In addition to lacking pigeonite and Fe-clinopyroxene types, integration or more effective modeling of ilmenite, glass, and agglutinates may also have a positive influence on these spectral and compositional results.

Modeling of lunar soil chemistry shows improvement in methodology but also suggests some retooling is necessary. An obvious relationship between spectral shape relative to Mg' appears to be an effective method of mineralogical determination. However, model Mg' values for lunar soils with lower Mg' prove inaccurate. Several factors may be at play here. Missing constituents in lunar soils characterized for reflectance relative to those analyzed for bulk chemistry is a possible

source of error; however a comparison of soil split bulk versus mineral show only minor differences (1.9 and 5 mean and max differences in Mg', respectively) relative to our modeling. Model selection based upon spectral shape and Mg' does show ambiguities in these two parameters for some lunar soils. But, these ambiguities usually occur towards models of lower Mg' assemblages and suggest our empirical estimates of optical constant variation with Mg' in mafic minerals may need improvement. For certain these estimates are questionable for mafics with low Mg' values, as these values are interpolated from higher Mg' samples [*Denevi et al., 2007; Lucey, 1998*]. Another factor may be our assumption that chemical equilibrium also entails one-to-one behavior between mafics. Although FAN and Mg-suite samples show equilibrium behavior, Mg' values between mafics are not necessarily one-to-one. A model update that allows mafic Mg' to adhere to a chemical equilibrium system, but does not necessarily mandate that have one-to-one behavior may be necessary. And finally, missing components may be a source of error here as well. Although ilmenite is a minor constituent in lunar soils (usually ~10 vol. % or less), it can carry a significant portion of the FeO budget (22.4 ± 15.8 %) for each soil. This may result in a 6.5 ± 5.6 swing in Mg'. Computations regarding this possibility conflict. A determination of Mg' from LSCC bulk chemistry minus the contribution of ilmenite relative to model Mg' does not improve, and actually worsens Mg' accuracy to a relative difference of 15.3 units. And while a determination of Mg' from reported LSCC mineralogy, again excluding ilmenite, is roughly similar to comparisons with initial bulk composition (14.4 and 13.2, respectively) it significantly improves the correlation of the overall data set between model and actual composition (**Fig. 10**). This trend allows a correction to be made that results in a mean difference between model and actual Mg' of 3.3 units (RMSE 4.4 units).

Conclusions

A new algorithm exploiting *Hapke* [1981; 1993; 2001]'s radiative transfer theory for compositional determination from hyperspectral data sets is tested here on a suite of lunar soils previously characterized by the LSCC. Here we found several important results:

- Our evaluation of model inputs, in the form of mineral optical constants, determined that a combination of *Lucey* [1998]'s clinopyroxene and *Denevi et al.* [2007]'s orthopyroxene optical constants provide the best spectral fits of lunar soils. However, we believe *Denevi et al.* [2007]'s approach toward estimating pyroxene optical constants has the most potential for improvement of this model as it begins to account for the influence of Fe²⁺ and Ca²⁺ on pyroxene reflectance spectra. But, these results suggest additional samples for further assessment of pyroxene optical constants is merited.
- The model performs well at replicating lunar soil reflectance spectra using a metric designed to quantify goodness of fit based upon spectral shape, contrast, slope, and FeO composition. After optimization of these spectral parameters, it is found that distinction of a model match in mineral and chemical space can be determined from a plot of spectral shape relative to Mg'.
- Mineralogical accuracy resulting from this technique has a mean absolute difference of ~5-15 vol % depending upon the mineral constituent. Estimates of high-Ca pyroxene (10.3 vol % mean difference) and plagioclase (13.8 vol % mean difference) show the most room for improvement. Although significant overlap is shown in lunar soil and resulting model compositions, differences result in inaccurate finer scale distinctions in mineral assemblage.
- Modeling lunar soil chemistry is reproduced with a average difference of ~11-15 and ~3-8 units before and after a correction is applied, respectively.

Future Work

The small but significant spectral mismatches between our models and LSCC spectra, despite optimization, suggests errors due to the optical constants of mafic minerals that dominantly influence spectral shape. More extensive data on optical constants is needed, and these may require samples with lunar-like minor and trace element compositions. To validate models that include extreme Mg', validation data that includes higher and lower values are needed.

Acknowledgements

This research utilizes spectra acquired by C.M. Pieters with the NASA RELAB facility at Brown University. This work was supported in part by NASA Planetary Geology and Geophysics grant NNG05GJ51G to P.G.L.

**CHAPTER 5. RADIATIVE TRANSFER MODELING OF NEAR-INFRARED
TELESCOPIC SPECTRA OF SELECTED LOCATIONS ON THE LUNAR NEARSIDE⁴**

⁴ Cahill, J. T. S., P. G. Lucey, K. R. Stockstill-Cahill, and B. R. Hawke (2010), Radiative transfer modeling of near-infrared telescopic spectra of selected locations on the lunar nearside, *J. Geophys. Res.-Planets*, *in prep.*

Abstract

Telescopic data sets with similar hyperspectral resolution to the Spectral Profiler (SELENE/KAGUYA) and Moon Mineralogy Mapper (M³; Chandrayaan-1) payloads have been utilized since the 1970's and 80's to interpret lunar surface composition and calibrate more recent data sets (e.g., Clementine). Here we examine ~60 telescopic spectra of the lunar nearside for composition using a version of Hapke's radiative transfer techniques. Matching model spectra are fitted to telescopic spectra using criteria that iteratively adjusts mineralogy and chemistry within well defined compositional spaces to choose a model with the highest goodness of fit. This is performed selecting from model spectra of varying Mg' as well as at a fixed Mg' value of 70 consistent with average Lunar Prospector results. These results are directly compared to lunar highlands and mare data sets of the Apollo sample collection. Modeling suggests significant mineralogic diversity in both fixed and variable Mg' modeling schemes. Nectaris basin spectra are dominantly anorthositic (63 to 93 vol% plagioclase) with geochemical similarities (mean 6.2 wt% FeO; mean Mg' 57.5) to ferroan anorthosite suite rocks. Remaining nearside spectra show more mafic lithologies, dominantly olivine-bearing noritic gabbros, but range from anorthositic norite and troctolite to peridotite lithologies similar to Mg-suite olivine-bearing gabbroic norites and gabbros.

Introduction

After decades of analysis the Apollo samples suggest a general picture of lunar crust formation from a magma ocean, consisting largely of anorthositic rocks and a secondary crust of basaltic lava filling topographic lows [*Smith et al.*, 1970; *Warren*, 1985; *Wood et al.*, 1970]. Despite the intense meteorite bombardment, some examples of ancient plutonic rocks have escaped extensive mixing based on several criteria, including low siderophiles that would indicate interaction with a chondritic impactor. Most of these rocks are anorthosites and a suite of more mafic rocks now called the magnesium-suite (Mg-suite). These suites have separate fractionation trends on a diagram plotting a samples mafic mineral Mg' (i.e., molar $(\text{Mg}/(\text{Mg}+\text{Fe})) \times 100$) and coexisting feldspar An (i.e., molar $(\text{Ca}/(\text{Ca}+\text{Na})) \times 100$), which suggest very different histories and roles in the formation of the lunar crust [*Shearer et al.*, 2006; *Warren and Kallemeyn*, 1984]. Ferroan anorthosites (FAN), interpreted to be the main primitive constituent of a dominantly anorthositic crust, show no correlation with these two geochemical parameters (a characteristic that is not well understood, but shared by some terrestrial anorthosite complexes) [*Herbert et al.*, 1978; *Longhi and Boudreau*, 1979; *Raedeke and McCallum*, 1980]. In contrast, Mg-suite rocks form a positive trend-line reminiscent of a single differentiating magma body, but are interpreted to represent separate smaller magma bodies that later intruded the anorthositic crust [*James and Flohr*, 1983; *Warner et al.*, 1976a]. Although much is known about these suites, gaining additional knowledge about their spatial distribution, volumetric proportions, and relative timing of formation is cited as a fundamental step toward a greater understanding of their provenance within the context of lunar geology [*Shearer et al.*, 2006; *Wieczorek et al.*, 2006].

New hyperspectral data sets returning from the SELENE/KAGUYA Spectral Profiler and Chandrayaan-1's Moon Mineralogy Mapper (M³) promise significant advances in our understanding of these compositional relationships and others [*Matsunaga et al.*, 2008; *Pieters et al.*, 2009a]. Recent detections of pure anorthosite, usually associated with the FAN lunar sample suite and lunar magma ocean formation, and a definitive and wide spread detection of H₂O or OH are only two examples already reported [*Haruyama et al.*, 2009; *Ohtake et al.*, 2009; *Pieters et al.*, 2009b; *Pieters et al.*, 2009c]. However, "older" Earth-based telescopic

hyperspectral data sets are scientifically no less significant and have provided valuable compositional information and a reference for calibration of more recent data sets for decades (e.g., [Cahill *et al.*, 2009; Le Mouélic *et al.*, 1999; Matsunaga *et al.*, 2008; McCord *et al.*, 1981; Pieters, 1986; Pieters and Pratt, 2000]) but remain to be evaluated with more recent analysis techniques. Previous examinations of these spectra inferred areas of highly anorthositic materials similar to FAN rocks (e.g., [Hawke *et al.*, 2003; Spudis *et al.*, 1984; Spudis *et al.*, 1989]), and areas with significant mafic mineral content similar to Mg-suite rocks (e.g., [Lucey *et al.*, 1986; Lucey and Hawke, 1989; Pieters, 1986; Spudis *et al.*, 1988]). Here we select 56 of these spectra for radiative transfer mixture modeling to derive quantitative estimate of mineral abundance and chemistry.

The locations of the materials these spectra represent are spread throughout the lunar nearside and can be placed into a few groups based upon location and geologic feature. Approximately half of the 56 spectra modeled are of deposits in and around Imbrium basin (e.g., Aristarchus Plateau and the Hadley-Apennine ridge). This region of the Moon garners considerable attention due to its inferred compositional complexity and proximity to scientifically significant deposits both in and outside the basin [Lucey *et al.*, 1986; Lucey and Hawke, 1989; Spudis *et al.*, 1988] (**Fig. 5.1-5.2**). Other spectra examined are of eastern Nectaris near Apollo 16, mare Frigoris, and several impact crater central peaks. Quantitative estimates of composition and how they fit into the generalized picture of lunar composition is provided.

Composition Extraction Algorithm

The composition extraction algorithm uses a non-linear mixing model based upon the work of Bruce Hapke [1981; 1993; 2001] and is summarized by Lawrence and Lucey [2007]. Combined with inputs of plausible mineralogy and basic chemistry it allows the computation of near-infrared spectral candidates that include the effects of space weathering [Denevi *et al.*, 2007; Lucey and Noble, 2008]. Here we use an algorithm presented by Cahill *et al.* [2009] which is aimed at hyperspectral data and retains a stepwise approach introduced by Lucey [2004]. In this approach several fixed Mg' values are selected to produce intermediate candidate fits of

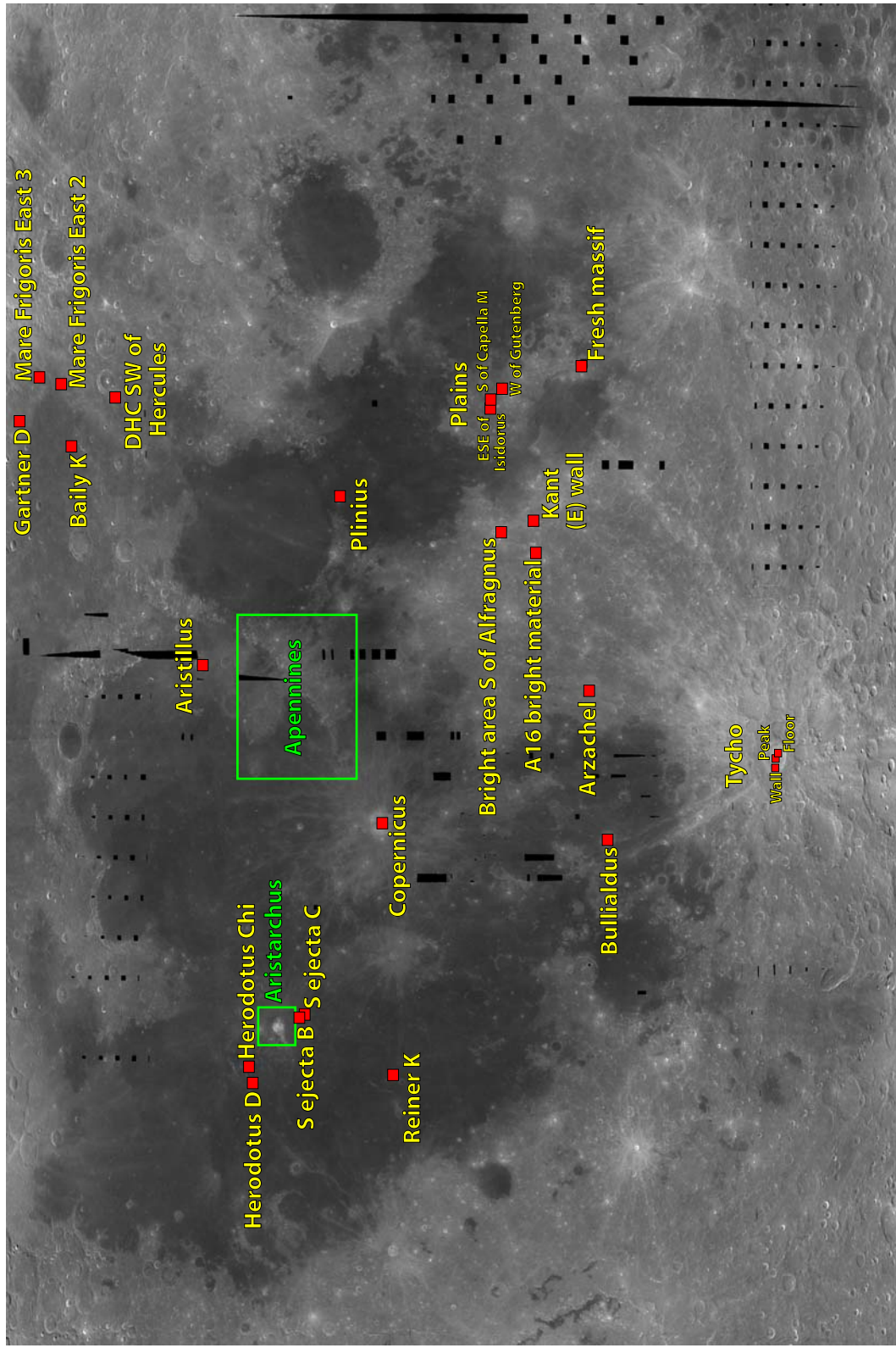


Figure 5.1: Clementine base map of the nearside of the Moon and locations of telescopic spectra analyzed in this study. The base map is cropped at 60°N to 60°S and 90°W to 90°E. Red squares denote where telescopic spectra were collected. Aristarchus Plateau and the Hadley-Apennine Ridge are outlined in green and enlarged in the next figure.

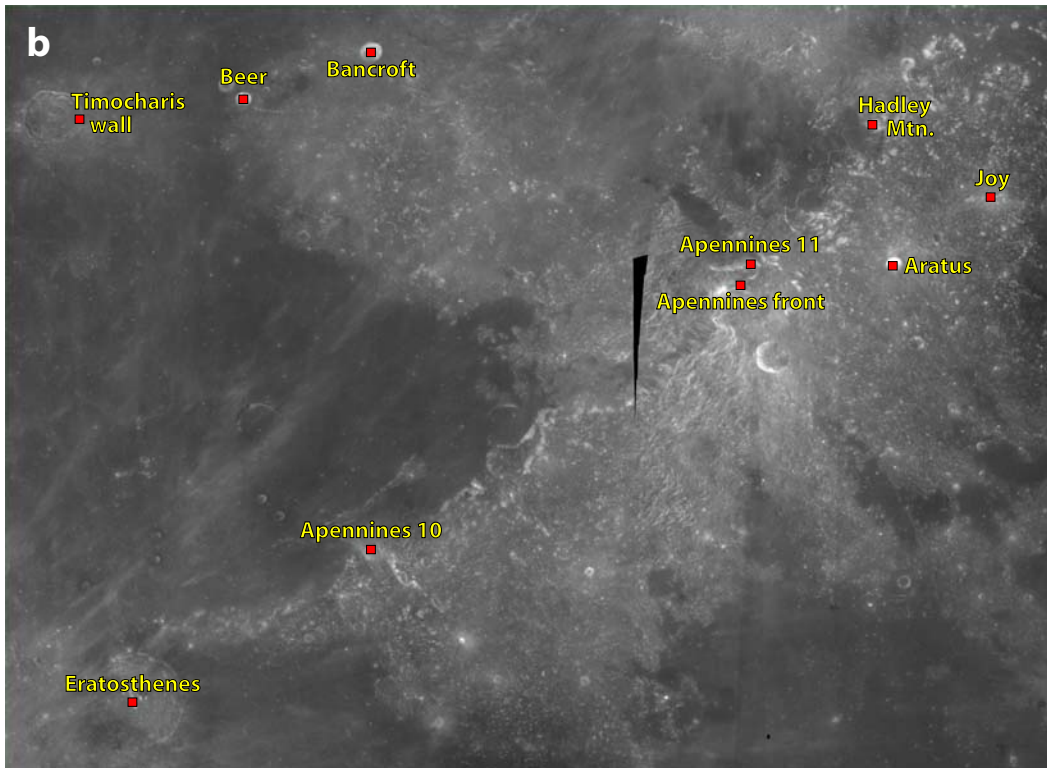
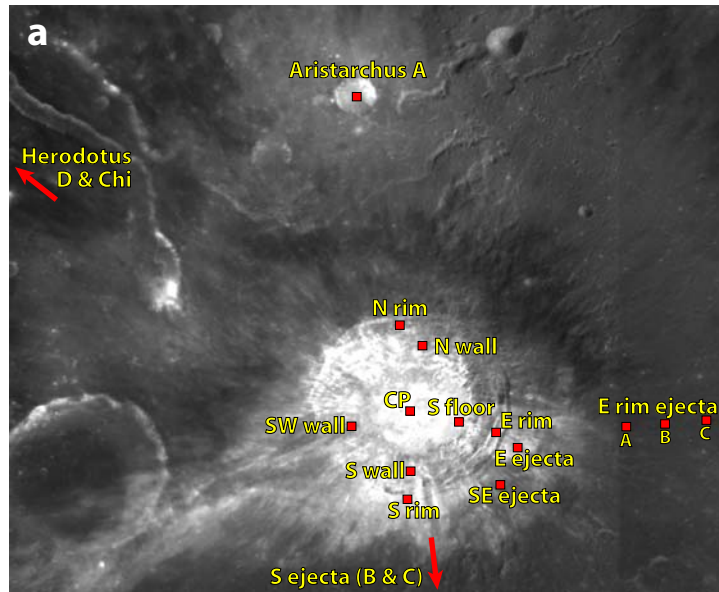


Figure 5.2: Clementine base maps of a) Aristarchus Plateau and crater and b) Hadley-Apennine Ridge. Red squares denote where telescopic spectra were collected. Clementine base map for Aristarchus Plateau and the Hadley-Apennine ridge are cropped at 26.3°N to 21.3°N, 49.8°W to 44.7°W and 29°N to 13°N, 14°W to 8°E, respectively.

unknowns for smaller portions of the plausible mineral and chemical parameter space. This is enhanced with a gradient descent spectrum and composition fitting process that prevents modeling from getting trapped in local minima.

The fitting process begins with four individual model fits conducted for each unknown spectrum. Each gradient descent process begins from one of four pure endmember starting compositions covering the system olivine, plagioclase, orthopyroxene and clinopyroxene at 1% compositional intervals, and Mg' ranging from 20 to 95 in 5 unit compositional steps. The space weathering components nanophase iron and agglutinates are allowed to vary in the fitting process (described below). The wide range of starting mineral abundances allow us to determine that the final fits are independent of starting composition, avoiding local minima.

From these four fits at each fixed Mg' we arrive at a final composition by optimizing a goodness of fit criterion used in a gradient descent algorithm (defined and described below). The set of model winners is selected by determining the one with the highest quality fit on a plot of spectral correlation (i.e., shape) versus Mg' (**Fig. 5.3**). Modal abundances of all four winning fits at that fixed Mg' are averaged to produce the final reported composition and its standard deviation (**Fig. 5.4**).

Spectral Computation and Mixing Model: Model spectra are computed using radiative transfer theory developed by *Hapke* [1981; 1993; 2001]. The spectra of mineral mixtures can be computed from linear mixtures of their component single scattering albedoes (i.e., the probability a photon will survive an encounter with a material) weighted by relative abundance and grain size. The reflectance of the mixture is then related to the mixture single scattering albedo by Hapke's equations that account for multiple anisotropic scattering, lunar-like backscatter behavior and photometric viewing geometry.

The single scattering albedo of the individual components are computed using Hapke's equations that relate the optical constants of the materials, their grain size and internal scattering behavior to the component single scattering albedo, including the effects of coating of nanophase

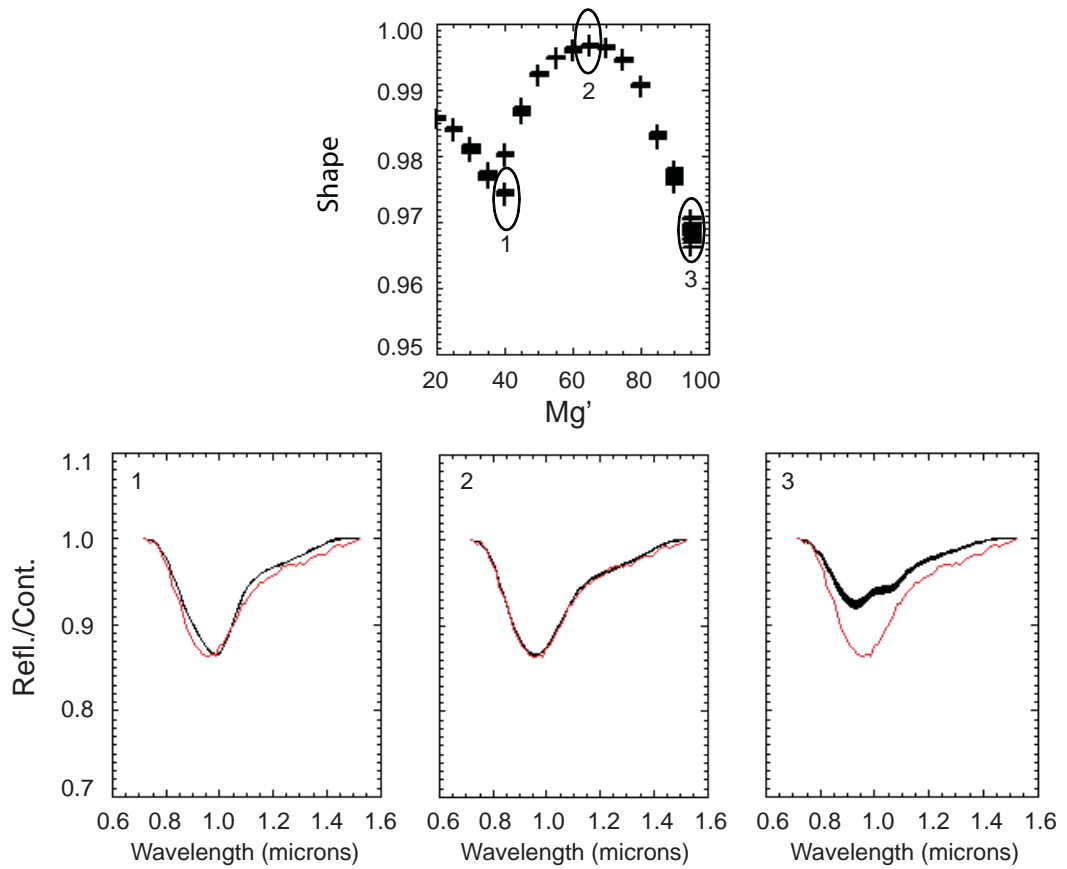


Figure 5.3: An example spectrum is examined with our model. A calculated estimate of model spectral shape relative to the spectral unknown is displayed relative to Mg' . Spectral comparisons are given for three different sets of models. Models for (2) are selected as the “winner” and averaged for a final model compositional estimate. The unknown spectrum is displayed in red and model spectra are displayed in black.

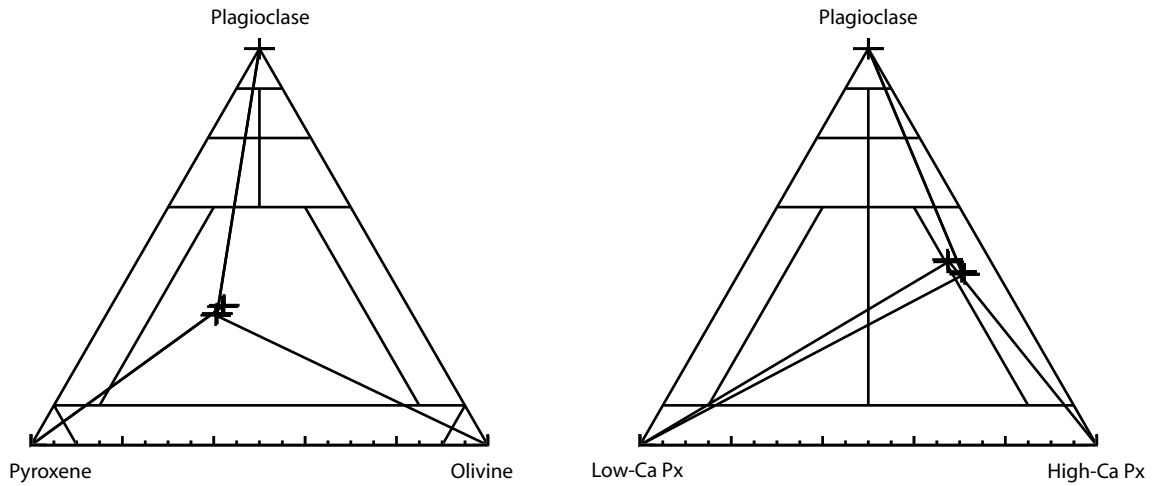


Figure 5.4: A visual representation of how our starting mineralogies of 100% olivine, 100% low-Ca pyroxene, 100% high-Ca pyroxene, and 100% plagioclase are iteratively adjusted until a spectral match is attained. The standard deviation of these four solutions gives us a measure of how well our model finds a compositionally-unique answer for each lunar soil.

iron. Optical constants are chosen in part based upon the results of modeling lunar soils by *Cahill et al.* [2010a]. In *Cahill et al.* [2010a]'s study multiple sets of optical constants for pyroxene are evaluated to find the best combination for modeling. Orthopyroxene optical constants derived by *Denevi et al.* [2007] and clinopyroxene optical constants derived by *Lucey* [1998] showed the most favorable results. *Denevi et al.* [2007]'s orthopyroxene optical constants are derived using a set of terrestrial pyroxene samples documented by *Cloutis et al.* [1985; 1986; 1990a; 1990b]. Optical constants for clinopyroxene and olivine were derived from spectra available from RELAB (<http://www.planetary.brown.edu/pds/LSCCsoil.htm>) using the methods of *Lucey* [1998]. Optical constants for plagioclase were derived from a reflectance spectrum of plagioclase (Anorthite HS201) in the U.S.G.S. spectral library [*Clark et al.*, 2003]. Iron optical constant data of *Paquin* [1995] are used to model sub-microscopic iron (SMFe). Agglutinates are treated as a dark and neutral optical component [*Keller et al.*, 1998] with a spectrally flat single scattering albedo of 0.1. Since a particularly strong relationship is observed between agglutinates and SMFe (e.g., [*Hapke*, 2001; *Keller and McKay*, 1997]) we link their relative proportions in the model.

Physical and Chemical Assumptions: We make simplifying assumptions for grain size, mineralogy, and mafic mineral Mg' to reduce the number of variables to a manageable number. Grain size is held to 15 μm , which is in agreement with the most optically dominant size fraction (10-20 μm) on the lunar surface [*Lucey et al.*, 2006; *Pieters et al.*, 1993]. Lunar mineralogy is simple and consists of plagioclase, pyroxene, olivine, ilmenite and the important non-mineral glass [*Heiken et al.*, 1991]. The impact on the spectra by typical variations in lunar chemistry and modal proportions of these materials is very large. Accounting for the diversity of mineral chemistries is impractical, particularly for pyroxene. Therefore, we use two pyroxene (low-calcium and high-calcium pyroxene) groups for modeling similar to other applications to multi- and hyperspectral data that show acceptable results [*Cahill and Lucey*, 2007; *Cahill et al.*, 2009; *Cahill et al.*, 2010a; *Denevi et al.*, 2008; *Lucey*, 2004; *Noble et al.*, 2006]. Model mafic mineral Mg' is assumed to be in "equilibrium" and is set equal among pyroxene and olivine. This is roughly consistent with highland FAN and Mg-suite plutonic rocks of the lunar sample collection [*Cahill and Lucey*, 2007; *Cahill et al.*, 2010a].

Fit Criteria: We use four metrics to assess the quality of the fit of the model to each spectrum: the similarity spectral slope, correlation, scale of and FeO of two spectra. We explicitly include the slope of the spectrum to better constrain the degree of space weathering that can affect both the shape and contrast of the spectrum. We include the contrast-normalized shape of the spectrum because it contains the richest information regarding presence and relative abundance of mafic minerals and their Mg'. Spectral contrast is explicitly included because of its strong dependence on degree of space weathering and plagioclase content. We also include FeO content to partly overcome the insensitivity of near-infrared spectra to feldspar content when mafic mineral content exceeds several percent. In a large number of numerical experiments these metrics were weighted relative to one another to maximize the accuracy of the inversion from spectrum to composition.

Slope, m , is determined from a straight line tangent to each spectrum near the 0.7 and 1.5 μm relative maxima. It is defined using the equation:

$$m = \frac{(R_{0.7} - R_{1.5})}{(\lambda_{0.7} - \lambda_{1.5})} \quad (1)$$

Here m is slope, R is reflectance, and λ is wavelength.

Quantitative estimates of spectral fit are determined using *Clark et al.* [2003]'s spectral shape and contrast matching algorithm. *Clark et al.* [2003]'s spectral comparison calculation is based upon the similarity between two spectra, which entails a calculation of the correlation coefficient (i.e., similarity in spectral shape) and spectral scale (i.e., similarity in spectral contrast). The algorithm is defined by these equations:

$$b = \frac{\sum S_u * S_o - (\sum S_u * \sum S_o) / n}{\sum S_o^2 - (\sum S_o)^2 / n} \quad (2)$$

$$b' = \frac{\sum S_u * S_o - (\sum S_u * \sum S_o) / n}{\sum S_u^2 - (\sum S_u)^2 / n} \quad (3)$$

$$b'' = b * b' \quad (4)$$

Here n is the number of spectral channels in the fit, S_o is the model spectrum, S_u is the telescopic spectrum (i.e., unknown), b is the spectral contrast between the reference and test spectrum and b' is an intermediate product. In equation 4, b'' is the correlation coefficient which quantifies the amount of correlations between the shapes of two spectra over all the wavelength channels available, regardless of differences in spectral contrast.

Model FeO content, is derived stoichiometrically from Mg' and mineralogy. The mean FeO abundance for each telescopic spectrum is collected from 5 km² spots (roughly similar to the telescopic spot size) on an FeO map computed from the Clementine reflectance data set using the algorithm of *Lawrence et al.* [2002]. The locality of each telescopic spectrum is confirmed by consulting photographs taken during data collection in conjunction with the lunar atlas of *Bussey and Spudis* [2004] and communication with one of the collection investigators (i.e., B.R. Hawke).

Gradient Descent Methodology: At the outset of the process, the initial mineral composition (i.e., four minerals and a neutral) is entered as well as a nominal value for space weathering components. The value of each parameter is both incremented and decremented in turn, and the effect of these small changes on the weighted fit criterion recorded. This criterion is defined by the equation:

$$g = (1 - b'')w_{b''} + |1 - b|w_b + \Delta m w_m + \Delta FeO w_{FeO} \quad (5)$$

Here g is the goodness of fit, $w_{b''}$ is the weight given to spectral shape, w_b is the weight given to contrast, w_m is the weight given to slope, and w_{FeO} is the weight given to FeO abundance. When all inputs are tested, new values for all parameters are updated in the direction that produced an

improvement in the aggregate metric, or left unchanged if no improvement was detected. This process is repeated until a candidate meets a preset goal criterion for spectral shape ($1-b'' < 0.01$), contrast ($|1-b| < 0.001$), slope ($\Delta m < 0.01$), and FeO ($\Delta \text{FeO} < 2$) or after an “exhaustive” search (500 iterations) finds the best possible match given the model and telescopic spectrum.

Telescopic Spectra

Fifty-six telescopic spectra collected in the 1970's and 1980's are selected for analysis here [McCord *et al.*, 1981; Pieters, 1986; Pieters and Pratt, 2000]. These observations were carried out at the University of Hawaii 2.2 m telescope at Mauna Kea Observatory and the McCord two-component circular-variable-filter (CVF) near infrared photometer with a indium antimonide detector [McCord *et al.*, 1981]. Spectra range from 0.6 to 2.5 μm and were collected using a rotating filter with a continuously variable band pass. Observations were taken with a 2.3 arcsec aperture that outlines a 5 km spot on the surface and at a 0.7 arcsec aperture for area outlines of ~ 1.5 km. All spectra have been scaled to unity at 1.02 microns.

This produced spectra representing the reflectance ratio between the observed area and the Apollo 16 landing site. Initially, bi-directional reflectance data for lunar soils were not available for calibration. So, data collected in relative reflectance were calibrated to scaled reflectance using a directional-hemispheric spectrum of a mature Apollo 16 soil (62231) collected by J.B. Adams. Here we convert each spectrum to bi-directional reflectance using the correction procedures explained by Pieters [1999] and Pieters and Pratt [2000]. Acquisition of 120 data points takes an extended period of time (i.e., several minutes) so the accuracy of each spectrum may be affected by instrumental stability and directional guiding on the Moon as well as changing sky conditions. Error bars shown in figures are the standard deviation of several spectra collected on independent runs taken in sequence.

Model Fits of Telescopic Spectra

Figures 5.5 and 5.6 show a sampling of the 56 telescopic spectra modeled in this study. Goodness of fit values for telescopic spectra average 0.588 and range from 0.045 to 7.931 (the

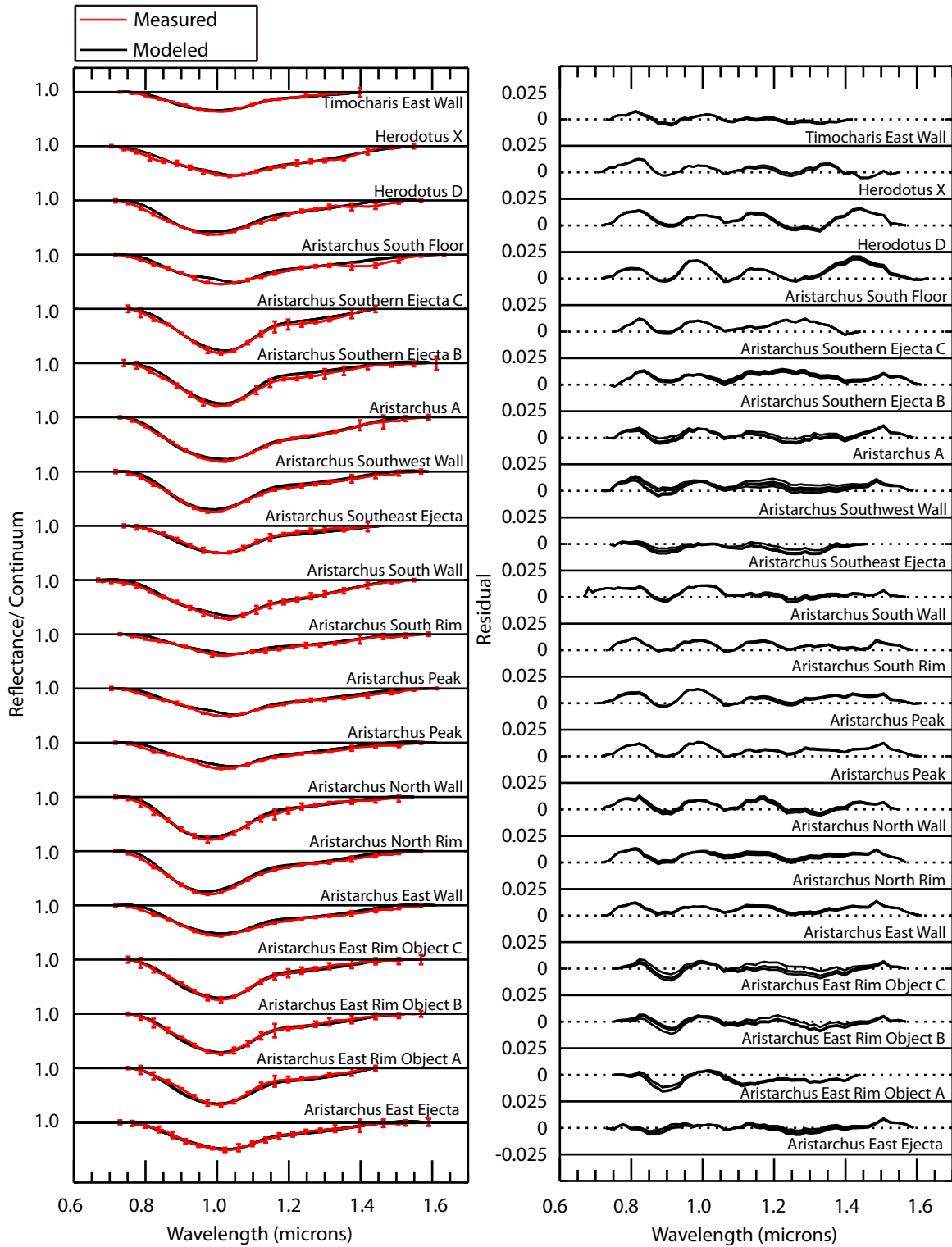


Figure 5.5: Continuum removed spectral comparisons between lunar telescopic (red) and model (black) spectra. Residual differences between model and telescopic spectra are displayed in the adjacent figure.

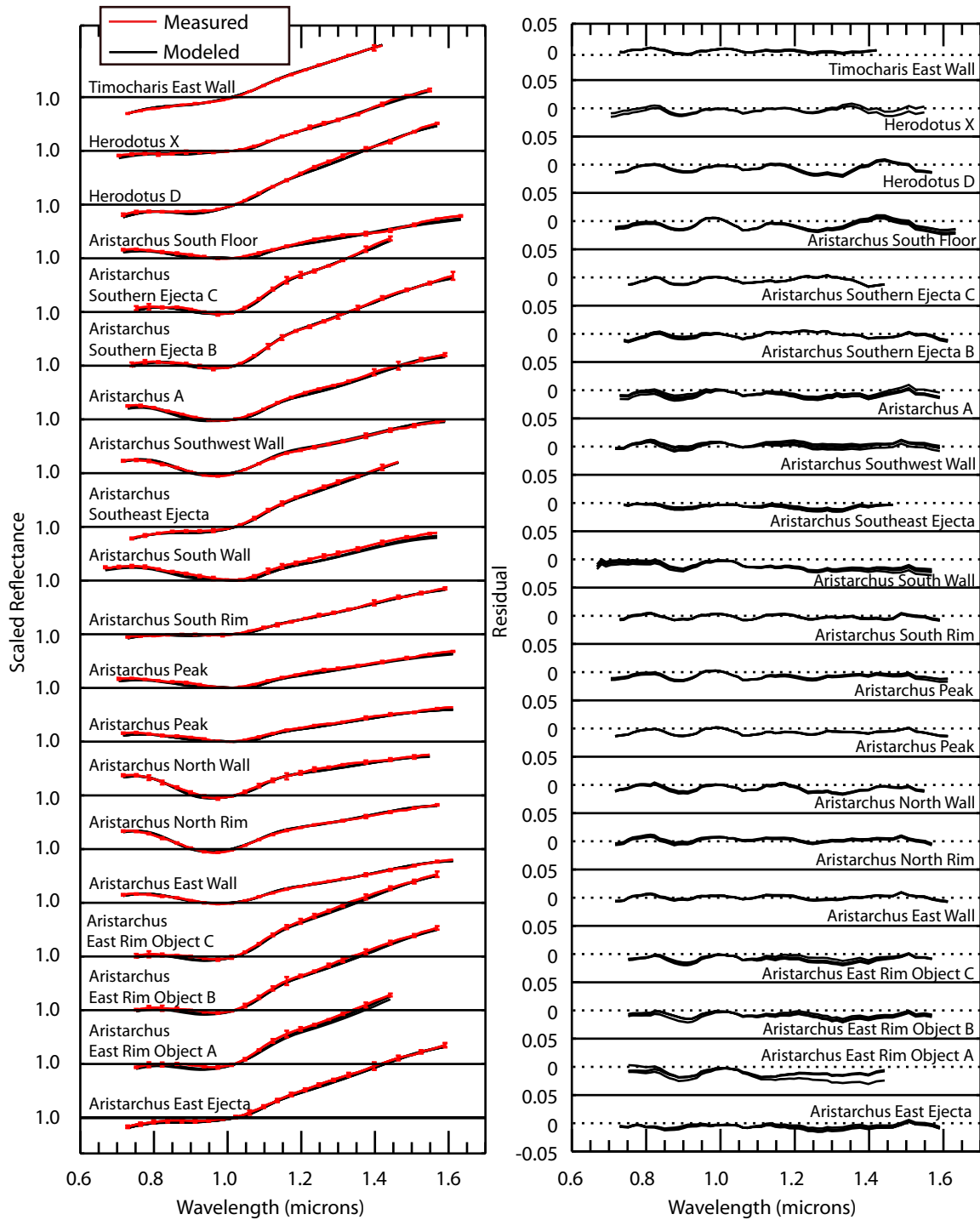


Figure 5.6: Comparisons of scaled lunar telescopic (red) and model (black) spectra scaled to 1.02 microns are displayed. Residual differences between model and lunar telescopic spectra are displayed in the adjacent figure.

closer to zero the better; **Table 5.1**). Average spectral correlation (b'' of 0.978), scale (b of 1.0; closer to 1.0 the better), and slope (Δm of 0.010) are well optimized. For spectral matches, differences that are not readily apparent in continuum removed or scaled reflectance are amplified in the residual difference plots displayed adjacent to each figure. Significant differences between measured and modeled FeO abundances (mean 0.98 wt%; max 5.2 wt%) are apparent for ~20 telescopic spectra and are the dominant reason for less precise goodness of fit values. Removing statistical contributions of spectra where modeling fails to match FeO abundance within 1 wt% improves the average goodness of fit value for the remaining models (~40) to 0.284. However, all fits show significant structure in the residuals indicating that either the optical constants of the mafic minerals, or the number of components, does not fully represent the spectra, some information is being lost in the fitting process.

Model Mineralogy Relative to Lunar Samples

Lunar Highlands and Mare Samples: Cahill and Lucey [2007] compiled modal mineralogy and basic chemistry (e.g., Mg') for each mineral constituent of approximately 100 lunar highland FAN and Mg-suite rocks. Here we report additional compositional data compiled for approximately 180 mare basalt analyses; however, only ~40 of these samples have literature reporting the relative proportions of low-Ca to high-Ca pyroxene and their corresponding Mg's that are used for comparison here (**Table B5.1; in Appendix B**). In **Figure 5.7**, lunar highlands rocks and mare basalts are directly compared in terms of modal mineralogy of the dominant silicate minerals (olivine, orthopyroxene, clinopyroxene, and plagioclase) on a modified version of Stöffler *et al.* [1980]'s lunar rock classification diagram. The majority of mare basalts have mineralogies more similar to gabbro and olivine-bearing noritic gabbro. A minor number of mare basalt samples also show modal mineralogies similar to noritic anorthosite, anorthositic norite, pyroxenite, and peridotite. Mare basalts are heavily laden with pyroxene (50-100 vol%) relative to most highland rocks, consisting dominantly of high-Ca pyroxene (30-70 vol%), significant proportions of low-Ca pyroxene (5-40 vol%), and olivine (0-55 vol%). Only olivine-bearing gabbroic norites and gabbros of the Mg-suite approach similar olivine and high-

Table 5.1: Measures of fit for telescopic spectra.

Region	Varying Mg'					Fixed Mg' 70				
	g	b''	b	ΔSlope	ΔFeO	g	b''	b	ΔSlope	ΔFeO
<u>Western Imbrium</u>										
Aristarchus Peak	0.298	0.981	1.001	0.000	0.0	0.400	0.974	1.000	0.000	0.0
Aristarchus Peak	0.783	0.979	1.000	0.022	3.6	0.467	0.973	1.000	0.000	0.4
Aristarchus Peak	0.925	0.974	0.999	0.035	4.2	0.574	0.973	1.000	0.001	1.5
Aristarchus Peak	0.747	0.981	0.999	0.017	3.9	0.469	0.981	1.000	0.000	1.6
Aristarchus East Wall	0.104	0.990	1.000	0.002	0.0	0.109	0.990	0.999	0.001	0.0
Aristarchus North Rim	0.058	0.994	1.000	0.002	0.0	0.078	0.992	1.000	0.001	0.0
Aristarchus North Wall	0.090	0.991	1.000	0.000	0.0	0.090	0.991	1.000	0.000	0.0
Aristarchus South Rim	0.434	0.977	0.997	0.002	0.7	0.408	0.974	1.000	0.001	0.0
Aristarchus South Wall	0.268	0.990	1.000	0.010	1.5	0.340	0.968	0.999	0.001	0.0
Aristarchus Southwest Wall	0.064	0.994	1.000	0.001	0.0	0.070	0.993	1.000	0.002	0.0
Aristarchus South Crater Floor	1.145	0.959	1.000	0.005	4.7	0.645	0.959	1.000	0.001	0.0
Aristarchus East Rim Object A	0.222	0.986	1.000	0.009	0.0	0.374	0.976	1.000	0.006	0.0
Aristarchus East Rim Object B	0.070	0.993	1.000	0.001	0.0	0.079	0.993	1.008	0.004	0.0
Aristarchus East Rim Object C	0.075	0.993	1.000	0.001	0.0	0.079	0.992	1.000	0.000	0.0
Aristarchus East Ejecta	0.087	0.992	1.000	0.003	0.0	0.094	0.991	1.000	0.004	0.0
Aristarchus Southeast Ejecta	0.129	0.989	1.000	0.000	0.0	0.112	0.991	1.000	0.000	0.0
Aristarchus A	0.065	0.994	0.999	0.000	0.0	0.057	0.994	1.000	0.000	0.0
Aristarchus Southern Ejecta B	0.072	0.993	1.001	0.000	0.0	0.083	0.992	1.000	0.000	0.0
Aristarchus Southern Ejecta C	0.081	0.992	1.000	0.000	0.0	0.116	0.988	1.000	0.000	0.0
Herodotus D	0.330	0.979	1.000	0.000	0.0	0.359	0.977	0.999	0.000	0.0
Herodotus X	0.667	0.983	1.000	0.045	3.1	0.866	0.947	1.000	0.001	0.4
<u>East/Southern Imbrium</u>										
<u>Eastern Imbrium</u>										
Aristillus Peak	0.247	0.984	1.000	0.001	0.0	0.247	0.984	1.000	0.001	0.0
<u>Southern Imbrium</u>										
Copernicus Peak	0.593	0.977	0.999	0.001	2.2	1.060	0.932	1.000	0.001	0.0
Copernicus Peak	0.158	0.989	1.000	0.000	0.3	0.529	0.976	1.000	0.001	2.4
<u>Southeastern Imbrium</u>										
Eratosthenes Peak	0.214	0.986	1.000	0.001	0.0	0.735	0.953	1.000	0.004	0.0
Apennine Front 1	0.865	0.962	1.000	0.005	2.5	0.915	0.943	1.000	0.000	0.3
Apennines 11	0.436	0.982	1.000	0.014	1.5	0.415	0.975	1.000	0.017	0.0
Apennines 10	0.063	0.994	1.000	0.000	0.0	0.073	0.993	1.000	0.000	0.0
Hadley Mountain	1.335	0.930	1.000	0.023	1.7	0.870	0.947	1.000	0.005	0.3
Aratus	0.291	0.986	1.000	0.001	0.9	0.304	0.986	1.000	0.001	1.0
Bancroft	0.331	0.985	0.996	0.000	0.9	0.257	0.984	0.999	0.001	0.0
Beer	1.013	0.971	1.000	0.002	5.3	0.659	0.961	1.000	0.000	0.5
Joy	0.466	0.983	1.000	0.029	0.3	0.447	0.979	1.000	0.019	0.1
Timocharis East Wall	0.294	0.981	1.000	0.000	0.0	0.373	0.976	0.998	0.001	0.0
<u>Western Oceanus Procellarum</u>										
Reiner K Crater	0.146	0.988	1.000	0.000	0.0	0.278	0.977	1.004	0.000	0.0

Table 5.1: Continued.

Region	Varying Mg'					Fixed Mg' 70				
	g	b''	b	ΔSlope	ΔFeO	g	b''	b	ΔSlope	ΔFeO
Eastern Nectaris										
Apollo 16 Bright Material	1.181	0.941	1.000	0.007	2.4	1.222	0.928	1.000	0.025	0.2
Bright Area South of Alfraganus	1.402	0.925	1.000	0.045	0.4	1.530	0.926	1.000	0.063	1.1
Kant East Wall	7.931	0.533	1.001	0.003	1.6	8.248	0.511	1.000	0.000	1.3
Fresh Massif	0.833	0.949	1.000	0.000	0.4	0.841	0.948	1.000	0.003	0.2
Plains East-Southeast of Isidorous D	0.927	0.949	1.000	0.061	0.0	0.909	0.942	0.998	0.000	0.0
Plains South of Capella M	0.681	0.965	1.000	0.002	1.3	0.820	0.962	1.000	0.000	2.2
Plains West of Gutenb eta	0.605	0.962	1.000	0.002	0.1	0.712	0.958	1.000	0.000	0.6
Tranquilitatis										
Plinius Peak	1.425	0.950	1.011	0.071	3.4	1.187	0.930	1.000	0.014	0.5
Nubium										
Bullialdus Peak	0.721	0.972	1.000	0.005	2.7	0.454	0.971	1.000	0.000	0.0
Arzachel Peak	0.263	0.983	1.000	0.000	0.0	0.275	0.983	1.000	0.000	0.0
Tycho Peak	0.230	0.983	1.000	0.054	0.3	0.317	0.982	1.000	0.017	1.3
Tycho Peak	0.141	0.991	1.000	0.002	0.0	0.167	0.990	1.000	0.007	0.0
Tycho Peak	0.141	0.991	1.000	0.005	0.0	0.278	0.990	1.000	0.041	0.0
Tycho Peak	0.212	0.987	1.000	0.001	0.8	0.136	0.987	1.000	0.001	0.0
Tycho Floor	0.297	0.986	0.999	0.000	0.7	0.302	0.986	1.000	0.000	0.8
Tycho Wall	0.169	0.988	1.000	0.007	0.3	0.169	0.988	1.000	0.007	0.3
Frigoris										
Hercules Dark Halo Crater	1.085	0.930	1.000	0.000	0.0	1.090	0.930	1.000	0.000	0.0
Gartner D	1.153	0.956	1.000	0.018	4.1	1.158	0.928	0.976	0.000	0.0
Baily K	0.045	0.996	1.000	0.001	0.0	0.078	0.994	1.000	0.015	0.0
Mare Frigoris East	0.090	0.991	0.999	0.001	0.0	0.090	0.991	0.999	0.001	0.0
Mare Frigoris East 3	0.238	0.986	1.001	0.007	0.0	0.324	0.980	1.000	0.003	0.0

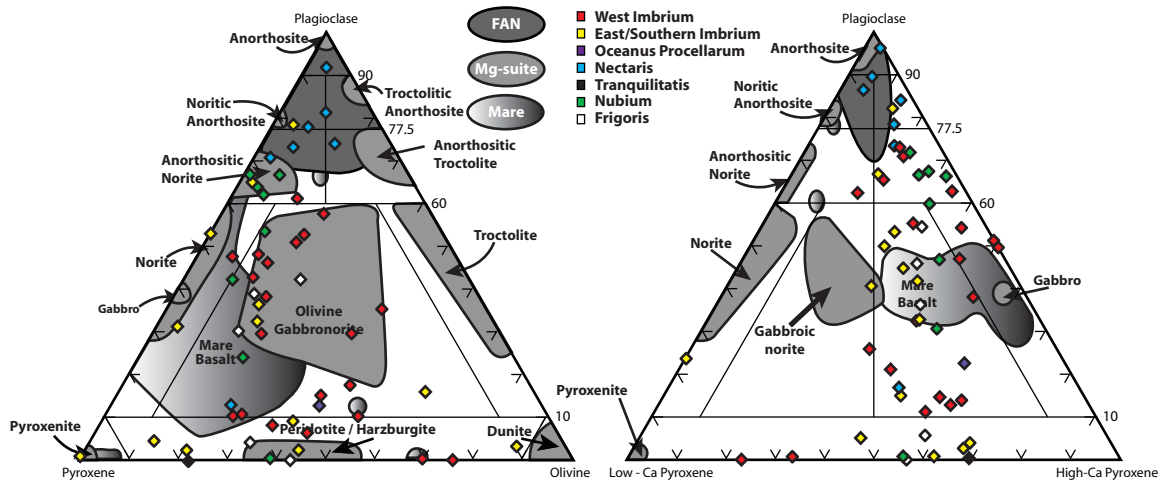


Figure 5.7: Model mineralogy of lunar telescopic spectra relative to the mineralogy of lunar highlands and mare rocks projected on the lunar rock classification system [Stöffler *et al.*, 1980].

Ca pyroxene abundances to that of mare basalts albeit at far higher Mg' and lower FeO content (**Fig. 5.8**).

Results

Model Composition: Model mineralogies of telescopic spectra are diverse. Approximately 20% of spectra modeled have anorthositic mineralogies similar to FAN and Mg-suite noritic anorthosites; however plagioclase abundance (60-93 vol%) and Mg' values (50-70) suggest greatest similarity to FAN rocks. The most anorthositic (70-93 vol% plagioclase) of these spectra are from deposits near Nectaris basin. Slightly less anorthositic (60-70 vol% plagioclase) deposits are modeled for deposits near Nubium and western Imbrium basins. These deposits have similar olivine abundances but are enriched with high-calcium pyroxene (17-29 vol%) relative to FAN and Mg-suite anorthositic norites.

The majority (~80%) of spectra are result in models with relatively mafic (e.g., >40 mafics) mineralogies that range in Mg' from 50-75 (**Fig. 5.8**). Although these are dominantly Imbrium materials, deposits near Nubium, Oceanus Procellarum, Tranquilitatis, and Frigoris basins are also represented here. While some of these have olivine abundances similar to olivine bearing gabbro-norites almost all of them are also characterized with elevated (60-80 vol%) high-calcium pyroxene abundances more similar to Mg-suite gabbro and mare basalts. A sizable percentage (~25%) of these spectra are also modeled with ultramafic and magnesian compositions (Mg' ranging from 80-95) more similar to peridotites, harzburgites, pyroxenites, and dunitites of the lunar Mg-suite. Modeled mineralogies of these spectra are relatively consistent with previous subjective interpretations of the minerals present for each spectrum (**Table 5.2**). However, the correlation between model Mg' and plagioclase abundance suggest that Mg' is possibly not being leveraged relative to FeO accurately. Although measures of spectral fit are good, nearly all telescopic spectra models with highly magnesian Mg' values (90-95) also underestimate FeO usually in more feldspathic (5-9 wt% FeO) lunar regions (**Table 5.2; Fig. 5.9**). Lunar rock and soil FeO abundance is anticorrelated with Al₂O₃ and plagioclase abundance [Lucey *et al.*, 2006]. Here, nearly all models of telescopic spectra with magnesian Mg' values fall off of this trend in

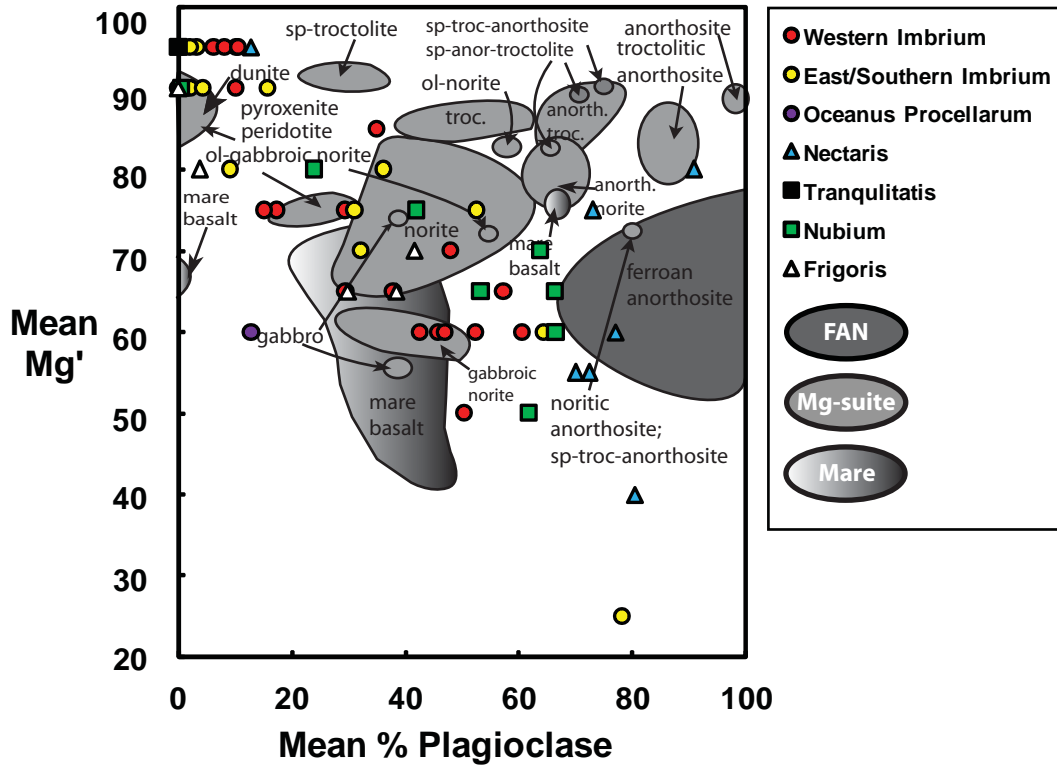


Figure 5.8: Mg' relative to plagioclase abundance of modeled telescopic spectra and lunar highlands and mare rocks.

Table 5.2. Model mineralogy determined from lunar telescopic spectra.

Region	%Ol	δ	%Opx	δ	%Cpx	δ	%Pl	δ	Mg ¹	FeO _{model}	FeO _{usr}	ΔFeO	This Study	Previous	Rock-Type	Reference
Western Imbrium																
Aristarchus Peak	51	0.3	18	0.1	21	0.6	10	0.3	90	7.0	7.0	0.0	Ol-Noritic Gabbro	Aug. Ol, Felds; Troctolite; Gabbro		Lucey et al. 1986; Pieters, 1986
Aristarchus Peak	43	8.5	20	0.3	31	7.1	6	1.8	95	3.4	7.0	-3.6	Peridotite	Aug. Ol, Felds; Troctolite; Gabbro		Lucey et al. 1986; Pieters, 1986
Aristarchus Peak	26	3.8	19	0.1	45	2.2	10	2.1	95	2.8	7.0	-4.2	Ol-Noritic Gabbro	Aug. Ol, Felds; Troctolite; Gabbro		Lucey et al. 1986; Pieters, 1986
Aristarchus Peak	35	12.1	19	0.2	39	8.9	8	3.3	95	3.1	7.0	-3.9	Peridotite	Aug. Ol, Felds; Troctolite; Gabbro		Lucey et al. 1986; Pieters, 1986
Aristarchus East Wall	21	0.2	7	0.1	15	0.8	57	0.5	65	9.9	9.9	0.0	Ol-Noritic Gabbro	Aug. Ol, Felds; Gabb-Anor		Lucey et al. 1986; Pieters, 1996
Aristarchus North Rim	19	0.2	13	0.4	15	1.0	52	0.5	60	12.2	12.2	0.0	Ol-Noritic Gabbro	Gabb-Anor		Lucey et al. 1986; Pieters, 1986
Aristarchus North Wall	12	0.4	13	0.1	27	1.4	48	0.9	70	8.7	8.7	0.0	Ol-Noritic Gabbro	Troctolite		Lucey et al. 1986; Pieters, 1986
Aristarchus South Rim	44	6.0	13	0.7	9	2.4	35	4.3	85	8.2	8.9	-0.7	Ol-Gabbroic Norite			Lucey et al. 1986; Pieters, 1986
Aristarchus South Wall	75	2.5	19	0.4	6	2.9	0	0.0	90	8.9	10.4	-1.5	Peridotite			Lucey et al. 1986; Pieters, 1986
Aristarchus Southwest Wall	14	0.6	8	0.7	18	2.9	61	1.7	60	9.3	9.3	0.0	Anor-Nor	Feldspar, Augite; Gabb-Anor		Lucey et al. 1986; Pieters, 1986
Aristarchus South Crater Floor	28	4.3	21	0.1	41	2.7	11	1.5	95	2.9	7.6	-4.7	Ol-Noritic Gabbro	Augite, Olivine, Feldspar		Lucey et al. 1986
Aristarchus East Rim Object A	19	0.3	3	1.2	28	2.4	50	1.3	50	13.3	13.3	0.0	Ol-Noritic Gabbro			Lucey et al. 1986
Aristarchus East Rim Object B	15	0.5	5	0.9	35	2.8	46	1.6	60	11.0	11.0	0.0	Ol-Noritic Gabbro			Lucey et al. 1986
Aristarchus East Rim Object C	22	0.9	9	0.7	40	4.0	29	2.4	65	13.4	13.4	0.0	Ol-Noritic Gabbro			Lucey et al. 1986
Aristarchus East Ejecta	46	0.6	14	0.5	23	3.0	17	1.9	75	14.8	14.8	0.0	Ol-Noritic Gabbro			Lucey et al. 1986
Aristarchus Southeast Ejecta	19	1.0	8	0.6	36	4.2	38	2.6	65	11.7	11.7	0.0	Ol-Noritic Gabbro	Feldspar, Augite		Lucey et al. 1986
Aristarchus A	40	0.4	14	0.5	16	2.3	29	1.4	75	13.1	13.1	0.0	Ol-Noritic Gabbro			Lucey et al. 1986
Aristarchus Southern Ejecta B	7	0.2	0	0.5	45	0.5	47	0.2	60	8.6	8.6	0.0	Gabbro			Lucey et al. 1986
Aristarchus Southern Ejecta C	14	0.1	0	0.2	44	0.1	43	0.0	60	10.5	10.5	0.0	Gabbro	Mare basalt		Lucey et al. 1986
Herodotus D	41	0.3	22	0.2	21	1.4	15	0.9	75	15.0	15.0	0.0	Ol-Gabbroic Norite	Olivine, Feldspar		Lucey et al. 1986
Herodotus X	69	5.2	21	0.0	10	4.8	0	0.4	95	4.3	7.4	-3.1	Peridotite			Lucey et al. 1986
East/Southern Imbrium																
Eastern Imbrium																
Aristillus Peak	20	0.2	25	0.3	23	0.3	32	0.2	70	12.7	12.7	0.0	Ol-Gabbroic Norite	Noritic		Pieters, 1986
Southern Imbrium																
Copernicus Peak	86	0.4	10	0.2	0	0.0	3	0.2	95	4.7	6.9	-2.2	Peridotite	Troctolite		Pieters, 1986
Copernicus Peak	62	2.5	8	0.4	15	2.9	16	0.1	90	7.2	6.9	0.3	Ol-Noritic Gabbro	Troctolite		Pieters, 1986
Southeastern Imbrium																
Eratosthenes Peak	43	0.2	16	0.6	38	2.2	2	1.4	90	6.6	6.6	0.0	Peridotite	Gabbroic		Pieters, 1986
Apennine Front 1	0	0.0	38	0.5	62	0.7	1	1.1	95	2.4	4.9	-2.5	Pyroxenite	Anor-Norite		Spudis et al., 1987
Apennines 11	13	2.2	44	0.7	39	1.7	4	2.4	90	5.6	7.1	-1.5	Pyroxenite	Norite		Spudis et al., 1987
Apennines 10	3	1.5	16	0.5	17	3.4	64	2.3	60	7.4	7.4	0.0	Anor-Gabbro	Norite		Spudis et al., 1987
Hadley Mountain	4	1.3	5	3.0	12	6.1	78	4.3	25	7.7	6.0	1.7	Gabbroic-Anor	Anor-Norite; Norite		Spudis et al., 1987; Pieters, 1986
Aratus	0	0.0	20	0.2	28	0.4	53	0.2	75	5.8	4.9	0.9	Noritic Gabbro	Noritic; Norite		Pieters, 1986; Spudis et al., 1987
Bancroft	18	2.1	18	1.0	28	1.6	36	4.6	80	7.9	8.8	-0.9	Ol-Noritic Gabbro			Spudis et al., 1987
Beer	21	0.9	25	0.1	53	0.8	2	0.2	95	2.8	8.1	-5.3	Peridotite	KREEP basalt		Spudis et al., 1987
Joy	4	2.7	23	1.6	41	10.6	31	7.6	75	8.4	8.7	-0.3	Noritic Gabbro	Noritic; Norite		Pieters, 1986; Spudis et al., 1987
Timocharis East Wall	39	0.9	23	0.3	29	2.6	9	1.8	80	12.3	12.3	0.0	Peridotite	Noritic Gabbro or Gabbroic Norite		Spudis et al., 1987
Western Oceanus Procellarum																
Reiner K Crater	42	0.5	12	0.7	33	2.6	13	1.5	60	21.9	21.9	0.0	Ol-Noritic Gabbro			

Table 5.2: Continued.

Region	%Ol	δ	%Opx	δ	%Cpx	δ	%Pl	δ	Mg ¹	FeO _{model}	FeO _{SR}	ΔFeO	This Study	Previous	Rock-Type	Reference
Eastern Nectaris																
Apollo 16 Bright Material	24	9.4	28	1.1	35	5.0	13	5.4	95	2.9	5.3	-2.4	Ol-Noritic Gabbro	Anorthositic		Spudis et al. 1989
Bright Area South of Alfraganus	15	2.2	8	1.1	4	0.7	73	4.0	75	5.4	4.9	0.4	Troctolitic-Anor	Anorthositic		Spudis et al. 1989
Kant East Wall	5	1	1	0	3	0	91	2	80	1.5	3.1	-1.6	Anorthosite	Anorthositic		Spudis et al. 1989
Fresh Massif	8	1.1	3	0.6	12	1.5	77	1.8	60	5.2	4.8	0.4	Gabbroic-Anor	Anorthositic		Spudis et al. 1989
Plains East-Southeast of Isidorous D	9	0.0	6	0.4	4	0.7	80	0.4	40	7.7	7.7	0.0	Gabbroic-Anor	Anorthositic		Spudis et al. 1989
Plains South of Capella M	4	1.2	9	1.0	17	0.9	70	2.3	55	6.7	8.0	-1.3	Gabbroic-Anor	Anorthositic		Spudis et al. 1989
Plains West of Gutenberg eta	7	1.1	6	0.9	14	3.6	72	2.5	55	6.8	7.0	-0.1	Gabbroic-Anor	Anorthositic		Spudis et al. 1989
Tranquillitatis																
Plinius Peak	23	2.6	24	0.1	54	2.7	0	0.0	95	2.8	6.2	-3.4	Peridotite	Gabbroic		Pieters, 1986
Nubium																
Bullialdus Peak	38	3.6	27	0.5	34	3.2	0	1.0	90	6.7	9.4	-2.7	Peridotite	Gabbroic		Pieters, 1986
Arzachel Peak	7	0.8	7	0.5	20	3.1	67	1.9	60	6.9	6.9	0.0	Anor-Gabbro	Noritic		Pieters, 1986
Tycho Peak	21	0.9	17	0.3	38	1.5	24	0.3	80	8.9	8.5	0.3	Ol-Noritic Gabbro	Gabbro		Pieters, 1986; Lucey et al. 1987
Tycho Peak	11	0.1	8	0.3	28	0.6	53	0.3	65	8.5	8.5	0.0	Ol-Noritic Gabbro	Gabbro		Pieters, 1986; Lucey et al. 1987
Tycho Peak	10	0.5	12	0.2	36	1.7	42	1.1	75	7.5	7.5	0.0	Ol-Noritic Gabbro	Gabbro		Pieters, 1986; Lucey et al. 1987
Tycho Peak	6	0.6	3	0.6	29	1.1	62	0.3	50	8.3	7.5	0.8	Anor-Gabbro	Gabbro		Pieters, 1986; Lucey et al. 1987
Tycho Floor	1	0.8	5	0.4	27	1.8	66	2.2	65	4.8	5.6	-0.7	Anor-Gabbro			Lucey et al. 1987
Tycho Wall	4	0.8	7	0.5	25	2.4	64	2.8	70	5.2	5.5	-0.3	Anor-Gabbro	Gabb-Anor		Pieters, 1986; Lucey et al. 1987
Frigoris																
Hercules Dark Halo Crater	16	0.0	15	0.1	30	0.2	38	0.1	65	12.0	12.0	0.0	Ol-Noritic Gabbro			Hawke et al. 2008
Gartner D	42	0.9	25	0.3	33	1.2	0	0.0	90	6.9	11.0	-4.1	Peridotite			Hawke et al. 2008
Baily K	17	2.1	18	0.3	35	5.3	30	3.6	65	13.5	13.5	0.0	Ol-Noritic Gabbro			Hawke et al. 2008
Mare Frigoris East	24	0.5	10	0.2	25	1.6	42	1.0	70	11.0	11.0	0.0	Ol-Noritic Gabbro			Hawke et al. 2008
Mare Frigoris East 3	33	0.4	25	0.2	39	1.2	4	0.6	80	12.0	12.0	0.0	Peridotite			Hawke et al. 2008

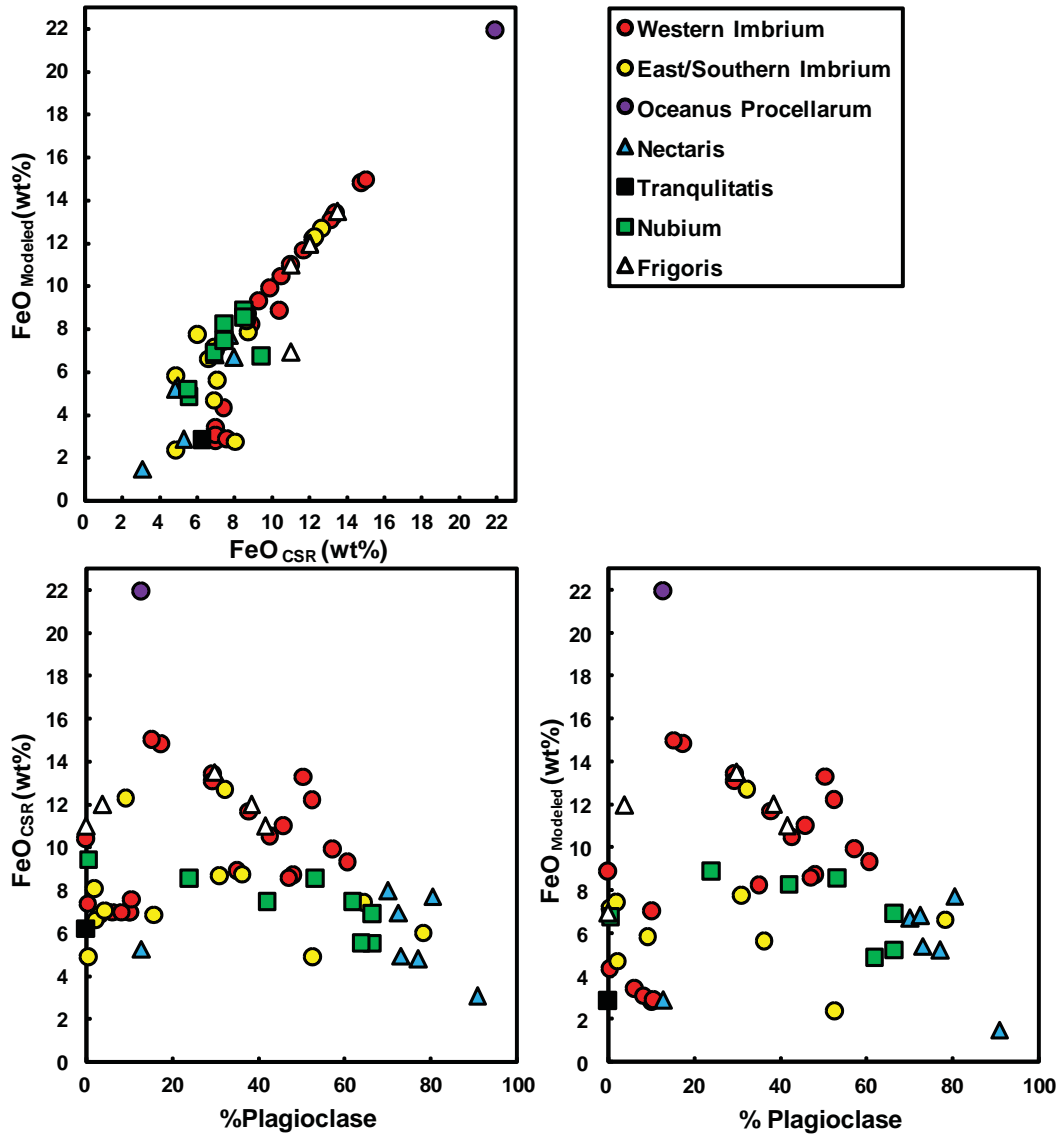


Figure 5.9: Model FeO relative to plagioclase abundance.

highly mafic (>80 vol%) assemblages (**Fig. 5.8**). This suspicious anticorrelation of Mg' and plagioclase abundance suggests that the algorithm is sacrificing the quality of the spectral fit in order to simultaneously match the band depth and FeO content.

Modeling at a Fixed Mg'

Acknowledging this potential problem modeling Mg' accurately may exist, we chose to also model telescopic spectra at a fixed Mg' of 70 roughly consistent with the average reported Mg' of Lunar Prospector [*Prettyman et al., 2002; Prettyman et al., 2006*]. Resulting goodness of fit values are virtually identical (average $g = 0.595$) to previous modeling. However, differences are apparent with model estimates of FeO abundance showing better agreement with those measured from Clementine (mean $\Delta\text{FeO} = 0.31$; **Fig. 5.10**), and slightly less accurate values for spectral correlation (mean $b'' = 0.964$). The similarity in goodness of fit for variable relative to fixed Mg' models is not unexpected as most (~40) telescopic spectra models estimate Mg' values near 70 already (mean Mg' 68). However, model mineralogy is less compositionally diverse, with telescopic spectra showing fewer ultramafic mineralogies. Plagioclase abundance increases significantly for nearly all previously ultramafic models (**Fig. 5.11; Table 5.3**). Western Imbrium (e.g., Aristarchus plateau) is dominantly consistent with an olivine-bearing gabbro-norites, but with much less low-Ca pyroxene than rocks of the lunar highlands. Some of these spectra have modeled mineralogies similar to mare basalts of the lunar sample suite. Nectaris basin spectra are still consistent with lunar highland anorthositic norite and anorthositic troctolite FANs but with slightly less plagioclase. East/Southern Imbrium (Hadley-Apennine mountains) and Nubium basin is less compositionally diverse (with the exception of Timocharis east wall peridotite) roughly ranging from anorthositic norite to olivine-bearing gabbro-norite. Frigoris basin spectra are consistent with olivine-bearing gabbro-norite.

Discussion

Model Performance: The algorithm presented determines composition using a relationship between the correlation of modeled and measured spectra relative to Mg'. In principle mafic mineral Mg' and FeO abundance change their representative reflectance spectra will also change

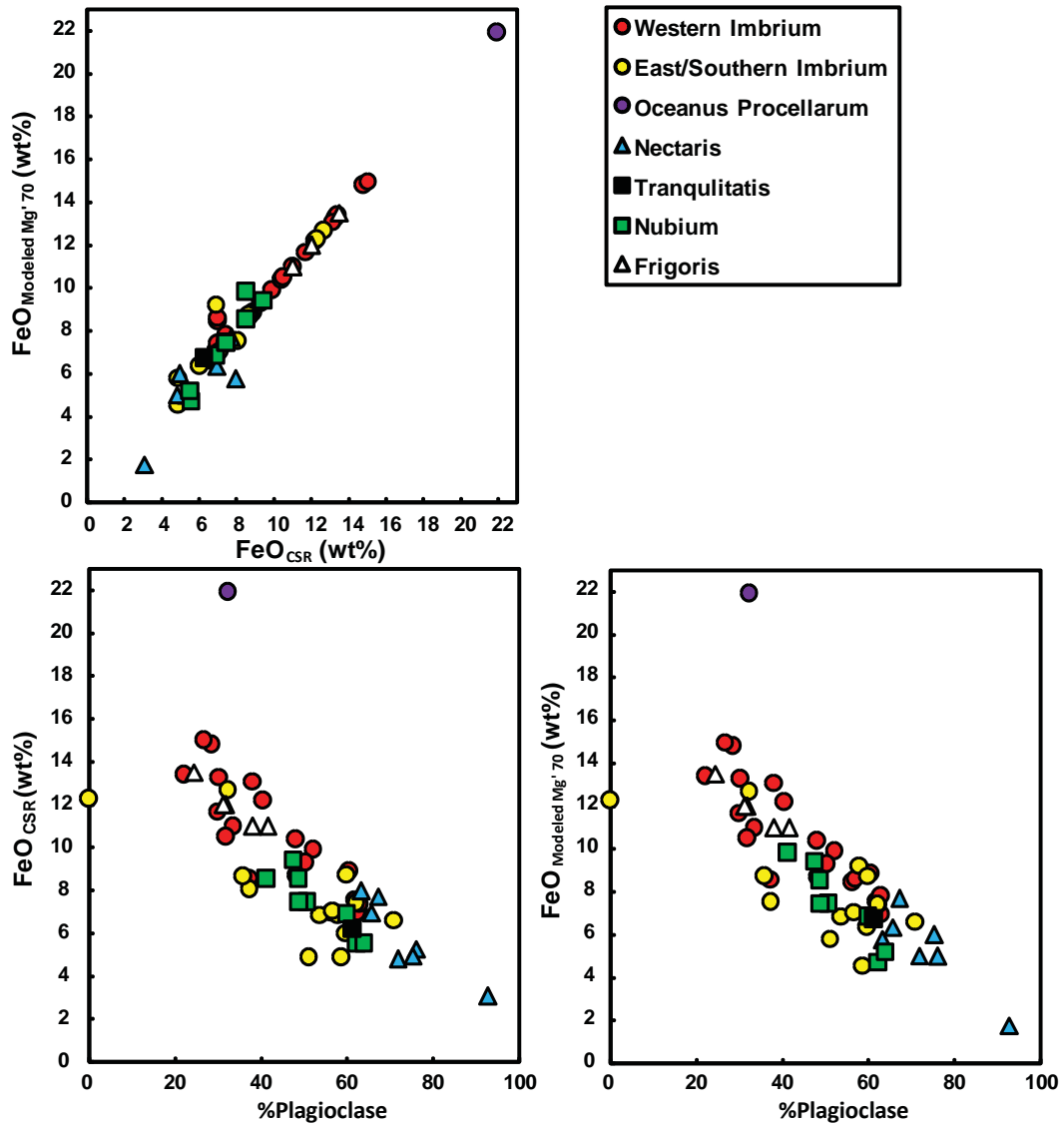


Figure 5.10: Model FeO relative to plagioclase abundance at a fixed Mg' of 70.

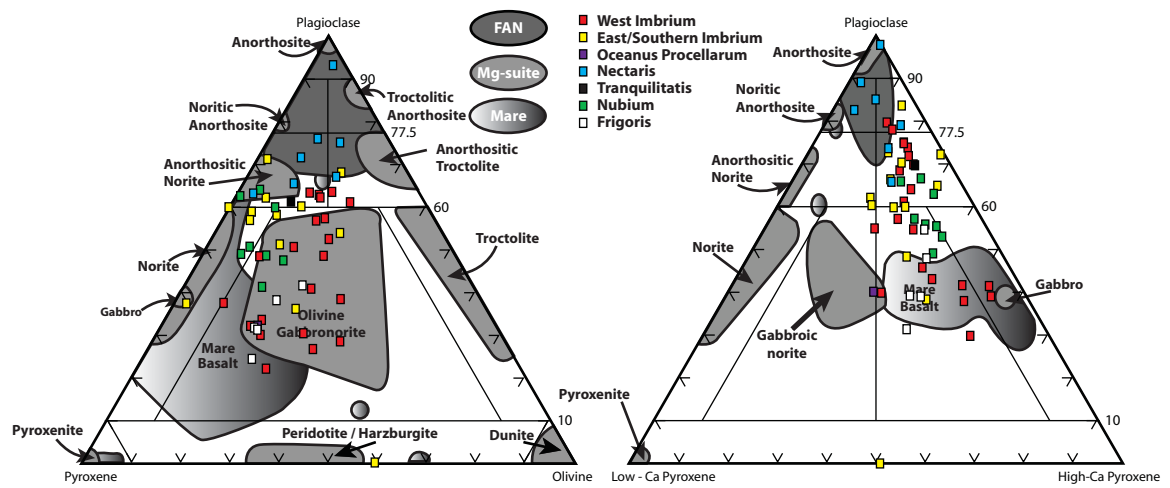


Figure 5.11: Model mineralogy of lunar telescopic spectra at a fixed Mg' of 70 relative to the mineralogy of lunar highlands and mare rocks projected on the lunar rock classification system [Stöffler et al., 1980].

Table 5.3: Model mineralogy determined from lunar telescopic spectra at a fixed Mg' of 70.

File	%Ol	δ	%Opx	δ	%Cpx	δ	%Pl	δ	Mg'	FeO _{model}	FeO _{csr}	ΔFeO	This Study	Rock-Type Previous	Reference
Western Imbrium															
Aristarchus Peak	15	0.2	6	0.2	17	0.6	63	0.4	70	7.0	7.0	0.0	Anor-Gabbro	Aug, Ol, Felds; Troctolite; Gabbro	Lucey et al. 1986; Pieters, 1986
Aristarchus Peak	17	2.0	6	0.7	15	1.8	62	2.0	70	7.4	7.0	0.4	Anor-Gabbro	Aug, Ol, Felds; Troctolite; Gabbro	Lucey et al. 1986; Pieters, 1986
Aristarchus Peak	19	1.6	6	0.4	18	2.3	56	3.2	70	8.5	7.0	1.5	Ol-Noritic Gabbro	Aug, Ol, Felds; Troctolite; Gabbro	Lucey et al. 1986; Pieters, 1986
Aristarchus Peak	21	2.3	6	0.5	17	1.1	57	2.9	70	8.6	7.0	1.6	Ol-Noritic Gabbro	Aug, Ol, Felds; Troctolite; Gabbro	Lucey et al. 1986; Pieters, 1986
Aristarchus East Wall	24	0.2	8	0.2	16	1.1	52	0.7	70	9.9	9.9	0.0	Ol-Noritic Gabbro	Aug, Ol, Felds; Gabb-Anor	Lucey et al. 1986; Pieters, 1996
Aristarchus North Rim	26	0.4	17	0.3	17	1.1	40	0.7	70	12.2	12.2	0.0	Ol-Gabbroic Norite	Gabb-Anor	Pieters, 1996
Aristarchus North Wall	12	0.4	13	0.1	27	1.4	48	0.9	70	8.7	8.7	0.0	Ol-Noritic Gabbro	Troctolite	Lucey et al. 1986; Pieters, 1986
Aristarchus South Rim	24	0.9	6	0.3	10	1.3	60	0.4	70	8.9	8.9	0.0	Anor-Troctolite	Troctolite	Lucey et al. 1986; Pieters, 1986
Aristarchus South Wall	25	0.3	8	0.4	19	1.5	48	0.9	70	10.4	10.4	0.0	Ol-Noritic Gabbro	Feldspar, Augite; Gabb-Anor	Lucey et al. 1986; Pieters, 1986
Aristarchus Southwest Wall	18	0.3	11	0.2	21	1.3	50	0.8	70	9.3	9.3	0.0	Ol-Noritic Gabbro	Feldspar, Augite; Gabb-Anor	Lucey et al. 1986; Pieters, 1986
Aristarchus South Crater Floor	17	0.1	6	0.2	15	0.8	62	0.5	70	7.6	7.6	0.0	Anor-Gabbro	Augite, Olivine, Feldspar	Lucey et al. 1986
Aristarchus East Rim Object A	30	0.7	12	0.2	28	2.4	30	1.6	70	13.3	13.3	0.0	Ol-Noritic Gabbro	Troctolite	Lucey et al. 1986
Aristarchus East Rim Object B	20	0.4	9	0.6	37	1.7	33	1.0	70	11.0	11.0	0.0	Ol-Noritic Gabbro	Troctolite	Lucey et al. 1986
Aristarchus East Rim Object C	26	0.7	12	0.6	40	3.0	22	1.9	70	13.4	13.4	0.0	Ol-Noritic Gabbro	Troctolite	Lucey et al. 1986
Aristarchus East Ejecta	38	0.5	11	0.4	23	1.9	28	1.2	70	14.8	14.8	0.0	Ol-Noritic Gabbro	Troctolite	Lucey et al. 1986
Aristarchus Southeast Ejecta	21	0.5	10	0.2	38	1.7	30	1.1	70	11.7	11.7	0.0	Ol-Noritic Gabbro	Troctolite	Lucey et al. 1986
Aristarchus A	33	0.2	11	0.1	17	0.3	38	0.2	70	13.1	13.1	0.0	Ol-Noritic Gabbro	Troctolite	Lucey et al. 1986
Aristarchus Southern Ejecta B	10	0.2	6	0.4	47	0.2	37	0.1	70	8.6	8.6	0.0	Ol-Noritic Gabbro	Troctolite	Lucey et al. 1986
Aristarchus Southern Ejecta C	18	0.4	6	0.4	44	1.4	32	0.9	70	10.5	10.5	0.0	Ol-Noritic Gabbro	Troctolite	Lucey et al. 1986
Herodotus D	33	0.2	19	0.2	21	0.8	27	0.4	70	15.0	15.0	0.0	Ol-Noritic Gabbro	Troctolite	Lucey et al. 1986
Herodotus X	19	0.7	6	0.3	12	0.9	63	0.4	70	7.8	7.4	0.4	Anor-Troctolite	Troctolite	Lucey et al. 1986
East/Southern Imbrium															
Eastern Imbrium															
Aristillus Peak	20	0.2	25	0.3	23	0.3	32	0.2	70	12.7	12.7	0.0	Ol-Gabbroic Norite	Noritic	Pieters, 1986
Southern Imbrium															
Copernicus Peak	26	0.8	1	0.3	20	1.4	54	1.1	70	6.9	6.9	0.0	Ol-Noritic Gabbro	Troctolite	Pieters, 1986
Copernicus Peak	11	0.6	5	0.4	27	2.4	58	1.5	70	9.2	6.9	2.4	Ol-Noritic Gabbro	Troctolite	Pieters, 1986
Southeastern Imbrium															
Eratothene Peak	2	1.0	11	0.8	16	0.7	71	1.9	70	6.6	6.6	0.0	Anor-Gabbro	Gabbroic	Pieters, 1986
Apennine Front 1	5	0.6	19	0.3	17	1.2	59	0.8	70	4.6	4.9	-0.3	Noritic Gabbro	Anor-Norite	Spudis et al., 1987
Apennines 11	6	1.1	20	0.5	18	2.3	57	1.5	70	7.1	7.1	0.0	Gabbroic Norite	Norite	Spudis et al., 1987
Apennines 10	6	1.4	13	0.9	19	1.7	62	0.9	70	7.4	7.4	0.0	Anor-Gabbro	Norite	Spudis et al., 1987
Hadley Mountain	0	0.0	17	0.3	24	0.6	60	0.3	70	6.4	6.0	0.3	Anor-Gabbro	Anor-Norite; Norite	Spudis et al., 1987; Pieters, 1986
Aratus	15	0.8	12	0.1	22	2.3	51	1.5	70	5.8	4.9	1.0	Ol-Noritic Gabbro	Noritic; Norite	Pieters, 1986; Spudis et al., 1987
Bancroft	15	1.3	8	0.5	17	1.2	60	1.9	70	8.8	8.8	0.0	Anor-Gabbro	-	Spudis et al., 1987
Beer	3	2.5	20	2.1	40	12.8	37	8.4	70	7.5	8.1	-0.5	Noritic Gabbro	KREEP basalt	Spudis et al., 1987
Joy	25	0.8	15	0.2	24	1.8	36	1.3	70	8.8	8.7	0.1	Ol-Noritic Gabbro	Noritic; Norite	Pieters, 1986; Spudis et al., 1987
Timocharis East Wall	59	0.1	20	0.2	21	0.1	0	0.0	70	12.3	12.3	0.0	Peridotite	Noritic Gabbro or Gabbroic Norite	Spudis et al., 1987
Western Oceanus Procellarum															
Reiner K Crater	20	0.2	25	0.3	23	0.3	32	0.2	70	21.9	21.9	0.0	Ol-Gabbroic Norite	Ol-Gabbroic Norite	

Table 5.3: Continued.

Region	%Ol	δ	%Opx	δ	%Cpx	δ	%Pl	δ	Mg	FeO _{model}	FeO _{csr}	Δ FeO	This Study	Previous	Rock-Type	Reference
Eastern Nectaris																
Apollo 16 Bright Material	10	0.7	7	0.4	7	0.3	76	1.3	70	5.0	5.3	-0.2	Anor-Norite	Anorthositic		Spudis et al. 1989
Bright Area South of Alfraganus	15	4.9	7	2.0	2	1.4	75	5.5	70	6.0	4.9	1.1	Anor-Troctolite	Anorthositic		Spudis et al. 1989
Kant East Wall	4	0.9	1	0.2	2	0.3	93	1	70	1.8	3.1	-1.3	Anorthosite	Anorthositic		Spudis et al. 1989
Fresh Massif	9	1.0	5	0.5	14	2.6	72	2.2	70	5.0	4.8	0.2	Anor-Gabbro	Anorthositic		Spudis et al. 1989
Plains East-Southeast of Isidorous D	18	0.1	11	0.1	4	0.3	67	0.2	70	7.7	7.7	0.0	Anor-Troctolite	Anorthositic		Spudis et al. 1989
Plains South of Capella M	3	1.5	14	0.8	20	1.7	63	1.9	70	5.8	8.0	-2.2	Anor-Gabbro	Anorthositic		Spudis et al. 1989
Plains West of Gutenb eta	10	3.0	10	1.6	14	2.3	66	4.6	70	6.4	7.0	-0.6	Anor-Gabbro	Anorthositic		Spudis et al. 1989
Tranquillitatis																
Plinius Peak	12	1.6	7	0.7	20	3.2	61	5.0	70	6.7	6.2	0.5	Anor-Gabbro	Gabbroic		Pieters, 1986
Nubium																
Bullialdus Peak	17	0.1	11	0.2	24	0.2	47	0.1	70	9.4	9.4	0.0	Ol-Noritic Gabbro	Gabbroic		Pieters, 1986
Azachel Peak	9	0.6	11	0.6	20	2.1	60	1.5	70	6.9	6.9	0.0	Anor-Gabbro	Noritic		Pieters, 1986
Tycho Peak	16	2.5	12	1.1	31	2.2	41	2.0	70	9.8	8.5	1.3	Ol-Noritic Gabbro	Gabbro		Pieters, 1986; Lucey et al. 1987
Tycho Peak	13	0.3	11	0.4	28	0.6	49	0.4	70	8.5	8.5	0.0	Ol-Noritic Gabbro	Gabbro		Pieters, 1986; Lucey et al. 1987
Tycho Peak	9	0.3	9	0.3	31	0.4	51	0.3	70	7.5	7.5	0.0	Noritic Gabbro	Gabbro		Pieters, 1986; Lucey et al. 1987
Tycho Peak	8	0.1	9	0.2	34	0.1	49	0.1	70	7.5	7.5	0.0	Noritic Gabbro	Gabbro		Pieters, 1986; Lucey et al. 1987
Tycho Floor	1	0.8	7	0.3	30	1.0	62	1.8	70	4.7	5.6	-0.8	Anor-Gabbro	Gabbro		Lucey et al. 1987
Tycho Wall	4	0.8	7	0.5	25	2.4	64	2.8	70	5.2	5.5	-0.3	Anor-Gabbro	Gabb-Anor		Pieters, 1986; Lucey et al. 1987
Frigoris																
Hercules Dark Halo Crater	19	0.1	19	0.3	30	0.2	32	0.1	70	12.0	12.0	0.0	Ol-Noritic Gabbro			Hawke et al. 2008
Gartner D	20	0.5	13	0.2	29	1.4	38	0.9	70	11.0	11.0	0.0	Ol-Noritic Gabbro			Hawke et al. 2008
Baily K	22	2.1	22	0.6	32	4.8	24	3.4	70	13.5	13.5	0.0	Ol-Noritic Gabbro			Hawke et al. 2008
Mare Frigoris East	24	0.5	10	0.2	25	1.6	42	1.0	70	11.0	11.0	0.0	Ol-Noritic Gabbro			Hawke et al. 2008
Mare Frigoris East 3	20	0.6	17	0.3	32	1.2	31	0.8	70	12.0	12.0	0.0	Ol-Noritic Gabbro			Hawke et al. 2008

in a systematically. This approach is similar in principle to the Modified Gaussian modeling (MGM) algorithm being tested to measure Mg' by *Isaacson et al.* [2008] where these systematic changes in spectra are tracked to infer composition. *Cahill et al.* [2010a] shows the radiative transfer used to model lunar soil spectra often compute inaccurate results as lunar soil Mg's approach more ferroan compositions. *Cahill et al.* [2010a] cited a lack of optical constants for more ferroan Mg' mafic minerals as a potential flaw in the modeling. Here, because most of the lunar highlands is reported to have an average Mg' of ~70 [*Prettyman et al.*, 2002; *Prettyman et al.*, 2006] we believed an application of our algorithm to telescopic spectra would be successful. The results presented here suggest additional problems exist.

Lunar soil Mg's are confined between 50 to 75 and do not test the accuracy of more magnesian derived compositions either. The poorly correlated trend reported by *Cahill et al.* [2010a] also suggested modeling may overestimate Mg' for more magnesian mineral mixtures (Mg' >75) as well; but no lunar soils are available to confirm this. Here the same algorithm appears to do just that, matching unknown and model spectra well but likely overestimating Mg' of many telescopic spectra. The main source of error here is the algorithm fails to match FeO abundance estimates of ~20 telescopic spectra even though spectral matches are achieved. This results in models with ultramafic assemblages and highly magnesian Mg' (90-95). Although assemblages with dominantly mafic mineralogy may increase the possibility that magnesian mafic minerals are present it does not guarantee it. Both magnesian anorthosites as well as ferroan mafic assemblages are hypothesized if not already known to exist on the Moon [*Cahill et al.*, 2009; *Korotev*, 2005a; *Shearer et al.*, 2006; *Warren*, 2005; *Wieczorek et al.*, 2006].

These mismatches, coupled with the undulated residuals, suggest that the shapes of the spectra of the mineral components are not sufficiently consistent with the shapes of the lunar minerals on the surface and in the soils to meaningfully extract Mg'. This strongly suggests that the current set of optical constants is not representing the spectral properties of the components minerals adequately, especially pyroxene, since this is the spectrally dominant mineral (owing to the combination of relatively high abundance and strong spectral features).

Another potential source of error is missing model mineral components. This model considers the dominant mafic silicates (olivine, clinopyroxene, and orthopyroxene) since they are the only ones known to show systematic variations in reflectance as a function of FeO content and Mg'. Thus each unknown spectrum's Mg' only reflects the mafic silicates and not the whole assemblage of minerals. A simple comparison of lunar soil average pyroxene and olivine Mg' relative to bulk chemistry Mg' shows that this relationship is not highly correlated (**Fig. 5.12a**).

Low- and high-TiO₂ mare soils show significantly higher Mg' values (mean 9 units; max 15 units higher) relative to bulk chemistry. Mare basalts show even larger differences (25 or 30 units) between the average Mg' of mafic minerals relative to bulk chemistry. Highland soils, which have little to no ilmenite, also have higher mafic mineral Mg's (average 2 units; max 5 units higher) than bulk chemistry. Mean Mg' of lunar soil pyroxene, olivine, and ilmenite relative to bulk chemistry suggests ilmenite may be a significant source of FeO that is not accounted for in our modeling (**Fig. 5.12b**). Although not perfect, this relationship is highly correlated for both highland (mean difference 1 units; and ranging from 0-4 units) and mare soils (mean difference 2 units; and ranging from 0-5 units). The answer is to add ilmenite as a model component however, ilmenite has few if no diagnostic absorption features to easily identify and help determine modal proportions. A possible solution to this is to also use an FeO estimate algorithm that takes into account the contribution of FeO from ilmenite, such as *Le Mouélic et al.* [2000; 2002]. Despite the potential and initial favorable results of this algorithm (e.g., [*Cahill et al.*, 2007; *Le Mouélic et al.*, 2000; *Le Mouélic et al.*, 2002]) it has yet to be fully tested on a global lunar scale and on steeper surface slopes.

Modeling Implications: Analysis of modeling telescopic spectra at fixed and variable Mg' values suggests aspects of each are useful for determination of lunar surface composition. While a significant number (~20) of models overestimate Mg', underestimate FeO (mean Δ FeO of 2.8 and max of 5.2 wt%) the majority of models (~40) have high quality goodness of fit values (mean g of 0.284) and match FeO abundance accurately (mean Δ FeO of 0.16). This suggests the majority of telescopic spectra are modeled effectively when allowing Mg' to vary and this is reflected in the

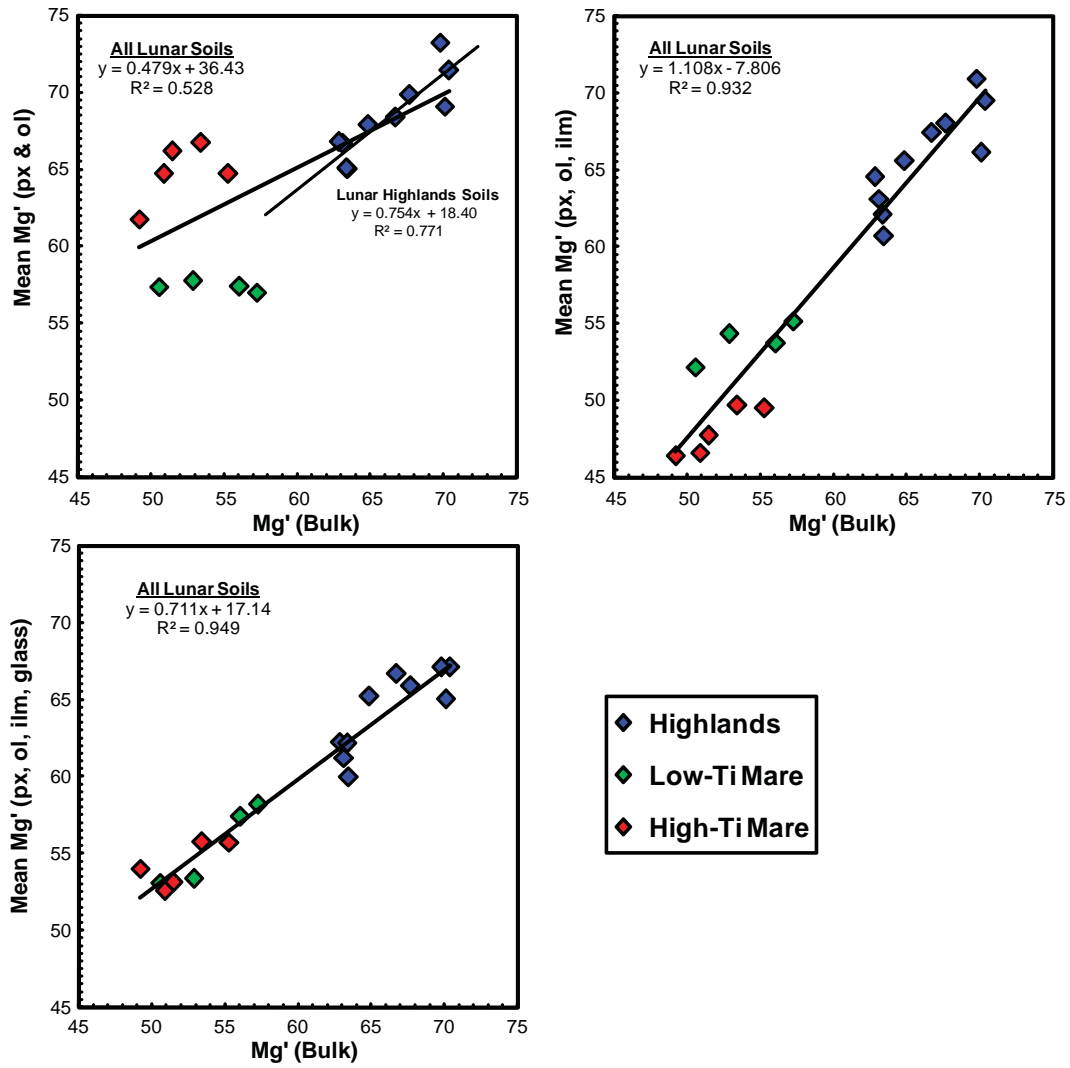


Figure 5.12: Mg' of lunar soil mineral relative to bulk chemistry.

similarity of mineral assemblages between both models. Some spectra do not fit into the fixed Mg' of 70 model at all. For example, Copernicus is previously interpreted to be mafic-rich (e.g., troctolitic to dunite mineralogies) by several studies (e.g., [Cahill *et al.*, 2009; Pieters, 1986; Tompkins and Pieters, 1999]). Results for Copernicus letting Mg' vary show it to have 60-85 vol% olivine which is consistent with previous interpretations, while fixing Mg' forces model mineralogy to have an anorthositic mineral assemblage.

Integration of these models suggest significant mineralogical diversity on the nearside of the Moon. Model mineral assemblages are relatively consistent with previous interpretations [Lucey *et al.*, 1986; Pieters, 1986; Spudis *et al.*, 1988; Spudis *et al.*, 1989], but offer additional benefits for compositional interpretation and estimates of accuracy. Model results suggest the presence of more olivine bearing (at least 10 vol% olivine) lithologies than previous interpretations could detect. Modeling also suggests much less low-Ca pyroxene than inferred by previous studies; however these results are qualified by Denevi *et al.* [2008] and Cahill *et al.* [2010a] who note that high-Ca pyroxene is often over-estimated and results in modest but significant underestimates of low-Ca pyroxene and plagioclase. Despite this deposits around Nectaris basin are still interpreted to be dominantly anorthositic but suggest slightly more mafics than the <25 vol% previously interpreted by Spudis *et al.* [1989]. Nectaris assemblages range from anorthositic-gabbroic and -troctolitic to anorthosite (Kant East Wall) in lithology. Spectra for Imbrium deposits near and from the Hadley-Apennine mountains region are dominantly of olivine-bearing noritic gabbro, but may range from anorthositic-gabbro (Apennine 10) to plausibly peridotite (Copernicus and Timocharis eastern wall). Aristarchus Plateau deposits are dominantly of olivine-bearing noritic gabbro lithologies but range from anorthositic-gabbro and -troctolite to gabbro and olivine-bearing noritic gabbro. Deposits near Nubium basin (i.e., Tycho, Bullialdus, and Arzachel) have assemblages ranging from anorthositic-gabbro to noritic gabbro and olivine-bearing noritic gabbro. Deposits near Frigoris basin have olivine-bearing noritic gabbro to peridotite assemblages.

Conclusions

Fifty-six telescopic spectra of the lunar nearside are examined with a variation of *Hapke* [1981; 1993; 2001]'s radiative transfer model techniques. These results show:

- The algorithm has difficulty modeling Mg' for approximately a third (~20) of the spectra modeled here. An inability to simultaneously match spectral parameters as well as FeO abundance result in underestimates of FeO and usually magnesian Mg' values (90-95) and mafic to ultramafic mineral assemblages. Underestimates of FeO abundance usually occur for lunar deposits with relatively feldspathic FeO abundances (5-9 wt%).
- Modeling at a fixed Mg' of 70, FeO abundance is better matched for nearly all spectra and comparable, although not superior, spectral fits are attained. These models are mineralogically diverse and sometimes change the resulting model mineralogy dramatically usually by increasing plagioclase content.
- The undulating pattern of the residuals between model and fits, and the very likely bias toward clinopyroxene rich model mineralogies indicates the computed spectra of the component minerals do not adequately represent the shape of the lunar component minerals. The magnitude of the residuals probably results in the insensitivity to Mg'. Improvements to the optical constants is likely required to mitigate this problem.
- Integration of fixed and variable Mg' modeling suggest nearside spectra of the Moon show significant mineralogic diversity that is relatively consistent with previous interpretations. Nectaris basin spectra are dominantly anorthositic (60 to 93 vol% plagioclase) and similar to ferroan anorthosite suite rocks. Remaining nearside spectra principally associated with Imbrium basin deposits show more mafic lithologies, dominantly olivine-bearing noritic gabbros, but mineralogically range from anorthositic norite and troctolite to plausibly peridotite lithologies. Olivine-bearing noritic gabbro assemblages are dominant in Imbrium (Aristarchus Plateau and Hadley-Apennine mountains). Mare Frigoris deposits also show mineralogic similarities to mare basalts, but are FeO poor in comparison, so are likely more similar to olivine-bearing gabbroic norites and gabbros of the lunar magnesium-suite as well.

Acknowledgements

This work was supported in part by NASA Planetary Geology and Geophysics grant NNG05GJ51G to P.G.L.

APPENDIX A

Spectral Class A

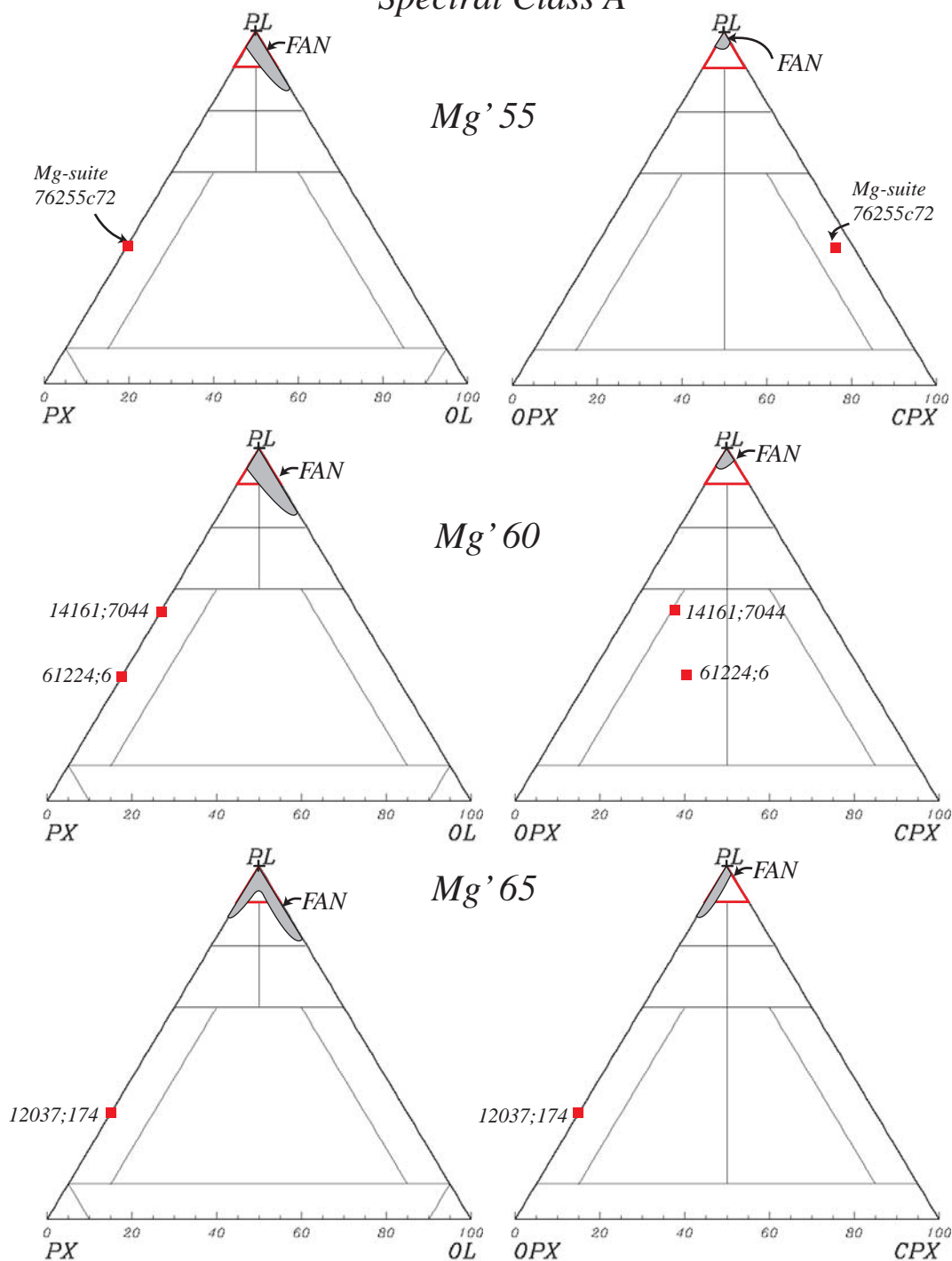


Figure A2.1a: Shown is the mineralogy of spectral models on pl-ol-px and pl-opx-cpx Stöfler diagrams that match spectral classes per Mg' compared to FAN (light grey envelopes-sample clusters; blue triangles-single samples) and Mg-suite (dark grey envelopes-sample clusters; red squares-single samples) sample data. Blue contours separate model mineral mixture data that have been calculated to have absolute reflectance values that fall within different ranges. This change in absolute reflectance is also highlighted by models having different symbols for that particular absolute reflectance range. *Tompkins and Pieters* [1999] original interpretation of the mineralogy of each spectral class is highlighted in red. A description of the results for each class is presented in the text of chapter 2.

Spectral Class A

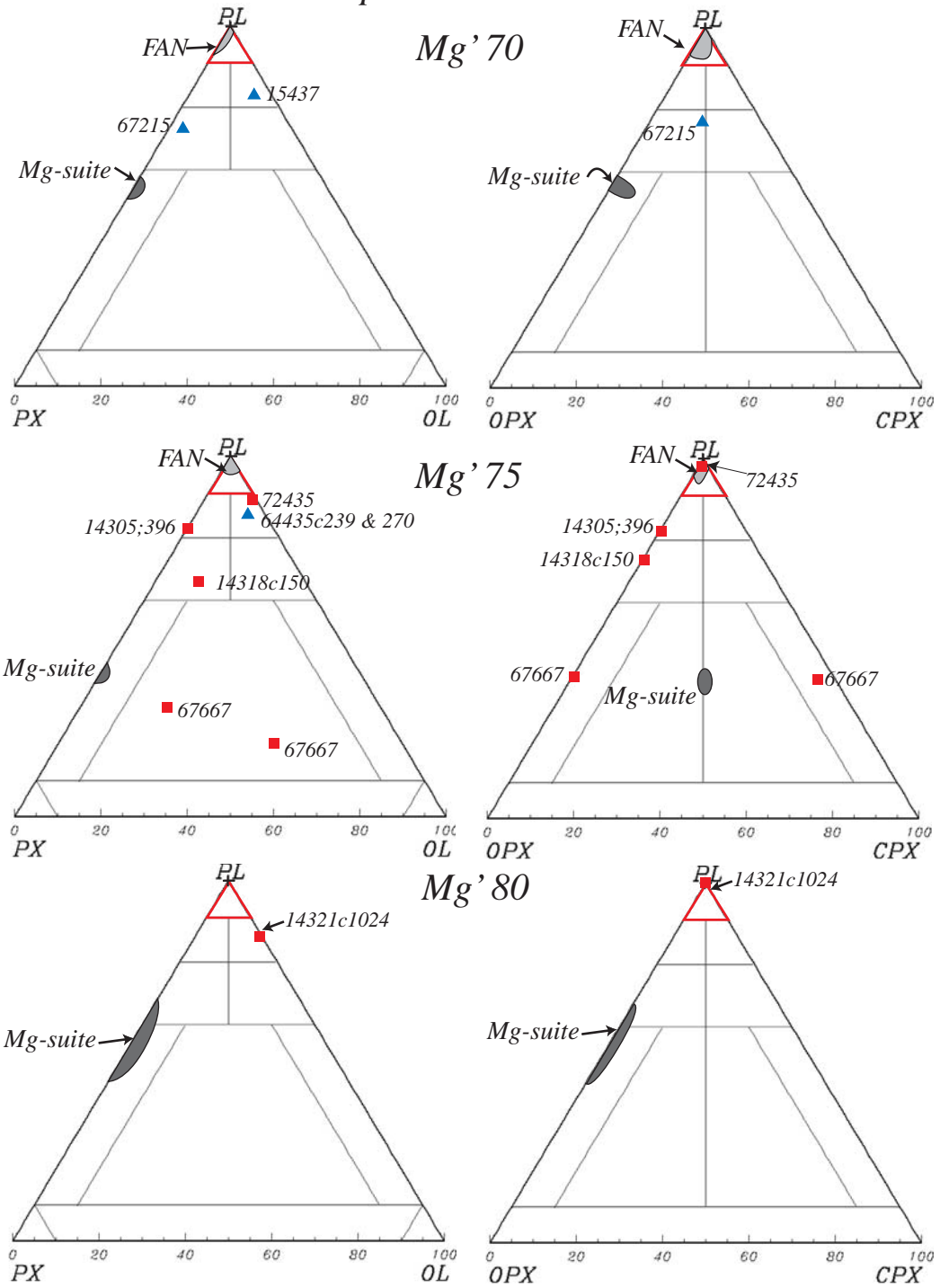


Figure A2.1b: cont.

Spectral Class A

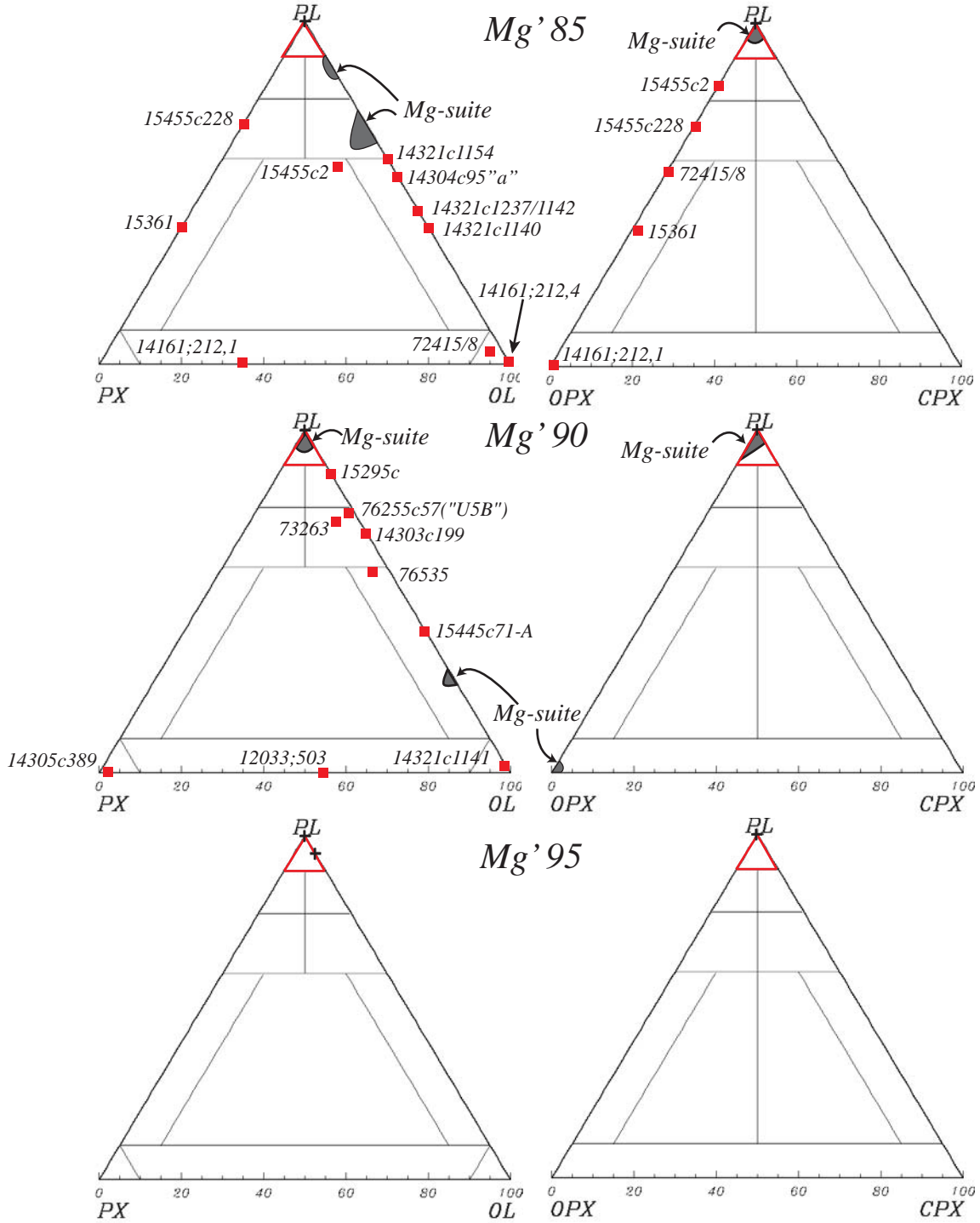


Figure A2.1c: cont.

Spectral Class AG

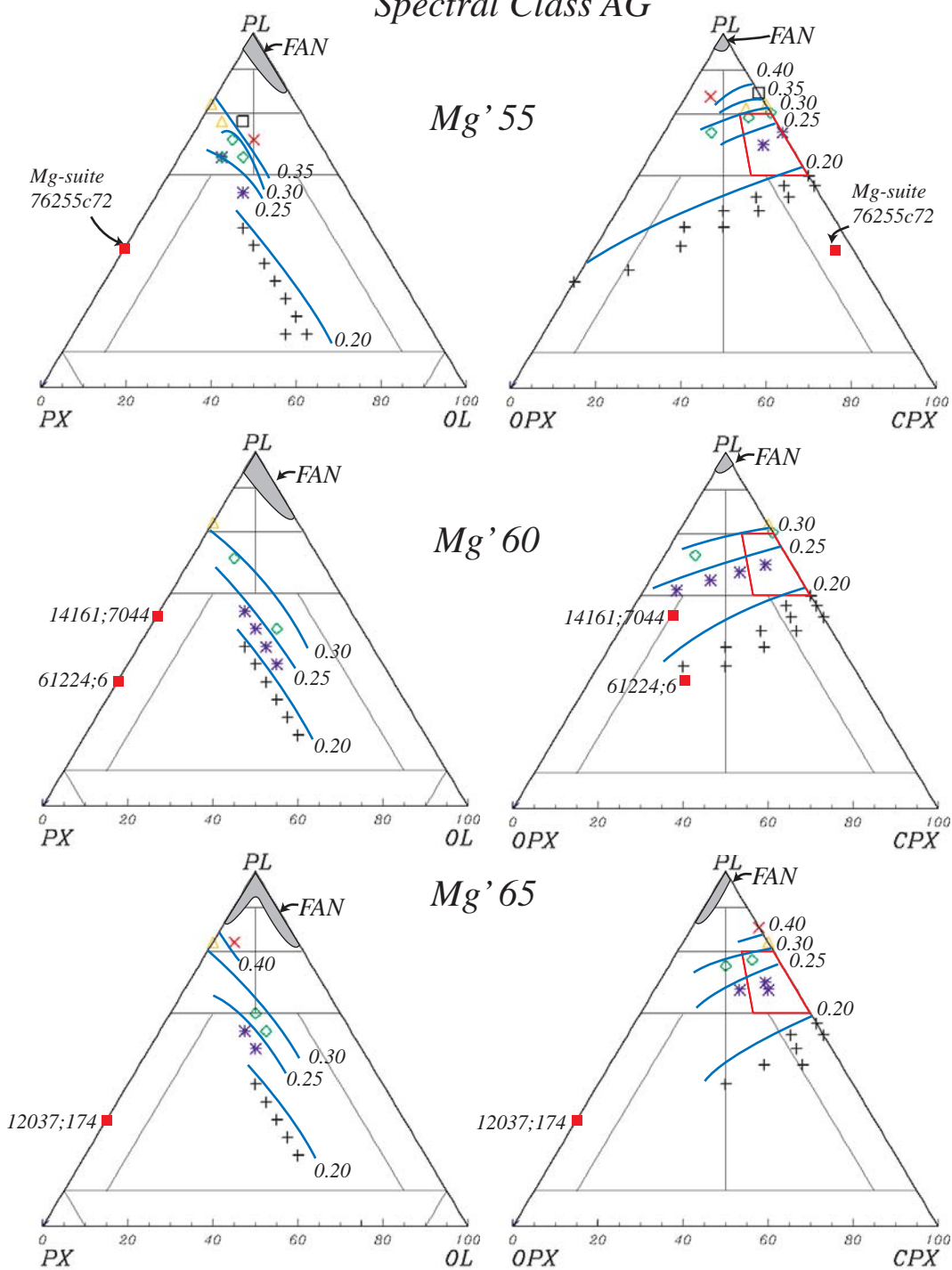


Figure A2.2a: cont.

Spectral Class AG

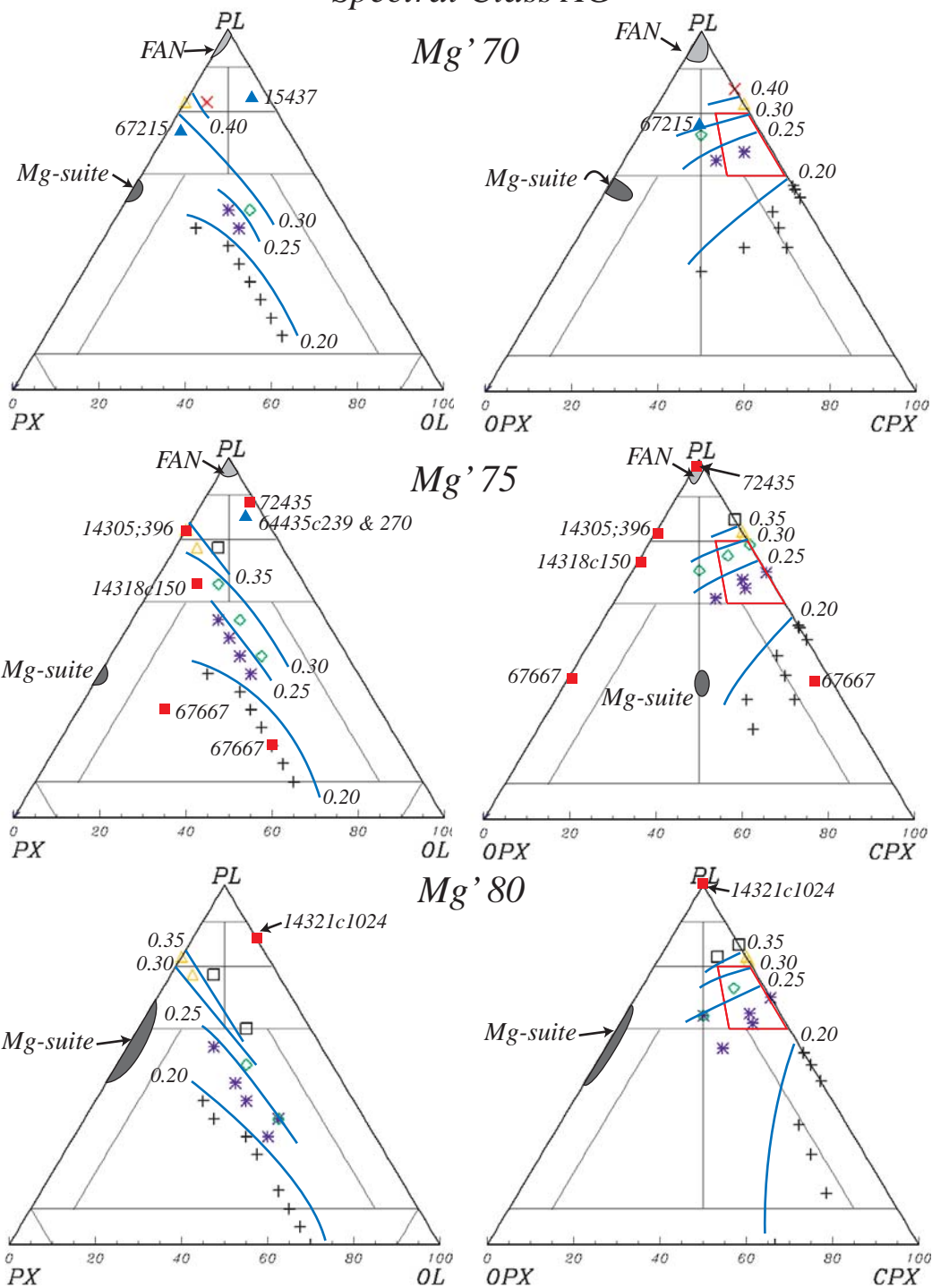


Figure A2.2b: cont.

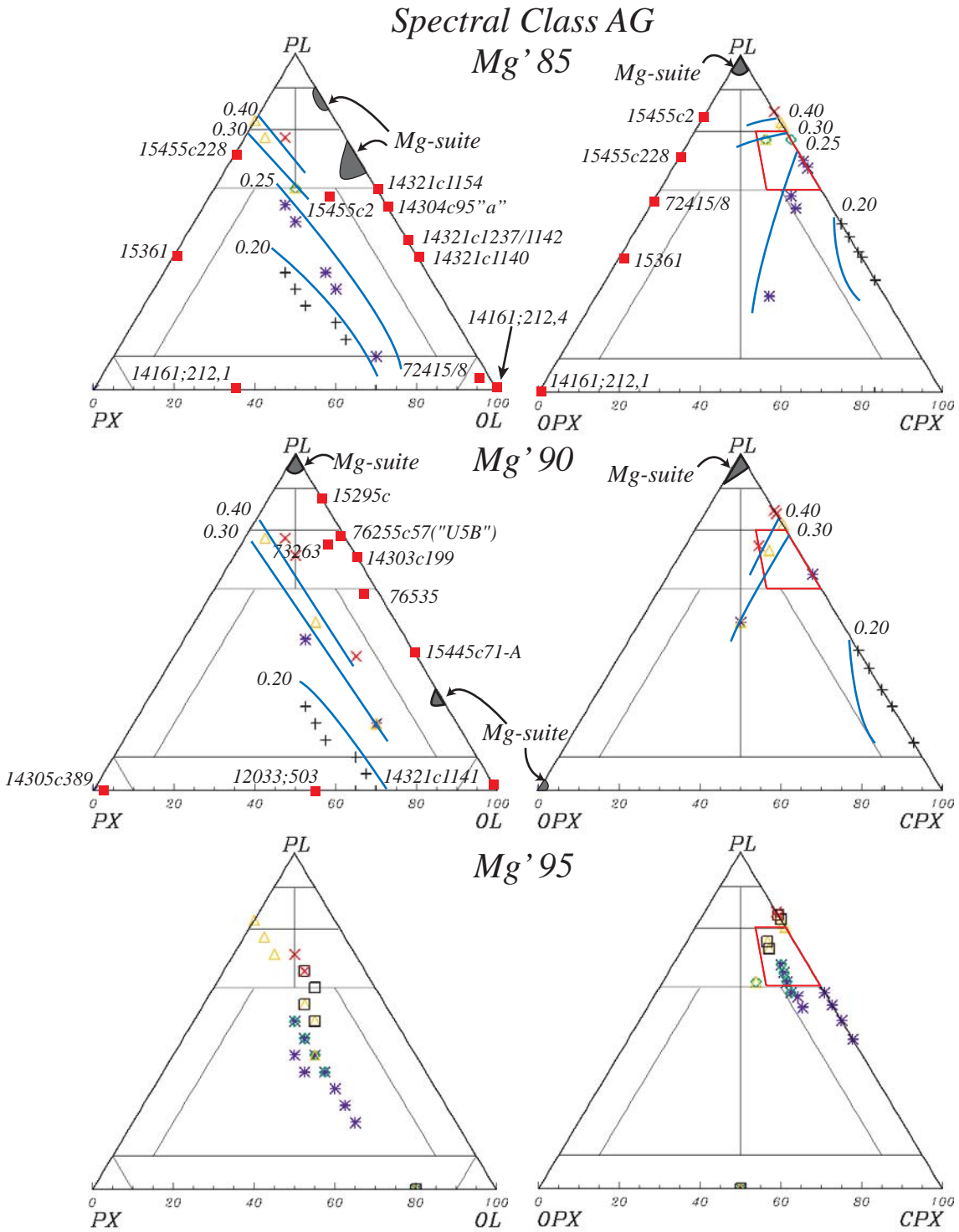


Figure A2.2c: cont.

Spectral Class AGN

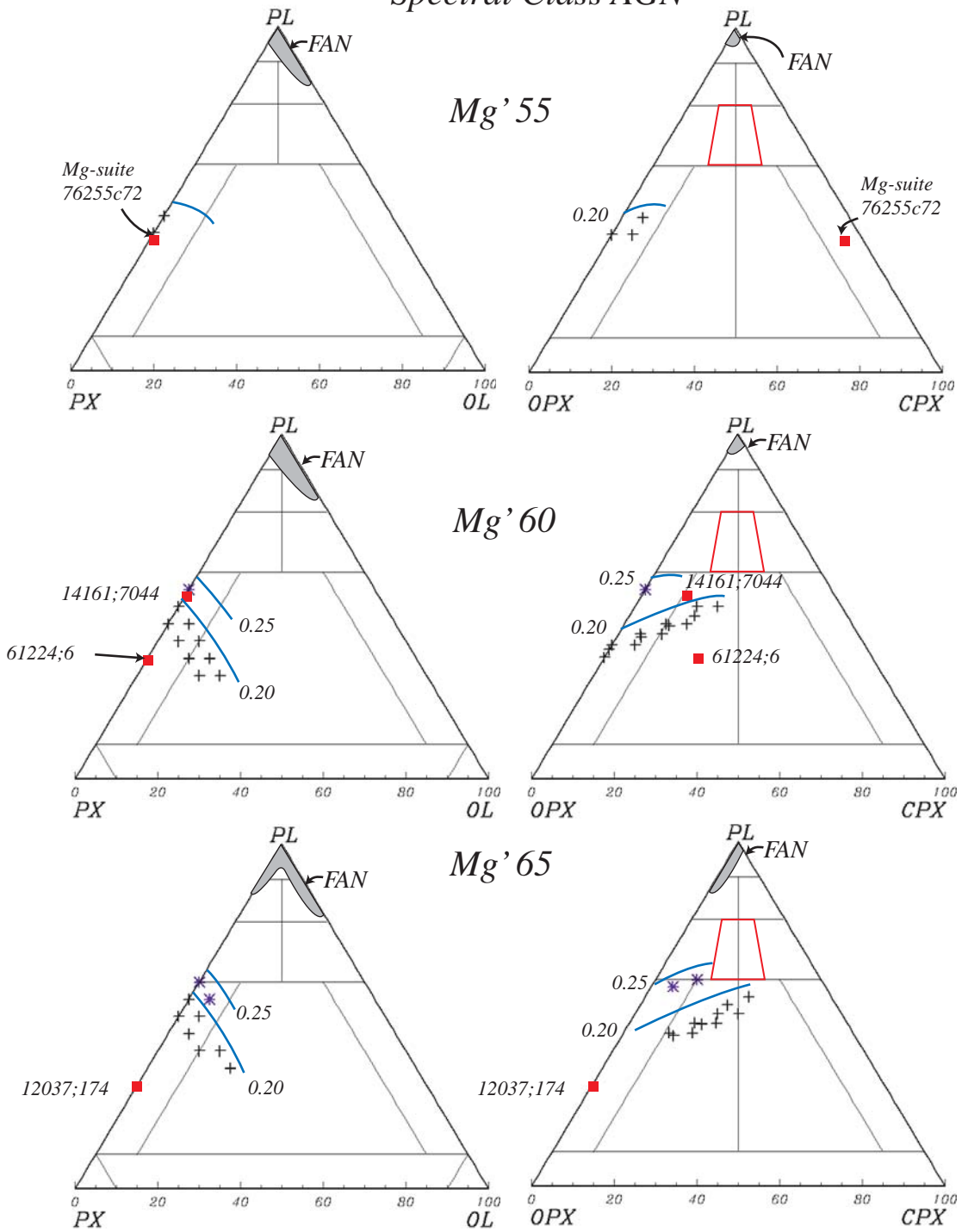


Figure A2.3a: cont.

Spectral Class AGN

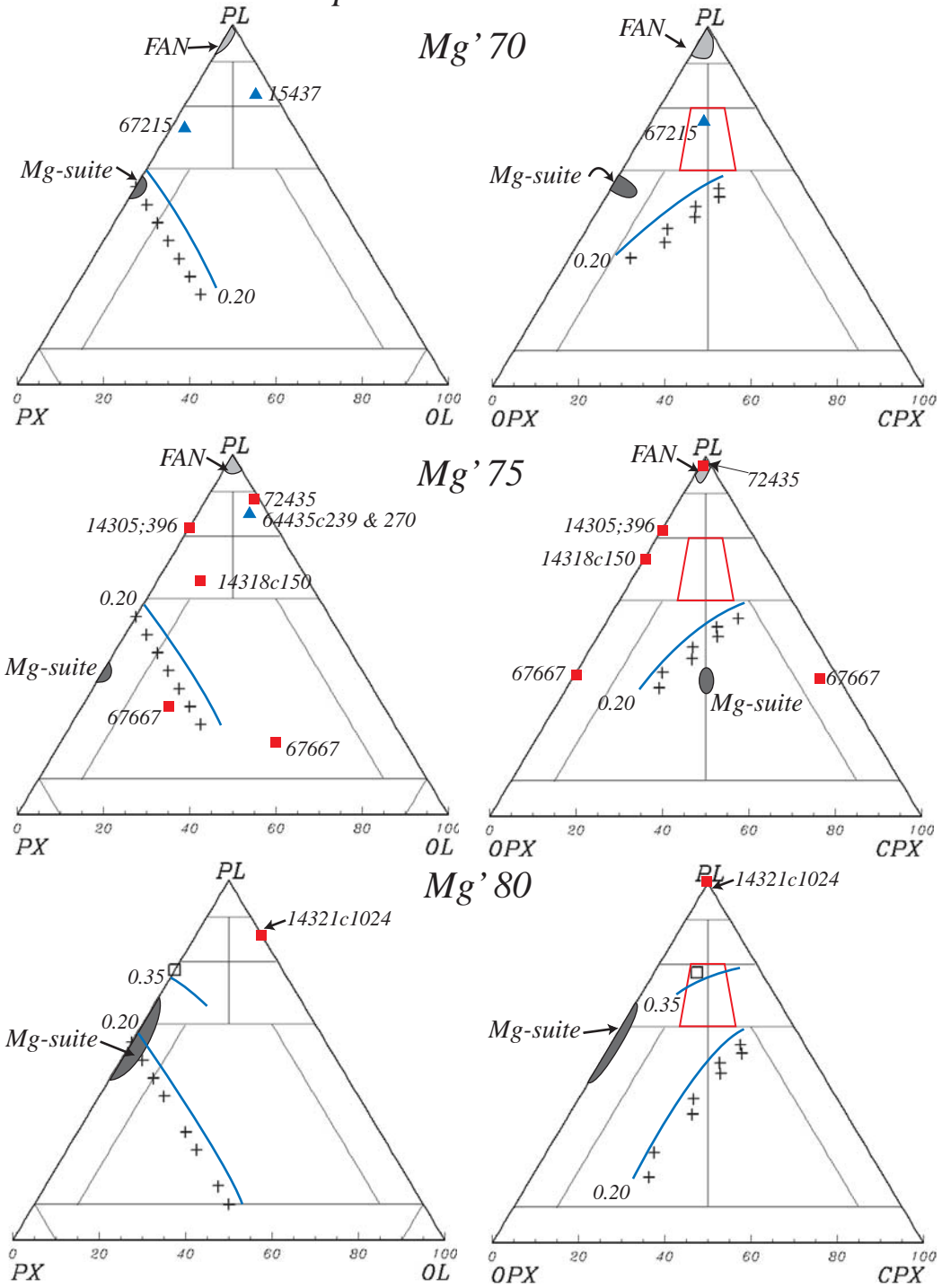


Figure A2.3b: cont.

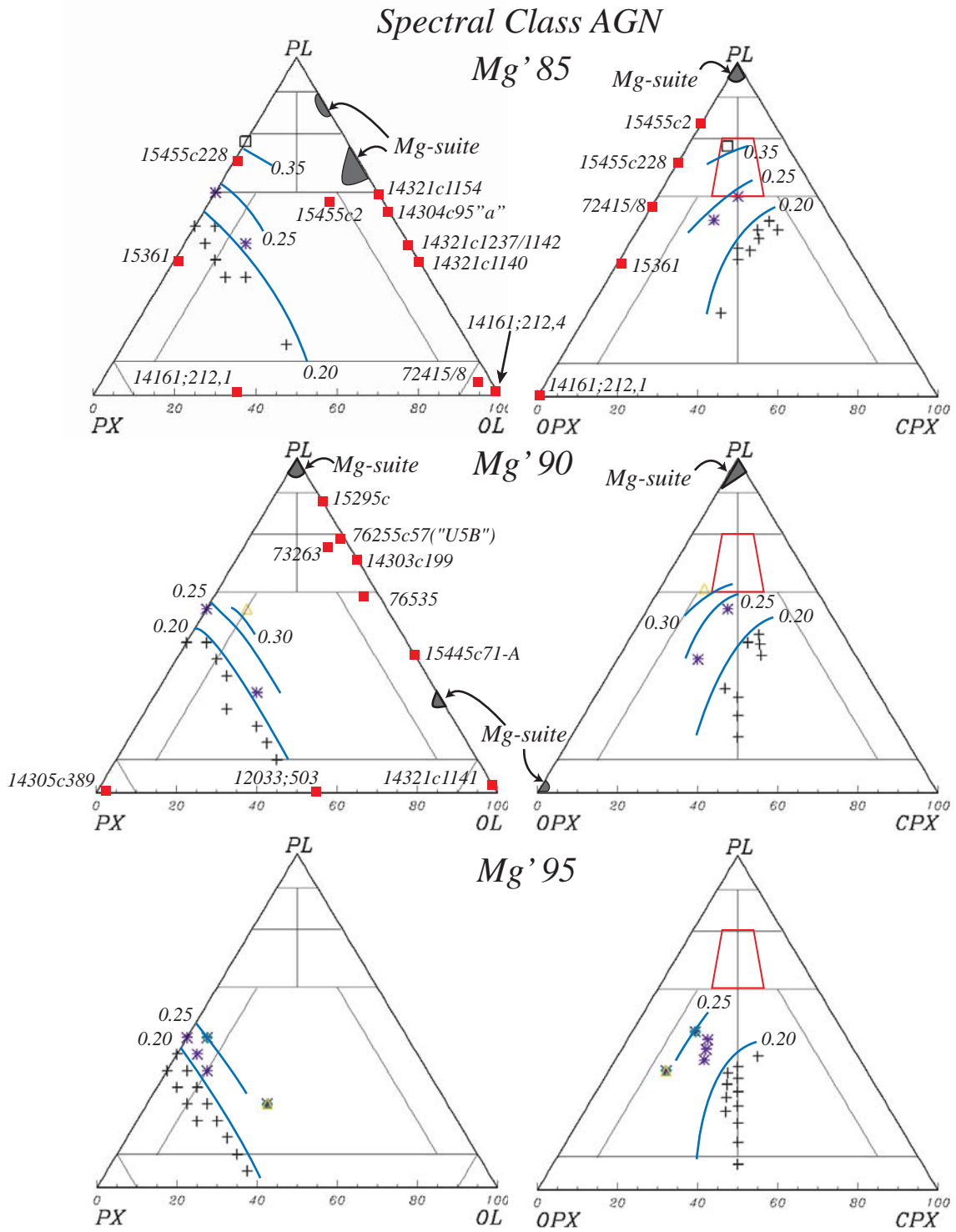


Figure A2.3c: cont.

Spectral Class AN

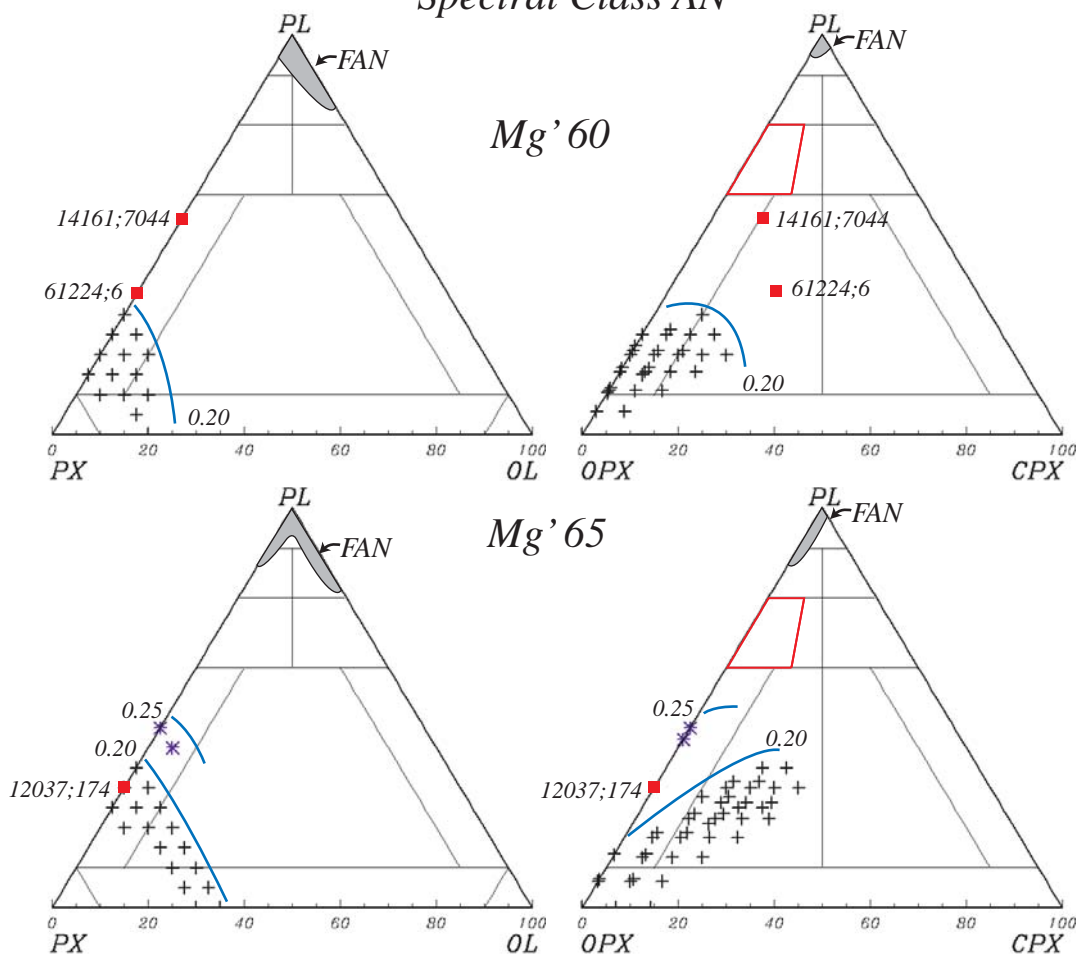


Figure A2.4a: cont.

Spectral Class AN

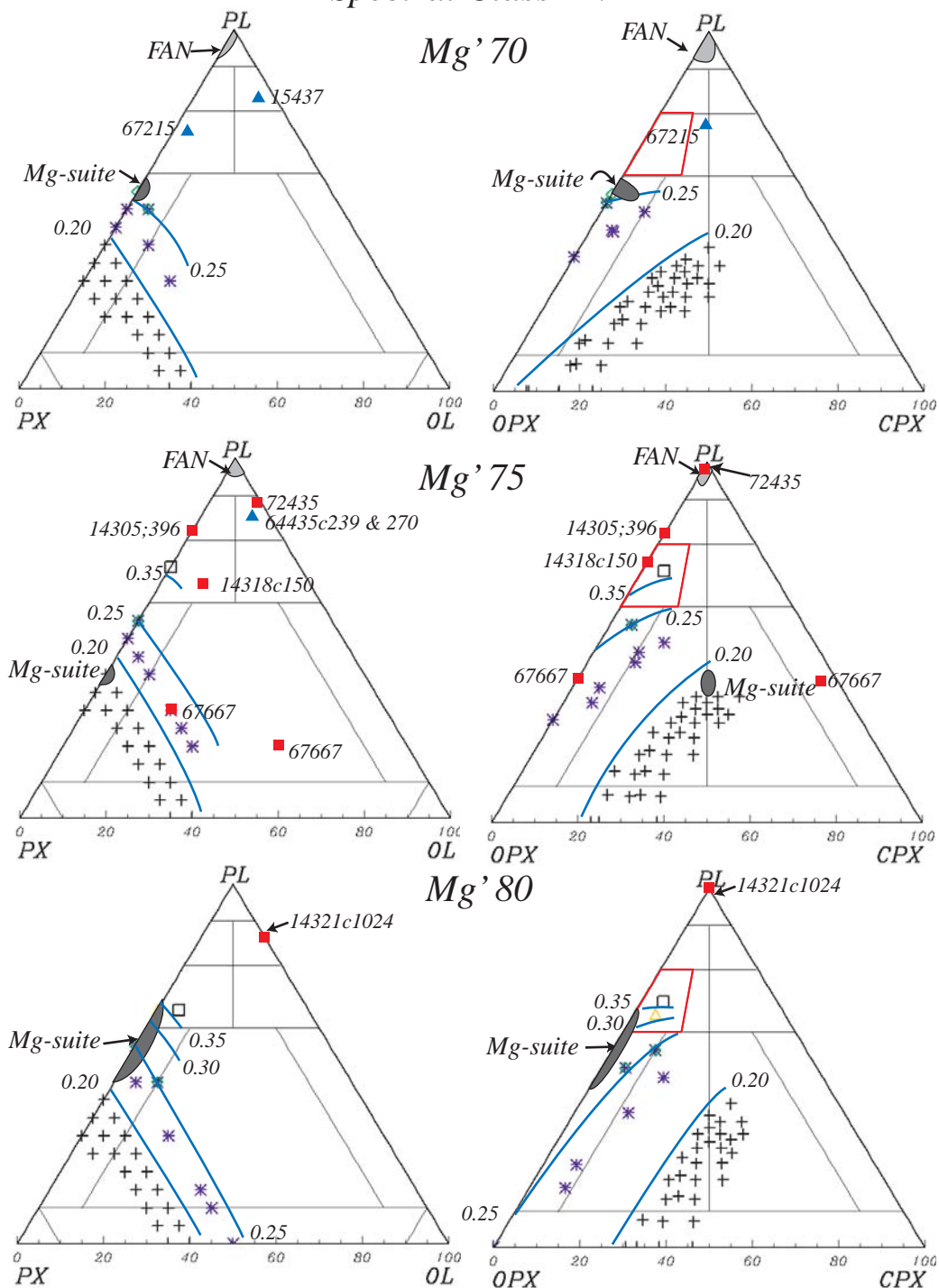


Figure A2.4b: cont.

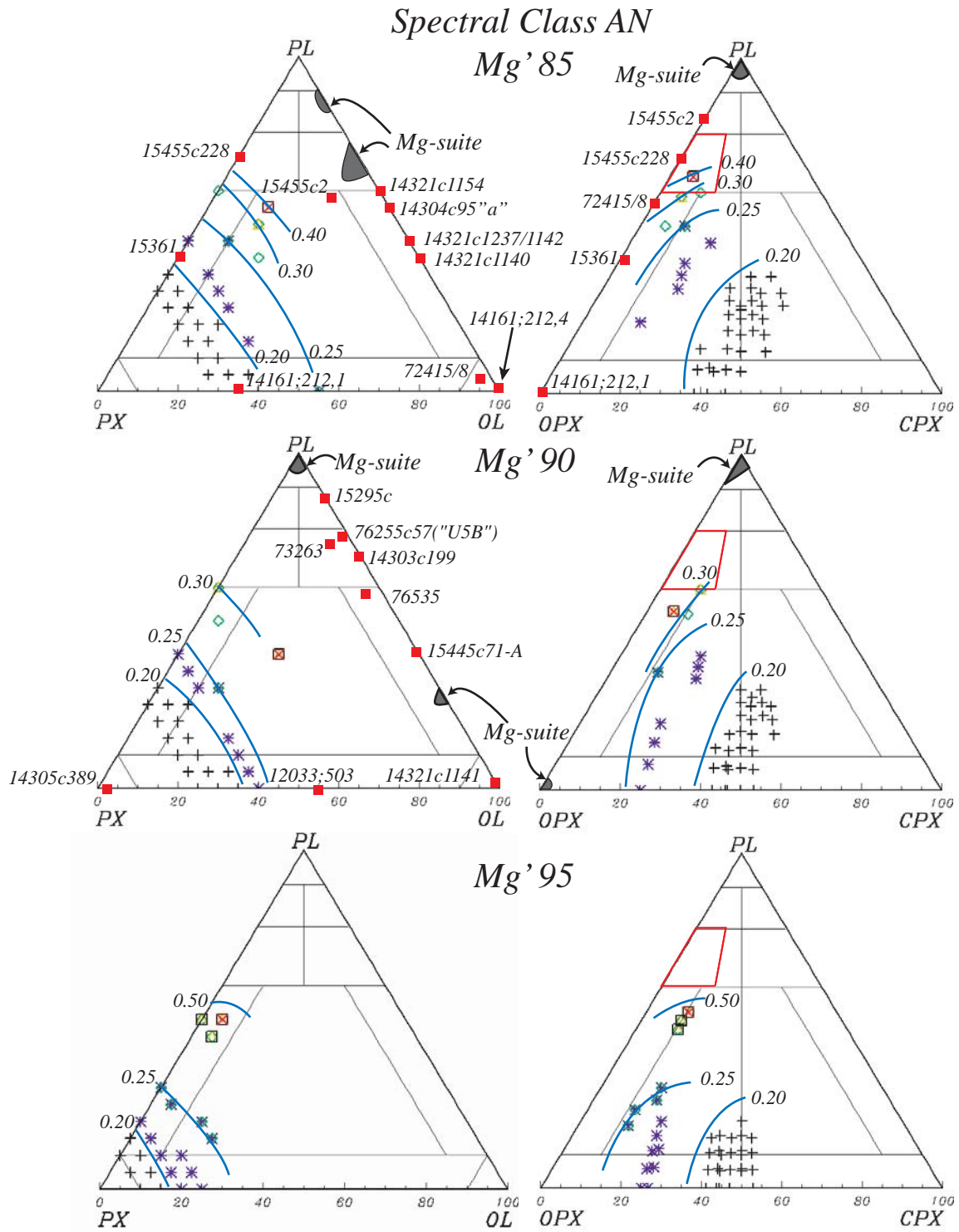


Figure A2.4c: cont.

Spectral Class AT

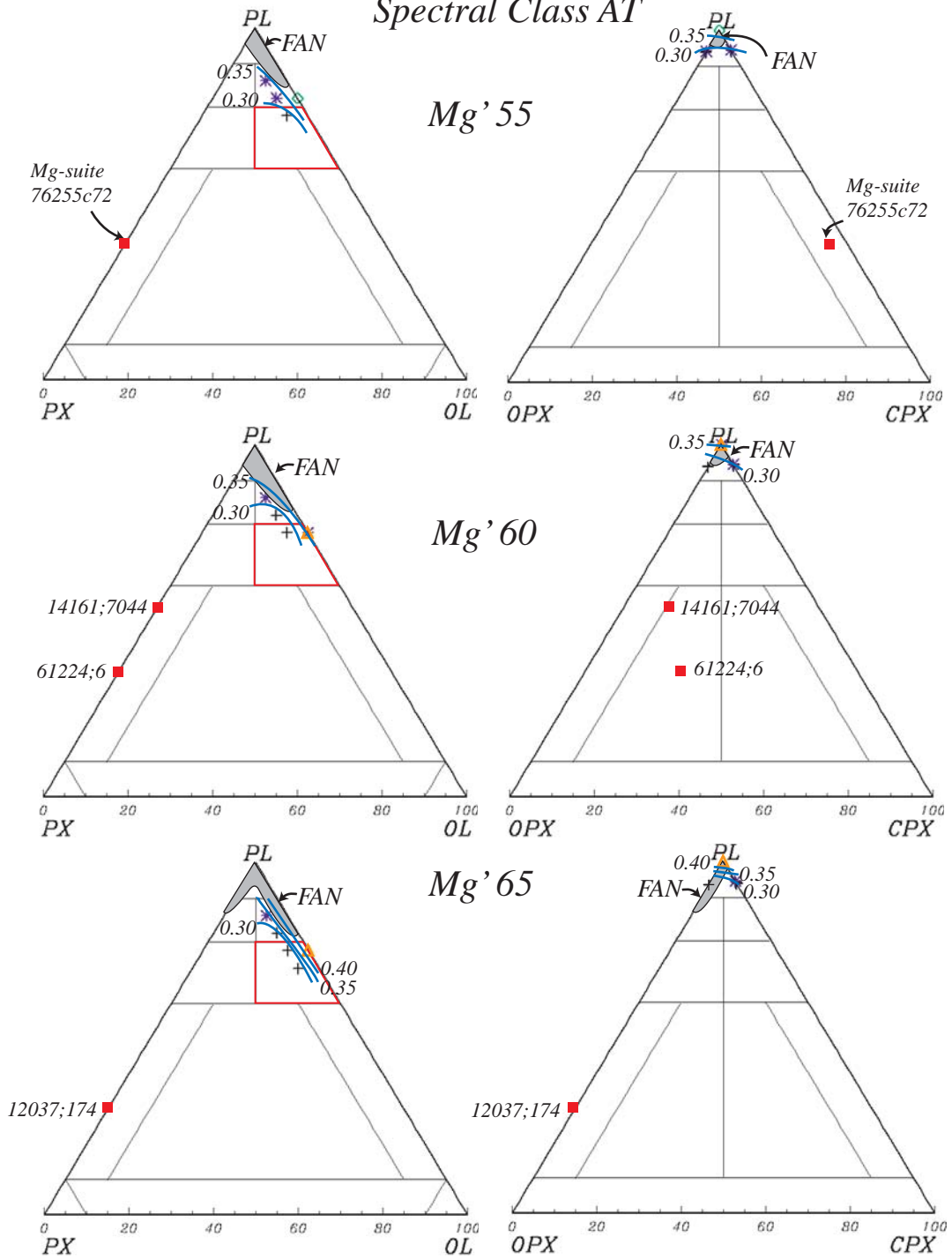
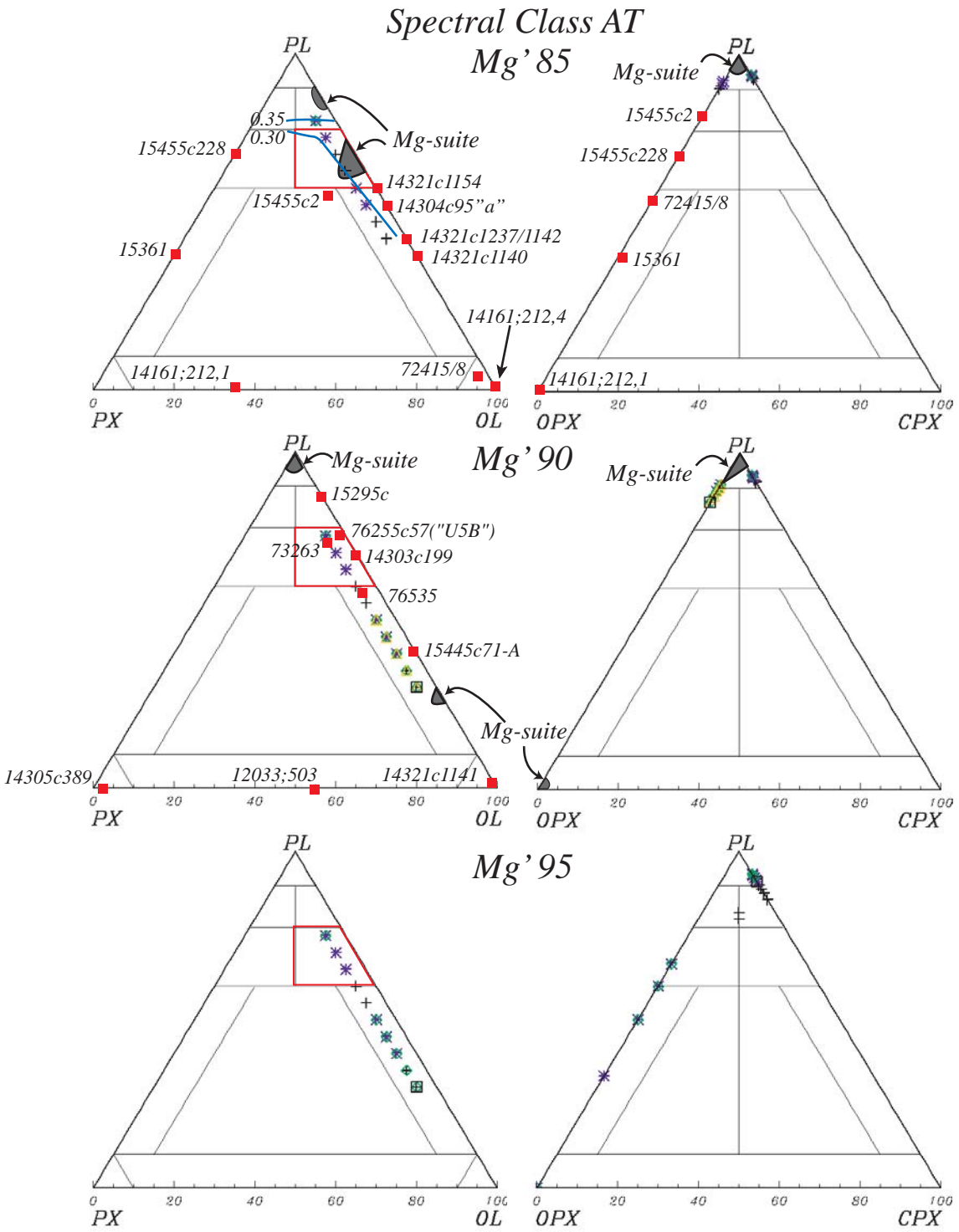


Figure A2.5a: cont.



Spectral Class G

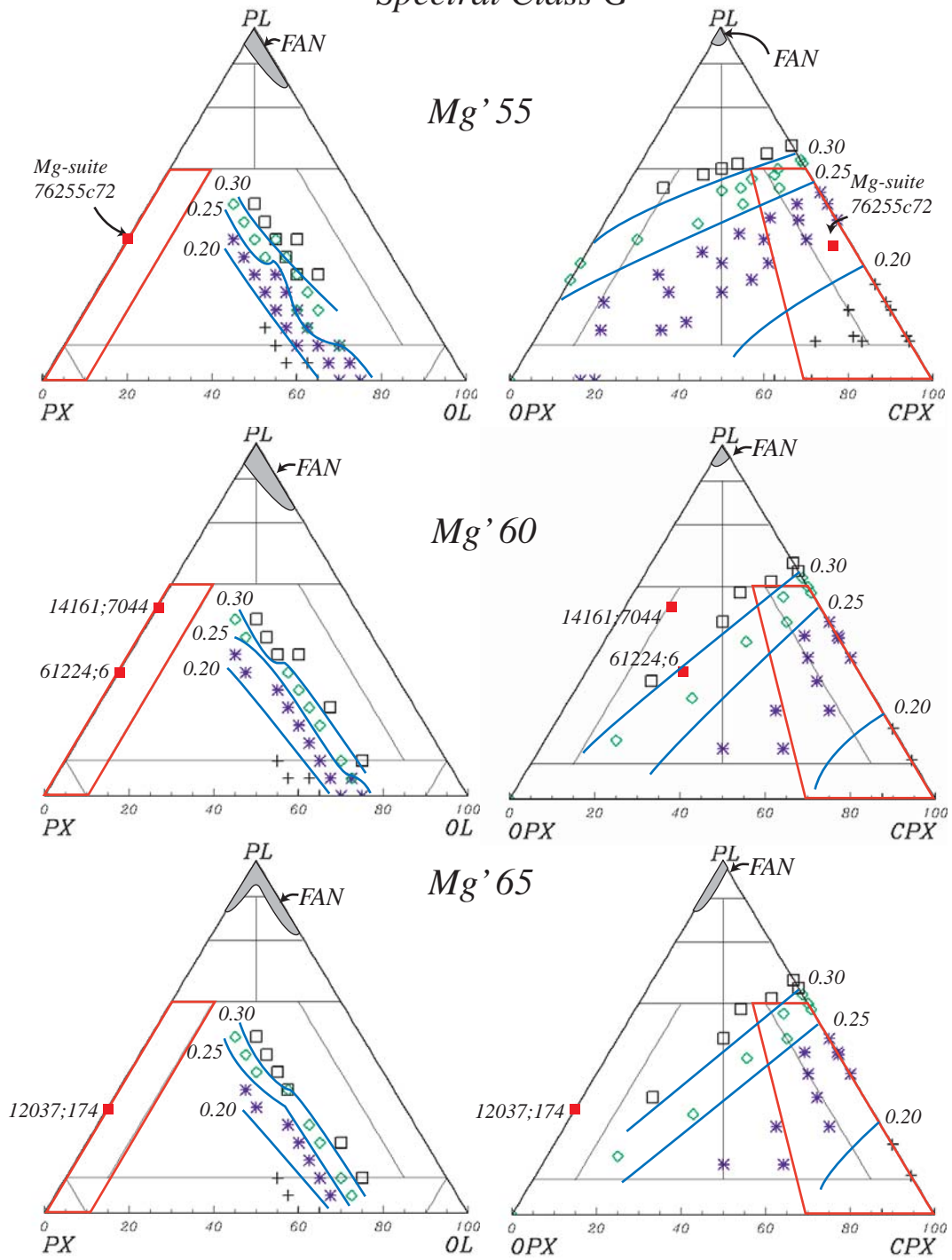
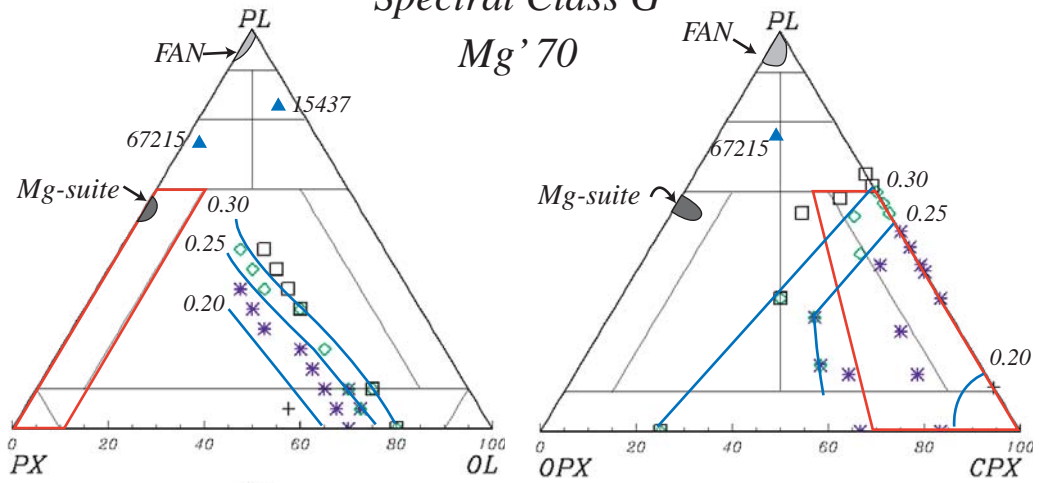


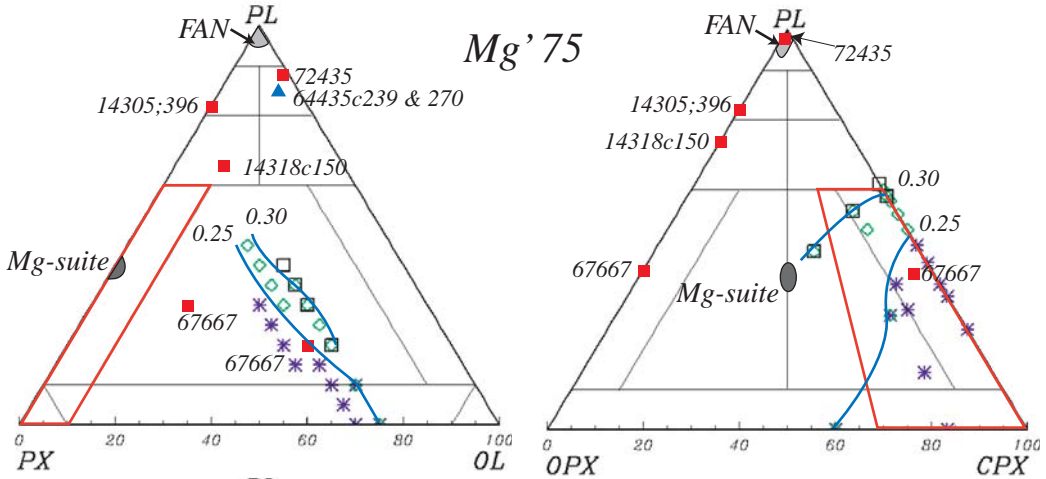
Figure A2.6a: cont.

Spectral Class G

Mg' 70



Mg' 75



Mg' 80

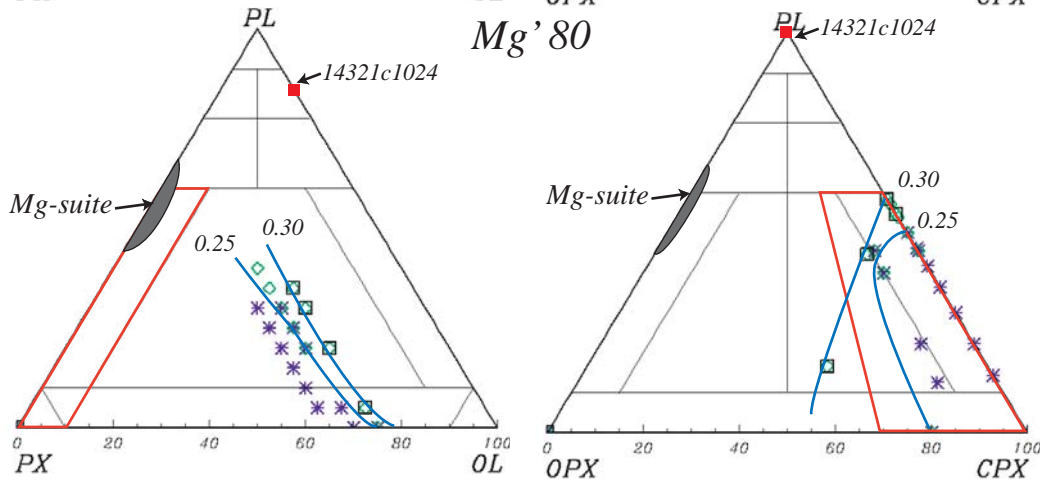


Figure A2.6b: cont.

Spectral Class GN

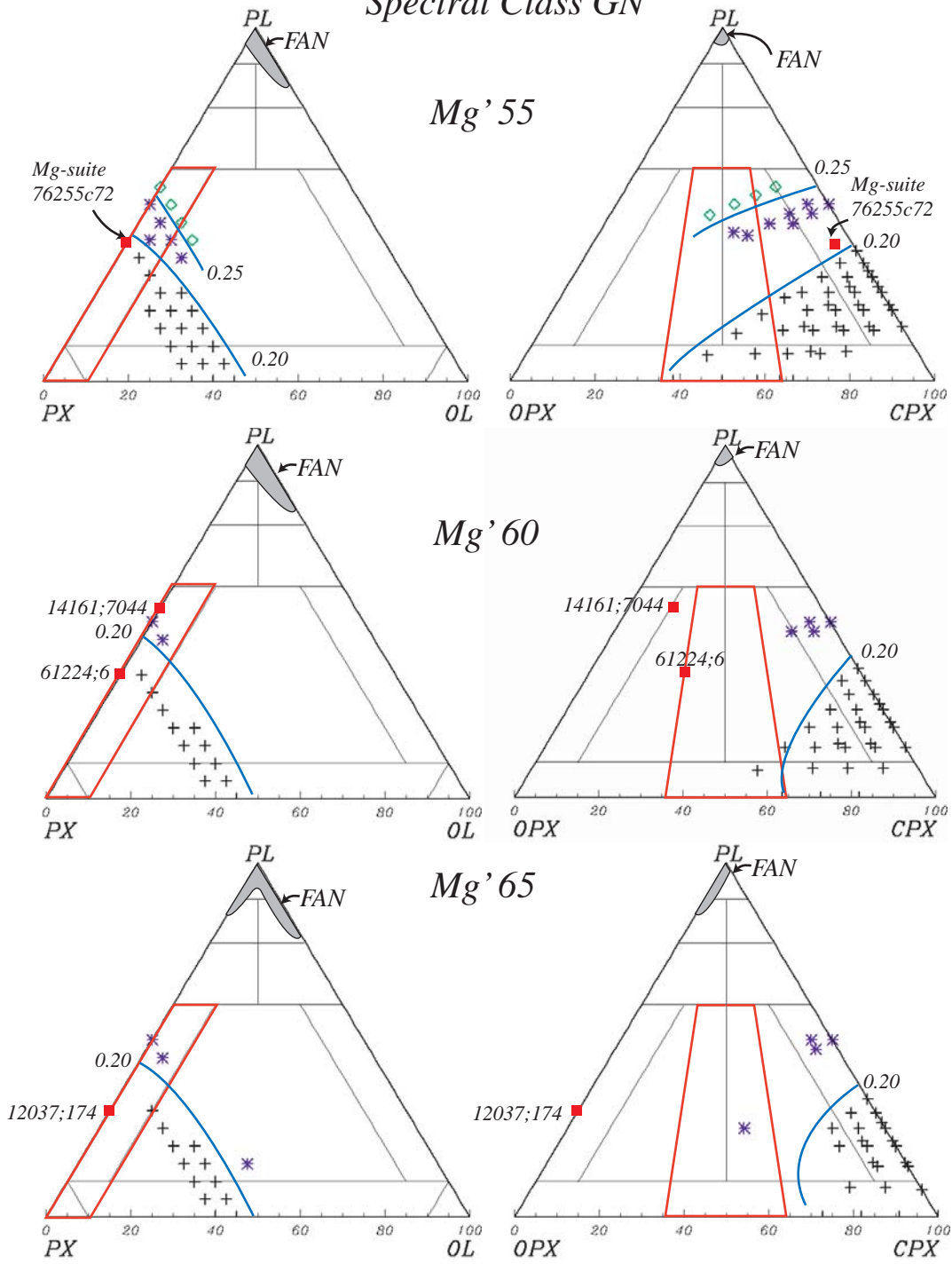


Figure A2.7a: cont.

Spectral Class GN

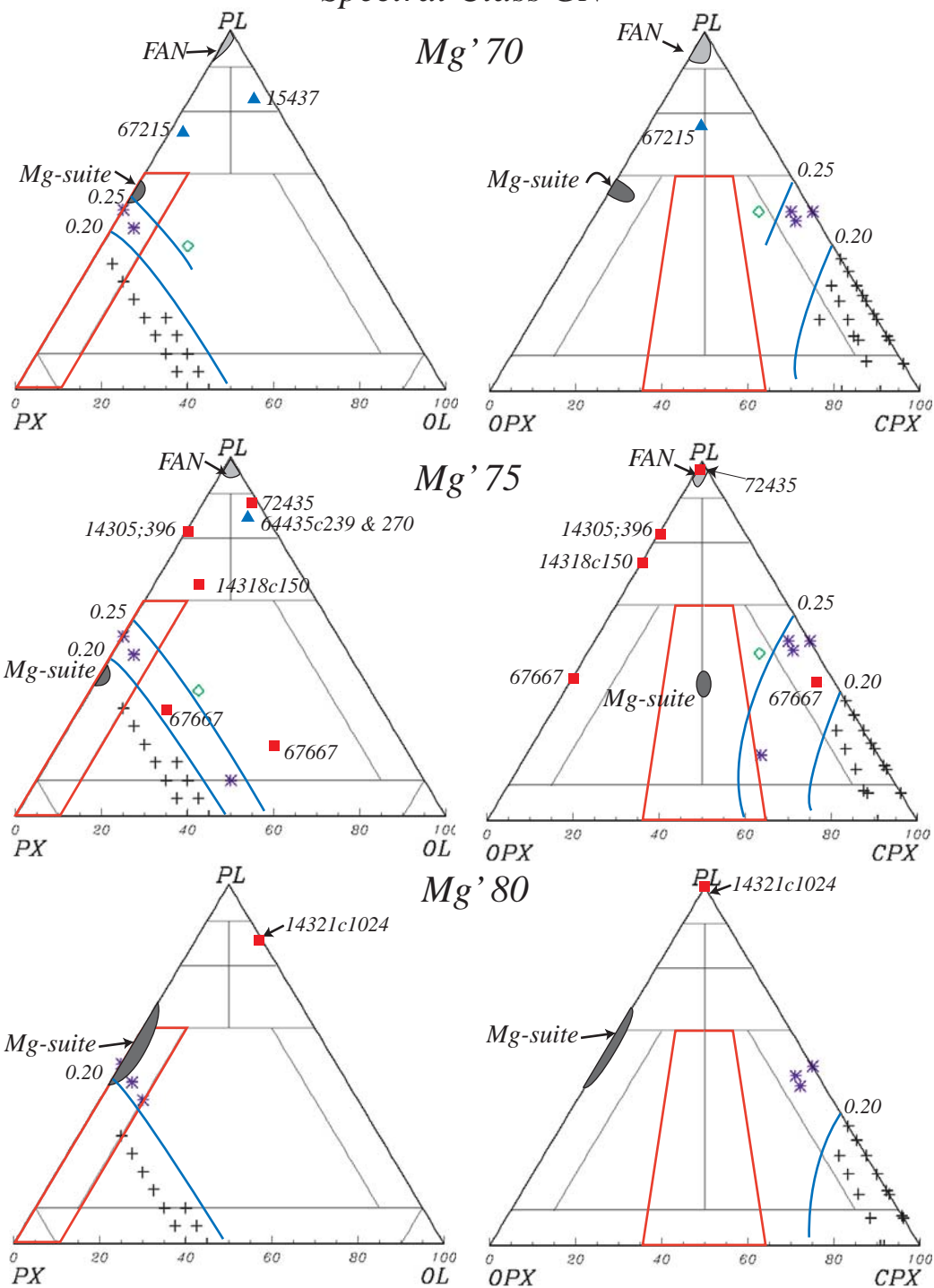
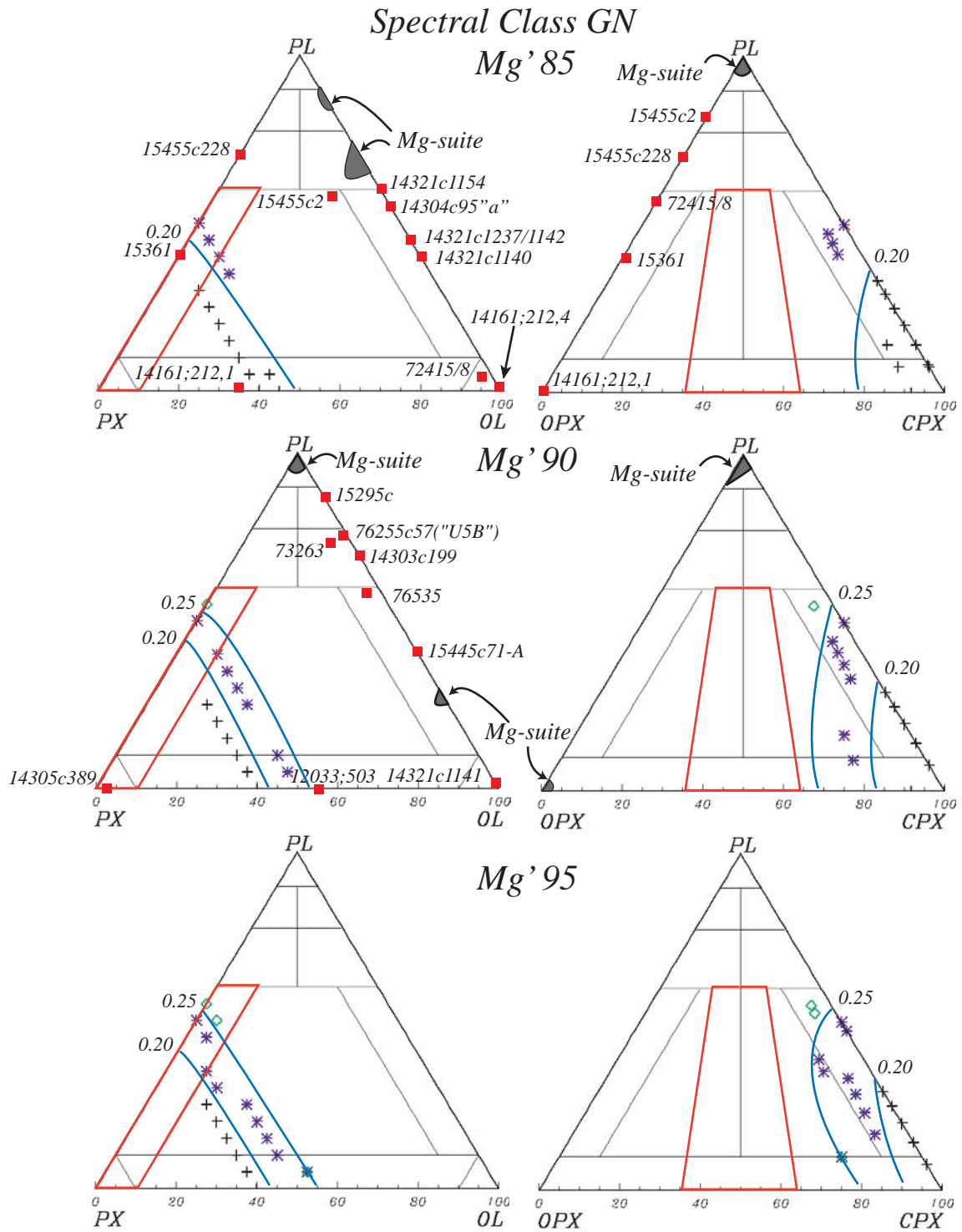


Figure A2.7b: cont.



Spectral Class GNTA1

Mg' 65

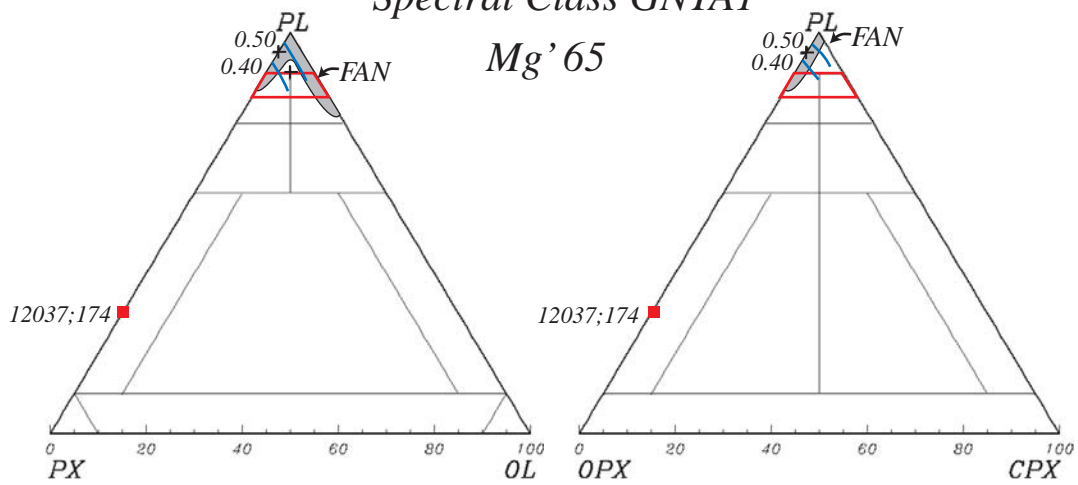


Figure A2.8a: cont.

Spectral Class GNTA1

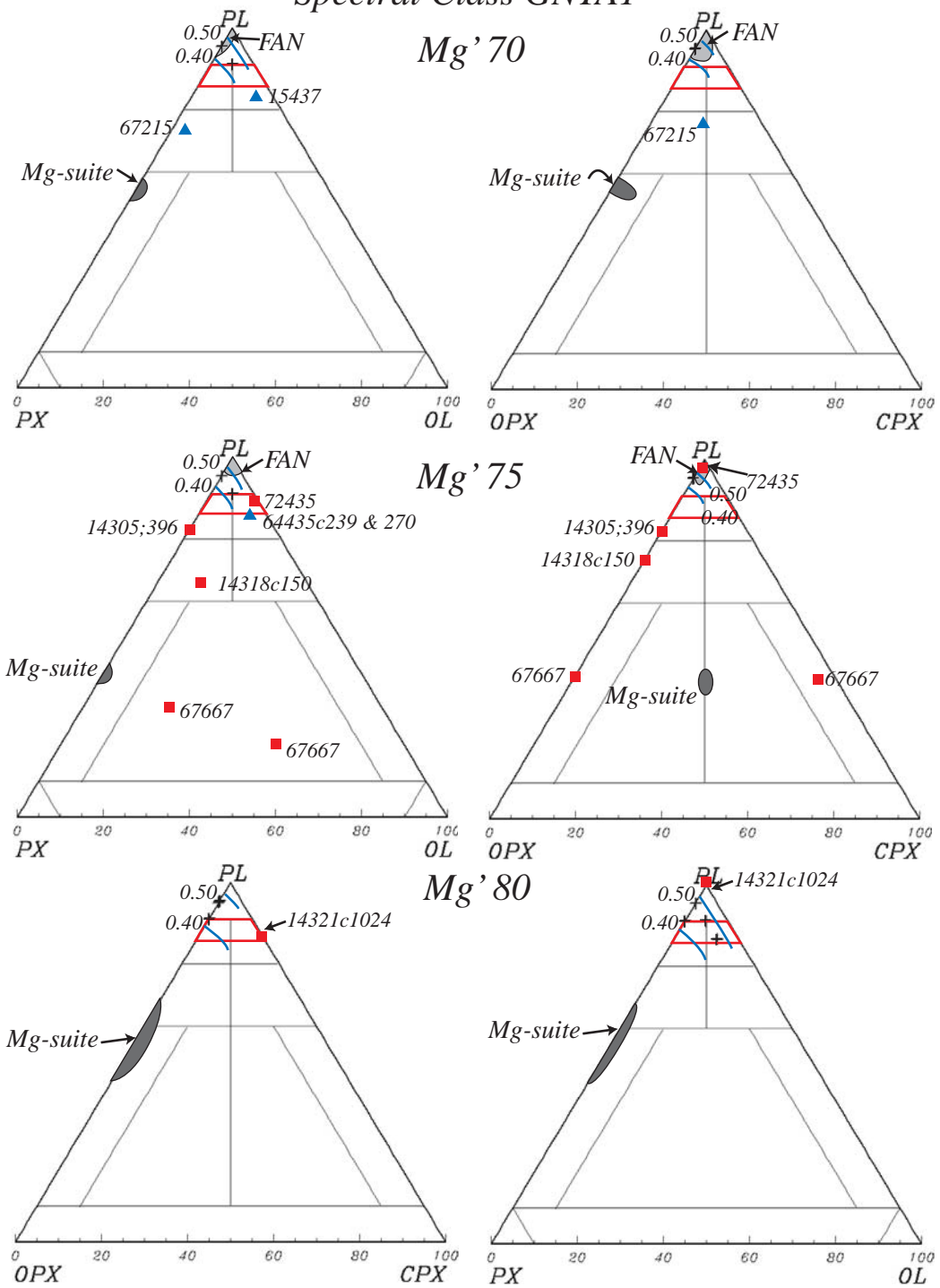


Figure A2.8b: cont.

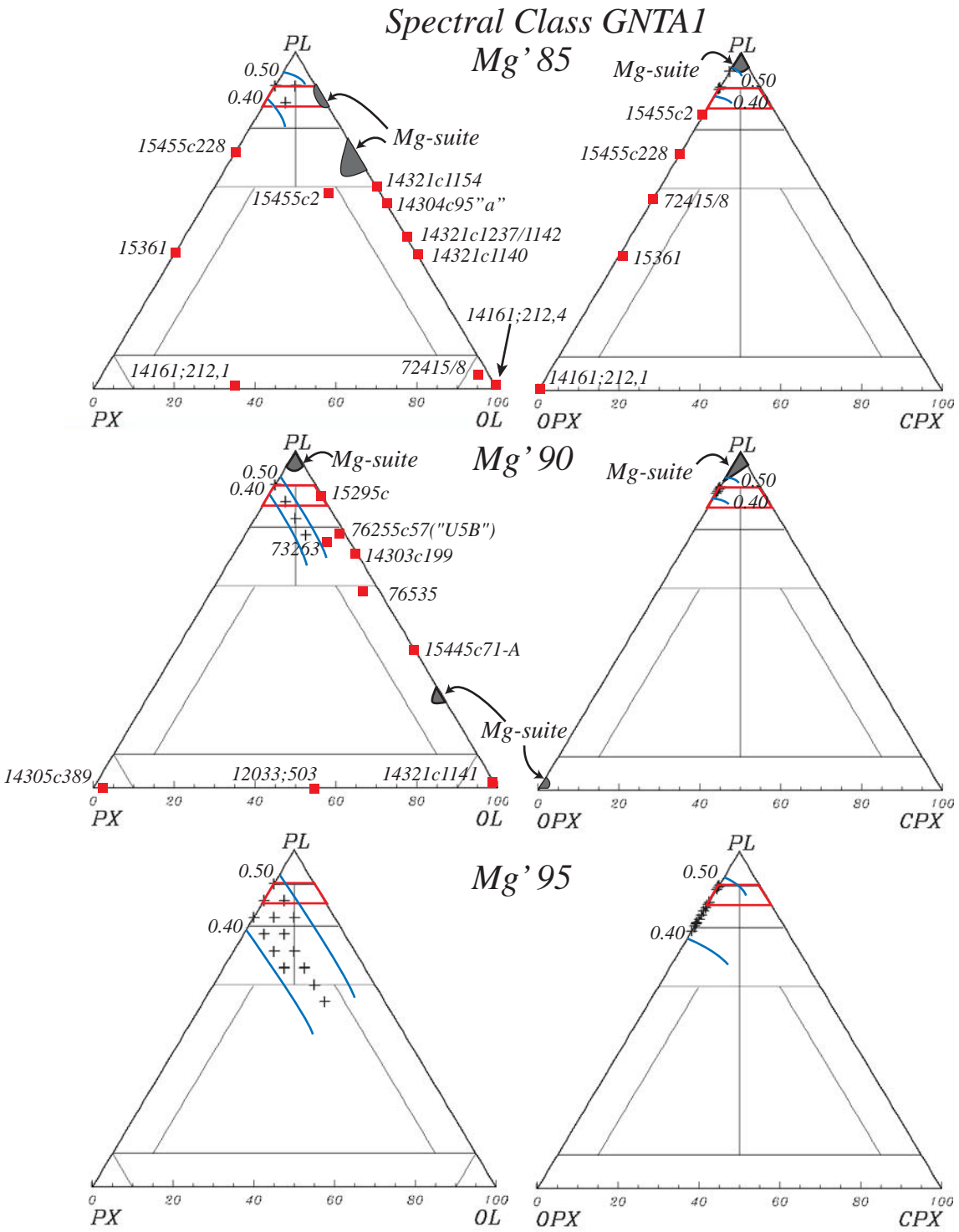


Figure A2.8c: cont.

Spectral Class GNTA2

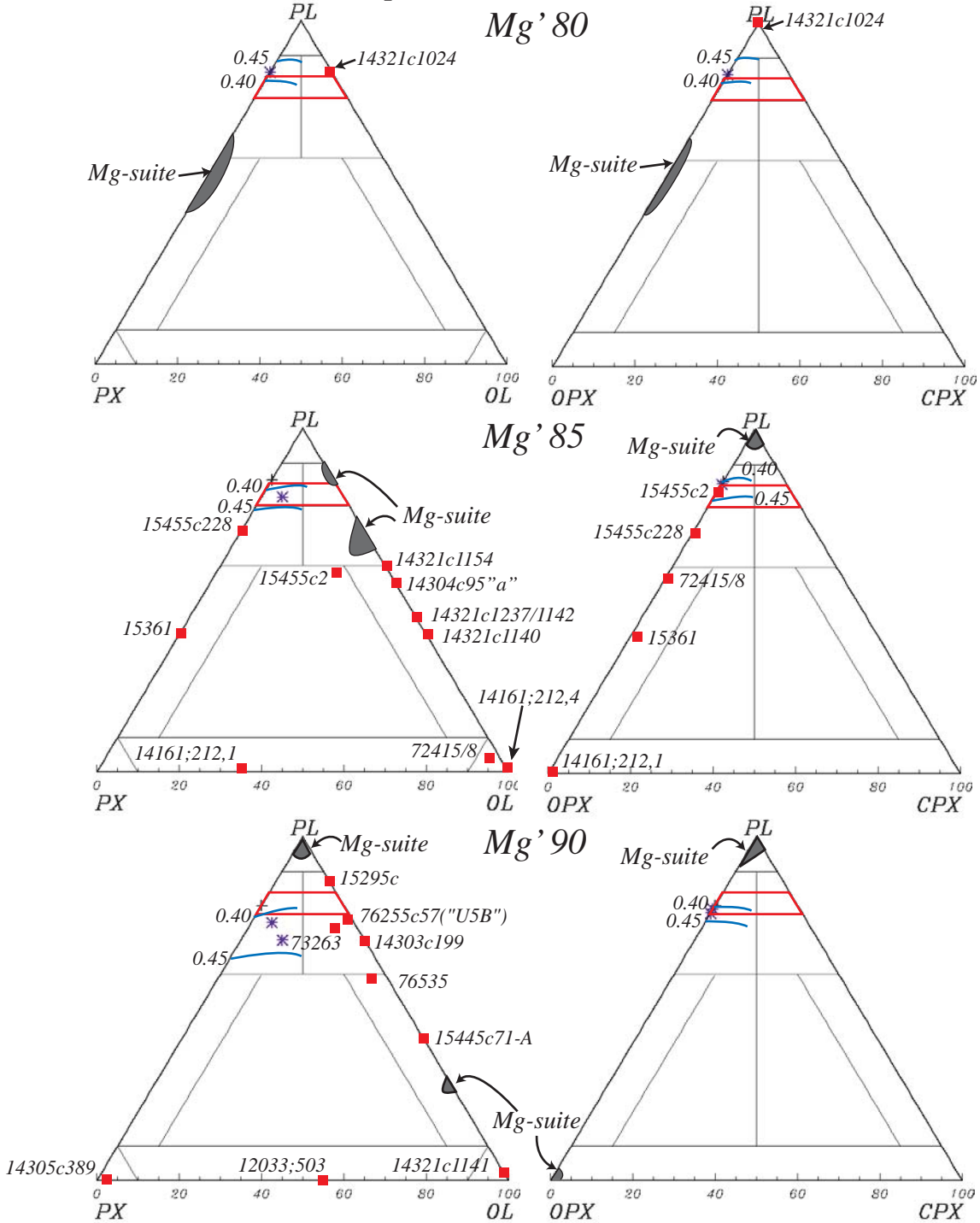


Figure A2.9a: cont.

Spectral Class GNTA2

Mg' 95

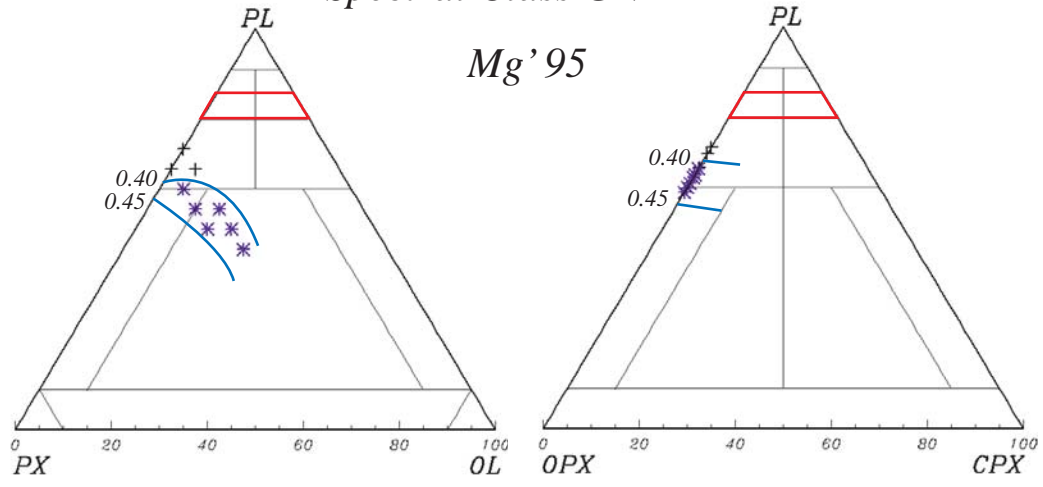


Figure A2.9b: cont.

Spectral Class N

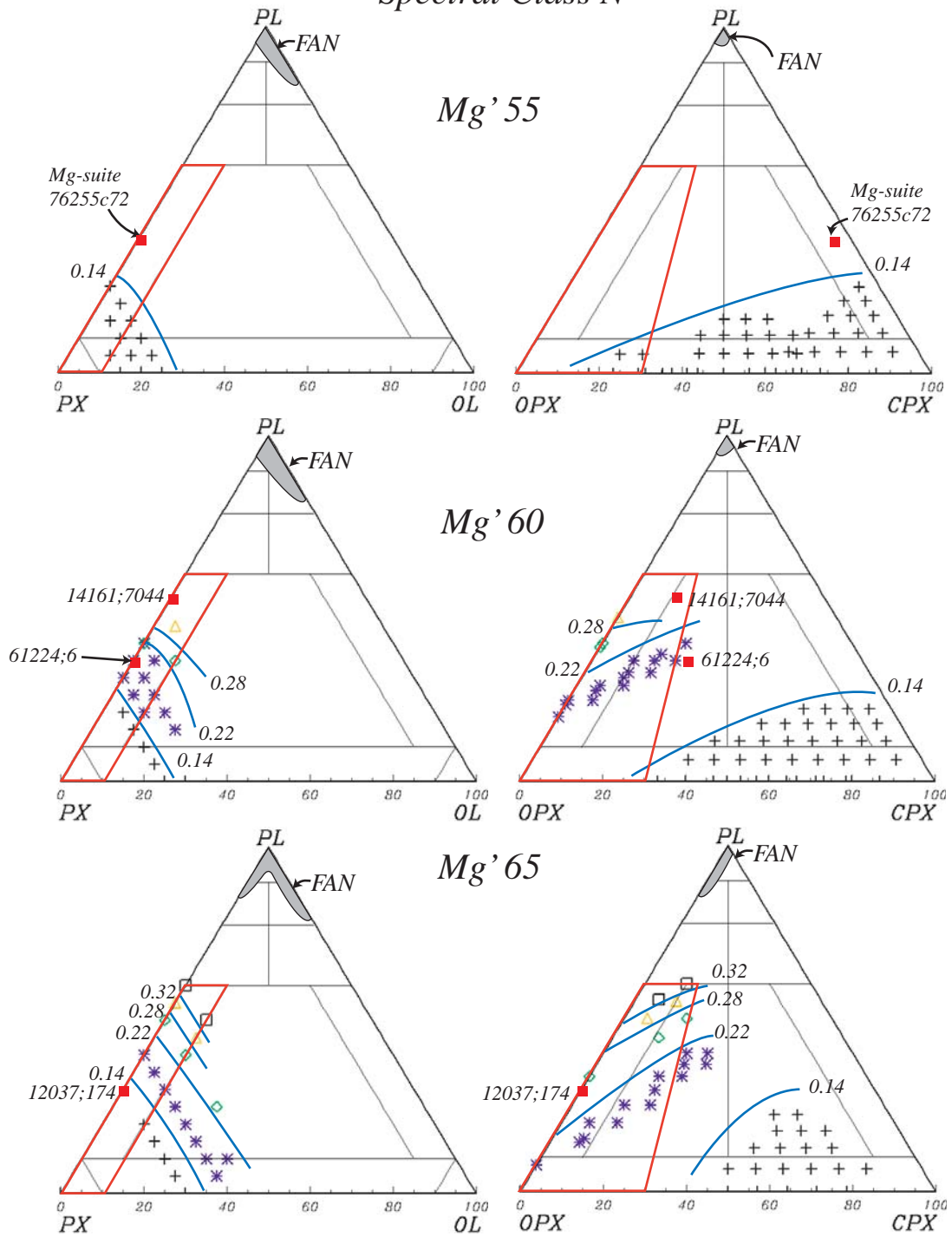


Figure A2.10a: cont.

Spectral Class N

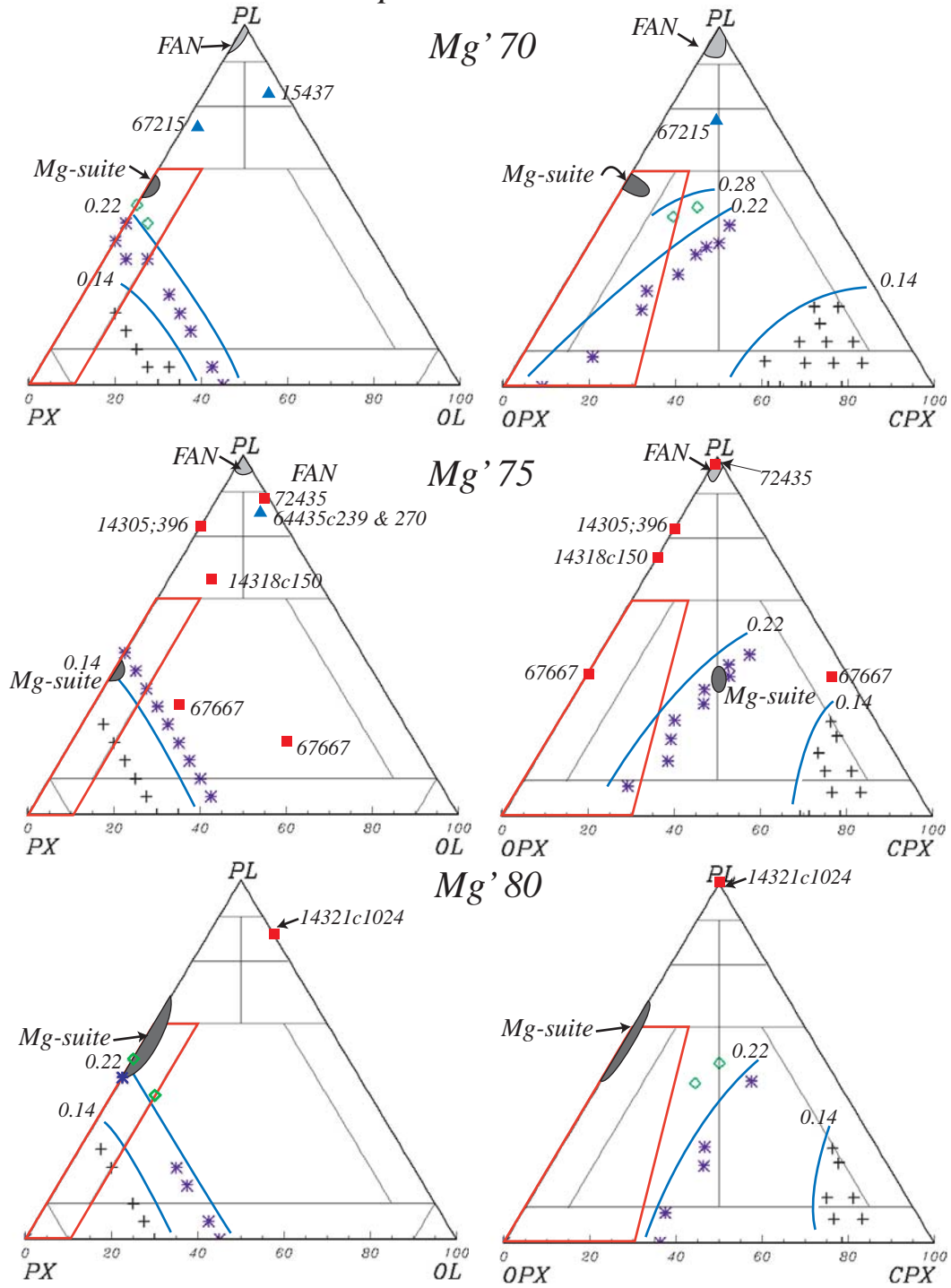


Figure A2.10b:

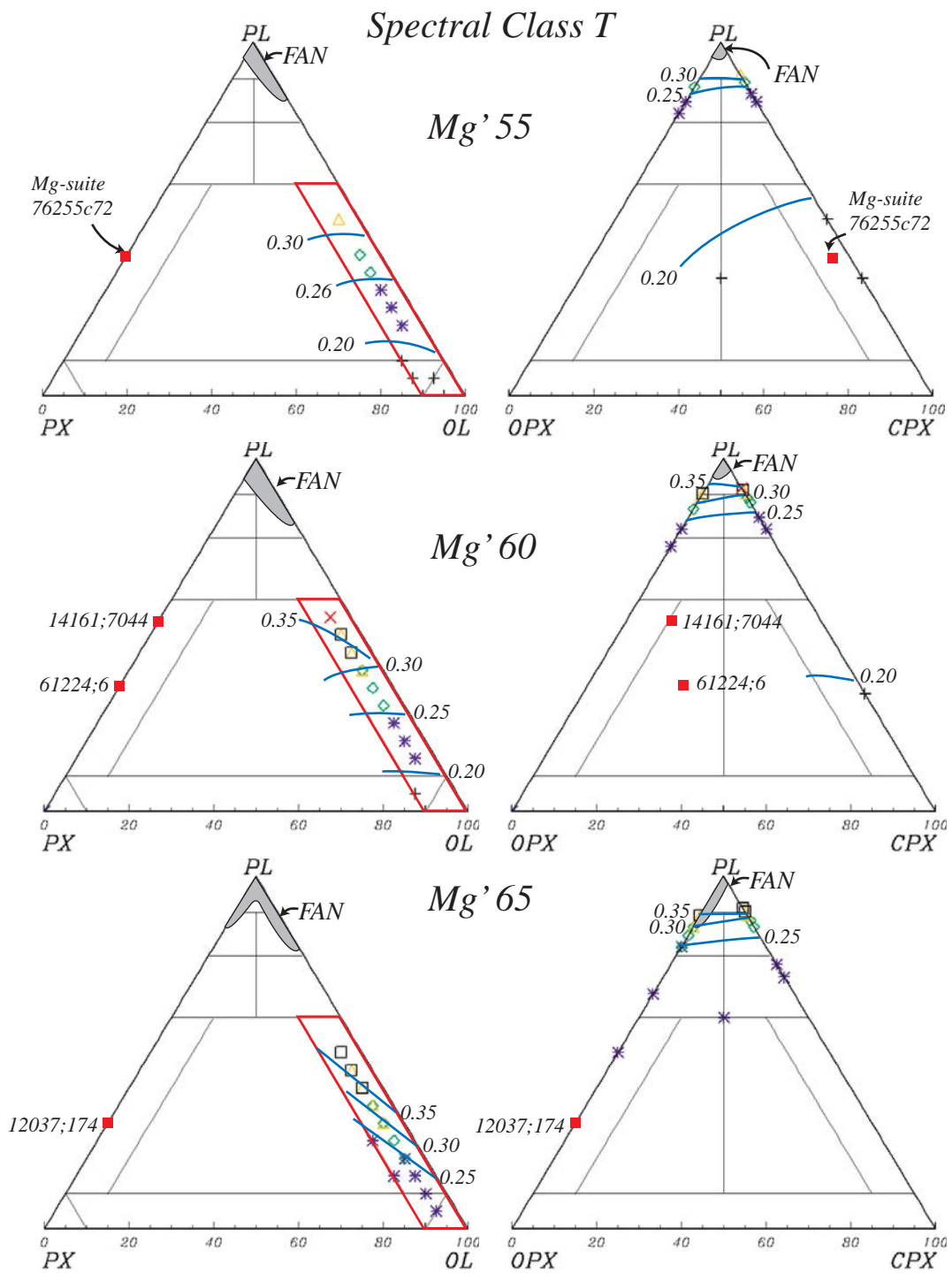
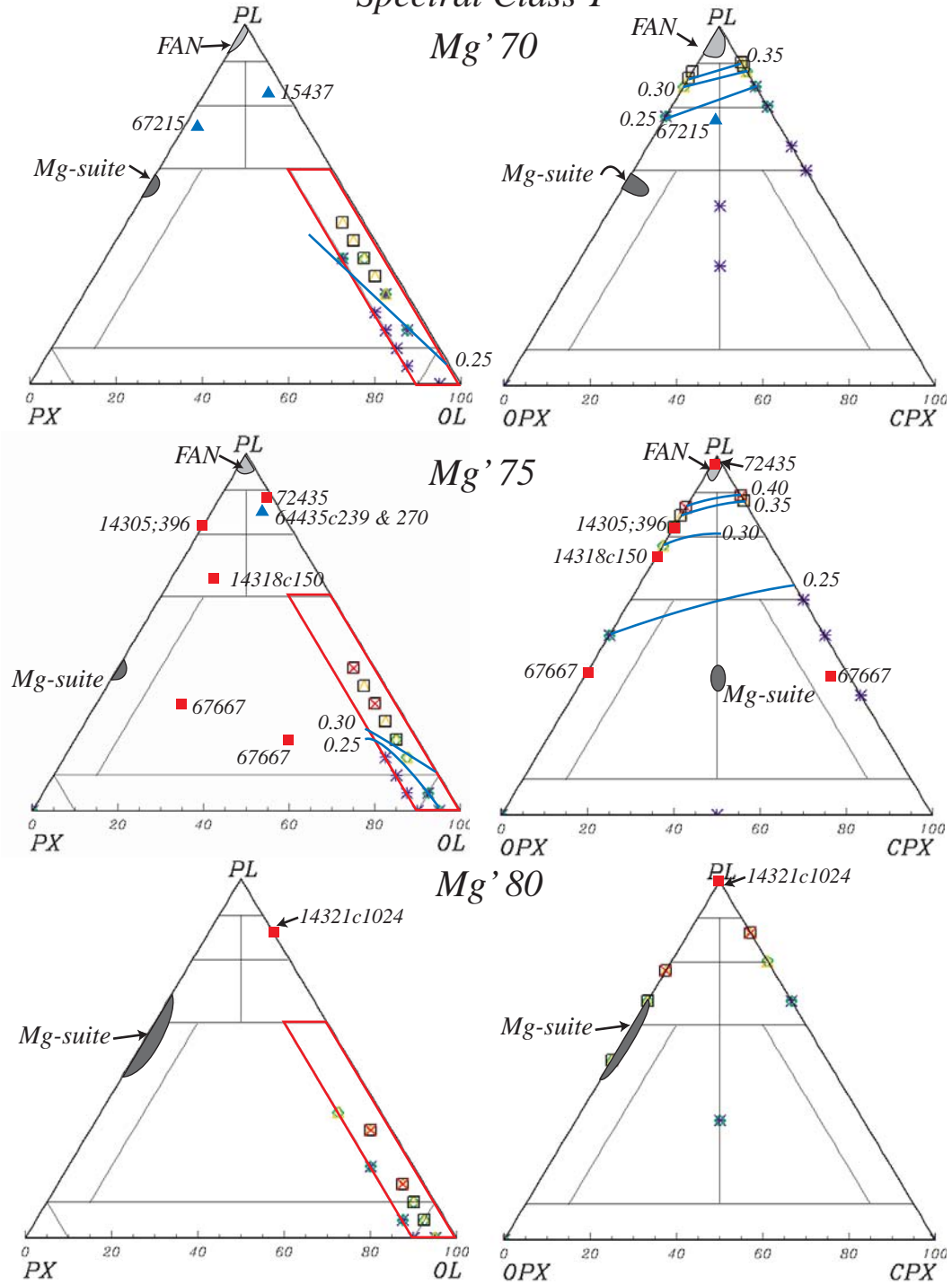


Figure A2.11a: cont.

Spectral Class T



Spectral Class T
Mg' 85

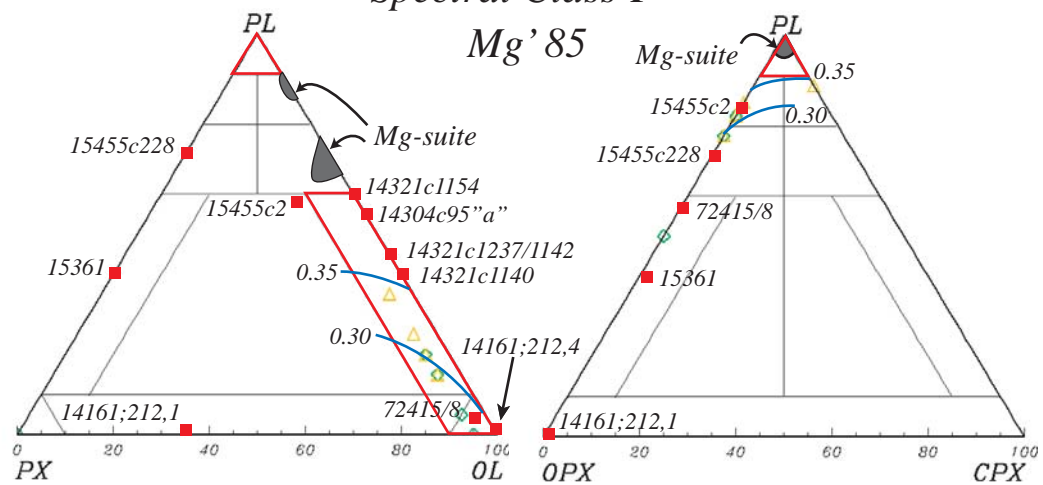


Figure A2.11c: cont.

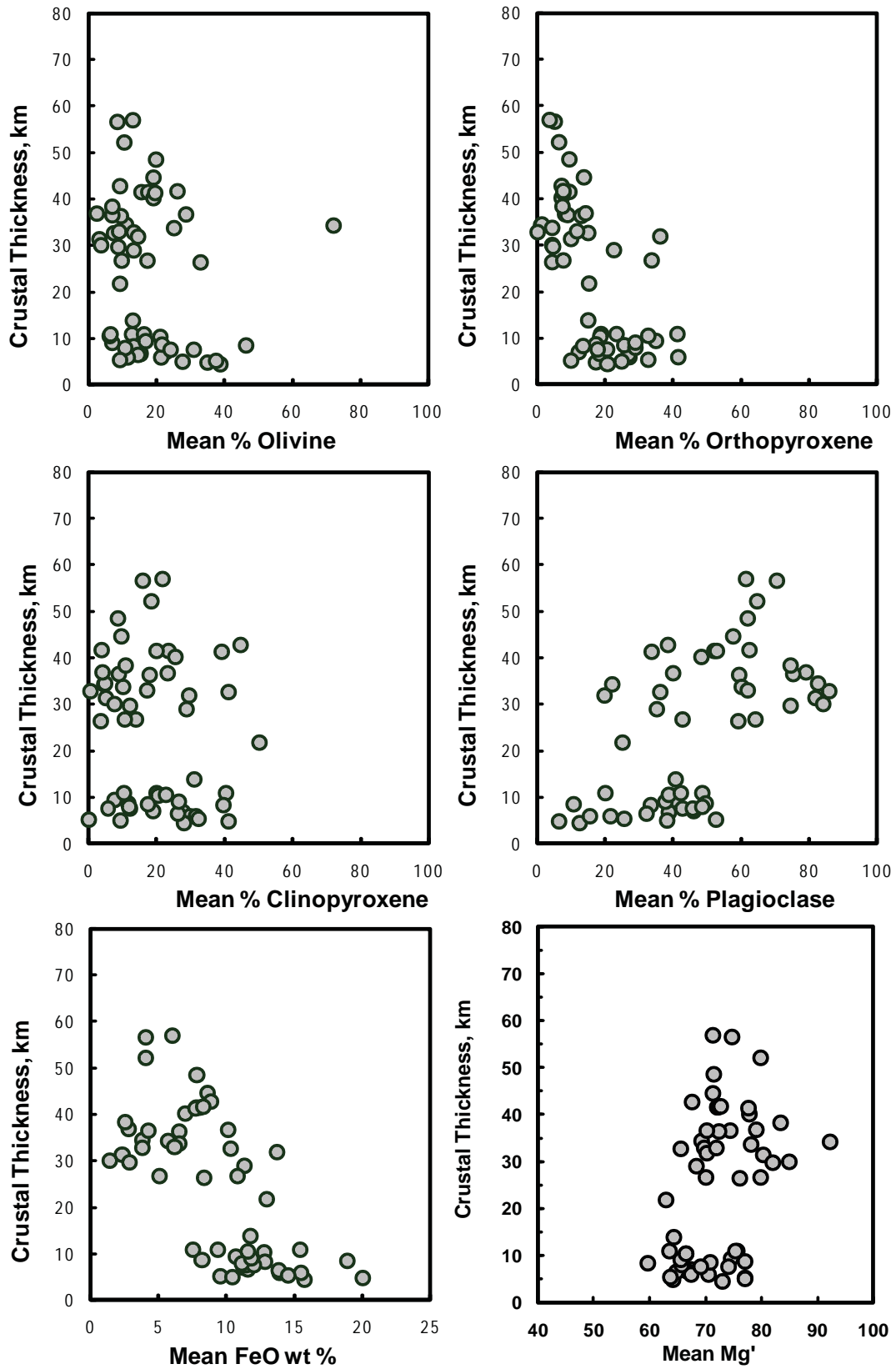


Figure A3.1: Mean lunar impact crater central peak mineralogy and chemistry versus crustal thickness (T_2).

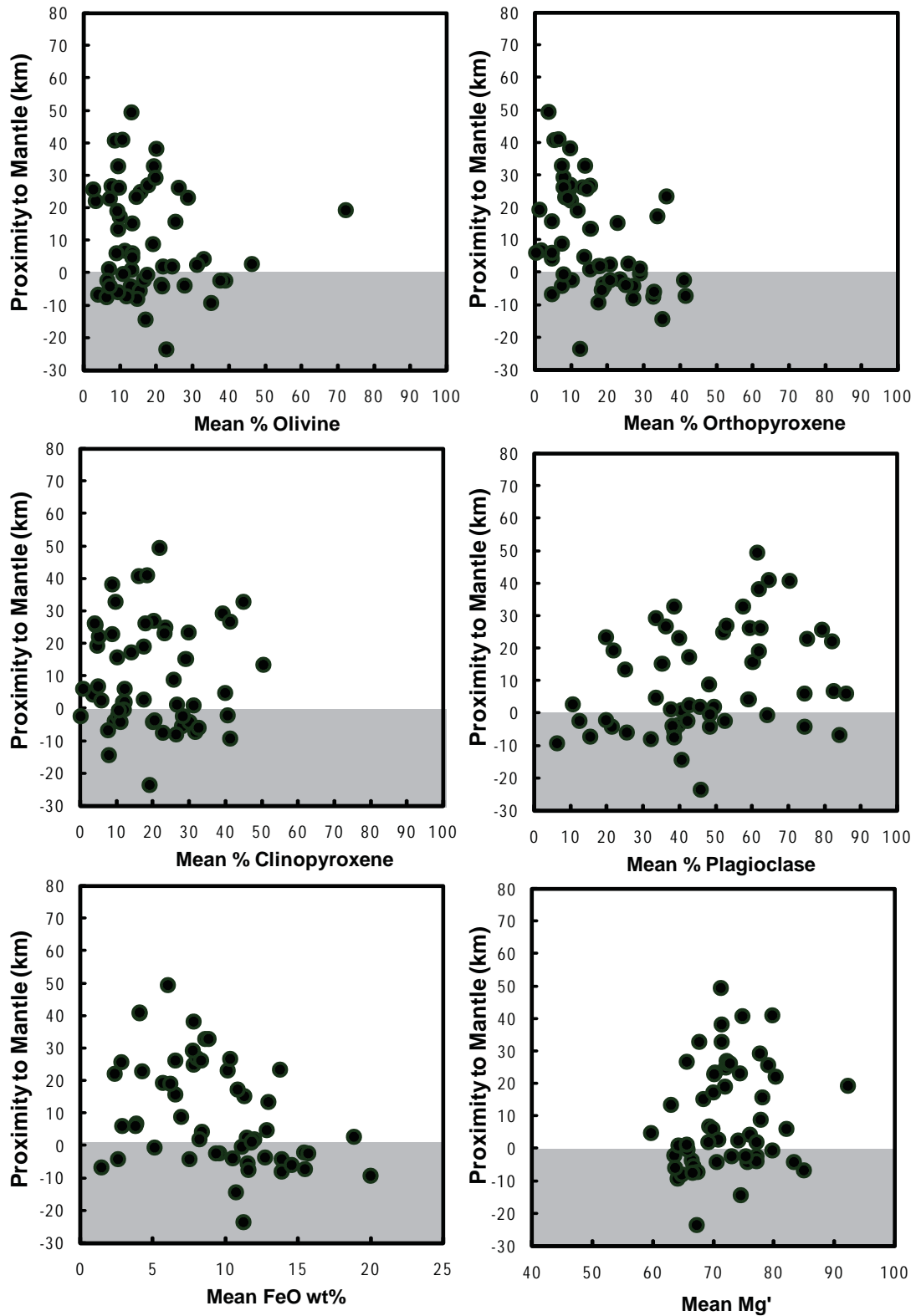


Figure A3.2: Mean lunar impact crater central peak mineralogy and chemistry versus peak origin relative to the crust mantle boundary (e.g., T₂-D₁). Proximity to mantle less than zero denotes materials plausible derived from the lunar mantle (in grey).

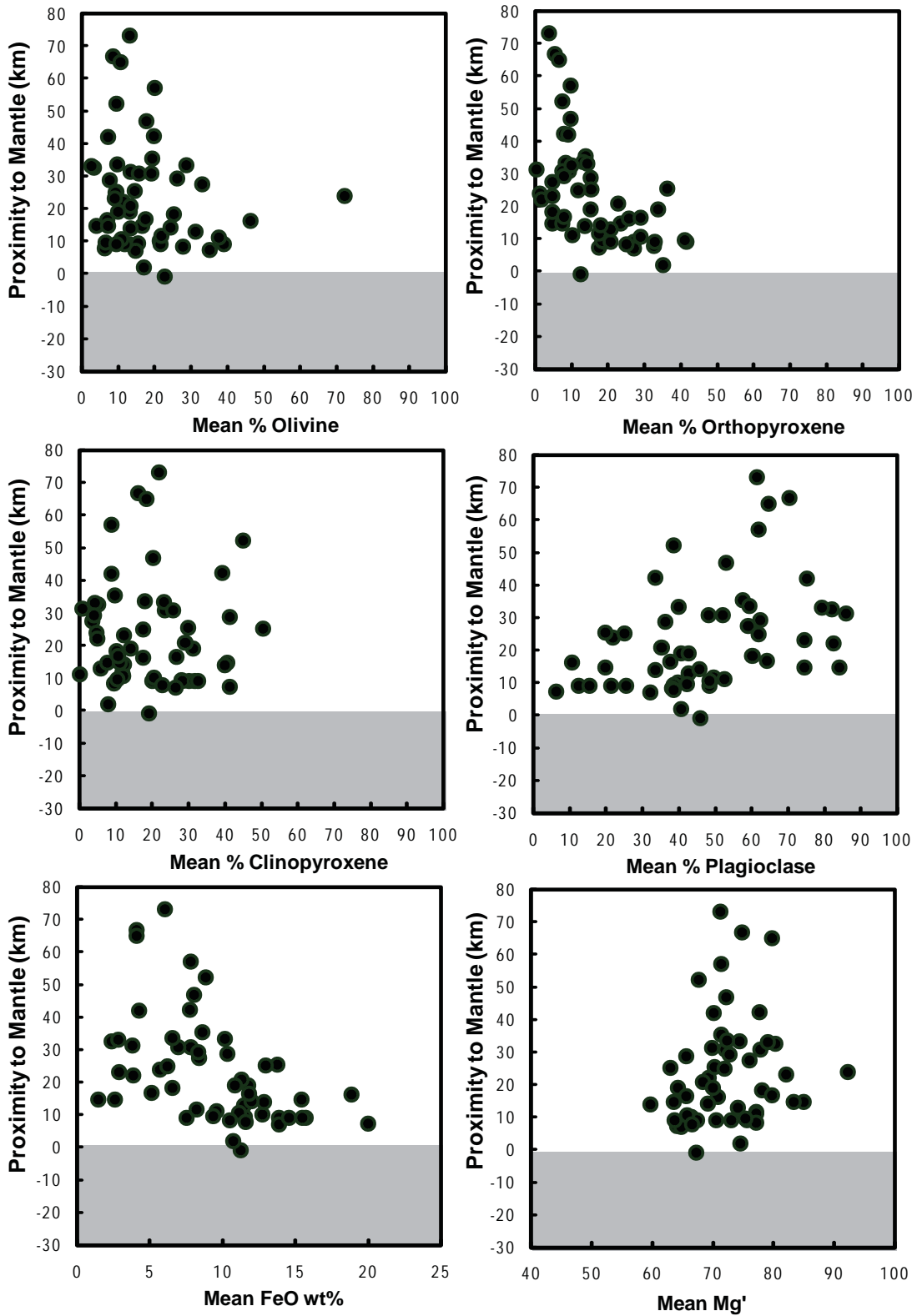


Figure A3.3: Mean lunar impact crater central peak mineralogy and chemistry versus peak origin relative to the crust mantle boundary (e.g., T₁-D₂).

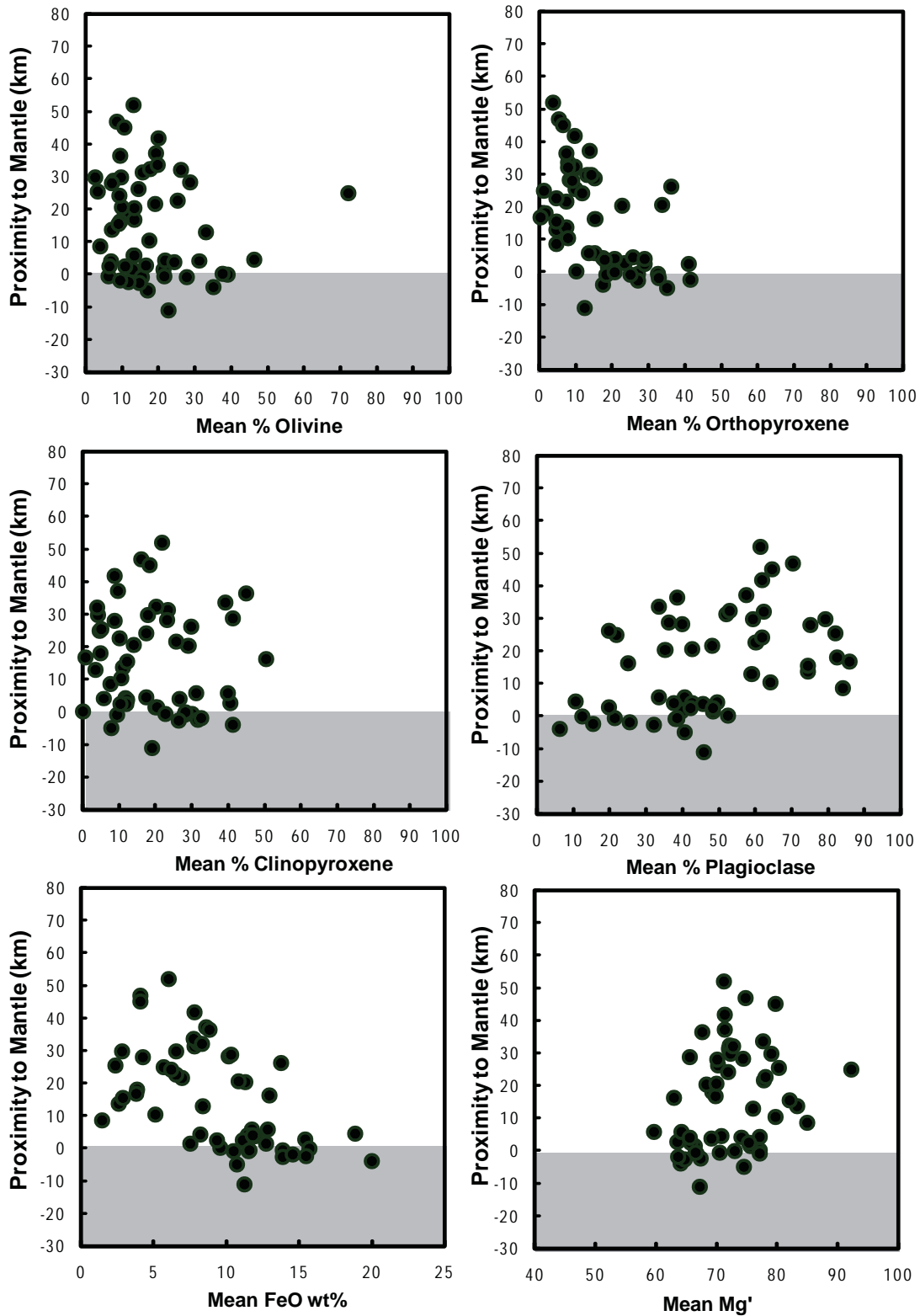


Figure A3.4: Mean lunar impact crater central peak mineralogy and chemistry versus peak origin relative to the crust mantle boundary (e.g., T₂-D₂).

APPENDIX B

Table B5.1: Mare basalt mineralogies (dominant silicates) and Mg'.

Classification	Sample #	Study	Pl	Px	Low-Ca Px	Mg'	High-Ca Px	Mg'	OI	Mg'	Mg' _{min}	Mg' _{bulk}	References
Apollo 11 High-Ti, High-K Basalts	10022	1	24.0	75.1	6.9	53.0	63.9	63.5	0.9	66.9	62.5	42.0	Planetary Materials; Papike et al. 1974 Beaty and Albee 1978
	10057	1	27.4	72.6	5.9	54.4	62.2	62.8	0.1	69.3	62.1	41.0	Planetary Materials; Papike et al. 1974 Beaty and Albee 1978
		2	31.8	68.1	5.9	54.4	62.2	62.8	0.1	69.3	62.1	41.0	Planetary Materials; Papike et al. 1974 Beaty and Albee 1978
	10017	1	36.1	63.9	5.3	57.7	62.9	63.0		62.6	62.6	40.0	Planetary Materials; Papike et al. 1974 Beaty and Albee 1978
		2	29.7	70.3	8.9	59.4	61.3	66.4	0.2	67.5	65.5	40.0	Planetary Materials; Papike et al. 1974 Beaty and Albee 1978
	10024	1	23.9	76.1	8.9	59.4	61.3	66.4	0.2	67.5	65.5	40.0	Planetary Materials; Papike et al. 1974 Beaty and Albee 1978
		2	25.6	74.4	8.9	59.4	61.3	66.4	0.2	67.5	65.5	40.0	Planetary Materials; Papike et al. 1974 Beaty and Albee 1978
	10072	1	26.2	73.8	8.9	59.4	61.3	66.4	0.2	67.5	65.5	40.0	Planetary Materials; Papike et al. 1974 Beaty and Albee 1978
		2	26.2	73.8	8.9	59.4	61.3	66.4	0.2	67.5	65.5	40.0	Planetary Materials; Papike et al. 1974 Beaty and Albee 1978
	Apollo 11 High-Ti, Low-K Basalts	10020	1	38.1	53.9	6.1	30.2	48.9	77.7	4.3	66.7	72.0	42.0
10045		2	26.4	67.7	4.6	18.7	43.2	67.5	6.2	67.6	63.3	38.0	Planetary Materials; Papike et al. 1974 Beaty and Albee 1978
		3	33.8	62.8	4.6	18.7	43.2	67.5	6.2	67.6	63.3	38.0	Planetary Materials; Papike et al. 1974 Beaty and Albee 1978
10062		4	37.9	54.3	6.1	30.2	48.9	77.7	4.3	66.7	72.0	42.0	Planetary Materials; Papike et al. 1974 Beaty and Albee 1978
		5	38.4	55.9	4.4	16.4	51.5	60.4	5.8	69.8	58.1	42.0	Planetary Materials; Papike et al. 1974 Beaty and Albee 1978
10003		1	32.3	63.9	4.6	18.7	43.2	67.5	6.2	67.6	63.3	38.0	Planetary Materials; Papike et al. 1974 Beaty and Albee 1978
		2	40.7	55.0	4.6	18.7	43.2	67.5	6.2	67.6	63.3	38.0	Planetary Materials; Papike et al. 1974 Beaty and Albee 1978
10050		1	29.6	64.2	12.1	50.4	46.9	57.0	0.6	41.6	55.5	48.0	Planetary Materials; Papike et al. 1974 Beaty and Albee 1978
		2	46.0	47.8	8.3	54.4	50.4	63.4	0.9	63.2	62.1	38.0	Planetary Materials; Papike et al. 1974 Beaty and Albee 1978
Apollo 17 High-Ti, Low-K Basalts		74235	1	41.4	58.0	9.0	12.8	48.8	58.7	0.5	0.5	51.0	35.0
	70215	2	35.9	64.1	10.6	8.8	46.4	58.7	0.1	0.5	49.3	37.0	Planetary Materials; Papike et al. 1974 Beaty and Albee 1978
		3	40.4	59.0	10.6	8.8	46.4	58.7	0.1	0.5	49.3	37.0	Planetary Materials; Papike et al. 1974 Beaty and Albee 1978
	74275	1	36.5	62.1	5.3	9.5	50.8	60.0	0.2	0.5	55.1	37.0	Planetary Materials; Papike et al. 1974 Beaty and Albee 1978
		2	40.4	58.7	6.6	13.9	48.3	58.0		52.7	52.7	37.0	Planetary Materials; Papike et al. 1974 Beaty and Albee 1978 Dowty et al. 1975
	74275	3	43.8	56.0	6.6	13.9	48.3	58.0		52.7	52.7	37.0	Planetary Materials; Papike et al. 1974 Beaty and Albee 1978 Dowty et al. 1975
		4	45.1	54.9	6.6	13.9	48.3	58.0		52.7	52.7	37.0	Planetary Materials; Papike et al. 1974 Beaty and Albee 1978 Dowty et al. 1975
	74235	1	32.4	65.6	6.6	13.9	48.3	58.0		52.7	52.7	37.0	Planetary Materials; Papike et al. 1974 Beaty and Albee 1978 Dowty et al. 1975
		2	37.2	53.8	6.6	13.9	48.3	58.0		52.7	52.7	37.0	Planetary Materials; Papike et al. 1974 Beaty and Albee 1978 Dowty et al. 1975
	74275	1	34.4	65.6	6.6	13.9	48.3	58.0		52.7	52.7	37.0	Planetary Materials; Papike et al. 1974 Beaty and Albee 1978 Dowty et al. 1975
2		19.7	65.8	6.6	13.9	48.3	58.0		52.7	52.7	37.0	Planetary Materials; Papike et al. 1974 Beaty and Albee 1978 Dowty et al. 1975	
74275	3	27.9	52.9	6.6	13.9	48.3	58.0		52.7	52.7	37.0	Planetary Materials; Papike et al. 1974 Beaty and Albee 1978 Dowty et al. 1975	
	4	23.4	52.4	6.6	13.9	48.3	58.0		52.7	52.7	37.0	Planetary Materials; Papike et al. 1974 Beaty and Albee 1978 Dowty et al. 1975	

Table B5.1. Continued.

Classification	Sample #	Study	Pi	Px	Low-Ca Px	Mg'	High-Ca Px	Mg'	Oi	Mg'	Mg' _{min}	Mg' _{bulk}	References
Apollo 17 High-Ti, Low-K Basalts	70017	1	33.8	64.9					1.3			49.0	Planetary Materials; Papike et al. 1974
	70035	2	34.9	61.7					3.4			49.0	Planetary Materials; Papike et al. 1974
		1	36.1	63.9	29.9				2.3			41.0	Papike et al. 1974
	75055	2	36.7	63.3	38.5								Planetary Materials; Papike et al. 1974
Apollo 12, Ilmenite Basalts	12022	1	13.8	67.3					18.9			47.0	Planetary Materials; Papike et al. 1976
	12063		25.0	71.8					3.2			45.0	Planetary Materials; Papike et al. 1976
	12051	1	26.3	73.7								38.0	Planetary Materials; Papike et al. 1976
	12005	2	35.5	64.5								62.0	Planetary Materials; Papike et al. 1976
Apollo 17, Ilmenite Basalts	70017	1	33.8	64.9					1.3				Longhi et al. 1974
	70035	2	33.6	65.2					1.2				Brown et al. 1975
		3	25.4	74.0					0.5				Roedder, Weiblen 1975
		1	34.9	63.9					1.2				Brown et al. 1975
70135	2	34.9	61.7					3.4					Weigand 1973
	3	27.6	72.4										Roedder and Weiblen 1975
	1	29.3	65.8					4.8					Roedder and Weiblen 1975
	2	36.7	59.7					3.6					Brown et al. 1975
Apollo 17, Ilmenite Basalts	70138	1	29.6	66.4					4.0				Neal et al. 1989
	70139		52.1	44.8					3.1				Neal et al. 1989
	70145		42.2	55.2					2.6				Neal et al. 1989
	70215	1	37.2	53.8					9.0				Longhi et al. 1974
70255	2	22.0	70.7						7.3				Dymek et al. 1975
	3	20.3	65.1					14.6					Brown et al. 1975
	4	22.0	70.6	70.6	69.6			69.5					Brown et al. 1975
		21.9	70.7					7.4					Brown et al. 1975
Ilmenite Basalt	75015		36.0	63.8					0.3				Brown et al. 1975
	75035	1	42.9	57.1									Longhi et al. 1974
		2	41.9	58.1									Brown et al. 1975
	75055	3	40.8	59.2									Meyer and Boctor 1974
75055	1	36.3	63.7										Brown et al. 1975
	2	39.8	60.2										Dymek et al. 1975
	3	36.1	63.9										Kriedelbaugh and Weill 1973
	4	39.5	60.5	7.1	18.4	53.4	56.4	51.9					
Vesicular Ilmenite Basalt	71055	1	31.0	66.2					2.8				Brown et al. 1974
		2	35.5	60.5					3.9				Dymek et al. 1975
		3	39.2	56.8					4.1				Taylor et al. 1992
		4	36.1	60.4	6.7	63.3	53.6	64.5	3.5	70.0	64.7		Dymek et al. 1975

Table B5.1: Continued.

Classification	Sample #	Study	Pl	Px	Low-Ca Px	Mg'	High-Ca Px	Mg'	OI	Mg'	Mg'_{min}	Mg'_{bulk}	References
Vuggy Ilmenite Basalt	75075		27.9	70.4					1.6				Brown et al. 1975
Apollo 12	12007		45.3	54.7	22.0	27.8	32.7	49.9			41.0		Baldrige et al. 1979
Pigeonite Basalts	12011		33.6	58.0	15.9	38.8	42.2	61.1	8.4	65.6	56.4		Baldrige et al. 1979
	12043		35.9	63.0	28.0	39.8	35.1	50.2	1.0	65.8	45.9		
	12052		19.3	76.3					4.4				42.0 Planetary Materials; Papike et al. 1974
	12053		22.3	75.5					2.2				42.0 Planetary Materials; Papike et al. 1974
	12065	1	19.8	77.0					3.2				42.0 Planetary Materials; Papike et al. 1974
		2	21.0	78.1					0.9				Planetary Materials; Papike et al. 1974
	12021	1	25.3	74.7									41.0 Planetary Materials; Papike et al. 1974
		2	24.4	75.6									Planetary Materials; Papike et al. 1974
		3	32.9	67.1									Planetary Materials; Papike et al. 1974
	12064		33.9	64.3					1.8				37.0 Planetary Materials; Papike et al. 1974
Apollo 15,	15597			100.0									44.0 Planetary Materials; Papike et al. 1974
Pigeonite Basalts	15595			100.0									45.0 Planetary Materials; Papike et al. 1974
	15499			98.1					1.9				45.0 Planetary Materials; Papike et al. 1974
	15476	1	26.2	73.8									43.0 Planetary Materials; Papike et al. 1974
		2	28.4	71.6									Planetary Materials; Papike et al. 1974
	15475		27.3	72.7									44.0 Planetary Materials; Papike et al. 1974
	15076		30.1	69.9									43.0 Planetary Materials; Papike et al. 1974
	15085		50.9	49.1									45.0 Planetary Materials; Papike et al. 1974
	15058		28.5	69.6					1.9				45.0 Planetary Materials; Papike et al. 1974
Apollo 12, Olivine Basalts	12009			31.3					68.7				50.0 Planetary Materials; Papike et al. 1976
	12004		15.9	70.3					13.8				51.0 Planetary Materials; Papike et al. 1976
	12002		19.6	63.5					16.9				55.0 Planetary Materials; Papike et al. 1976
	12075	1	6.5	71.4					22.1				55.0 Planetary Materials; Papike et al. 1976
		2	14.4	63.2					22.4				Planetary Materials; Papike et al. 1976
	12018		21.2	66.6					12.2				56.0 Planetary Materials; Papike et al. 1976
	12020		22.1	65.7					12.2				55.0 Planetary Materials; Papike et al. 1976
	12040	1	20.8	48.4					30.8				58.0 Planetary Materials; Papike et al. 1976
		2	23.5	52.9					23.5				Planetary Materials; Papike et al. 1976
	12035		21.1	44.6					34.3				55.0 Planetary Materials; Papike et al. 1976
Apollo 15, Olivine Basalts	15545	1	25.1	65.7					9.2				45.0 Planetary Materials; Papike et al. 1976
		2	25.3	70.8					3.9				Planetary Materials; Papike et al. 1976
	15556		40.0	59.9					0.1				39.0 Planetary Materials; Papike et al. 1976
	15016		23.7	68.3					8.0				47.0 Planetary Materials; Papike et al. 1976
	15555	1	26.3	68.4					5.3				47.0 Planetary Materials; Papike et al. 1976
		2	32.0	55.2					12.8				Longhi et al. 1972
		3	28.5	61.7					9.8				McGee et al. 1977

Table B5.1: Continued.

Classification	Sample #	Study	Pl	Px	Low-Ca Px	Mg'	High-Ca Px	Mg'	OI	Mg'	Mg' _{min}	Mg' _{bulk}	References
Apollo 15, Olivine Basalts		4	36.8	42.1					21.1				Hever et al. 1972
		5	36.8	42.1					21.1				Nord et al. 1973
Vesicular Olivine Basalt	15016	1	25.8	65.6					8.6				Brown et al. 1972
		2	23.7	68.3					8.0				Paplike et al. 1976
		3	22.3	69.7					8.0				McGee et al. 1977
High-Al; Feldspathic Basalt	12031		45.0	55.0									Beaty et al. 1979
	12038		47.4	52.6									Beaty et al. 1979
	12072		41.6	52.3	17.9	37.0	34.5	62.8	6.1	70.6	55.7		Beaty et al. 1979
	14310	1	61.1	38.9	31.7		7.2						Gancarz et al. 1971
	impact melt	2	68.7	31.3									Carlson et al. 1978
non-mare basalt		3	68.0	32.0									Ridley et al. 1972
		4	56.2	43.8									Brown et al. 1972
		5	61.9	38.1	38.1								Longhi et al. 1972
	Luna 20-22012		68.0	17.5	16.4	75.9	1.2	61.9	14.5	78.0	76.4		Albee et al. 1977
Apollo 14, High-Al Basalts	14053		44.4	55.6									Planetary Materials; Dickenson et al. 1985
	14702		42.2	55.0					2.8				Planetary Materials; Dickenson et al. 1985
Luna 16, High-Al Basalts	B-1		44.4	55.6									Planetary Materials; Dickenson et al. 1985
Apollo 17, VLT Basalts	70008-356		35.3	62.2									Planetary Materials; Vaniman and Paplike 1977; Laut et al. 1978; Taylor et al. 1978
	70008-370		29.8	65.6					5.5		52.0		Planetary Materials; Vaniman and Paplike 1977; Laut et al. 1978; Taylor et al. 1978
Luna 24, VLT Basalts	24077-4		12.7	37.6									Planetary Materials; Vaniman and Paplike 1977; Laut et al. 1978; Taylor et al. 1978
	24174-7		35.0	59.5					49.8				Planetary Materials; Vaniman and Paplike 1977; Laut et al. 1978; Taylor et al. 1978
	14053		55.6	44.4					5.5				Planetary Materials; Vaniman and Paplike 1977; Laut et al. 1978; Taylor et al. 1978
		interior exterior	45.9 42.9	52.4 52.8					1.7 4.3				Gancarz et al. 1971 Patchen and Taylor 2004 Patchen and Taylor 2004
VLT basalt	Luna24170	1	35.3	54.7					10.0				Bence et al. 1977
		2	35.3	54.7					10.0				Bence and Grove 1978
		3	30.0	65.0					5.0				Lumatic Asylum 1978
		4	24.5	62.2					13.3				Taylor et al. 1977

Table B5.1: Continued.

Classification	Sample #	Study	Pl	Px	Low-Ca Px	Mg'	High-Ca Px	Mg'	OI	Mg'	Mg'_{min}	Mg'_{bulk}	References
KREEP Basalt	15382	1	59.0	41.0									Dowty et al. 1976
		2	43.6	56.4	56.4								Crawford and Hollister 1977
		3	51.2	48.8									Taylor et al. 1991
	15386	1	41.2	58.8									Steele et al. 1972
		2	50.0	50.0									Taylor et al. 1991
	15434-66		36.9	63.1									Crawford and Hollister 1977
	15263-42		54.9	45.1									Simon et al. 1988
	15303-51		63.3	36.7									Simon et al. 1988
	15304-46		53.7	46.3									Simon et al. 1988
	15314-109		50.8	49.2									Simon et al. 1988
15434-181		49.6	50.4									Simon et al. 1988	
Mare Basalt clast	60639		35.4	59.6				5.1					Dowty et al. 1976; Delano 1975; Warner et al. 1976
Luna Basalts	Luna16B1		44.4	55.6									Albee
	Luna16G37		52.6	31.6				15.8					Steele
	Luna16G36		34.8	47.2				18.0					Hollister
Unclassified	10029		42.3	57.3	13.5	54.4	43.9	52.2	0.4	45.2	52.7		Beaty and Albee 1978
	10032		29.6	70.3	8.9	59.3	61.3	68.6	0.1	67.1	67.4		Beaty and Albee 1978
	10049		32.4	67.6	2.8	52.1	64.8	60.0			59.7		Beaty and Albee 1978
	10060-71			93.8	1.2		92.6	67.8	6.2	69.9	67.1		Beaty and Albee 1978
	10062		46.1	47.8	4.6	18.7	43.2	61.7	6.1	68.3	58.8		Beaty and Albee 1978
	10069		31.2	68.8	5.7		63.1	59.6	0.1	68.6	54.7		Beaty and Albee 1978
	10071		32.5	65.8	6.1	55.9	59.6	63.4	1.7	68.1	62.9		Beaty and Albee 1978
	10071-31 Iota		47.1	52.9	10.6	15.7	42.3	47.2			40.9		Beaty and Albee 1978
	10072		30.5	69.0	6.6	48.7	62.4	62.9	0.6	66.6	61.6		Beaty and Albee 1978
	10085,12-7			95.0	95.0	67.9			5.0	70.4	68.1		Beaty and Albee 1978
	10085-914		36.8	62.1	10.7		51.4		1.1	67.3			Beaty et al. 1979
	10085-924		40.4	46.9	2.7		44.3		12.7	68.9			Beaty et al. 1979
	10085-925		40.0	60.0	4.9		55.2						Beaty et al. 1979
	10085-926		40.0	53.8	4.8		48.9		6.2	71.6			Beaty et al. 1979
	10092-6		37.7	56.2	4.7	53.4	51.5	67.8	6.0	68.2	66.7		Beaty and Albee 1978
	74255		33.5	62.6	16.0	63.2	46.6	71.1	3.9	70.3	69.2		Dymek et al. 1975
	10002-118		37.9	59.5	4.9		54.6		2.7	69.7			Beaty et al. 1979
	10002-121		41.0	58.5	8.3	68.0	50.3	60.4	0.5	49.0	61.4		Beaty et al. 1979

REFERENCES

- Baker, M. B., and C. T. Herzberg (1980), Spinel cataclasites in 15445 and 72435, paper presented at Proc. Lunar Planet. Sci. Conf., Pergamon Press, Inc., Houston, TX.
- Bence, A. E., J. W. Delano, J. J. Papike, and K. L. Cameron (1974), Petrology of the highlands massifs and Taurus-Littrow - an analysis of the 2-4 mm soil fraction, *Proc. Lunar Planet. Sci. Conf.*, 5, 785-827.
- Bersch, M. G., G. J. Taylor, K. Keil, and M. D. Norman (1991), Mineral Compositions in Pristine Lunar Highland Rocks and the Diversity of Highland Magmatism, *Geophys. Res. Lett.*, 18(11), 2085-2088.
- Borg, L. E., M. Norman, L. Nyquist, D. Bogard, G. Snyder, L. A. Taylor, and M. Lindstrom (1999), Isotopic studies of ferroan anorthosite 62236: A young lunar crustal rock from a light-rare-earth-element-depleted source, *Geochim Cosmochim Acta*, 63, 2679-2691.
- Burns, R. G. (1993), *Mineralogical applications of crystal field theory*, 2nd ed., 551 pp., Cambridge University Press, Cambridge [England] ; New York, NY, USA.
- Bussey, D. B. J., and P. D. Spudis (2004), *The Clementine Atlas of the Moon*, Cambridge University Press.
- Cahill, J. T., P. G. Lucey, J. J. Gillis, and D. Steutel (2004), Verification of quality and compatibility for the newly calibrated Clementine NIR data set, paper presented at Lunar and Planet. Sci. Conf. XXXV, Houston, TX.

- Cahill, J. T., and P. G. Lucey (2007), Radiative transfer modeling of lunar highlands spectral classes and relationship to lunar samples, *J. Geophys. Res.-Planets*, *112*, 10.1029/2006JE002868.
- Cahill, J. T., P. G. Lucey, and S. Le Mouélic (2007), Apollo 17 landing site: evaluating a joint UVVIS-NIR FeO algorithm that nullifies topographic shading effects on lunar reflectance spectra, *Lunar Planet. Sci. Conf., XXXVIII*, #1967.
- Cahill, J. T. S., P. G. Lucey, and M. A. Wieczorek (2009), Compositional variations of the lunar crust: Results from radiative transfer modeling of central peak spectra, *J. Geophys. Res.-Planets*, 10.1029/2008JE003282.
- Cahill, J. T. S., P. G. Lucey, K. R. Stockstill-Cahill, and B. R. Hawke (2010a), Radiative transfer modeling of near-infrared reflectance of lunar highland and mare soils *J. Geophys. Res.-Planets*, *accepted pending revision*.
- Cahill, J. T. S., P. G. Lucey, K. R. Stockstill-Cahill, and B. R. Hawke (2010b), Radiative transfer modeling of near-infrared telescopic spectra of selected locations on the lunar nearside, *J. Geophys. Res.-Planets*, *in prep*.
- Chambers, J. G., L. A. Taylor, and A. Patchen (1995), Quantitative mineralogical characterization of lunar high-Ti mare basalts and soils for oxygen production, *J. Geophys. Res.*, *100*(E7), 14,391-314,401.
- Cintala, M. J., and R. A. F. Grieve (1998), Scaling impact melting and crater dimensions: Implications for the lunar cratering record, *Meteorit. Planet. Sci.*, *33*, 889-912.
- Clark, B. E., P. Lucey, P. Helfenstein, J. F. Bell, C. Peterson, J. Veverka, T. McConnochie, M. S. Robinson, B. Bussey, S. L. Murchie, N. I. Izenberg, and C. R. Chapman (2001), Space

weathering on Eros: Constraints from albedo and spectral measurements of Psyche crater, *Meteoritics & Planetary Science*, *36*(12), 1617-1637.

Clark, R. N., G. A. Swayze, K. E. Livo, R. F. Kokaly, S. J. Sutley, J. B. Dalton, R. R. McDougal, and C. A. Gent (2003), Imaging spectroscopy: Earth and planetary remote sensing with the USGS Tetracorder and expert systems, *J. Geophys. Res.*, *108*(E12), 5131.

Cloutis, E. A. (1985), Interpretive techniques for reflectance spectra of mafic silicates, Univ. of Hawaii, Honolulu.

Cloutis, E. A., M. J. Gaffey, T. L. Jackowski, and K. L. Reed (1986), Calibrations of Phase Abundance, Composition, and Particle-Size Distribution for Olivine-Ortho-Pyroxene Mixtures from Reflectance Spectra, *Journal of Geophysical Research-Solid Earth and Planets*, *91*(B11), 1641-1653.

Cloutis, E. A., M. J. Gaffey, D. G. W. Smith, and R. S. Lambert (1990a), Reflectance Spectra of Mafic Silicate Opaque Assemblages with Applications to Meteorite Spectra, *Icarus*, *84*(2), 315-333.

Cloutis, E. A., M. J. Gaffey, D. G. W. Smith, and R. S. J. Lambert (1990b), Metal Silicate Mixtures - Spectral Properties and Applications to Asteroid Taxonomy, *Journal of Geophysical Research-Solid Earth and Planets*, *95*(B6), 8323-8338.

Cloutis, E. A., J. M. Sunshine, and R. V. Morris (2004), Spectral reflectance-compositional properties of spinels and chromites: Implications for planetary remote sensing and geothermometry, *Meteoritics & Planetary Science*, *39*(4), 545-565.

Croft, S. K. (1980), Cratering flow fields: Implications for the excavation and transient expansion stages of crater formation, *Proc. Lunar Planet. Sci. Conf.*, *11*, 2347-2378.

- Dence, M. R. (1968), Shock zoning at Canadian craters: Petrography and structural implications, in *Shock metamorphism of natural materials*, edited by B. M. French and N. M. Short, pp. 169-184, Mono Book Corp., Baltimore.
- Denevi, B., P. G. Lucey, E. J. Hochberg, and D. Steutel (2007), Near-infrared optical constants of pyroxene as a function of iron and calcium content, *J. Geophys. Res.-Planets*, 10.1029/2006JE002802.
- Denevi, B. W., P. G. Lucey, and S. B. Sherman (2008), Radiative transfer modeling of near-infrared spectra of lunar mare soils: Theory and measurement, *J. Geophys. Res.-Planets*, 113(E2), 10.1029/2007je002929.
- Dixon, J. R., and J. J. Papike (1975), Petrology of anorthosites from the Descartes region of the moon: Apollo 16, *Proc. Lunar Planet. Sci. Conf.*, 6, 263-291.
- Dowty, E., K. Keil, and M. Prinz (1974), Igenous rocks from Apollo 16 rake sample (abstract), *Proc. Lunar Planet. Sci. Conf.*, 5, 174-176.
- Dymek, R. F., A. L. Albee, and A. A. Chodos (1976), Petrology and origin of Boulders #2 and #3, Apollo17 Station 2, *Proc. Lunar Planet. Sci. Conf.*, 7, 2335-2378.
- Ebihara, M., R. Wolf, P. H. Warren, and E. Anders (1992), Trace elements in 59 mostly highland Moon rocks, *Proc. Lunar Planet. Sci.*, 22, 417-426.
- Fischer, E. M., and C. M. Pieters (1994), Remote Determination of Exposure Degree and Iron Concentration of Lunar Soils Using Vis-Nir Spectroscopic Methods, *Icarus*, 111(2), 475-488.

- Fischer, E. M., and C. M. Pieters (1996), Composition and exposure age of the Apollo 16 Cayley and Descartes regions from Clementine data: Normalizing the optical effects of space weathering, *J. Geophys. Res.-Planets*, *101*(E1), 2225-2234.
- Floss, C., O. B. James, J. J. McGee, and G. Crozaz (1998), Lunar ferroan anorthosite petrogenesis: Clues from trace element distributions in FAN subgroups., *Geochimica Et Cosmochimica Acta*, *62*, 1255-1283.
- Gaddis, L. R., C. M. Pieters, and B. R. Hawke (1985), Remote-Sensing of Lunar Pyroclastic Mantling Deposits, *Icarus*, *61*(3), 461-489.
- Gillis-Davis, J. J., P. G. Lucey, and B. R. Hawke (2006), Testing the relation between UVVIS color and TiO₂ content of the Lunar Maria, *Geochimica et Cosmochimica Acta*, *70*(24), 6079-6102.
- Goodrich, C. A., G. J. Taylor, K. Keil, G. W. Kallemeyn, and P. H. Warren (1986), Alkali Norite, Troctolites, and Vhk Mare Basalts from Breccia-14304, *J. Geophys. Res.-Solid Earth and Planets*, *91*(B4), D305-D318.
- Hapke, B. (1981), Bidirectional Reflectance Spectroscopy .1. Theory, *J. Geophys. Res.*, *86*(NB4), 3039-3054.
- Hapke, B. (1993), *Theory of Reflectance and Emittance Spectroscopy*, Cambridge University Press, New York.
- Hapke, B. (2001), Space weathering from Mercury to the asteroid belt, *J. Geophys. Res.-Planets*, *106*(E5), 10039-10073.

- Haruyama, J., M. Ohtake, T. Matsunaga, T. Morota, C. Honda, Y. Yokota, M. Abe, Y. Ogawa, H. Miyamoto, A. Iwasaki, C. M. Pieters, N. Asada, H. Demura, N. Hirata, J. Terazono, S. Sasaki, K. Saiki, A. Yamaji, M. Torii, and J. L. Josset (2009), Long-Lived Volcanism on the Lunar Farside Revealed by SELENE Terrain Camera, *Science*, *323*(5916), 905-908, DOI 10.1126/science.1163382.
- Haskin, L. A., P. A. Helmke, D. P. Blanchard, J. W. Jacobs, and K. Telander (1973), Major and trace element abundances in samples from the lunar highlands, *Proc. Lunar Planet. Sci. Conf.*, *4*, 1275-1296.
- Hawke, B. R., P. G. Lucey, G. J. Taylor, J. F. Bell, C. A. Peterson, D. T. Blewett, K. Horton, and G. A. Smith (1991), Remote-Sensing Studies of the Orientale Region of the Moon - a Pre-Galileo View, *Geophysical Research Letters*, *18*(11), 2141-2144.
- Hawke, B. R., C. A. Peterson, P. G. Lucey, G. J. Taylor, D. T. Blewett, B. A. Campbell, C. R. Coombs, and P. D. Spudis (1993), Remote sensing studies of the terrain northwest of Humorum Basin, *Geophys. Res. Lett.*, *20*, 419-422.
- Hawke, B. R., C. A. Peterson, D. T. Blewett, D. B. J. Bussey, P. G. Lucey, G. J. Taylor, and P. D. Spudis (2003), Distribution and modes of occurrence of lunar anorthosite, *J. Geophys. Res.-Planets*, *108*(E6), 5050.
- Heiken, G., D. T. Vaniman, and B. M. French (1991), *Lunar Sourcebook: A User's Guide to the Moon*, XIX, 736 , 716 color plates pp., Cambridge University Press, New York.
- Heiken, G. H., and D. S. McKay (1974), Petrography of Apollo 17 soils, *Proc. Lunar Sci. Conf. 5th*, 843-860.

- Herbert, F., M. J. Drake, and C. P. Sonnett (1978), Geophysical and geochemical evolution of the lunar magma ocean, *Proceedings of the Lunar and Planetary Science Conference, IX*, 249-264.
- Hess, P. C. (1994), Petrogenesis of Lunar Troctolites, *J. Geophys. Res.-Planets*, 99(E9), 19083-19093.
- Higgins, S. J., L. A. Taylor, J. G. Chambers, A. Patchen, and D. S. McKay (1996), X-ray digital-imaging petrography: Technique development for lunar mare soils, *Meteoritics & Planetary Science*, 31(3), 356-361.
- Isaacson, P. J., and C. M. Pieters (2008), Detecting a broader lunar magnesian suite with orbital spectroscopy, *Lunar and Planetary Science Conference, XXXIX*, #1783.
- James, O. B., and J. J. McGee (1979), Consortium breccia 73255: Genesis and history of two coarse-grained "norite" clasts, *Proc. Lunar Planet. Sci. Conf.*, 10, 713-743.
- James, O. B. (1980), Rocks of the early lunar crust, *Proc. Lunar and Planet. Sci. Conf.*, 11th, 365-393.
- James, O. B., and M. K. Flohr (1983), Subdivision of the Mg-suite noritic rocks into Mg-gabbro-norites and Mg-norites, *Proc. Lunar Planet. Sci. Conf.*, 13th, Part 2, in *J. Geophys. Res., suppl.*, 88, A603-A614.
- James, O. B., M. K. Flohr, and M. M. Lindstrom (1984), Petrology and geochemistry of lunar dimict breccia 61015, *Proc. Lunar Planet. Sci. Conf.*, 89, C63-C86.

- James, O. B., M. M. Lindstrom, and M. K. Flohr (1989), Ferroan Anorthosite from Lunar Breccia 64435: Implications for the Origin and History of Lunar Ferroan Anorthosites, *Proc. Lunar Planet. Sci. Conf., XIV*, 219-243.
- James, O. B., M. M. Lindstrom, and J. J. McGee (1991), Lunar ferroan anorthosite 60025: Petrology and chemistry of mafic lithologies, *Proc. Lunar Planet. Sci. Conf., 21*, 63-87.
- Jolliff, B. L., L. A. Haskin, R. O. Colson, and M. Wadhwa (1993), Partitioning in Ree-Saturating Minerals - Theory, Experiment, and Modeling of Whitlockite, Apatite, and Evolution of Lunar Residual Magmas, *Geochimica Et Cosmochimica Acta*, 57(16), 4069-4094.
- Jolliff, B. L., and L. A. Haskin (1995), Cogenetic Rock Fragments from a Lunar Soil - Evidence of a Ferroan Noritic-Anorthosite Pluton on the Moon, *Geochimica Et Cosmochimica Acta*, 59(11), 2345-2374.
- Jolliff, B. L., J. J. Gillis, L. A. Haskin, R. L. Korotev, and M. A. Wieczorek (2000), Major lunar crustal terranes: Surface expressions and crust-mantle origins, *J. Geophys. Res.-Planets*, 105(E2), 4197-4216.
- Keller, L. P., and D. S. McKay (1997), The nature and origin of rims on lunar soil grains, *Geochimica Et Cosmochimica Acta*, 61(11), 2331-2341.
- Keller, L. P., S. Wentworth, and D. McKay (1998), Space Weathering: Reflectance spectroscopy and TEM analysis of individual lunar soil grains, *Proceedings of Lunar and Planetary Science, XXVIX*, abstract #1762.
- Khan, A., K. Mosegaard, and K. L. Rasmussen (2000), A new seismic velocity model for the Moon from a monte carlo inversion of the Apollo lunar seismic data, *Geophys. Res. Lett.*, 27, 1591-1594.

- Khan, A., and K. Mosegaard (2002), An enquiry into the lunar interior--A non-linear inversion of the Apollo lunar seismic data, *J. Geophys. Res.*, *107*(E6), 2001JE001658.
- Knapp, S. A., J. W. Shervais, and L. A. Taylor (1984), Consortium breccia 14321: Petrology of the pristine highlands clasts, *Proc. Lunar Planet. Sci. Conf.*, *15*, 431-432.
- Korotev, R. L. (2000), The great lunar hot spot and the composition and origin of the Apollo mafic ("LKFM") impact-melt breccias, *Journal of Geophysical Research-Planets*, *105*(E2), 4317-4345.
- Korotev, R. L., and J. J. Gillis (2001), A new look at the Apollo 11 regolith and KREEP, *Journal of Geophysical Research-Planets*, *106*(E6), 12339-12353.
- Korotev, R. L., B. L. Jolliff, R. A. Zeigler, J. J. Gillis, and L. A. Haskin (2003), Feldspathic lunar meteorites and their implications for compositional remote sensing of the lunar surface and the composition of the lunar crust, *Geochim. Cosmochim. Acta*, *67*(24), 4895-4923.
- Korotev, R. L. (2005a), Lunar geochemistry as told by lunar meteorites, *Chemie Der Erde-Geochemistry*, *65*(4), 297-346.
- Korotev, R. L. (2005b), The myth of the magnesian suite of lunar "highlands" rocks, *Meteoritics & Planetary Science*, *40*(9), A86-A86.
- Lawrence, D. J., W. C. Feldman, R. C. Elphic, R. C. Little, T. H. Prettyman, S. Maurice, P. G. Lucey, and A. B. Binder (2002), Iron abundances on the lunar surface as measured by the Lunar Prospector gamma-ray and neutron spectrometers, *J. Geophys. Res.-Planets*, *107*(E12), 5130.

- Lawrence, S. J., and P. G. Lucey (2007), Radiative transfer mixing models of meteoritic assemblages, *J. Geophys. Res.-Planets*, *112*(E7), 10.1029/2006je002765.
- Le Mouélic, S., Y. Langevin, and S. Erard (1999), A new data reduction approach for the Clementine NIR data set: Application to Aristillus, Aristarchus, and Kepler, *J. Geophys. Res.*, *104*(E2), 3833-3843.
- Le Mouélic, S., Y. Langevin, S. Erard, P. Pinet, S. Chevrel, and Y. Daydou (2000), Discrimination between maturity and composition of lunar soils from integrated Clementine UV-visible/near-infrared data: Application to the Aristarchus Plateau, *J. Geophys. Res.-Planets*, *105*(E4), 9445-9455.
- Le Mouélic, S., P. G. Lucey, Y. Langevin, and B. R. Hawke (2002), Calculating iron contents of lunar highland materials surrounding Tycho crater from integrated Clementine UV-visible and near-infrared data, *J. Geophys. Res.-Planets*, *107*(E10), 5074.
- Li, L. (2006), Partial least squares modeling to quantify lunar soil composition with hyperspectral reflectance measurements, *J. Geophys. Res.-Planets*, *111*(E4), 10.1029/2005je002598.
- Lindstrom, M. M., S. A. Knapp, J. W. Shervais, and L. A. Taylor (1984), Magnesian Anorthosites and Associated Troctolites and Dunite in Apollo-14 Breccias, *J. Geophys. Res.*, *89*, C41-C49.
- Lognonne, P., J. Gagnepain-Beyneix, and H. Chenet (2003), A new seismic model of the Moon: Implication for structure, thermal evolution and formation of the Moon, *Earth & Planet. Sci. Lett.*, *211*(1), 27-44.

- Longhi, J., and A. E. Boudreau (1979), Complex igneous processes and the formation of primitive lunar crustal rocks., *Proceedings of the Lunar and Planetary Science Conference, X*, 2085-2105.
- Longhi, J. (1980), A model of early lunar differentiation, *Proc. Lunar Planet. Sci. Conf., 11th*, 289-315.
- Longhi, J. (2003), A new view of lunar ferroan anorthosites: Post magma ocean petrogenesis, *Journal of Geophysical Research, 108*(E8), 5083.
- Lucey, P. G., B. R. Hawke, C. M. Pieters, J. W. Head, and T. B. Mccord (1986), A Compositional Study of the Aristarchus Region of the Moon Using near-Infrared Reflectance Spectroscopy, *Journal of Geophysical Research-Solid Earth and Planets, 91*(B4), D344-D354.
- Lucey, P. G., and B. R. Hawke (1989), A remote mineralogical perspective on gabbroic units in the lunar highlands, *Proc. Lunar Planet. Sci. Conf., 19th*, 355-363.
- Lucey, P. G., G. J. Taylor, and E. Malaret (1995), Abundance and Distribution of Iron on the Moon, *Science, 268*(5214), 1150-1153.
- Lucey, P. G. (1998), Model near-infrared optical constants of olivine and pyroxene as a function of iron content, *J. Geophys. Res.-Planets, 103*(E1), 1703-1713.
- Lucey, P. G., D. T. Blewett, G. J. Taylor, and B. R. Hawke (2000), Imaging of lunar surface maturity, *J. Geophys. Res.-Planets, 105*(E8), 20377-20386.
- Lucey, P. G. (2004), Mineral maps of the Moon, *Geophys. Res. Lett., 31*(8), 10.1029/2003GL019406.

- Lucey, P. G., J. J. Gillis, and D. Steutel (2004), Global images of Mg-number derived from Clementine data, *Lunar Planet. Sci. Conf., 35th*, abstract # 1717.
- Lucey, P. G. (2006), Radiative transfer modeling of the effect of mineralogy on some empirical methods for estimating iron concentration from multispectral imaging of the Moon, *J. Geophys. Res.-Planets*, 111.
- Lucey, P. G., R. L. Korotev, J. J. Gillis-Davis, L. A. Taylor, D. J. Lawrence, B. A. Campbell, R. C. Elphic, W. C. Feldman, L. L. Hood, D. Hunten, M. Mendillo, S. Nobel, J. J. Papike, R. C. Reedy, S. Lawson, T. H. Prettyman, O. Gasnault, and S. Maurice (2006), Understanding the Lunar Surface and Space-Moon Interactions, in *New Views of the Moon*, edited by B. L. Jolliff, Reviews in Mineralogy and Geochemistry.
- Lucey, P. G., and S. K. Noble (2008), Experimental test of a radiative transfer model of the optical effects of space weathering, *Icarus*, 197(1), 348-353.
- Ma, M.-S., R. A. Schmitt, G. J. Taylor, R. D. Warner, and K. Keil (1981), Chemical and petrographic study of spinel troctolite in 67435: Implication for the origin of Mg-rich plutonic rocks, *Proc. Lunar Planet. Sci. Conf.*, 12, 640-642.
- Marti, K., U. Aeschlimann, P. Eberhardt, J. Geiss, N. Grogler, D. T. Jost, J. C. Laul, M.-S. Ma, and R. A. Schmitt (1983), Pieces of the ancient lunar crust: Ages and composition of clasts in consortium breccia 67915, *Proc. Lunar Planet. Sci. Conf.*, 88, B165-B175.
- Marvin, U. B., and P. H. Warren (1980), A pristine eucrite-like gabbro from Descartes and its exotic kindred, *Proc. Lunar Planet. Sci. Conf.*, 11, 507-521.

- Marvin, U. B., J. W. Carey, and M. M. Lindstrom (1989), Cordierite-spinel troctolite, a new magnesium-rich lithology from the lunar highlands, *Science*, **243**, 925-928.
- Matsunaga, T., M. Ohtake, J. Haruyama, Y. Ogawa, R. Nakamura, Y. Yokota, T. Morota, C. Honda, M. Torii, M. Abe, T. Nimura, T. Hiroi, T. Arai, K. Saiki, H. Takeda, N. Hirata, S. Kodama, T. Sugihara, H. Demura, N. Asada, J. Terazono, and H. Otake (2008), Discoveries on the lithology of lunar crater central peaks by SELENE Spectral Profiler, *Geophys. Res. Lett.*, **35**(23), 10.1029/2008glo35868.
- McCord, T. B., R. N. Clark, B. R. Hawke, L. A. McFadden, P. D. Owensby, C. M. Pieters, and J. B. Adams (1981), Moon: Near-infrared spectral reflectance, a good first look, *J. Geophys. Res.*, **86**(B11), 10,883-810,892.
- McDowell, J. (2004), Lunar crater database, <http://host.planet4589.org/astro/lunar/>.
- McGee, J. J. (1993), Lunar ferroan anorthosites - Mineralogy, composition variations, and petrogenesis, *J. Geophys. Res.*, **98**(E5), 9089-9105.
- Melosh, H. J. (1989), *Impact Cratering: A Geologic Process*, 245 pp., Oxford Univ. Press, New York.
- Meyer, H. O. A., and R. H. McCallister (1973), Mineralogy and petrology of Apollo 16: Rock 60215,13, *Proc. Lunar Planet Sci. Conf.*, **4**, 661-665.
- Minkin, J. A., C. L. Thompson, and E. C. T. Chao (1977), Apollo 16 white boulder consortium samples 67455 and 67475 - Petrologic investigation, *Proc. Lunar Planet Sci. Conf.*, **8**.
- Morris, R. W., G. J. Taylor, H. E. Newsom, K. Keil, and S. R. Garcia (1990), Highly Evolved and Ultramafic Lithologies from Apollo-14 Soils, *Proc. Lunar Planet Sci. Conf.*, **20**, 61-75.

- Morrison, D. A. (1998), Did a thick South Pole-Aitken basin melt sheet differentiate to form cumulates? (abstract), *Lunar Planet. Sci., XXIX (CD-ROM)*, abstract 1657.
- Nehru, C. E., R. D. Warner, K. KEIL, and G. J. Taylor (1978), Metamorphism of brecciated ANT rocks - Anorthositic troctolite 72559 and norite 78527, *Proc. Lunar Planet Sci. Conf., 9*, 773-788.
- Noble, S. K., C. M. Pieters, L. A. Taylor, R. V. Morris, C. C. Allen, D. S. McKay, and L. P. Keller (2001), The optical properties of the finest fraction of lunar soil: implications for space weathering, *Meteoritics & Planetary Science*, *36*(1), 31-42.
- Noble, S. K., C. M. Pieters, T. Hiroi, and L. A. Taylor (2006), Using the modified Gaussian model to extract quantitative data from lunar soils, *J. Geophys. Res.-Planets*, *111*(E11), 10.1029/2006je002721.
- Nord, G. L., and M.-V. Wandless (1983), Petrology and comparative thermal and mechanical histories of clasts in breccia 62236, *Proc. Lunar Planet Sci. Conf., 88*, A645-A657.
- Norman, M. D., L. Nyquist, D. Bogard, L. Borg, H. Weismann, D. Garrison, R. Young, C.-Y. Shih, and C. Schwandt (2000), Age and origin of the highlands crust of the Moon: Isotopic and petrologic studies of a ferroan noritic anorthosite clast from Descartes Breccia 67215, *Lunar Planet. Sci. Conf., 31st*, #1552.
- Norman, M. D., L. E. Borg, L. E. Nyquist, and D. D. Bogard (2003), Chronology, geochemistry, and petrology of a ferroan noritic anorthosite clast from Descartes breccia 67215: Clues to the age, origin, structure, and impact history of the lunar crust, *Meteoritics & Planetary Science*, *38*(4), 645-661.

- O'Keefe, J. D., and T. J. Ahrens (1993), Planetary cratering mechanics, *Journal of Geophysical Research*, **98**(17011-17028).
- Ohtake, M., T. Matsunaga, J. Haruyama, Y. Yokota, T. Morota, C. Honda, Y. Ogawa, M. Torii, H. Miyamoto, T. Arai, N. Hirata, A. Iwasaki, R. Nakamura, T. Hiroi, T. Sugihara, H. Takeda, H. Otake, C. M. Pieters, K. Saiki, K. Kitazato, M. Abe, N. Asada, H. Demura, Y. Yamaguchi, S. Sasaki, S. Kodama, J. Terazono, M. Shirao, A. Yamaji, S. Minami, H. Akiyama, and J. L. Josset (2009), The global distribution of pure anorthosite on the Moon, *Nature*, **461**(7261), 236-U110, Doi 10.1038/Nature08317.
- Papike, J. J., G. W. Fowler, and C. K. Shearer (1994), Orthopyroxene as a recorder of lunar crust evolution: An ion microprobe investigation of Mg-suite norites., *American Mineralogist*, **79**, 796-800.
- Papike, J. J., G. W. Fowler, and C. K. Shearer (1996), Ion microprobe investigation of plagioclase and orthopyroxene from lunar Mg-suite norites: implications for calculating parental melt REE concentrations and for assessing post crystallization REE redistribution., *Geochimica Et Cosmochimica Acta*, **60**, 3967-3978.
- Paquin, R. A. (Ed.) (1995), *Properties of metals*, McGraw-Hill, New York.
- Pieters, C., Y. Shkuratov, V. Kaydash, D. Stankevich, and L. Taylor (2006), Lunar soil characterization consortium analyses: Pyroxene and maturity estimates derived from Clementine image data, *Icarus*, **184**(1), 83-101.
- Pieters, C. M. (1978), Mare basalt types on the front side of the moon: A summary of spectral reflectance data., *Proc. Lunar Planet Sci. Conf.*, **9th**, 2825.

- Pieters, C. M. (1982), Copernicus Crater Central Peak - Lunar Mountain of Unique Composition, *Science*, 215(4528), 59-61.
- Pieters, C. M. (1986), Composition of the Lunar Highland Crust from near-Infrared Spectroscopy, *Reviews of Geophysics*, 24(3), 557-578.
- Pieters, C. M. (1993), Compositional diversity and stratigraphy of the lunar crust derived from reflectance spectroscopy, in *Remote geochemical analysis: elemental and mineralogical composition (Topics in remote sensing 4)*, edited by P. A. J. Englert and C. M. Pieters, pp. xxiii, 594, Cambridge University Press, Cambridge New York.
- Pieters, C. M., E. M. Fischer, O. Rode, and A. Basu (1993), Optical effects of space weathering: The role of the finest fraction, *J. Geophys. Res.*, 98(E11), 20,817-820,824.
- Pieters, C. M., S. Tompkins, J. W. Head, and P. C. Hess (1997), Mineralogy of the mafic anomaly in the South Pole-Aitken Basin: Implication for excavation of the lunar mantle, *Geophys. Res. Lett.*, 24(15), 1903-1906.
- Pieters, C. M. (1999), The Moon as a calibration standard enabled by lunar samples, *New views of the Moon II: Understanding the Moon through the integration of diverse datasets*, #8025.
- Pieters, C. M., and S. Pratt (2000), Earth-based near-infrared collection of spectra for the Moon: A new PDS data set, *Lunar and Planet. Sci. XXXI*, abstract #2059.
- Pieters, C. M., L. A. Taylor, S. K. Noble, L. P. Keller, B. Hapke, R. V. Morris, C. C. Allen, D. S. McKay, and S. Wentworth (2000), Space weathering on airless bodies: Resolving a mystery with lunar samples, *Meteoritics & Planetary Science*, 35(5), 1101-1107.

- Pieters, C. M., J. W. Head, L. Gaddis, B. Jolliff, and M. Duke (2001), Rock types of South Pole-Aitken basin and extent of basaltic volcanism, *Journal of Geophysical Research-Planets*, *106*(E11), 28001-28022.
- Pieters, C. M., and T. Hiroi (2004), RELAB (Reflectance Experiment Laboratory): A NASA multiuser spectroscopy facility, *Lunar and Planetary Science Conference, XXXV*, Abstract 1720.
- Pieters, C. M., J. Boardman, B. Buratti, A. Chatterjee, R. Clark, T. Glavich, R. Green, J. Head, P. Isaacson, E. Malaret, T. McCord, J. Mustard, N. Petro, C. Runyon, M. Staid, J. Sunshine, L. Taylor, S. Tompkins, P. Varanasi, and M. White (2009a), The Moon Mineralogy Mapper (M³) on Chandrayaan-1, *Current Science*, *96*(4), 500-505.
- Pieters, C. M., J. Boardman, B. Buratti, R. Clark, J.-P. Combe, R. Green, J. N. Goswami, J. W. Head, M. Hicks, P. Isaacson, R. Klima, G. Kramer, S. Kumar, S. Lundeen, E. Malaret, T. B. McCord, J. Mustard, J. Nettles, N. Petro, C. Runyon, M. Staid, J. Sunshine, L. Taylor, S. Tompkins, and P. Varanasi (2009b), Mineralogy of the lunar crust in spatial context: First results from the Moon Mineralogy Mapper (M³), *Lunar and Planetary Science Conference, XXXX*, 2052.
- Pieters, C. M., J. N. Goswami, R. N. Clark, M. Annadurai, J. Boardman, B. Buratti, J.-P. Combe, M. D. Dyar, R. Green, J. W. Head, C. Hibbitts, M. Hicks, P. Isaacson, R. Klima, G. Kramer, S. Kumar, E. Livo, S. Lundeen, E. Malaret, T. McCord, J. Mustard, J. Nettles, N. Petro, C. Runyon, M. Staid, J. Sunshine, L. A. Taylor, S. Tompkins, and P. Varanasi (2009c), Character and Spatial Distribution of OH/H₂O on the Surface of the Moon Seen by M³ on Chandrayaan-1, *Science*, *10.1126/science.1178658*.

- Prettyman, T. H., D. J. Lawrence, D. T. Vaniman, R. C. Elphic, and W. C. Feldman (2002), Classification of regolith materials from Lunar Prospector data reveals a magnesium-rich highland province, *Workshop on Moon Beyond 2002*, #3069.
- Prettyman, T. H., J. J. Hagerty, R. C. Elphic, W. C. Feldman, D. J. Lawrence, G. W. McKinney, and D. T. Vaniman (2006), Elemental composition of the lunar surface: Analysis of gamma ray spectroscopy data from Lunar Prospector, *J. Geophys. Res.-Planets*, *111*(E12007), 10.1029/2005JE002656.
- Prinz, M., E. Dowty, K. Keil, and T. E. Bunch (1973), Spinel troctolite and anorthosite in Apollo 16 samples, *Science*, *179*(4068), 74-76.
- Raedeke, L. D., and I. S. McCallum (1980), A comparison of fractionation trends in the lunar crust and the Stillwater Complex, in *Proceedings of the Conference on the Lunar Highlands Crust*, edited by J. J. Papike and R. B. Merrill, pp. 133-153, Pergamon Press.
- Reid, A. M., A. R. Duncan, and S. H. Richardson (1977), In search of LKFM, *Proc. Lunar Sci. Conf.*, *8th*, 2321-2338.
- Ridley, W. I., N. J. Hubbard, J. M. Rhodes, H. Wiesmann, and B. M. Bansal (1973), The petrology of lunar breccia 15445 and petrogenetic implications, *J. Geol.*, *81*, 621-631.
- Roddy, D. J. (1977), Large-scale impact and explosion craters: Comparisons of morphological and structural analogs, in *Impacts and Explosion Cratering*, edited by D. J. Roddy, et al., pp. 815-841, Pergamon Press, New York.
- Roedder, E., and P. W. Weiblen (1974), Petrology of clasts in lunar breccia 67915, *Proc. Lunar Planet. Sci. Conf.*, *5*, 303-318.

- Rose, H. J. J., P. A. Baedeker, S. Berman, R. P. Christian, E. J. Dwornick, R. B. Finkelman, and M. M. Schnepfe (1975), Chemical composition of rocks and soils returned by the Apollo 15, 16, and 17 missions, *Proc. Lunar Planet. Sci. Conf.*, *6*, 1363-1373.
- Ryder, G., and J. F. Bower (1977), Petrology of Apollo 15 black-and-white rocks 15445 and 15455 - Fragments of the Imbrium impact melt sheet, *Proc. Lunar Planet. Sci. Conf.*, *8*, 1895-1923.
- Ryder, G., and J. A. Wood (1977), Serenitatis and Imbrium impact melts: Implications for large-scale layering in the lunar crust, *Proc. Lunar Planet. Sci. Conf.*, *8th*, 655-668.
- Ryder, G., and M. Norman (1978), *Catalog of pristine non-mare materials Part 1, Anorthosites*, Northrop Services, Inc., Houston, TX.
- Ryder, G. (1979), The chemical components of highlands breccias, *Proc. Lunar Planet. Sci. Conf.*, *10th*, 561-581.
- Ryder, G., and M. D. Norman (1979), A summary of the petrology and geochemistry of pristine highlands rocks, *Proc. Lunar Planet. Sci. Conf.*, *10*, 531-559.
- Ryder, G., and M. D. Norman (1980), *Catalog of Apollo 16*, NASA Johnson Space Center Curatorial Facility, Houston, TX.
- Ryder, G. (1985), *Catalog of Apollo 15 rocks*, Lunar and Planetary Institute; Northrop Services, Inc., Houston.
- Shearer, C. K., and H. E. Newsom (2000), W-Hf isotope abundances and the early origin and evolution of the Earth-Moon system, *Geochimica Et Cosmochimica Acta*, *64*(20), 3599-3613.

- Shearer, C. K., P. C. Hess, M. A. Wieczorek, M. E. Pritchard, E. M. Parmentier, L. E. Borg, J. Longhi, L. T. Elkins-Tanton, C. R. Neal, I. Antonenko, R. M. Canup, A. N. Halliday, T. L. Grove, B. H. Hager, D.-C. Lee, and U. Wiechert (2006), Chapter 4: Thermal and Magmatic Evolution of the Moon, in *New Views of the Moon*, edited by B. L. Jolliff, Mineralogical Society of America.
- Shervais, J. W., L. A. Taylor, J. C. Laul, and M. R. Smith (1984), Pristine Highland Clasts in Consortium Breccia-14305 - Petrology and Geochemistry, *J. Geophys. Res.*, **89**, C25-C40.
- Shervais, J. W., and J. J. McGee (1998a), KREEP in the western lunar highlands: Ion and electron microprobe study of alkali suite anorthosites and norites from Apollo 12 and 14., *American Mineralogist*, **84**(5-6), 806-820.
- Shervais, J. W., and J. J. McGee (1998b), Ion and electron microprobe study of troctolites, norite, and anorthosites from Apollo 14: Evidence for urKREEP assimilation during petrogenesis of Apollo 14 Mg-suite rocks, *Geochimica Et Cosmochimica Acta*, **62**(17), 3009-3023.
- Shih, C.-Y., B. M. Bansal, H. Wiesmann, E. J. Dasch, L. E. Nyquist, and D. D. Bogard (1990), Sm-Nd age of a pristine norite clast from breccia 15445, paper presented at Lunar Planet. Sci. Conf., Houston, TX.
- Smith, J. V., A. T. Anderson, R. C. Newton, E. J. Olsen, P. J. Wyllie, A. V. Crewe, M. S. Isaacson, and D. Johnson (1970), Petrologic history of the Moon inferred from petrography, mineralogy, and petrogenesis of Apollo 11 rocks, in *Proceedings of the Apollo 11 Lunar Science Conference*, edited, pp. 897-925, Pergamon Press, New York.
- Solomon, S. C., and J. Longhi (1977), Magma oceanography, 1, Thermal evolution, paper presented at Proc. Lunar Planet. Sci. Conf., Houston, TX.

- Solomon, S. C., and J. W. Head (1980), Lunar Mascon Basins - Lava Filling, Tectonics, and Evolution of the Lithosphere, *Reviews of Geophysics*, *18*(1), 107-141.
- Spudis, P. D., B. R. Hawke, and P. Lucey (1984), Composition of Orientale Basin Deposits and Implications for the Lunar Basin-Forming Process, *J. Geophys. Res.*, *89*, C197-C210.
- Spudis, P. D., and P. A. Davis (1986), A chemical and petrologic model of the lunar crust and implications for lunar crustal origin., *Proceedings of the Lunar and Planetary Science Conference, XVII*, E84-E90.
- Spudis, P. D., B. R. Hawke, and P. Lucey (1988), Materials and Formation of the Imbrium Basin, *Proc. Lunar and Planet. Sci. Conf.*, *18th*, 155-168.
- Spudis, P. D., B. R. Hawke, and P. G. Lucey (1989), Geology and deposits of the lunar Nectaris basin, *Proc. of the 19th Lunar Sci. Conf.*, 51-59.
- Steele, I. M., and J. V. Smith (1973), Mineralogy and petrology of some Apollo 16 rocks and fines: General petrologic model of moon, *Proc. Lunar Planet. Sci. Conf.*, *4*, 519-536.
- Stöffler, D., H.-D. Knoll, U. B. Marvin, C. H. Simonds, and P. H. Warren (1980), Recommended classification and nomenclature of lunar highland rock—A committee report, in *Proceedings of the conference on the lunar highland crust*, edited by J. J. Papike and R. B. Merrill, pp. 51-70, Pergamon Press, New York.
- Stöffler, D., A. Bischoff, R. Borchardt, A. Burghele, A. Deutsch, E. K. Jessberger, R. Ostertag, H. Palme, B. Spettel, W. U. Reimold, K. Wacker, and H. Wanke (1985), Composition and Evolution of the Lunar Crust in the Descartes Highlands, Apollo-16, *J. Geophys. Res.*, *90*, C449-C506.

- Sunshine, J. M., and C. M. Pieters (1993), Estimating Modal Abundances from the Spectra of Natural and Laboratory Pyroxene Mixtures Using the Modified Gaussian Model, *J. Geophys. Res.-Planets*, *98*(E5), 9075-9087.
- Taylor, L. A., and A. B. Mosie (1979), *Breccia guidebook #3, 67915*, NASA Johnson Space Center, Houston, TX.
- Taylor, L. A., A. Patchen, D. H. S. Taylor, J. G. Chambers, and D. S. McKay (1996), X-ray digital imaging petrography of lunar mare soils: Modal analyses of minerals and glasses, *Icarus*, *124*(2), 500-512.
- Taylor, L. A., C. Pieters, L. P. Keller, R. V. Morris, D. S. McKay, A. Patchen, and S. Wentworth (2001a), The effects of space weathering on Apollo 17 mare soils: Petrographic and chemical characterization, *Meteoritics & Planetary Science*, *36*(2), 285-299.
- Taylor, L. A., C. M. Pieters, L. P. Keller, R. V. Morris, and D. S. McKay (2001b), Lunar Mare Soils: Space weathering and the major effects of surface-correlated nanophase Fe, *J. Geophys. Res.-Planets*, *106*(E11), 27985-27999.
- Toksöz, M. N., F. Press, A. Dainty, K. Anderson, G. Latham, M. Ewing, J. Dorman, D. Lammlein, G. Sutton, and F. Duennebier (1972), Structure, composition, and properties of lunar crust, *Proc. Lunar Sci. Conf.*, *3rd*, 2527-2544.
- Tompkins, S., C. M. Pieters, J. F. Mustard, P. Pinet, and S. D. Chevrel (1994), Distribution of Materials Excavated by the Lunar Crater Bullialdus and Implications for the Geologic History of the Nubium Region, *Icarus*, *110*(2), 261-274.

- Tompkins, S., and C. M. Pieters (1999), Mineralogy of the lunar crust: Results from Clementine, *Meteor. Planet. Sci.*, *34*(1), 25-41.
- Warner, J. L., C. H. Simonds, and W. C. Phinney (1976a), Genetic distinction between anorthosites and Mg-rich plutonic rocks: New data from 76255, paper presented at Proc. Lunar Planet. Sci. Conf., Houston, TX.
- Warner, J. L., C. H. Simonds, and W. C. Phinney (1976b), Genetic distinction between anorthosites and Mg-rich plutonic rocks, *J. Geophys. Res., Proc. Lunar Sci. Conf.*, *8*, 2215-2235.
- Warner, J. L., C. H. Simonds, P. E. McGee, and A. Cochran (1978), Luna 24: Lateral heterogeneity in the lunar crust, in *Mare Crisium: The view from Luna 24*, edited by R. B. Merrill and J. J. Papike, pp. 229-244, Pergamon Press, New York.
- Warren, P. H., and J. T. Wasson (1977), Pristine nonmare rocks and the nature of the lunar crust, *Proc. Lunar and Planet. Sci. Conf.*, *8th*, 2215-2235.
- Warren, P. H., and J. T. Wasson (1978), Compositional-petrographic investigation of pristine non-mare rocks., *Proc. Lunar Planet. Sci. Conf.*, *9th*, 185-217.
- Warren, P. H. (1979), Certain pristine nonmare rocks formed as cumulates from the magma ocean (but many others did not), *Geochim Cosmochim Acta, Proceedings of the Conference on the Lunar Highlands Crust*, 192-194.
- Warren, P. H., and J. T. Wasson (1979), The compositional-petrographic search for pristine nonmare rocks-third foray., *Proc. Lunar Planet. Sci. Conf.*, *10th*, 583-610.

- Warren, P. H., and J. T. Wasson (1980), Further foraging for pristine nonmare rocks: Correlations between geochemistry and longitude, *Proc. Lunar Planet. Sci. Conf., 11th*, 431-470.
- Warren, P. H., G. J. Taylor, K. Keil, C. Marshal, and J. T. Wasson (1981), Foraging westward for pristine nonmare rocks: Complications for petrogenetic models., *Proc. Lunar Planet. Sci. Conf., 7th*, 21-40.
- Warren, P. H., G. J. Taylor, K. Keil, C. Marshall, and J. T. Wasson (1982), Foraging westward for pristine nonmare rocks: Complications for petrogenetic models, *Proc. Lunar Planet. Sci. Conf., 12th*, 21-40.
- Warren, P. H., G. J. Taylor, K. Keil, G. W. Kallemeyn, P. S. Rosener, and J. T. Wasson (1983a), Sixth foray for pristine nonmare rocks and an assessment of the diversity of lunar anorthosites, *Proc. Lunar Planet. Sci. Conf., 13th*, 88, A615-A630.
- Warren, P. H., G. J. Taylor, K. Keil, G. W. Kallemeyn, D. N. Shirley, and J. T. Wasson (1983b), Seventh Foray - Whitlockite-Rich Lithologies, a Diopside-Bearing Troctolitic Anorthosite, Ferroan Anorthosites, and Creep, *Proc. Lunar Planet. Sci. Conf., 13th*, 88, B151-B164.
- Warren, P. H., G. J. Taylor, K. Keil, D. N. Shirley, and J. T. Wasson (1983c), Petrology and Chemistry of 2 Large Granite Clasts from the Moon, *Earth Planet. Sci. Lett.*, 64(2), 175-185.
- Warren, P. H., and G. W. Kallemeyn (1984), Pristine Rocks (8th Foray) - Plagiophile Element Ratios, Crustal Genesis, and the Bulk Composition of the Moon, *Journal of Geophysical Research*, 89, C16-C24.

- Warren, P. H. (1985), The magma ocean concept and lunar evolution, *Ann. Rev. Earth Planet. Sci.*, *13*, 201-240.
- Warren, P. H. (1986), Anorthosite assimilation and the origin of the Mg/Fe-related bimodality of pristine moon rocks: support for the magmasphere hypothesis, paper presented at Proc. Lunar Planet. Sci. Conf., 16th, J. Geophys. Res., Houston, TX.
- Warren, P. H., D. N. Shirley, and G. W. Kallemeyn (1986), A potpourri of pristine lunar rocks, including a VHK mare basalt and a unique, augite-rich Apollo 17 anorthosite, *Proc. Lunar Planet. Sci. Conf.*, *16th*, *91*, D319-D330.
- Warren, P. H., E. A. Jerde, and G. W. Kallemeyn (1990), Pristine Moon Rocks - an Alkali Anorthosite with Coarse Augite Exsolution from Plagioclase, a Magnesian Harzburgite, and Other Oddities, *Proc. Lunar Planet. Sci. Conf.*, *20*, 31-59.
- Warren, P. H., E. A. Jerde, and G. W. Kallemeyn (1991), Pristine Moon Rocks - Apollo-17 Anorthosites, *Proc. Lunar Planet. Sci. Conf.*, *21*, 51-61.
- Warren, P. H. (2005), "New" lunar meteorites: Implications for composition of the global lunar surface, lunar crust, and the bulk Moon, *Meteor. Planet. Sci.*, *40*(3), 477-506.
- Warren, P. H., F. Ulf-Moller, and G. W. Kallemeyn (2005), "New" lunar meteorites: Impact melt and regolith breccias and large-scale heterogeneities of the upper lunar crust, *Meteor. Planet. Sci.*, *40*(7), 989-1014.
- Whitaker, E. A. (1972), Lunar color boundaries and their relationship to topographic features, *The Moon*, *4*(3/4), 348-355.

- Wieczorek, M. A., and R. J. Phillips (1998), Potential anomalies on a sphere: Applications to the thickness of the lunar crust, *Journal of Geophysical Research-Planets*, *103*(E1), 1715-1724.
- Wieczorek, M. A., and R. J. Phillips (2000), The "Procellarum KREEP Terrane": Implications for mare volcanism and lunar evolution, *J. Geophys. Res.-Planets*, *105*(E8), 20417-20430.
- Wieczorek, M. A., and M. T. Zuber (2001), The composition and origin of the lunar crust: Constraints from central peaks and crustal thickness modeling, *Geophys. Res. Lett.*, *28*(21), 4023-4026.
- Wieczorek, M. A., B. L. Jolliff, A. Khan, M. E. Pritchard, B. P. Weiss, J. G. Williams, L. L. Hood, K. Righter, C. R. Neal, C. K. Shearer, I. S. McCallum, S. Tompkins, B. R. Hawke, C. Peterson, J. J. Gillis, and B. Bussey (2006), Chapter 3: The Constitution and Structure of the Lunar Interior, in *New Views of the Moon*, edited by B. L. Jolliff, et al., Mineralogical Society of America.
- Wilcox, B. B., P. G. Lucey, and B. R. Hawke (2006), Radiative transfer modeling of compositions of lunar pyroclastic deposits, *Journal of Geophysical Research*, *111*, 10.1029/2006JE002686.
- Williams, K. K., and M. T. Zuber (1998), Measurement and analysis of lunar basin deposits from Clementine altimetry, *Icarus*, *131*, 107-122.
- Wood, J. A., J. S. Dickey Jr., U. B. Marvin, and B. N. Powell (1970), Lunar anorthosites and a geophysical model for the Moon, *Proc. of the Apollo 11 Lunar Science Conference*, 965-988.